Graduate School Form
30 Updated 12/26/2015

PURDUE UNIVERSITY
GRADUATE SCHOOL
Thesis/Dissertation Acceptance

This is to certify that the thesis/dissertation prepared

By Daniele Prada

Entitled

A HYBRIDIZABLE DISCONTINUOUS GALERKIN METHOD FOR NONLINEAR POROUS MEDIA VISCOELASTICITY WITH APPLICATIONS IN OPHTHALMOLOGY

For the degree of Doctor of Philosophy

Is approved by the final examining committee:

Giovanna Guidoboni Chair	Bernardo N. Cockburn
Luoding Zhu	
Julia Concetta Arciero	
Alon Harris	

To the best of my knowledge and as understood by the student in the Thesis/Dissertation Agreement, Publication Delay, and Certification Disclaimer (Graduate School Form 32), this thesis/dissertation adheres to the provisions of Purdue University's "Policy of Integrity in Research" and the use of copyright material.

Approved by Major Professor(s): Giovanna Guidoboni

Approved by: Evgeny Mukhin 12/3/2016

Head of the Departmental Graduate Program Date

A HYBRIDIZABLE DISCONTINUOUS GALERKIN METHOD FOR NONLINEAR POROUS MEDIA VISCOELASTICITY WITH APPLICATIONS IN OPHTHALMOLOGY

A Dissertation

Submitted to the Faculty

of

Purdue University

by

Daniele Prada

In Partial Fulfillment of the

Requirements for the Degree

of

Doctor of Philosophy

December 2016

Purdue University

Indianapolis, Indiana

And if I have the gift of prophecy and comprehend all mysteries and all knowledge;
if I have all faith so as to move mountains but do not have love, I am nothing.

The New American Bible, 1 Cor 13, 2.

ACKNOWLEDGMENTS

I am really grateful to all the people that have been supporting and collaborating with me over the last four years, in particular to my adviser and major professor, Giovanna Guidoboni. She is a great, honest, and passionate scientist and I really enjoyed working with her. Special thanks also to Alon Harris, director of clinical research at the Glick Eye Institute in Indianapolis, for believing in the work of my team and mentoring us on ocular physiology. Another great scientist and generous person I have been working with is Riccardo Sacco, associate professor in Numerical Analysis at Politecnico di Milano, Italy.

I had the honor of collaborating with many other excellent scientists: Bernardo Cockburn (University of Minnesota), Francisco Sayas and Allan Hungria (University of Delaware), Ray Sheppard (Scientific Applications and Performance Tuning at Indiana University), Christophe Prud'homme and Marcela Szopos (Université de Strasbourg, France), Julia Arciero (Indiana University-Purdue University Indianapolis), Rafael Grytz (University of Alabama at Birmingham), Samuele Terragni, Brent Siesky and Amelia Huang (Indiana University), Paola Causin (Università Statale di Milano, Italy), Silvia Bertoluzza (CNR-IMATI di Pavia, Italy). I also wish to acknowledge the valuable contribution of Alessandra Cantagallo, who realized the anatomic drawings (Figures 1.1, 1.2, 4.1, 4.2, 4.3, 4.4, 4.5) shown in this thesis and published in the journal *Survey of Ophthalmology* [1].

This work has been partially supported by a grant from Research to Prevent Blindness (RPB, New York, NY, USA), NSF DMS-1224195, NIH 1R21EY022101-01A1, an Indiana University Collaborative Research Grant of the Office of the Vice President for Research, the Chair Gutenberg funds of the Cercle Gutenberg (France) the Labex IRMIA (Université de Strasbourg, France), Lilly Endowment, Inc. for the Indiana University Pervasive Technology Institute, Indiana METACyt Initiative

at IU, partially supported by Lilly Endowment, Inc. The funding parties did not have any role in the study design, collection of data, analysis of data, writing of the manuscript.

Finally, I really thank the most important people in my life: my girlfriend Alessandra and my family, for all their love and support.

TABLE OF CONTENTS

Page

LIST OF TABLES vii

LIST OF FIGURES x

ABBREVIATIONS xiv

ABSTRACT xv

1 INTRODUCTION 1

2 ELEMENTS OF POROUS MEDIA THEORY 6
2.1 The Averaging Approach 6
2.2 Mixture Kinematics and Deformation 9
2.2.1 Describing Material Compressibility and Incompressibility in Deformable Porous Media 19
2.3 Balance Equations and Entropy Inequality 22
2.3.1 Balance of Mass 25
2.3.2 Balance of Linear Momentum 26
2.3.3 Balance of Angular Momentum 29
2.3.4 Balance of Energy 33
2.3.5 The Entropy Inequality 36
2.4 Constitutive Modeling 39
2.4.1 Principle of Material Objectivity 43
2.4.2 The Saturation and Incompressibility Constraints 48
2.4.3 Constitutive Variables and Evaluation of the Entropy Inequality 52
2.4.4 Linear Viscoelastic Models for the Solid Constituent 57
2.4.5 Darcy Law for the Fluid Constituent 89
2.5 A Poro-Viscoelastic Model 91

3 A HYBRIDIZABLE DISCONTINUOUS GALERKIN METHOD FOR POROUS MEDIA VISCOELASTICITY 96
3.1 Problem Setting 98
3.1.1 Existence of Solutions 101
3.2 Numerical Algorithm 107
3.2.1 Temporal Semi-Discretization 108
3.2.2 Fixed-Point Iteration 108
3.2.3 Spatial Discretization by the HDG Method 112
3.3 Numerical Experiments 122
3.3.1 Convergence Tests in 2D 123

Page

3.3.2 Sensitivity Analysis . . . 128
3.3.3 The Problem of Locking . . . 135
3.3.4 Convergence tests in 3D . . . 143
3.3.5 The Sponge's Problem . . . 148

4 MATHEMATICAL MODELING OF THE OPTIC NERVE HEAD PERFUSION . . . 155
4.1 Anatomy and Vascular Supply of the ONH . . . 156
4.1.1 Anatomy . . . 156
4.1.2 Vascular Supply . . . 159
4.2 Techniques for *In Vivo* Studies of ONH Hemodynamics . . . 164
4.2.1 Laser Doppler Flowmetry . . . 164
4.2.2 OCT Angiography . . . 166
4.2.3 Color Doppler Imaging . . . 167
4.2.4 Laser Speckle Flowgraphy . . . 168
4.3 Mathematical Modeling of ONH Mechanics and Hemodynamics . . . 169
4.3.1 Mechanics of the ONH . . . 170
4.3.2 Hemodynamics of the ONH . . . 171
4.4 Mathematical Modeling of Tissue Viscoelasticity and its Influence on the ONH Hemodynamics . . . 173
4.4.1 Methods . . . 175
4.4.2 Results . . . 184
4.4.3 Discussion . . . 192

5 CONCLUSIONS AND FUTURE DIRECTIONS . . . 194

LIST OF REFERENCES . . . 197

APPENDICES

Appendix A. Constitutive equations in mixed form . . . 210

Appendix B. Scaling . . . 212

Appendix C. Error tables . . . 215

VITA . . . 244

LIST OF TABLES

Table		Page
2.1	The governing equations for a binary porous model with one solid phase $\alpha = S$ and one fluid phase $\alpha = F$ satisfying assumptions 1–7.	44
2.2	The closed system of governing equations for a viscous fluid ($\alpha = F$) streaming through a viscoelastic solid constituent ($\alpha = S$).	93
3.1	Data for the eight meshes used in the experiments.	123
3.2	Combinations of U_{ref} and P_{ref} tested in the sensitivity analysis.	132
3.3	Data for the seven meshes used in the 3D experiments.	143
3.4	Boundary conditions in the 3D validation test cases.	144
3.5	Number of fixed point iterations in the nonlinear test case 2 in 3D.	146
3.6	Performance of the fixed point algorithm on test case 4 in 3D for $k = 1$ on the five coarsest meshes shown in Table 3.3.	149
4.1	Techniques for *in vivo* studies of ONH hemodynamics	165
4.2	Model geometrical and physical parameters. See Figure 4.7 for parameter definition.	177
C.1	Linear stationary validation test in 2D. Relative errors for different triangulations with the lowest order method $k = 1$.	215
C.2	Linear stationary validation test in 2D. Relative errors for different triangulations for $k = 2$.	216
C.3	Linear stationary validation test in 2D. Relative errors for different triangulations for $k = 3$.	217
C.4	Nonlinear stationary validation test in 2D. Relative errors for different triangulations for $k = 1$.	218
C.5	Nonlinear stationary validation test in 2D. Relative errors for different triangulations for $k = 2$.	219
C.6	Nonlinear stationary validation test in 2D. Relative errors for different triangulations for $k = 3$.	220
C.7	Linear time dependent validation test in 2D. Absolute errors for different triangulations for $k = 1$.	221

Table Page

C.8 Linear time dependent validation test in 2D. Absolute errors for different triangulations for $k = 2$. 222

C.9 Linear time dependent validation test in 2D. Absolute errors for different triangulations for $k = 3$. 223

C.10 Nonlinear time dependent validation test in 2D. Absolute errors for different triangulations for $k = 1$. 224

C.11 Nonlinear time dependent validation test in 2D. Absolute errors for different triangulations for $k = 2$. 225

C.12 Nonlinear time dependent validation test in 2D. Absolute errors for different triangulations for $k = 3$. 226

C.13 Effect of varying the elastic Lamé parameters in the validation test case 1 in 2D. Local bases of degree $k = 1$ have been used. The fluid pressure $p_h|_K$ was taken in $P^{k+1}(K)$. 227

C.14 Accuracy of $\mathbf{u}_h$ and $\hat{\mathbf{u}}_h$ is restored in test case 1 in 2D by taking the characteristic total stress $\sigma_c = 2\mu_e = 1.2 \times 10^7\,\mathrm{Pa}$, and all the other characteristic parameters equal to 1. 228

C.15 Accuracy of $\mathbf{u}_h$ and $\hat{\mathbf{u}}_h$ is restored in test case 2 in 2D by taking the characteristic total stress $\sigma_c = 2\mu_e = 1.2 \times 10^7\,\mathrm{Pa}$, and all the other characteristic parameters equal to 1. 229

C.16 Approximation errors for $P_{\mathrm{ref}}/U_{\mathrm{ref}} = 1 \times 10^4\,\mathrm{Pa\,m^{-1}}$ in the validation test case 1 in 2D. Local bases of degree $k = 1$ have been used. The fluid pressure $p_h|_K$ was taken in $P^{k+1}(K)$. 230

C.17 Approximation errors for $P_{\mathrm{ref}} = 1 \times 10^4\,\mathrm{Pa}, U_{\mathrm{ref}} = 1\,\mathrm{m}$ in the validation test case 2 in 2D. Local bases of degree $k = 1$ have been used. The fluid pressure $p_h|_K$ was taken in $P^{k+1}(K)$. 231

C.18 Effect of reducing the temporal step size Δt in the linear time dependent test case 3 in 2D. The mesh was fixed and Δt was taken as $\Delta t = T/r$ with $r = [20, 40, 80, 160, 320, 640, 1280, 2560]$. We used the formulation with $p_h|_K \in P^{k+1}(K), k = 1$. Absolute errors increase as Δt decreases. . . . 232

C.19 Effect of reducing the temporal step size Δt in the linear time dependent test case 3 in 2D. The mesh was fixed and Δt was taken as $\Delta t = T/r$ with $r = [20, 40, 80, 160, 320, 640, 1280, 2560]$. We used the formulation with $p_h|_K \in P^{k+1}(K), k = 4$. Absolute errors decrease linearly with Δt as expected. 233

C.20 Linear stationary validation test in 3D. Relative errors for different triangulations with the lowest order method $k = 1$. 234

Table Page

C.21 Linear stationary validation test in 3D. Relative errors for different triangulations and polynomial degree $k = 2$. 235

C.22 Linear stationary validation test in 3D. Relative errors for different triangulations and polynomial degree $k = 3$. 236

C.23 Nonlinear stationary validation test in 3D. Relative errors for different triangulations for $k = 1$. 237

C.24 Nonlinear stationary validation test in 3D. Relative errors for different triangulations for $k = 2$. 238

C.25 Nonlinear stationary validation test in 3D. Relative errors for different triangulations for $k = 3$. 239

C.26 Linear time dependent validation test in 3D. Absolute errors for different triangulations for $k = 1$. 240

C.27 Linear time dependent validation test in 3D. Absolute errors for different triangulations for $k = 2$. 241

C.28 Linear time dependent validation test in 3D. Absolute errors for different triangulations for $k = 3$. 242

C.29 Nonlinear time dependent validation test in 3D. Absolute errors for different triangulations for $k = 1$. 243

LIST OF FIGURES

Figure Page

1.1 Anatomy and vascular supply of the optic nerve head (ONH). The ONH includes the superficial nerve fiber layer, the prelaminar region, the laminar region, and the retrolaminar region [1]. 2

1.2 Zoom of the laminar region [1]. 3

2.1 Comparison between arbitrary volume elements dv in classical continuum mechanics (top) and in the theory of porous media (bottom). In classical continuum mechanics, dv is assumed to be made of one material only, whereas, in the theory of porous media, dv has its own complex microstructure. In the bottom figure, dv is assumed to consist of a solid and a fluid constituents. 7

2.2 Illustration of the statistical distribution of a binary porous medium consisting of living tissue and blood. 10

2.3 Representation of the motion of a solid phase and a fluid phase in a porous medium. 12

2.4 The reference configuration $B_{0\alpha}$ is mapped to the current configuration B by the mapping φ_α which carries the material point $\mathbf{X}_\alpha \in B_{0\alpha}$ to the point $\mathbf{x}(\mathbf{X}_\alpha, t) \in B$ and the material point $\mathbf{X}_\alpha + d\mathbf{X}_\alpha$ to $\mathbf{x}(\mathbf{X}_\alpha + d\mathbf{X}_\alpha, t)$. The undeformed line element $d\mathbf{X}_\alpha$ is carried to the deformed line element $d\mathbf{x}$. 16

2.5 Illustration of motivation for a multiplicative decomposition of the deformation gradient of the solid phase. The position vectors $\mathbf{X}_S$ and $\mathbf{x}$ represent the centroids of the volume elements in the reference and the actual placements, respectively, whereas $\mathbf{X}_{SR(\text{micro})}$ and $\mathbf{x}_{SR(\text{micro})}$ denote all the possible points in the volume elements. 19

2.6 Representation of the multiplicative decomposition of the deformation gradient for homogeneous deformations. 21

Figure Page

2.7 Phenomena common to many viscoelastic materials. For each row, the graph on the left represents a particular stress (σ) or strain (ε) input, whereas the graph on the right represents the corresponding strain or stress output: (first row) instantaneous elasticity; (second row) instantaneous elasticity (a) and creep (b) under constant stress; (third row) instantaneous elasticity (c) and stress relaxation (d) under constant strain; (fourth row) instantaneous elasticity (e), creep (f), instantaneous recovery (g), delayed recovery (h), and permanent set (i). 59

2.8 Behavior of a linear spring. 60

2.9 Behavior of a linear dashpot. 61

2.10 Behavior of a Maxwell model: (top) Maxwell model; (graphs on the left) creep and recovery; (graphs on the right) stress relaxation. 63

2.11 Behavior of a Voigt model: (left) Voigt model; (right) creep and recovery. 66

2.12 Behavior of a Kelvin model: (top) Kelvin model; (graphs on the left) creep and recovery; (graphs on the right) stress relaxation. 69

2.13 Generalized Maxwell model. 72

2.14 Generalized Kelvin model. 73

2.15 A discrete spectrum of the relaxation function. 76

2.16 Oscillating stress σ, strain ε and loss angle δ. 76

2.17 Magnitude of the complex modulus $|E^*|$ and internal damping $\tan\delta$ with a logarithmic scale for the frequency ω for a Kelvin model. 80

2.18 Extension of the Voigt model (see Figure 2.11) to three dimensions. . . 84

3.1 Examples of limiter functions that can be used in Algorithm 3.2.2 to ensure that the fluid volume fraction n is within physical limits, i.e. $0 < n < 1$. The limiter Π_{Lip} is only Lipschitz continuous and leads to limit cycles in the fixed-point iterations, whereas Π_{C^1} is $C^1(\mathbb{R})$ and does not cause such behavior. 112

3.2 Carman-Kozeny law for the permeability coefficient. 126

3.3 Domain and boundary conditions for the Barry and Mercer problem [86]. 136

3.4 The problem of Barry and Mercer: dimensionless fluid pressure computed by the HDG method at time $t^* = \pi/2$ (left) and $t^* = 3\pi/2$ (right), plotted on the deformed meshes. The solid displacement field has not been amplified. 138

Figure Page

3.5 HDG errors in Barry and Mercer's problem. The displacement error contains a kink at the initial time step. 139

3.6 Fluid pressure computed by the HDG method at the first time step using the time interval $\Delta t^* = 0.1\pi/2$ and permeability $\kappa = 1 \times 10^{-2}\,\mathrm{m}^2\,\mathrm{Pa}^{-1}\,\mathrm{s}^{-1}$. The solution does not exhibit nonphysical oscillations. 140

3.7 Fluid pressure computed by the HDG method at the first time step using a short time interval $\Delta t^* = 1 \times 10^{-5}\pi/2$ and low permeability $\kappa = 1 \times 10^{-6}\,\mathrm{m}^2\,\mathrm{Pa}^{-1}\,\mathrm{s}^{-1}$. Pressure oscillations are suppressed to a very good degree. 141

3.8 Dependence of the HDG solution on the Poisson's ratio in Barry and Mercer's problem. 142

3.9 The sponge problem: dimensionless fluid pressure and dimensionless Darcy velocity computed by the HDG method at the first and last time steps, i.e. $t^* = 0.005 + \Delta t^*$ and $t^* = 1$, respectively. In Figures 3.9(c) and 3.9(d), the Darcy velocity is characterized with streamlines, colored with the magnitude of the vector field. The streamlines are augmented with little pointers. The pointers face in the direction of the velocity, and their size is proportional to the magnitude of the velocity. 153

3.10 Effect of element size on the error of the HDG solution: (top-left) total stress; (top-right) solid displacement; (bottom-left) Darcy velocity; (bottom-right) fluid pressure. The element sizes $h = \sqrt{3}/2, \sqrt{3}/4$, and $\sqrt{3}/8$ correspond to a mesh with $384, 3072$, and 24576 tetrahedra, respectively. 154

4.1 Anatomy and vascular supply of the optic nerve head (ONH). The ONH includes the superficial nerve fiber layer, the prelaminar region, the laminar region, and the retrolaminar region [1]. 157

4.2 Superficial nerve fiber layer (SNFL). The SNFL receives oxygenated blood primarily from retinal arterioles. These small vessels, called epipapillary vessels, originate in the peripapillary SNFL and run toward the center of the ONH [1]. 159

4.3 Prelaminar region. The prelaminar region is mainly supplied by direct branches of the short posterior ciliary arteries (PCAs) and by branches of the circle of Zinn-Haller. The circle of Zinn-Haller, if present, is a complete or incomplete ring of arterioles within the perineural sclera formed by the confluence of branches of the short PCAs [1]. 160

Figure Page

4.4 Laminar region. Blood flow to the laminar region is provided by centripetal branches of the short PCAs. The centripetal branches arise either directly from the short PCAs or from the circle of Zinn-Haller. The lamina cribrosa is shown as a 3D network, as suggested in recent *in vivo* imaging studies based on optical coherence tomography (OCT) [127–130], and in finite element modeling studies [115, 131, 132] of the lamina cribrosa microarchitecture [1]. 161

4.5 Retrolaminar region. The retrolaminar region is supplied by the central retinal artery (CRA) and the pial system. The pial system is an anastomosing network of capillaries located immediately within the pia mater [1]. 163

4.6 Schematic representation of the mathematical model describing the lamina cribrosa in the ONH [74]. 174

4.7 Schematic representation of the geometry of the lamina cribrosa used in the numerical experiments: (top left and top right) geometrical parameters; (bottom left and bottom right) boundary surfaces: Γ_{pre}, prelaminar surface; Γ_{retro}, retrolaminar surface; Γ_{sclera}, interface with the sclera; Γ_{vessels}, interface with the central retinal vessels. See Table 4.2 for parameter values. 176

4.8 Data from Palko et al. [167] fitted using the Voigt model described in Chapter 2. The poor fit denotes that a more appropriate viscoelastic model is needed for the lamina cribrosa. 180

4.9 Model predictions for the continuous laminar displacement map in the sagittal direction for the experiment by Yang et al. [173]. Data are displayed on the deformed mesh. 186

4.10 Comparison between model predictions and experimental measurements of the anterior lamina displacements. Changes of maximum optic disc depth ΔMaxD with respect to the baseline at IOP$-$CSFp$=15$ mmHg are reported as a function of the IOP$-$CSFp difference. The predictions of the mathematical model (green line) are compared with experimental data by Morgan et al. [174]. 189

4.11 (top) IOP fluctuation pattern tested in the model; (bottom) integrated time rate of change of blood kinetic energy W in response to IOP variations treating the lamina cribrosa as an elastic (blue curve) or a viscoelastic (green curve) medium. 191

ABBREVIATIONS

BC	Boundary Condition
CDI	Color Doppler Imaging
CRA	Central Retinal Artery
CRV	Central Retinal Vein
CSFp	Cerebrospinal Fluid Pressure
EDV	End Diastolic Velocity
GMRES	Generalized Minimal Residual
HDG	Hybridizable Discontinuous Galerkin
IOP	Intraocular Pressure
LDF	Laser Doppler Flowmetry
LSFG	Laser Speckle Flowgraphy
OCT	Optical Coherence Tomography
ONH	Optic Nerve Head
OPP	Ocular Perfusion Pressure
PCA	Poster Ciliary Artery
PSV	Peak Systolic Velocity
RGC	Retinal Ganglion Cell
RLTp	Retro Laminar Tissue Pressure
SNFL	Superficial Nerve Fiber Layer

ABSTRACT

Prada, Daniele. Ph.D., Purdue University, December 2016. A Hybridizable Discontinuous Galerkin Method for Nonlinear Porous Media Viscoelasticity with Applications in Ophthalmology. Major Professor: Giovanna Guidoboni.

The interplay between biomechanics and blood perfusion in the optic nerve head (ONH) has a critical role in ocular pathologies, especially glaucomatous optic neuropathy. Elucidating the complex interactions of ONH perfusion and tissue structure in health and disease using current imaging methodologies is difficult, and mathematical modeling provides an approach to address these limitations.

The biophysical phenomena governing the ONH physiology occur at different scales in time and space and porous media theory provides an ideal framework to model them. We critically review fundamentals of porous media theory, paying particular attention to the assumptions leading to a continuum biphasic model for the phenomenological description of fluid flow through biological tissues exhibiting viscoelastic behavior. The resulting system of equations is solved via a numerical method based on a novel hybridizable discontinuous Galerkin finite element discretization that allows accurate approximations of stresses and discharge velocities, in addition to solid displacement and fluid pressure. The model is used to theoretically investigate the influence of tissue viscoelasticity on the blood perfusion of the lamina cribrosa in the ONH. Our results suggest that changes in viscoelastic properties of the lamina may compromise tissue perfusion in response to sudden variations of intraocular pressure, possibly leading to optic disc hemorrhages.

1. INTRODUCTION

Glaucoma is an optic neuropathy characterized by progressive death of retinal ganglion cells (RGCs) and irreversible vision loss. Glaucoma is the second leading cause of blindness world-wide [2], and yet its etiology and treatment remain unclear. The main modifiable risk factor in glaucoma patients is elevated intraocular pressure (IOP) [3–7]; however, a high percentage of individuals with elevated IOP (a condition called ocular hypertension) never develop glaucoma [8], and many glaucoma patients continue to experience disease progression despite lowering IOP to target levels or have no history of elevated IOP - a condition called normal tension glaucoma [9]. Thus, it has been hypothesized that different individuals may have different susceptibilities to glaucomatous damage for the same IOP level. The identification of the factors determining IOP susceptibility is one of the main open questions in the field [10].

In glaucoma the location of damage to nerve cells is hypothesized to be predominantly in the ONH (see Figure 1.1) [11]. Elevated IOP may induce mechanical damage on the RGCs (*mechanical hypothesis*) and/or alterations in ocular circulation (*hemodynamical hypothesis*), compromising the functionality of the RGCs and their axons and progressively leading to vision loss. It is reasonable to expect that mechanical deformations of a living tissue would affect blood flow within the tissue. On the other hand, alterations in blood flow might lead to structural changes in the tissue that would alter its mechanical properties.

Elucidating the complex interactions of ONH blood perfusion and tissue structure in health and disease using current imaging methodologies is difficult, and mathematical modeling provides an approach to address these limitations. One of the main difficulties lies in the fact that the biophysical phenomena governing the ONH physiology occur at different scales in time and space. For example, the ocular perfusion

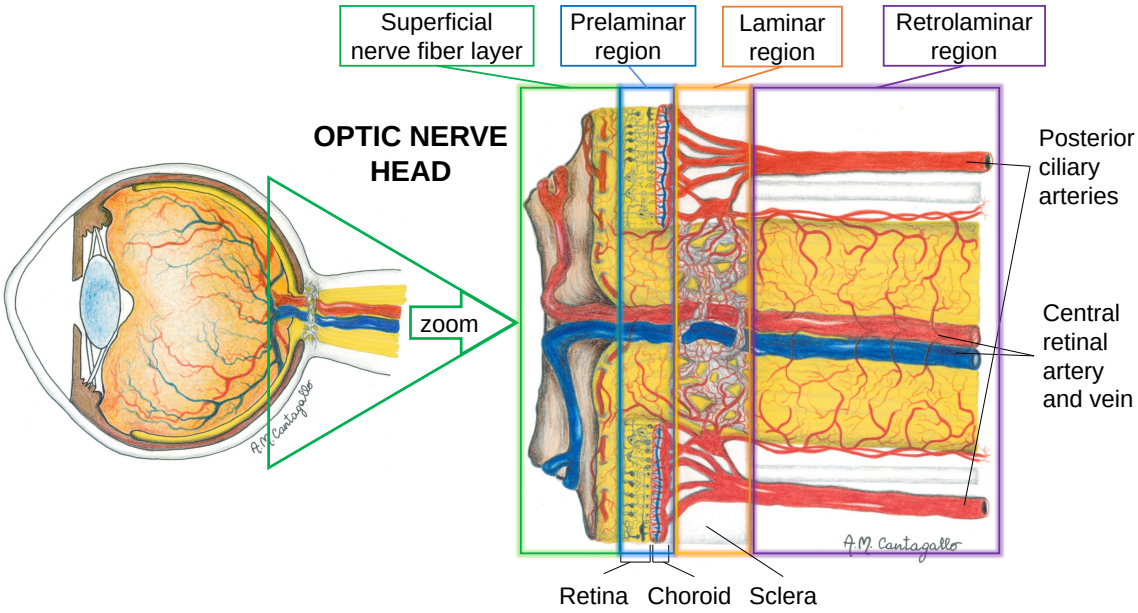

Figure 1.1. Anatomy and vascular supply of the optic nerve head (ONH). The ONH includes the superficial nerve fiber layer, the prelaminar region, the laminar region, and the retrolaminar region [1].

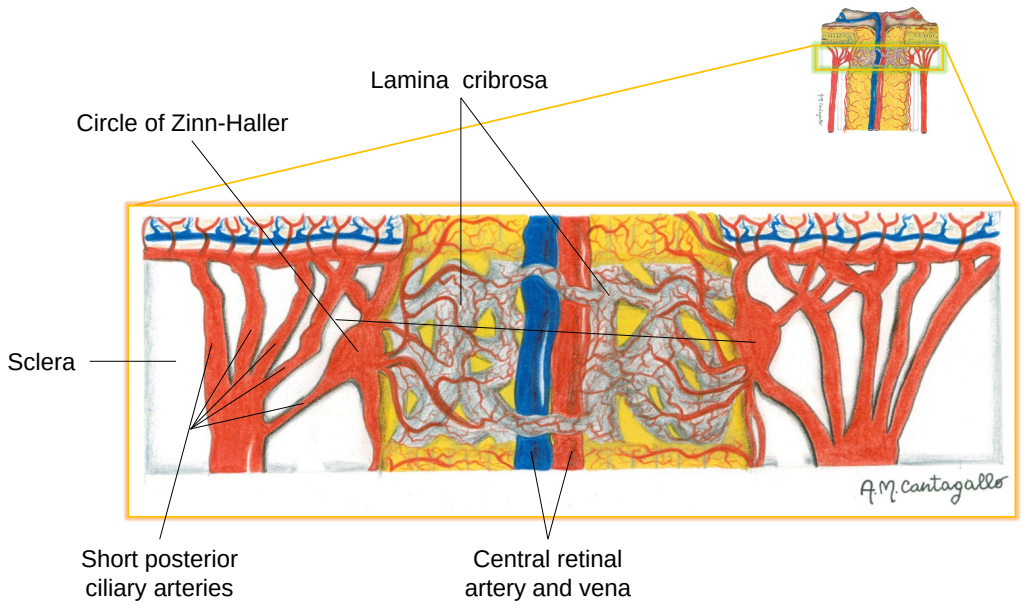

Figure 1.2. Zoom of the laminar region [1].

pressure (OPP), which is the pressure available to drive blood through the intraocular vasculature [12], undergoes significant changes within one cardiac cycle ($\approx 1\,\mathrm{s}$), whereas the biomechanically induced remodeling of the collagen network in the ONH takes several months or years. Different space scales are also involved: blood perfusion of the lamina cribrosa in the ONH ranges over at least 3 orders of magnitude as we progress from the capillaries running within the laminar beams ($\approx 1 \times 10^{-6}\,\mathrm{m}$) to the dimensions of the optic nerve canal ($\approx 1 \times 10^{-3}\,\mathrm{m}$) [1].

Porous media theory [13] provides an ideal framework to model materials with several components characterized by a variety of spatial scales. Within this theory, the complex composition and geometrical arrangement of the components are homogenized, so that physical quantities, such as velocity, stress, and fluid pressure are averages of the individual molecular counterparts. We use this approach to describe the blood perfusion of the lamina cribrosa in the ONH, whose complex structure is

depicted in Figure 1.2. The lamina is treated as a poro-viscoelastic material, where blood vessels are viewed as pores in a solid matrix. This model provides a theoretical description of the coupling between lamina biomechanics and hemodynamics.

There is a huge literature about numerical methods for solving poro-elastic models, whereas less works focus on the poro-viscoelastic case. Typically, the Backward Euler method has been adopted for time discretization, whereas various techniques, including finite difference schemes [14] and finite element methods [15], have been proposed for spatial discretization. Within the context of finite element methods, two main strategies have been investigated. For a fluid-solid mixture under the assumption of full saturation, the first strategy consists in formulating the problem in terms of the displacement of the solid phase $\mathbf{u}$ and the fluid pressure p, which are then approximated using the Taylor-Hood finite element space [16]. This approach is also called a *two-field formulation*. The second strategy consists in formulating the problem in terms of the original pair $(\mathbf{u}, p)$, as well as the total stress tensor $\underline{\underline{\sigma}}$ and the discharge velocity $\mathbf{v}$, which are usually variables of primary interest, especially within the context of biomechanical applications. This approach is also called a *four-field formulation*. In the four-field formulation, the Taylor-Hood finite element space is still used to approximate $\mathbf{u}$ and p, whereas the Raviart-Thomas finite element space [16] is chosen to approximate the pair $(\underline{\underline{\sigma}}, \mathbf{v})$. Yet another finite element approach is proposed by Phillips and Wheeler [17, 18], where $\mathbf{v}$ and p are approximated by Raviart-Thomas elements, and the displacement $\mathbf{u}$ by a family of discontinuous Galerkin methods.

In this work, we adopt the Backward Euler method for time discretization and the four-field finite element approach for spatial discretization. We extend the four-field approach using hybridizable discontinuous Galerkin (HDG) methods [19], thus approximating all the variables at optimal convergence with respect to the choice of approximating spaces. HDG methods require less degrees of freedom in the solution of the global system than other discontinuous Galerkin methods of comparable accuracy.

This thesis is organized as follows. In Chapter 2, we critically review fundamentals of porous media theory. We pay particular attention to the assumptions leading to a continuum biphasic model for the phenomenological description of fluid flow through biological tissues exhibiting viscoelastic behavior. In Chapter 3, we present the numerical method for the solution of the resulting system of equations. In Chapter 4, the model discussed in the two previous chapters is used to theoretically investigate the influence of tissue viscoelasticity on the perfusion of the lamina cribrosa in the ONH. Our results suggest that changes in viscoelastic properties of the lamina may compromise tissue perfusion in response to sudden variations of IOP, possibly leading to disc hemorrhages. Conclusions are outlined in Chapter 5. In Appendix A, we show how the constitutive equation for the total stress tensor $\underline{\underline{\sigma}}$ can be formulated in mixed form in the four-field method. In Appendix B, the poro-viscoelastic model considered in this thesis is rewritten in terms of dimensionless variables. Error tables for the validation tests discussed in Chapter 3 are given in Appendix C.

2. ELEMENTS OF POROUS MEDIA THEORY

In many areas of engineering, such as chemical engineering, material science, soil mechanics, as well as biomechanics, materials can consist of several solid components. These solid components can contain closed and open pores, such as ceramics and soils. The pores can be filled with fluids, which may interact with the solid components. Modeling these interactions is a delicate subject.

Whenever the exact description of the location of the pores and the thermodynamics of the components down to the microscale is not accessible, or even redundant, the heterogeneous composition of the mixture can be described through a homogenization approach. This approach led to the theory of porous media. There is plenty of literature about porous media theory and its application to different areas of engineering. In this chapter, we will provide few fundamental concepts that will be used throughout this thesis. The main references used for this chapter are the works of de Boer [13], Coussy [20], Whitaker [21], and Markert [22].

2.1 The Averaging Approach

In the theory of porous media, an arbitrary volume element dv is associated with *every* point in space identified by the position vector $\mathbf{x}$ with respect to a Cartesian reference frame whose origin is denoted by $\mathbf{0}$ and the directions of the orthogonal axes are denoted by $\mathbf{e}_1, \mathbf{e}_2$ and $\mathbf{e}_3$. Such a volume can be thought of as a statistically representative of the material in the neighborhood of $\mathbf{x}$. In general, its characteristic dimension should be much smaller than the characteristic dimension of the problem being modeled, and larger than its largest micro-structural dimension [23]. Unlike classical continuum mechanics, where a volume element is assumed to consist of one

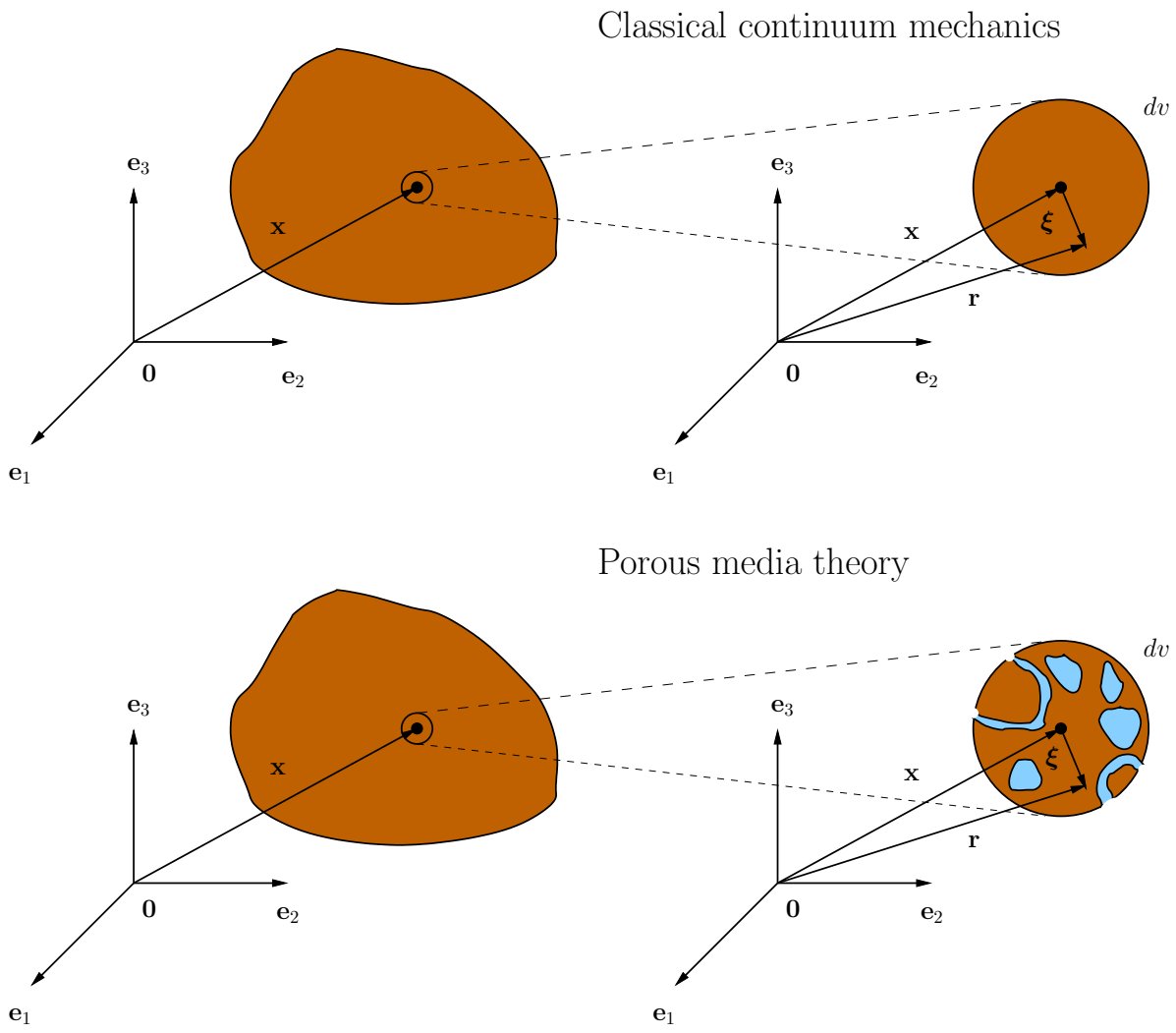

Figure 2.1. Comparison between arbitrary volume elements dv in classical continuum mechanics (top) and in the theory of porous media (bottom). In classical continuum mechanics, dv is assumed to be made of one material only, whereas, in the theory of porous media, dv has its own complex micro-structure. In the bottom figure, dv is assumed to consist of a solid and a fluid constituents.

material only, in the theory of porous media dv is not uniform, in general, consisting of various materials with different properties and shapes (see Figure 2.1).

The geometrical characterization of the pore structure and the exact location of the individual components of the body are disregarded in the averaging approach: the components are *spread* over the space that is shaped by the porous solid, so that each spatial point is simultaneously occupied by all the constituents. In the following, the terms *control space* or *domain* will be used to refer to the space shaped by the porous solid, interchangeably.

For a fixed point in space $\mathbf{x}$, homogenized, or averaged, quantities can be obtained by integrating a microscopic quantity over the region of an elementary volume dv centered at $\mathbf{x}$. Let $\mathbf{r}$ describe the position of a constituent within dv, $\mathbf{x}$ the position vector at the center of dv (see Figure 2.1), and t the time. First, we introduce an indicator function χ_α for each constituent α

$$\chi_\alpha = \chi_\alpha(\mathbf{r}, t) = \begin{cases} 1 & \text{for } \mathbf{r} \in dv_\alpha, \\ 0 & \text{for } \mathbf{r} \in dv_\beta \end{cases}, \qquad \beta \neq \alpha,$$

where the partial volume occupied by constituent α, dv_α, is given by

$$dv_\alpha(\mathbf{x}, t) = \int_{dv} \chi_\alpha(\mathbf{r}, t)\, d\mathbf{r}.$$

The *volume fraction* n_α is defined as the ratio between the partial volume dv_α and the total volume dv

$$n_\alpha(\mathbf{x}, t) = \frac{dv_\alpha}{dv} = \frac{1}{dv} \int_{dv} \chi_\alpha(\mathbf{r}, t)\, d\mathbf{r}. \tag{2.1}$$

In this work, we will assume that the control space shaped by a porous medium is completely filled by its κ constituents. This *saturation constraint* can be expressed as

$$\sum_{\alpha=1}^{\kappa} n_\alpha = 1. \tag{2.2}$$

The indicator function χ_α allows to derive average macroscopic quantities from microscopic quantities. For example, let the microscopic true density of the constituent materials be denoted by

$$\rho_{\alpha T} = \rho_{\alpha T}(\mathbf{r}, t).$$

The corresponding macroscopic field is

$$\rho_{\alpha R}(\mathbf{x},t) = \frac{1}{dv_\alpha}\int_{dv} \rho_{\alpha T}(\mathbf{r},t)\chi_\alpha(\mathbf{r},t)\,d\mathbf{r}. \tag{2.3}$$

The quantity $\rho_{\alpha R}$ represents the real density of a constituent α averaged over the real volume it occupies inside dv. Another important quantity is

$$\rho_\alpha(\mathbf{x},t) = \frac{1}{dv}\int_{dv} \rho_{\alpha T}(\mathbf{r},t)\chi_\alpha(\mathbf{r},t)\,d\mathbf{r}, \tag{2.4}$$

which is called *partial density* and represents the averaged reduced density of a constituent after being *smeared* over the volume element dv. The macroscopic real and partial densities, denoted by $\rho_{\alpha R}$ and ρ_α, respectively, are related by

$$\rho_\alpha(\mathbf{x},t) = n_\alpha(\mathbf{x},t)\rho_{\alpha R}(\mathbf{x},t). \tag{2.5}$$

The idea of deriving macroscopic quantities from microscopic quantities is somewhat similar to the continuum hypothesis in continuum mechanics. In the continuum hypothesis we assume that we can replace the discrete particles by a continuous distribution of matter, so that kinematic quantities such as acceleration, velocity and displacement are the averages of the individual molecular counterparts. Similarly, in porous media theory, we introduce distributed masses and forces that are function of the position vector $\mathbf{x}$ and, due to the volume fraction concept, can be interpreted as the integral average values of the real quantities (see equations (2.3), (2.4) and Figure 2.2).

2.2 Mixture Kinematics and Deformation

Kinematics in porous media theory is based on two fundamental assumptions:

Assumption 1. Each spatial point of the actual placement is *simultaneously* occupied by material points of all κ constituents at time t. The material points proceed from different reference positions $\mathbf{X}_\alpha$ at time $t = t_0$.

Assumption 2. Each constituent is assigned an independent state of motion.

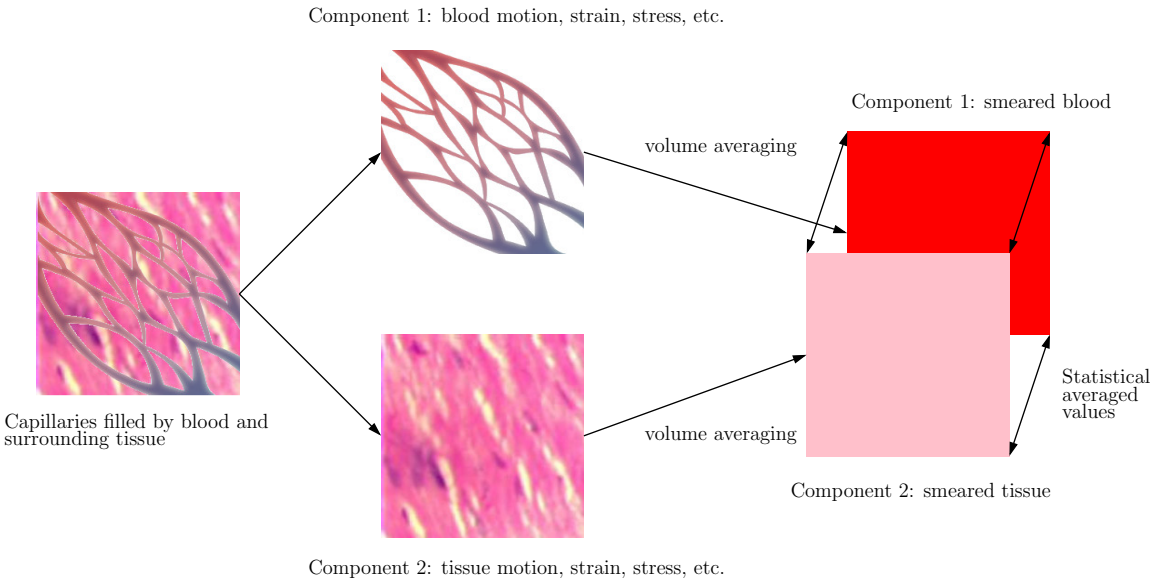

Figure 2.2. Illustration of the statistical distribution of a binary porous medium consisting of living tissue and blood.

To account for an independent state of motion for each constituent, we need to introduce a function φ_α from its reference configuration $B_{0\alpha}$ to the actual placement B, sometimes called a *deformation map*. The position $\mathbf{x}$ at time t is given by the continuous map

$$\begin{aligned} \varphi_\alpha \colon B_{0\alpha} \times [0,T) &\to B \\ (\mathbf{X}_\alpha, t) \qquad &\to \mathbf{x} = \varphi_\alpha(\mathbf{X}_\alpha, t), \end{aligned} \tag{2.6}$$

with $B_{0\alpha} \subset \mathbb{R}^3, B \subset \mathbb{R}^3$. In the following, $\varphi_\alpha(\mathbf{X}_\alpha, t)$ will also be denoted by $\mathbf{x}(\mathbf{X}_\alpha, t)$. The position vector $\mathbf{x}$ is an element of the control space of the porous solid at time t. If we consider a porous medium made by two phases, precisely one solid phase and one fluid phase, Assumption 1 implies

$$\mathbf{x} = \varphi_S(\mathbf{X}_S, t) = \varphi_F(\mathbf{X}_F, t),$$

as depicted in Figure 2.3. In the last equation, the current position is treated as a function of the original position. This is called a *Lagrangian* or material description. Any other field is also treated as a function of the original position. In general, it is not necessary to require that the initial configurations of the solid and fluid phases be the same (see Figure 2.3). If there is no relative motion among the components α, than all φ_α are the same and all $B_{0\alpha}$ are the same. However, if there is relative motion among the components of the mixture, then φ_α and $B_{0\alpha}$ will be different for each α.

On physical grounds, we expect that matter cannot be destroyed and matter does not interpenetrate. A deformation map will be consistent with these conditions if it is one-to-one and the Jacobian of the mapping remains nonzero. The Jacobian of the mapping is the determinant of the tensor

$$\begin{aligned} \underline{\underline{F}}_\alpha \colon B_{0\alpha} \times [0,T) &\to \mathbb{R}^3 \times \mathbb{R}^3 \\ (\mathbf{X}_\alpha, t) \qquad &\to \underline{\underline{F}}_\alpha = \nabla_\alpha \varphi_\alpha = \frac{\partial \mathbf{x}}{\partial \mathbf{X}_\alpha}, \end{aligned}$$

which is called *deformation gradient*. It describes the mapping from reference line elements to deformed line elements. The operator ∇_α denotes partial differentiation

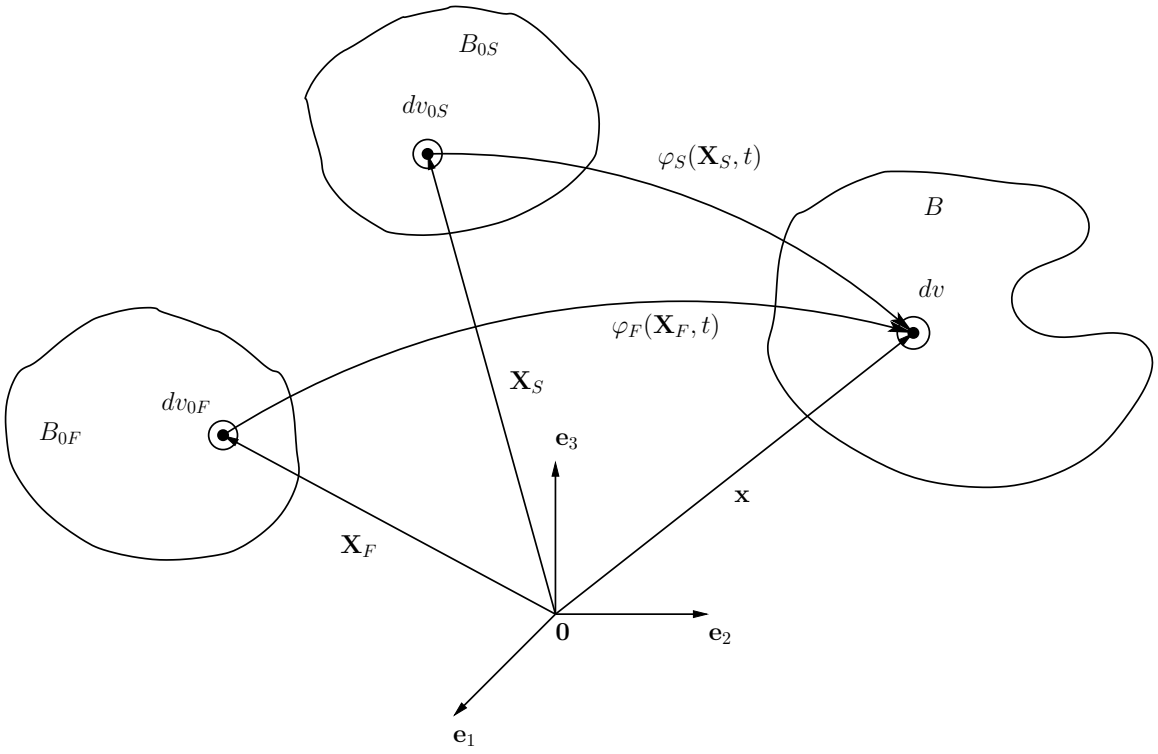

Figure 2.3. Representation of the motion of a solid phase and a fluid phase in a porous medium.

with respect to the coordinates $\mathbf{X}_\alpha$ in the reference configuration of constituent α. Its components are given by

$$F_\alpha^{IJ} = \frac{\partial x^I}{\partial X_\alpha^J}, \qquad \text{for } I, J \in \{1, 2, 3\}.$$

Our physical constraints demand that

$$J_\alpha = \det \underline{\underline{F}}_\alpha \neq 0, \tag{2.7}$$

at each position $\mathbf{x} = \varphi_\alpha(X_\alpha, t)$ and time t. Even more, we require $J_\alpha > 0$, which ensures that material lines preserve their relative orientations: a constituent cannot deform into its mirror image. If equation (2.7) is satisfied, then a (local) inverse mapping can be constructed that gives the reference position of constituent α as a function of the current position

$$\begin{aligned} \varphi_\alpha^{-1} \colon B \times [0, T) &\to B_{0\alpha} \\ (\mathbf{x}, t) &\to \mathbf{X}_\alpha = \varphi_\alpha^{-1}(\mathbf{x}, t). \end{aligned} \tag{2.8}$$

In equation (2.8), the current position is the independent variable and this is called *Eulerian* or spatial description. In the Eulerian description, we observe the changes over time at a fixed point in the physical space. In the following, $\varphi_\alpha^{-1}(\mathbf{x}, t)$ will also be denoted by $\mathbf{X}_\alpha(\mathbf{x}, t)$.

The change in position of a material point of a constituent α between configurations $B_{0\alpha}$ and B is given by the *displacement* vector field

$$\mathbf{U}_\alpha = \mathbf{U}_\alpha(\mathbf{X}_\alpha, t) = \mathbf{x}(\mathbf{X}_\alpha, t) - \mathbf{X}_\alpha. \tag{2.9}$$

In equation (2.9), the displacement is treated as a function of the Lagrangian coordinates $\mathbf{X}_\alpha$. It can also be expressed from the Eulerian viewpoint as follows

$$\mathbf{u}_\alpha = \mathbf{u}_\alpha(\mathbf{x}, t) = \mathbf{x} - \mathbf{X}_\alpha(\mathbf{x}, t). \tag{2.10}$$

The *velocity* of a material point of a constituent α in the Lagrangian representation is given by

$$\mathbf{V}_\alpha(\mathbf{X}_\alpha, t) = \left.\frac{\partial \mathbf{U}_\alpha(\mathbf{X}_\alpha, t)}{\partial t}\right|_{\mathbf{X}_\alpha} = \left.\frac{\partial (\mathbf{x}(\mathbf{X}_\alpha, t) - \mathbf{X}_\alpha)}{\partial t}\right|_{\mathbf{X}_\alpha} = \left.\frac{\partial \mathbf{x}(\mathbf{X}_\alpha, t)}{\partial t}\right|_{\mathbf{X}_\alpha}, \tag{2.11}$$

where $\mathbf{X}_\alpha$ is held fixed during differentiation. In the Eulerian framework, the velocity must be defined as a function of a specific fixed point in space. Hence, the Eulerian velocity must be calculated by finding the material coordinate of component α that occupies the spatial location $\mathbf{x}$ at time t, namely

$$\mathbf{X}_\alpha = \varphi_\alpha^{-1}(\mathbf{x}, t),$$

so that

$$\mathbf{v}_\alpha(\mathbf{x}, t) = \left.\frac{\partial \mathbf{u}_\alpha(\mathbf{x}, t)}{\partial t}\right|_{\mathbf{X}_\alpha} = \left.\frac{\partial \mathbf{x}}{\partial t}\right|_{\mathbf{X}_\alpha} = \mathbf{V}_\alpha(\mathbf{X}_\alpha(\mathbf{x}, t), t).$$

The *acceleration* in the Lagrangian representation is given by

$$\mathbf{A}_\alpha(\mathbf{X}_\alpha, t) = \left.\frac{\partial \mathbf{V}_\alpha(\mathbf{X}_\alpha, t)}{\partial t}\right|_{\mathbf{X}_\alpha} = \left.\frac{\partial^2 \mathbf{U}_\alpha(\mathbf{X}_\alpha, t)}{\partial t^2}\right|_{\mathbf{X}_\alpha} = \left.\frac{\partial^2 \mathbf{x}(\mathbf{X}_\alpha, t)}{\partial t^2}\right|_{\mathbf{X}_\alpha}.$$

In the Eulerian framework, the velocity of a constituent α at a fixed point in space can change either because: (i) the material velocity changes with time or (ii) the material point is carried past the fixed point in space. Hence, the Eulerian acceleration is given by

$$\mathbf{a}_\alpha(\mathbf{x}, t) = \left.\frac{\partial \mathbf{v}(\mathbf{x}, t)}{\partial t}\right|_{\mathbf{X}_\alpha} = \left.\frac{\partial \mathbf{v}(\mathbf{x}(\mathbf{X}_\alpha, t), t)}{\partial t}\right|_{\mathbf{X}_\alpha}.$$

After application of the chain rule, the above equation becomes

$$\mathbf{a}_\alpha(\mathbf{x}, t) = \frac{\partial \mathbf{v}_\alpha}{\partial t} + \mathbf{v}_\alpha \cdot \nabla \mathbf{v}_\alpha. \tag{2.12}$$

The symbol ∇ denotes differentiation with respect to $\mathbf{x}$, as it clearly appears from the component form

$$a_\alpha^I(\mathbf{x}, t) = \frac{\partial v_\alpha^I}{\partial t} + v_\alpha^J \frac{\partial v_\alpha^I}{\partial x^J}.$$

We use the Einstein summation convention according to which any index that appears twice represents a sum over all values of that index. The first term $\partial \mathbf{v}_\alpha / \partial t$ corresponds to mechanism (i) mentioned above, whereas the second term $\mathbf{v}_\alpha \cdot \nabla \mathbf{v}_\alpha$ corresponds to mechanism (ii). The quantity $\nabla \mathbf{v}_\alpha$ is called the *spatial velocity gradient* and is defined as

$$\begin{aligned} \underline{\underline{L}}_\alpha \colon B \times [0, T) &\to \mathbb{R}^3 \times \mathbb{R}^3 \\ (\mathbf{x}, t) &\to \underline{\underline{L}}_\alpha = \nabla \mathbf{v}_\alpha(\mathbf{x}, t). \end{aligned}$$

The argument used to determine the acceleration can be used to define the rate of change of any property associated with the continuum. As the individual constituents follow, in general, different motions, different rates of change must be introduced. In the Lagrangian framework, for a scalar field $\Gamma(\mathbf{X}_\alpha, t) = \gamma(\mathbf{x}(\mathbf{X}_\alpha, t), t)$ the *material time derivative*, following the motion of constituent α, is

$$(\Gamma)'_\alpha = \frac{\partial \Gamma}{\partial t}. \tag{2.13}$$

In the Eulerian framework, using again the chain rule

$$(\gamma)'_\alpha = \frac{\partial \gamma}{\partial t} + \frac{\partial \gamma}{\partial x^K}\frac{\partial x^K}{\partial t} = \frac{\partial \gamma}{\partial t} + v^K_\alpha \frac{\partial \gamma}{\partial x^K} = \frac{\partial \gamma}{\partial t} + \mathbf{v}_\alpha \cdot \nabla \gamma. \tag{2.14}$$

Observe that the material derivative satisfies the usual product and chain rules for derivatives. From equation (2.11), the material velocity gradient of the constituent α is given by

$$(\underline{\underline{F}}_\alpha)'_\alpha = \nabla_\alpha \mathbf{V}_\alpha, \quad \text{or} \quad (F^{IJ}_\alpha)'_\alpha = \frac{\partial F^{IJ}_\alpha}{\partial t} = \frac{\partial}{\partial t}\left(\frac{\partial x^I(\mathbf{X}_\alpha, t)}{\partial X^J_\alpha}\right) = \frac{\partial V^I_\alpha}{\partial X^J_\alpha}. \tag{2.15}$$

The spatial velocity gradient is connected to the material velocity gradient by

$$(\underline{\underline{F}}_\alpha)'_\alpha = \underline{\underline{L}}_\alpha \underline{\underline{F}}_\alpha, \tag{2.16}$$

as it follows from equation (2.15) and the chain rule

$$(F^{IJ}_\alpha)'_\alpha = \frac{\partial V^I_\alpha}{\partial X^J_\alpha} = \frac{\partial V^I_\alpha(\mathbf{X}_\alpha(\mathbf{x}, t))}{\partial x^K}\frac{\partial x^K}{\partial X^J_\alpha} = \frac{\partial v^I_\alpha}{\partial x^K}\frac{\partial x^K}{\partial X^J_\alpha}.$$

The spatial velocity gradient $\underline{\underline{L}}_\alpha$ can be decomposed into the sum of its symmetric part $\underline{\underline{D}}_\alpha$ and its skew-symmetric part $\underline{\underline{W}}_\alpha$

$$\underline{\underline{L}}_\alpha = \underline{\underline{D}}_\alpha + \underline{\underline{W}}_\alpha,$$

with

$$\underline{\underline{D}}_\alpha = \frac{1}{2}(\underline{\underline{L}}_\alpha + \underline{\underline{L}}^T_\alpha), \qquad \underline{\underline{W}}_\alpha = \frac{1}{2}(\underline{\underline{L}}_\alpha - \underline{\underline{L}}^T_\alpha).$$

In order to quantify the deformation of a porous solid, we use line elements in the reference and actual placements (see Figure 2.4). Let $d\mathbf{X}_\alpha$ be a line element connecting two material points in the reference configuration $B_{0\alpha}$, and $d\mathbf{x}$ the corresponding

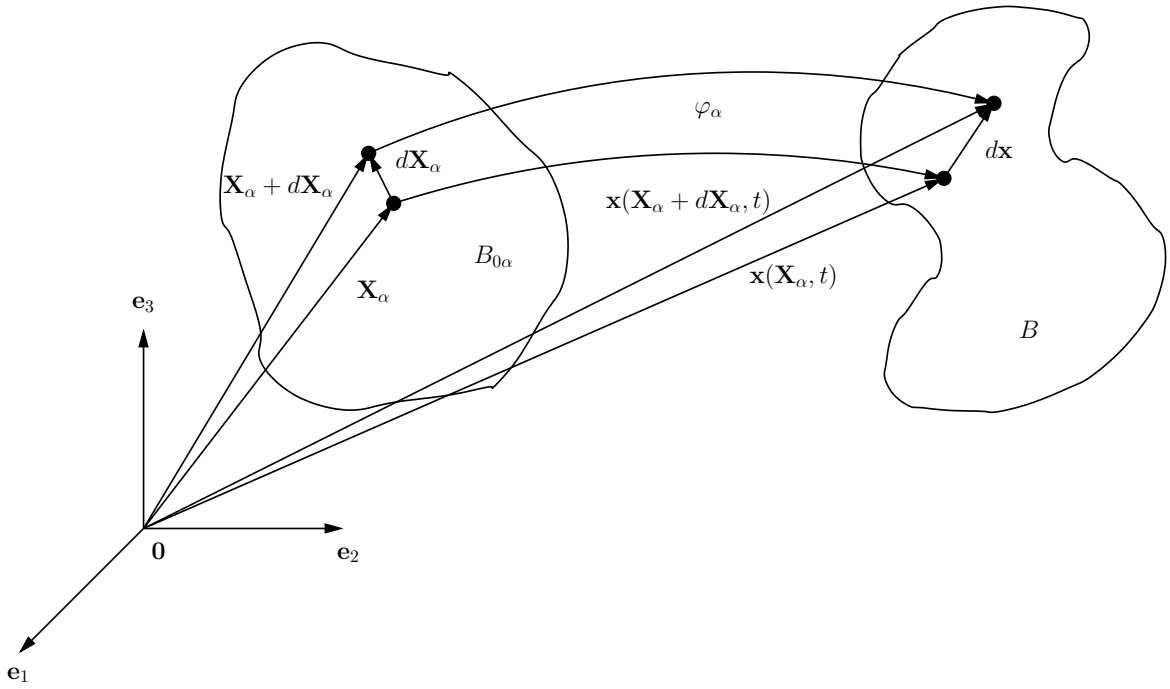

Figure 2.4. The reference configuration $B_{0\alpha}$ is mapped to the current configuration B by the mapping φ_α which carries the material point $\mathbf{X}_\alpha \in B_{0\alpha}$ to the point $\mathbf{x}(\mathbf{X}_\alpha, t) \in B$ and the material point $\mathbf{X}_\alpha + d\mathbf{X}_\alpha$ to $\mathbf{x}(\mathbf{X}_\alpha + d\mathbf{X}_\alpha, t)$. The undeformed line element $d\mathbf{X}_\alpha$ is carried to the deformed line element $d\mathbf{x}$.

line element in the actual configuration. Assuming that the norm of $d\mathbf{X}_\alpha$ is very small, from Taylor's theorem we get

$$d\mathbf{x} \approx \underline{\underline{F}}_\alpha d\mathbf{X}_\alpha. \tag{2.17}$$

Using the Kronecker delta δ^{IJ} defined as

$$\delta^{IJ} = \begin{cases} 1 & \text{if } I = J, \\ 0 & \text{if } I \neq J, \end{cases}$$

a measure of whether the line element has changed in length is given by

$$\begin{aligned} d\mathbf{x} \cdot d\mathbf{x} - d\mathbf{X}_\alpha \cdot d\mathbf{X}_\alpha &= F_\alpha^{KI} dX_\alpha^I F_\alpha^{KJ} dX_\alpha^J - dX_\alpha^K dX_\alpha^K \\ &= (F_\alpha^{KI} F_\alpha^{KJ} - \delta^{KI}\delta^{KJ}) dX_\alpha^I dX_\alpha^J \\ &= (C_\alpha^{IJ} - \delta^{IJ}) dX_\alpha^I dX_\alpha^J, \end{aligned} \tag{2.18}$$

where the tensor $\underline{\underline{C}}_\alpha$ is called the *right Cauchy-Green deformation tensor* and is defined as

$$\begin{aligned} \underline{\underline{C}}_\alpha \colon B_{0\alpha} \times [0,T) &\to \mathbb{R}^3 \times \mathbb{R}^3 \\ (\mathbf{X}_\alpha, t) &\to \underline{\underline{C}}_\alpha = \underline{\underline{F}}_\alpha^T(\mathbf{X}_\alpha, t)\underline{\underline{F}}_\alpha(\mathbf{X}_\alpha, t). \end{aligned} \tag{2.19}$$

Its components represent the square of the lengths of the deformed material line elements relative to the undeformed ones, i.e., from the Lagrangian viewpoint. If the length of the line element does not change, then $C_\alpha^{IJ} - \delta^{IJ} = 0$ for all I, J. To keep track of this, the *Green-Lagrange strain tensor* is introduced

$$\begin{aligned} \underline{\underline{E}}_\alpha \colon B_{0\alpha} \times [0,T) &\to \mathbb{R}^3 \times \mathbb{R}^3 \\ (\mathbf{X}_\alpha, t) &\to \underline{\underline{E}}_\alpha = \frac{1}{2}(\underline{\underline{C}}_\alpha(\mathbf{X}_\alpha, t) - \underline{\underline{I}}), \end{aligned} \tag{2.20}$$

where $\underline{\underline{I}}_\alpha$ is the identity tensor defined on $B_{0\alpha} \times [0,T)$. From equation (2.9), the deformed position $\mathbf{x}$ can be written as

$$\mathbf{x} = \mathbf{X}_\alpha + \mathbf{U}_\alpha.$$

Using Taylor's theorem as in (2.17), we get

$$d\mathbf{x} \approx \nabla_\alpha(\mathbf{X}_\alpha + \mathbf{U}_\alpha)\, d\mathbf{X}_\alpha = (\underline{\underline{I}} + \nabla_\alpha \mathbf{U}_\alpha)\, d\mathbf{X}_\alpha,$$

which, compared to (2.17), provides

$$\underline{\underline{F}}_\alpha = \underline{\underline{I}} + \nabla_\alpha \mathbf{U}_\alpha. \tag{2.21}$$

By (2.19), (2.20) and (2.21), the Green-Lagrange strain tensor becomes

$$\begin{aligned} \underline{\underline{E}}_\alpha &= \frac{1}{2}\big(\underline{\underline{C}}_\alpha - \underline{\underline{I}}\big) = \frac{1}{2}\big(\underline{\underline{F}}_\alpha^T \underline{\underline{F}}_\alpha - \underline{\underline{I}}\big) \\ &= \frac{1}{2}\big(\big(\underline{\underline{I}} + \nabla_\alpha \mathbf{U}_\alpha\big)^T \big(\underline{\underline{I}} + \nabla_\alpha \mathbf{U}_\alpha\big) - \underline{\underline{I}}\big) \\ &= \frac{1}{2}\big(\nabla_\alpha^T \mathbf{U}_\alpha + \nabla_\alpha \mathbf{U}_\alpha + \big(\nabla_\alpha^T \mathbf{U}_\alpha\big)\big(\nabla_\alpha \mathbf{U}_\alpha\big)\big). \end{aligned} \tag{2.22}$$

From the Eulerian viewpoint, using Taylor's theorem as before, we have

$$d\mathbf{X}_\alpha \approx \underline{\underline{H}}_\alpha d\mathbf{x},$$

where the tensor $\underline{\underline{H}}_\alpha$ is defined as

$$\begin{aligned} \underline{\underline{H}}_\alpha \colon B \times [0,T) &\to \mathbb{R}^3 \times \mathbb{R}^3 \\ (\mathbf{x}, t) \qquad &\to \underline{\underline{H}}_\alpha = \nabla \mathbf{X}_\alpha(\mathbf{x}, t) = \underline{\underline{F}}_\alpha^{-1}(\mathbf{x}, t). \end{aligned}$$

Thus, the Eulerian equivalent of equation (2.18) is

$$\begin{aligned} d\mathbf{x} \cdot d\mathbf{x} - d\mathbf{X}_\alpha \cdot d\mathbf{X}_\alpha &= dx^K dx^K - H_\alpha^{KI} dx^I H_\alpha^{KJ} dx^J \\ &= (\delta^{KI}\delta^{KJ} - H_\alpha^{KI} H_\alpha^{KJ}) dx^I dx^J \\ &= (\delta^{IJ} - \mathcal{C}_\alpha^{IJ}) dx^I dx^J, \end{aligned} \tag{2.23}$$

where the tensor $\underline{\underline{\mathcal{C}}}_\alpha$ is called the *Cauchy deformation tensor* and is the defined as

$$\begin{aligned} \underline{\underline{\mathcal{C}}}_\alpha \colon B \times [0,T) &\to \mathbb{R}^3 \times \mathbb{R}^3 \\ (\mathbf{x}, t) \qquad &\to \underline{\underline{\mathcal{C}}}_\alpha = \underline{\underline{H}}_\alpha^T \underline{\underline{H}}_\alpha = \underline{\underline{F}}_\alpha^{-T} \underline{\underline{F}}_\alpha^{-1} = (\underline{\underline{F}}_\alpha \underline{\underline{F}}_\alpha^T)^{-1}. \end{aligned}$$

The components of $\underline{\underline{\mathcal{C}}}_\alpha$ represent the square of lengths of the undeformed line elements relative to the deformed lengths, i.e. from the Eulerian viewpoint. The corresponding strain tensor is called the *Almansi strain tensor* and is defined as

$$\begin{aligned} \underline{\underline{A}}_\alpha \colon B \times [0,T) &\to \mathbb{R}^3 \times \mathbb{R}^3 \\ (\mathbf{x}, t) \qquad &\to \underline{\underline{A}}_\alpha = \frac{1}{2}(\underline{\underline{\mathcal{I}}} - \underline{\underline{\mathcal{C}}}_\alpha(\mathbf{x}, t)), \end{aligned}$$

where $\underline{\underline{\mathcal{I}}}$ is the identity tensor defined on $B \times [0,T)$. The components of $\underline{\underline{A}}_\alpha$ represent the change in lengths of material line elements from the Eulerian viewpoint.

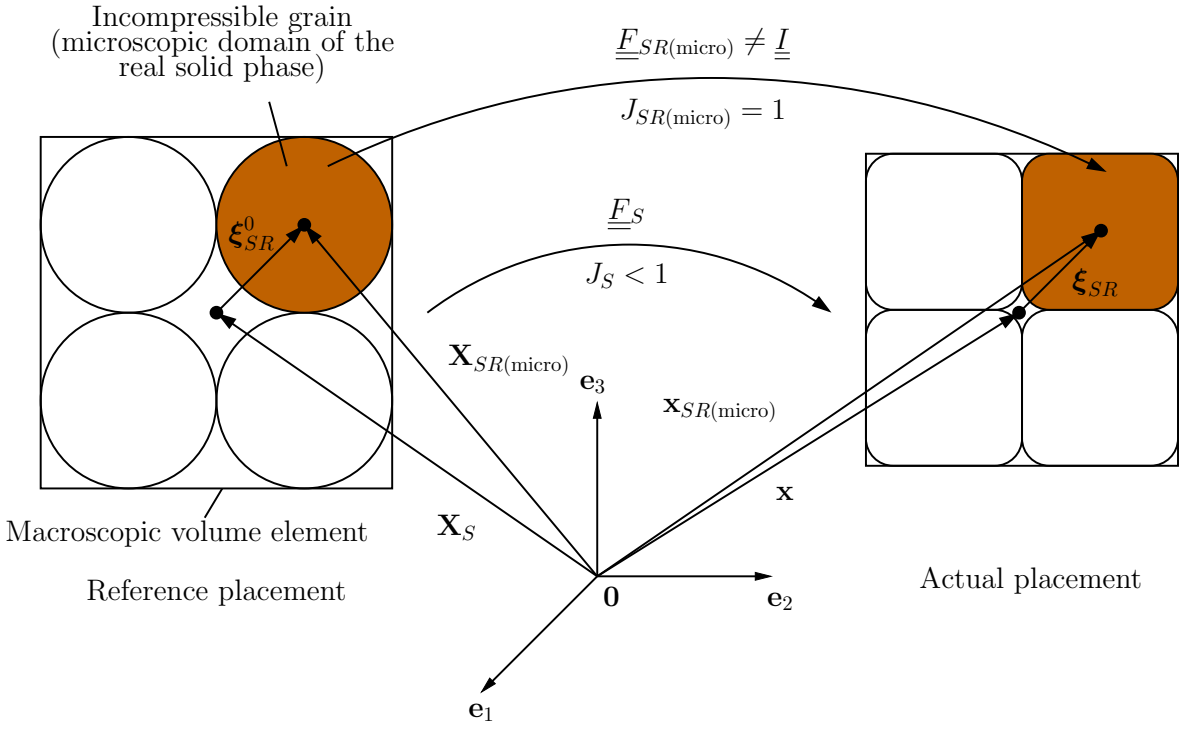

Figure 2.5. Illustration of motivation for a multiplicative decomposition of the deformation gradient of the solid phase. The position vectors $\mathbf{X}_S$ and $\mathbf{x}$ represent the centroids of the volume elements in the reference and the actual placements, respectively, whereas $\mathbf{X}_{SR(\text{micro})}$ and $\mathbf{x}_{SR(\text{micro})}$ denote all the possible points in the volume elements.

2.2.1 Describing Material Compressibility and Incompressibility in Deformable Porous Media

In conclusion of this section, we will spend few words about how to describe the compressibility and incompressibility of materials within porous media theory. This is particularly important when it comes to constitutive modeling, as it will be described in later sections.

For example, let us consider a macroscopic volume element filled with a granular solid phase, and a gas, as depicted in Figure 2.5. The solid grains are supposed to be incompressible, which means that a hydrostatic stress state in the grains does

not change their volume. Although the grains are incompressible, forces acting on the porous medium can cause a change of the pore structure, leading to an overall change in volume of the control space (see Figure 2.5). Hence, the incompressibility condition cannot be expressed by the deformation gradient $\underline{\underline{F}}_S$ of the partial solid constituent, which is a macroscopic quantity associated with the *smeared* solid phase. Instead, the compressibility condition must be expressed by physical quantities at the microscale. In principle, one could introduce a function φ_{SR} describing the motion of the *real solid* material at the microscale

$$\begin{aligned} \varphi_{SR}\colon B_{0S} \times [0,T) \ &\rightarrow B \\ (\mathbf{X}_{SR(\text{micro})}, t) &\rightarrow \mathbf{x}_{SR(\text{micro})} = \varphi_{SR(\text{micro})}(\mathbf{X}_{SR(\text{micro})}, t), \end{aligned} \tag{2.24}$$

where $\mathbf{X}_{SR(\text{micro})}$ and $\mathbf{x}_{SR(\text{micro})}$ are the position vectors of the real solid material at the level of the microscale in the reference and the actual placements, respectively (see Figure 2.5). The incompressibility condition could be formulated by requiring the determinant $J_{\text{SR(micro)}}$ of the deformation gradient $\underline{\underline{F}}_{\text{SR(micro)}}$ to be 1. However, the motion function $\varphi_{SR(\text{micro})}$ is unknown and cannot be determined by the porous media approach, which works with microscopic averaged quantities. Thus, it is necessary to transfer the microscopic deformation behavior of the real solid phase to the macroscale. To this end, the deformation gradient $\underline{\underline{F}}_S$ is decomposed into the product of two tensors

$$\underline{\underline{F}}_S = \underline{\underline{F}}_{SN}\underline{\underline{F}}_{SR},$$

where $\underline{\underline{F}}_{SR}$ is the part reflecting the microscopic deformations of the real solid material at the macroscale, whereas $\underline{\underline{F}}_{SN}$ describes the remaining part of the deformation of the porous medium, namely the change of the pores in size and shape.

Within porous media theory, the multiplicative decomposition

$$\underline{\underline{F}}_\alpha = \underline{\underline{F}}_{\alpha N}\underline{\underline{F}}_{\alpha R}, \tag{2.25}$$

is introduced for each constituent α. In the case of homogeneous deformations, this decomposition leads to an intermediate state (see Figure (2.6)).

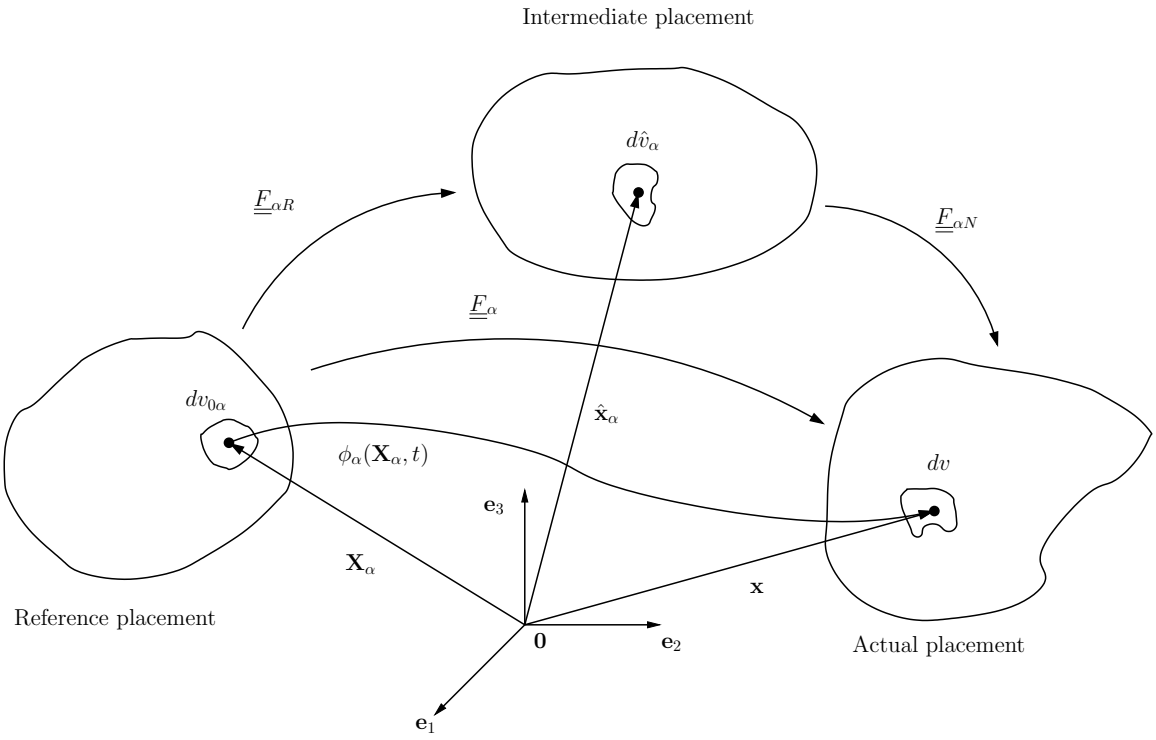

Figure 2.6. Representation of the multiplicative decomposition of the deformation gradient for homogeneous deformations.

From continuum mechanics [24], the relationship between the volume elements in the reference and the actual placements for constituent α ($dv_{0\alpha}$ and dv, respectively) is given by

$$dv = J_\alpha dv_{0\alpha}. \tag{2.26}$$

Using the multiplicative decomposition (2.25), we get

$$dv = J_{\alpha N} J_{\alpha R} dv_{0\alpha},$$

where $J_{\alpha N} = \det \underline{\underline{F}}_{\alpha N}$, $J_{\alpha R} = \det \underline{\underline{F}}_{\alpha R}$. Then, a differential volume $d\hat{v}_\alpha$, at a material point $\mathbf{X}_\alpha$ of a local intermediate placement is related to the volume elements in the reference placement and the actual placement by

$$d\hat{v}_\alpha = J_{\alpha R}\, dv_{0\alpha}, \qquad dv = J_{\alpha N}\, d\hat{v}_\alpha. \tag{2.27}$$

We interpreted $\underline{\underline{F}}_{\alpha R}$ as that part of the deformation gradient that includes the whole deformation of the real material of the constituent α. Thus, its determinant must represent the volume strain of the real material. If the constituent α is incompressible, it means that $d\hat{v}_\alpha = dv_{0\alpha}$. Equation (2.27) hence implies

$$J_{\alpha R} = 1. \tag{2.28}$$

2.3 Balance Equations and Entropy Inequality

According to Truesdell [25], each constituent α can be described by individual balance equations accounting for interactions between them by additional production terms. The balance equations of the whole mixture are obtained as the sum of the balance equations of each constituent and must formally become the corresponding balance equations of a one-component body.

Let $f_\alpha \colon B \to \mathbb{R}$ and $\mathbf{f}_\alpha \colon B \to \mathbb{R}^3$ be volume-specific scalar- and vector-valued densities of a physical quantity to be balanced associated with constituent α. Follow-

ing Truesdell [25] and classical continuum mechanics of a one-component body, the general balance equations of constituent α read:

$$\left(\int_\Omega f_\alpha \, dv\right)'_\alpha = \int_{\partial\Omega} g_\alpha \, dS + \int_\Omega h_\alpha \, dv + \int_\Omega \tilde{f}_\alpha \, dv, \tag{2.29}$$

$$\left(\int_\Omega \mathbf{f}_\alpha \, dv\right)'_\alpha = \int_{\partial\Omega} \mathbf{g}_\alpha \, dS + \int_\Omega \mathbf{h}_\alpha \, dv + \int_\Omega \tilde{\mathbf{f}}_\alpha \, dv, \tag{2.30}$$

where:

- $(\cdot)'_\alpha$ denotes the material derivative following the motion of constituent α;
- Ω is an arbitrary volume in the actual configuration B;
- g_α and $\mathbf{g}_\alpha$ are the surface densities per unit current area representing the boundary fluxes of the physical quantity over the surface $\partial\Omega$;
- h_α and $\mathbf{h}_\alpha$ are volume densities describing the *external* source of the physical quantity;
- $\tilde{f}_\alpha$ and $\tilde{\mathbf{f}}_\alpha$ represent the productions of the physical quantity due to the coupling of constituent α with the other constituents.

Balance relations of mass, linear momentum, angular momentum, and energy have the same form as equations (2.29) and (2.30) for appropriate choices of the partial (i.e. smeared) quantities f_α, $\mathbf{f}_\alpha$, g_α, $\mathbf{g}_\alpha$, h_α, $\mathbf{h}_\alpha$, $\tilde{f}_\alpha$, and $\tilde{\mathbf{f}}_\alpha$.

From (2.29) and (2.30), it follows that, in order to formulate balance relations in local (differential) form, we need to take the time derivative of integrals over material volumes in the reference (undeformed) and the actual (deformed) configurations. Let Γ be a scalar function defined in the reference configuration $B_{0\alpha}$

$$\begin{aligned} \Gamma \colon B_{0\alpha} \times [0, T) &\to \mathbb{R} \\ (\mathbf{X}_\alpha, t) \qquad &\to \Gamma = \Gamma(\mathbf{X}_\alpha, t), \end{aligned}$$

and Ω_0 be any volume inside $B_{0\alpha}$. The material derivative of the integral of Γ over Ω_0, following the motion of constituent α, is

$$\left(\int_{\Omega_0} \Gamma \, dv_{0\alpha}\right)'_\alpha .$$

Since the undeformed volume Ω_0 is fixed, we can take the time derivative under the integral, and so, from equation (2.13), it follows

$$\left(\int_{\Omega_0} \Gamma \, dv_{0\alpha}\right)'_\alpha = \int_{\Omega_0} (\Gamma)'_\alpha \, dv_{0\alpha} = \int_{\Omega_0} \frac{\partial \Gamma}{\partial t} \, dv_{0\alpha}.$$

Now take a function γ defined on the actual configuration

$$\begin{aligned} \gamma \colon B \times [0,T) &\to \mathbb{R} \\ (\mathbf{x}, t) \qquad &\to \gamma = \gamma(\mathbf{x}, t). \end{aligned} \tag{2.31}$$

and consider the material derivative of its integral over a volume $\Omega \subseteq B$

$$\left(\int_\Omega \gamma \; dv\right)'_\alpha. \tag{2.32}$$

In order to take the time derivative inside the integral, we have to take into account that both γ and the domain of integration Ω depend on time. In such situations, the *Reynolds transport theorem* is used [24]:

Theorem 2.3.1 (Reynolds transport theorem) *Given a function γ defined on the actual configuration, the material derivative of its integral over a volume $\Omega \subseteq B$, following the motion of constituent α, can be rewritten as*

$$\left(\int_\Omega \gamma \; dv\right)'_\alpha = \int_\Omega ((\gamma)'_\alpha + \gamma \nabla \cdot \mathbf{v}_\alpha) \, dv. \tag{2.33}$$

Proof This theorem proceeds as follows:

1. the material volume Ω is mapped to the equivalent volume $\Omega_{0\alpha}$ in the reference configuration for constituent α;

2. due to the previous step, the domain of integration $\Omega_{0\alpha}$ is now fixed and the time derivative is taken inside the integral;

3. the integral is transformed back to the material volume Ω.

Observe that steps 1–3 are equivalent to taking the derivative under the integral in (2.32) and applying it to the volume element dv as well. In fact, with the help of the following transport theorem [20]

$$(dv)'_\alpha = \nabla \cdot \mathbf{v}_\alpha \, dv, \tag{2.34}$$

and by the product rule for derivatives, we get

$$\left(\int_\Omega \gamma \; dv\right)'_\alpha = \int_\Omega (\gamma \, dv)'_\alpha = \int_\Omega ((\gamma)'_\alpha \, dv + \gamma (dv)'_\alpha) = \int_\Omega ((\gamma)'_\alpha + \gamma \nabla \cdot \mathbf{v}_\alpha) \, dv,$$

which coincides with equation (2.32). In the following, we will be using this second approach to take the material derivative of integrals over material volumes. □

2.3.1 Balance of Mass

In accordance with de Boer [13], we assume that, for each constituent α, the rate of change of its mass M_α equals a supply term $\int_\Omega \tilde{\rho}_\alpha \, dv$, possibly caused by the other constituents, where $\tilde{\rho}_\alpha$ describes mass exchange between the constituents and Ω is any material volume in the space shaped by the porous solid in the actual configuration. Thus, we get

$$(M_\alpha)'_\alpha = \left(\int_\Omega \rho_\alpha \, dv\right)'_\alpha = \int_\Omega \tilde{\rho}_\alpha \, dv. \tag{2.35}$$

The mass supply term $\tilde{\rho}_\alpha$ will have to be described by a constitutive law satisfying the saturation constraint (2.2) and the Second Law of Thermodynamics, i.e. the entropy inequality. Comparing (2.29) and (2.35), it appears that we made the following choices

$$f_\alpha = \rho_\alpha, \qquad g_\alpha = 0, \qquad h_\alpha = 0, \qquad \tilde{f}_\alpha = \tilde{\rho}_\alpha. \tag{2.36}$$

In particular, this means that we are neglecting boundary mass fluxes ($g_\alpha = 0$) and there is neither injection nor sequestration of mass from the outside ($h_\alpha = 0$). These assumptions allow to model a wide range of phenomena. For example, in order to model transport of solutes in standard continuum mechanics, boundary fluxes of mass must be included in the balance of mass, leading to Fick's law [23]. In porous media theory, instead, the transport of solutes is accounted for by appropriate constitutive laws for the interaction terms in the balance of linear momentum, rather than by including boundary fluxes in the balance of mass [26].

In equation (2.35), the material time derivative can be taken under the integral provided that we use the transport theorem (2.34) to account for the fact that the integration volume is not fixed. Hence:

$$\left(\int_\Omega \rho_\alpha \, dv\right)'_\alpha = \int_\Omega (\rho_\alpha \, dv)'_\alpha = \int_\Omega ((\rho_\alpha)'_\alpha dv + \rho_\alpha (dv)'_\alpha)$$
$$= \int_\Omega ((\rho_\alpha)'_\alpha + \rho_\alpha \nabla \cdot \mathbf{v}_\alpha) \, dv = \int_\Omega \tilde{\rho}_\alpha \, dv.$$

The equation must be satisfied for any arbitrary choice of Ω, which means that the integrand is zero and we have the Eulerian expression for the balance of mass

$$\boxed{(\rho_\alpha)'_\alpha + \rho_\alpha \nabla \cdot \mathbf{v}_\alpha = \tilde{\rho}_\alpha}, \qquad \text{or} \qquad \boxed{\frac{\partial \rho_\alpha}{\partial t} + \nabla \cdot (\rho_\alpha \mathbf{v}_\alpha) = \tilde{\rho}_\alpha}. \tag{2.37}$$

If all mass exchanges are excluded, relation (2.35) becomes

$$\left(\int_\Omega \rho_\alpha \, dv\right)'_\alpha = \int_\Omega (\rho_\alpha \, dv)'_\alpha = 0,$$

whose local form is

$$(\rho_\alpha dv)'_\alpha = 0 \qquad \text{or} \qquad \rho_\alpha dv = \text{ constant } = \rho_\alpha^{0\alpha} \, dv_{0\alpha}.$$

The quantities $dv_{0\alpha}$ and $\rho_\alpha^{0\alpha}$ represent the volume element and the partial density of the constituent α (subscript index) in the reference placement at the position $\mathbf{X}_\alpha$ (superscript index), respectively. From equation (2.26), we get the Lagrangian expression for the *conservation* of mass

$$\rho_\alpha J_\alpha \, dv_{0\alpha} = \rho_\alpha^{0\alpha} \, dv_{0\alpha}, \qquad \rho_\alpha = \rho_\alpha^{0\alpha} J_\alpha^{-1}. \tag{2.38}$$

2.3.2 Balance of Linear Momentum

The balance equation of linear momentum states that the material derivative with respect to constituent α of the linear momentum $\mathbf{P}_\alpha$ is equal to the resultant force $\mathcal{F}_\alpha$

$$(\mathbf{P}_\alpha)'_\alpha = \mathcal{F}_\alpha. \tag{2.39}$$

The linear momentum $\mathbf{P}_\alpha$ for the constituent α is defined by

$$\mathbf{P}_\alpha = \int_\Omega \rho_\alpha \mathbf{v}_\alpha \, dv.$$

Applying the product rule for the material derivative and the transport theorem (2.34) gives

$$\begin{aligned}
(\mathbf{P}_\alpha)'_\alpha &= \left(\int_\Omega \rho_\alpha \mathbf{v}_\alpha \, dv \right)'_\alpha = \int_\Omega (\rho_\alpha \mathbf{v}_\alpha \, dv)'_\alpha \\
&= \int_\Omega (\rho_\alpha \mathbf{v}_\alpha)'_\alpha \, dv + \rho_\alpha \mathbf{v}_\alpha (dv)'_\alpha \\
&= \int_\Omega ((\rho_\alpha)'_\alpha \mathbf{v}_\alpha + \rho_\alpha (\mathbf{v}_\alpha)'_\alpha + \rho_\alpha \mathbf{v}_\alpha \nabla \cdot \mathbf{v}_\alpha) \, dv \\
&= \int_\Omega (\rho_\alpha \mathbf{a}_\alpha + ((\rho_\alpha)'_\alpha + \rho_\alpha \nabla \cdot \mathbf{v}_\alpha) \, \mathbf{v}_\alpha) \, dv,
\end{aligned}$$

where $\mathbf{a}_\alpha = (\mathbf{v}_\alpha)'_\alpha$ is the Eulerian acceleration (2.12). By the balance of mass (2.37), the above expression becomes

$$(\mathbf{P}_\alpha)'_\alpha = \int_\Omega (\rho_\alpha \mathbf{a}_\alpha + \tilde{\rho}_\alpha \mathbf{v}_\alpha) \, dv. \tag{2.40}$$

The resultant force $\mathcal{F}_\alpha$ can be due to:

- *External forces acting on the exposed surface of the constituent α:* these forces are due to contact between bodies and are composed by a tangential friction and a normal pressure. If $\mathbf{t}_\alpha$ is the force per unit area of the deformed surface ∂B acting on constituent α, the corresponding resultant force on the volume Ω is

$$\mathcal{F}_\alpha^S = \int_{\partial\Omega} \mathbf{t}_\alpha \, dS.$$

- *External body forces acting throughout the region under consideration*: body forces include gravity, electromagnetic forces and the fictitious forces that result from writing the balance equations in a rotating frame. A body force is usually expressed as a force density per unit mass, $\mathbf{b}_\alpha$, or a force density per unit volume, $\rho_\alpha \mathbf{b}_\alpha$. Hence, the resultant external body force acting on constituent α is

$$\mathcal{F}_\alpha^V = \int_\Omega \rho_\alpha \mathbf{b}_\alpha \, dv.$$

- *Body forces coming from the interaction with the other constituents:* if $\tilde{\mathbf{p}}$ is the interaction force per unit volume, the corresponding resultant force on volume Ω is

$$\mathcal{F}_\alpha^I = \int_\Omega \tilde{\mathbf{p}}_\alpha \, dv.$$

The resultant force $\mathcal{F}_\alpha$ is then

$$\mathcal{F}_\alpha = \mathcal{F}_\alpha^S + \mathcal{F}_\alpha^V + \mathcal{F}_\alpha^I = \int_{\partial\Omega} \mathbf{t}_\alpha \, dS + \int_\Omega \rho_\alpha \mathbf{b}_\alpha \, dv + \int_\Omega \tilde{\mathbf{p}}_\alpha \, dv. \tag{2.41}$$

Thus, the balance of linear momentum has the same structure as equation (2.30), with

$$\mathbf{f}_\alpha = \rho_\alpha \mathbf{v}_\alpha, \qquad \mathbf{g}_\alpha = \mathbf{t}_\alpha, \qquad \mathbf{h}_\alpha = \rho_\alpha \mathbf{b}_\alpha, \qquad \tilde{\mathbf{f}}_\alpha = \tilde{\mathbf{p}}_\alpha.$$

By Cauchy's theorem [24]

$$t_\alpha^J = T_\alpha^{IJ} n^I, \tag{2.42}$$

where T_α^{IJ} is called the *Cauchy stress tensor* and represents the force per unit area of the actual (deformed) configuration decomposed with respect to the basis vectors associated with the Eulerian coordinate $\mathbf{x}$. Vector $\mathbf{n}$ is the unit normal at the surface of the deformed volume Ω. The components of the stress tensor could also be represented in the basis vectors associated with the Lagrangian coordinates $\mathbf{X}_\alpha$ in the deformed position, yielding the so called *body stress* tensor. Yet other alternative forms of the stress tensor are formed by considering the force per unit area in the reference (undeformed) configuration. This leads to the definition of the *first* and *second Piola-Kirchhoff* stress tensors, respectively [24].

By equations (2.39), (2.40), (2.41), (2.42), and the divergence theorem [24], we get the balance equation for the linear momentum in local form

$$\boxed{\rho_\alpha \mathbf{a}_\alpha + \tilde{\rho}_\alpha \mathbf{v}_\alpha = \frac{\partial \mathbf{T}_\alpha^I}{\partial x^I} + \rho_\alpha \mathbf{b}_\alpha + \tilde{\mathbf{p}}_\alpha}, \tag{2.43}$$

where $\mathbf{T}_\alpha^I$ is the Ith row of the Cauchy stress tensor. Observe that, in the last equation, the divergence operator is applied to $\underline{\underline{T}}_\alpha$ row wise. In the next section, we

will show that $\underline{\underline{T}}_\alpha$ is symmetric for non polar materials. Thus, in equation (2.43), the divergence operator could also be applied to $\underline{\underline{T}}_\alpha$ column wise without altering the result.

2.3.3 Balance of Angular Momentum

The *balance of angular momentum* states that the material time derivative of the angular momentum $\mathbf{H}^{\mathbf{z}}_\alpha$ about a fixed point $\mathbf{z}$ is equal to the resultant torque $\mathcal{L}^{\mathbf{z}}_\alpha$ about the point $\mathbf{z}$

$$(\mathbf{H}^{\mathbf{z}}_\alpha)'_\alpha = \mathcal{L}^{\mathbf{z}}_\alpha. \tag{2.44}$$

The total angular momentum of the deformed volume Ω about the point $\mathbf{z}$ is assumed to be given by

$$\mathbf{H}^{\mathbf{z}}_\alpha = \int_\Omega (\mathbf{x}-\mathbf{z}) \times \rho_\alpha \mathbf{v}_\alpha \, dv. \tag{2.45}$$

The resultant torque $\mathcal{L}^{\mathbf{z}}_\alpha$ is assumed to be due to:

- surface traction exerting a net torque on the body about the point $\mathbf{z}$

$$\mathcal{L}^{\mathbf{z},S}_\alpha = \int_{\partial\Omega} (\mathbf{x}-\mathbf{z}) \times \mathbf{t}_\alpha \, dS; \tag{2.46}$$

- torques due to body forces

$$\mathcal{L}^{\mathbf{z},V}_\alpha = \int_\Omega (\mathbf{x}-\mathbf{z}) \times \rho_\alpha \mathbf{b}_\alpha \, dv, \tag{2.47}$$

- torques due to linear momentum coupling terms $\tilde{\mathbf{p}}_\alpha$

$$\mathcal{L}^{\mathbf{z},\widetilde{V}}_\alpha = \int_\Omega (\mathbf{x}-\mathbf{z}) \times \tilde{\mathbf{p}}_\alpha \, dv. \tag{2.48}$$

Thus, the balance of angular momentum (2.44) has the same structure as equation (2.30) with:

$$\mathbf{f}_\alpha = (\mathbf{x}-\mathbf{z}) \times \rho_\alpha \mathbf{v}_\alpha, \qquad \mathbf{g}_\alpha = (\mathbf{x}-\mathbf{z}) \times \mathbf{t}_\alpha, \tag{2.49}$$

$$\mathbf{h}_\alpha = (\mathbf{x}-\mathbf{z}) \times \rho_\alpha \mathbf{b}_\alpha, \qquad \tilde{\mathbf{f}}_\alpha = (\mathbf{x}-\mathbf{z}) \times \tilde{\mathbf{p}}_\alpha. \tag{2.50}$$

Equations (2.49)–(2.50) are valid only for *non-polar* materials. Polar materials respond to spin inertia, as well as surface and body torques. The body of work that includes these effects is called Cosserat theory or the theory of micro-polar materials [27]. It encompasses anisotropic fluids, liquid crystals with rigid molecules, rigid suspensions, magnetic fluids, clouds with dust, muddy fluids, biological fluids, animal blood with rigid cells, chopped fiber composites, bones, concrete with sand. For these materials, equations (2.49), (2.50) become:

$$\mathbf{f}_\alpha = (\mathbf{x}-\mathbf{z}) \times \rho_\alpha \mathbf{v}_\alpha + \rho_\alpha \underline{\underline{\Theta}}_\alpha \omega_\alpha, \qquad \mathbf{g}_\alpha = (\mathbf{x}-\mathbf{z}) \times \mathbf{t}_\alpha + \mathbf{M}_\alpha, \tag{2.51}$$

$$\mathbf{h}_\alpha = (\mathbf{x}-\mathbf{z}) \times \rho_\alpha \mathbf{b}_\alpha + \rho_\alpha \mathbf{c}_\alpha, \qquad \tilde{\mathbf{f}}_\alpha = (\mathbf{x}-\mathbf{z}) \times \tilde{\mathbf{p}}_\alpha + \tilde{\mathbf{m}}_\alpha, \tag{2.52}$$

where:

- $\underline{\underline{\Theta}}_\alpha$ and ω_α are the partial tensor of inertia and angular velocity about the axis of rotation;
- $\mathbf{M}_\alpha$ is a surface torque;
- $\mathbf{c}_\alpha$ is a body torque per unit mass;
- $\tilde{\mathbf{m}}_\alpha$ is an angular momentum coupling due to the interaction with the other constituents.

Considering non-polar materials, from equations (2.44)–(2.48), it follows that

$$\begin{aligned}(\mathbf{H}^{\mathbf{z}}_\alpha)'_\alpha &= \left(\int_\Omega (\mathbf{x}-\mathbf{z}) \times \rho_\alpha \mathbf{v}_\alpha \, dv\right)'_\alpha = \mathcal{L}^{\mathbf{z}}_\alpha = \mathcal{L}^{\mathbf{z},S}_\alpha + \mathcal{L}^{\mathbf{z},V}_\alpha + \mathcal{L}^{\mathbf{z},\tilde{V}}_\alpha \\ &= \int_{\partial\Omega} (\mathbf{x}-\mathbf{z}) \times \mathbf{t}_\alpha \, dS + \int_\Omega (\mathbf{x}-\mathbf{z}) \times (\rho_\alpha \mathbf{b}_\alpha + \tilde{\mathbf{p}}_\alpha) \, dv.\end{aligned}$$

The vector $\mathbf{z}$ is a constant so it can be taken outside all integrals to yield

$$\begin{aligned}&\left(\int_\Omega \mathbf{x} \times \rho_\alpha \mathbf{v}_\alpha \, dv\right)'_\alpha - \int_{\partial\Omega} \mathbf{x} \times \mathbf{t}_\alpha \, dS - \int_\Omega \mathbf{x} \times (\rho_\alpha \mathbf{b}_\alpha + \tilde{\mathbf{p}}_\alpha) \, dv \\ &= \mathbf{z} \times \left[\left(\int_\Omega \rho_\alpha \mathbf{v}_\alpha \, dv\right)'_\alpha - \int_{\partial\Omega} \mathbf{t}_\alpha \, dS - \int_\Omega (\rho_\alpha \mathbf{b}_\alpha + \tilde{\mathbf{p}}_\alpha) \, dv\right].\end{aligned}$$

The term in square brackets is zero from the linear momentum balance in integral form (2.44) and hence

$$\left(\int_\Omega \mathbf{x}\times\rho_\alpha\mathbf{v}_\alpha\,dv\right)'_\alpha - \int_{\partial\Omega}\mathbf{x}\times\mathbf{t}_\alpha\,dS - \int_\Omega \mathbf{x}\times(\rho_\alpha\mathbf{b}_\alpha+\tilde{\mathbf{p}}_\alpha)\,dv = \mathbf{0}. \tag{2.53}$$

By applying the product rule for the material derivative and the transport theorem (2.34), we have

$$\begin{aligned}\left(\int_\Omega \mathbf{x}\times\rho_\alpha\mathbf{v}_\alpha\,dv\right)'_\alpha &= \int_\Omega (\,\mathbf{x}\times\rho_\alpha\mathbf{v}_\alpha\,dv\,)'_\alpha \\ &= \int_\Omega \big(\,(\mathbf{x}\times\rho_\alpha\mathbf{v}_\alpha)'_\alpha\,dv + (\mathbf{x}\times\rho_\alpha\mathbf{v}_\alpha)(dv)'_\alpha\,\big) \\ &= \int_\Omega \big(\,\rho_\alpha\mathbf{v}_\alpha\times\mathbf{v}_\alpha + \mathbf{x}\times(\rho_\alpha\mathbf{v}_\alpha)'_\alpha + \mathbf{x}\times\rho_\alpha(\nabla\cdot\mathbf{v}_\alpha)\mathbf{v}_\alpha\,\big)\,dv.\end{aligned}$$

By the definition of vector product $\mathbf{v}_\alpha\times\mathbf{v}_\alpha=\mathbf{0}$, so

$$\begin{aligned}\left(\int_\Omega \mathbf{x}\times\rho_\alpha\mathbf{v}_\alpha\,dv\right)'_\alpha &= \int_\Omega \big(\,\mathbf{x}\times(\rho_\alpha\mathbf{v}_\alpha)'_\alpha + \mathbf{x}\times\rho_\alpha(\nabla\cdot\mathbf{v}_\alpha)\mathbf{v}_\alpha\,\big)\,dv \\ &= \int_\Omega \big(\,\mathbf{x}\times(\,(\rho_\alpha)'_\alpha\mathbf{v}_\alpha+\rho_\alpha\mathbf{a}_\alpha\,) + \mathbf{x}\times\rho_\alpha(\nabla\cdot\mathbf{v}_\alpha)\mathbf{v}_\alpha\,\big)\,dv \\ &= \int_\Omega \mathbf{x}\times(\,\rho_\alpha\mathbf{a}_\alpha + (\,(\rho_\alpha)'_\alpha+\rho_\alpha(\nabla\cdot\mathbf{v}_\alpha)\,)\,\mathbf{v}_\alpha\,)\,dv.\end{aligned}$$

Using the balance of mass (2.37), we obtain

$$\left(\int_\Omega \mathbf{x}\times\rho_\alpha\mathbf{v}_\alpha\,dv\right)'_\alpha = \int_\Omega \mathbf{x}\times(\rho_\alpha\mathbf{a}_\alpha+\tilde{\rho}_\alpha\mathbf{v}_\alpha)\,dv. \tag{2.54}$$

Now let us focus on the surface integral in equation (2.53). Let e_{IJK}, for $I,J,K\in\{1,2,3\}$, denote the *Levi-Civita symbol*, whose components are defined as

$$e_{IJK} = \begin{cases} 0 & \text{when any two indices are equal;} \\ +1 & \text{when } I,J,K \text{ is an even permutation of } 1,2,3; \\ -1 & \text{when } I,J,K \text{ is an odd permutation of } 1,2,3. \end{cases} \tag{2.55}$$

Using e_{IJK}, the I-th component of the cross product of $\mathbf{x}$ and $\mathbf{t}_\alpha$ can be expressed as

$$[\mathbf{x}\times\mathbf{t}_\alpha]_I = e_{IJK}\,x^J\,t_\alpha^K,$$

and, by Cauchy's theorem (2.42)

$$[\mathbf{x} \times \mathbf{t}_\alpha]_I = e_{IJK}\, x^J\, T_\alpha^{LK} n^L.$$

Introducing the tensor $\mathcal{A}^{LI} = e_{IJK}\, x^J\, T_\alpha^{LK}$, we can then write

$$\int_{\partial\Omega} [\mathbf{x} \times \mathbf{t}_\alpha]_I \, dS = \int_{\partial\Omega} \mathcal{A}^{LI} n^L dS.$$

By the divergence theorem [24]

$$\int_{\partial\Omega} \mathcal{A}^{LI} n^L dS = \int_\Omega \frac{\partial \mathcal{A}^{LI}}{\partial x^L}\, dv.$$

Unfolding the definition of $\mathcal{A}^{LI}$ and denoting by $\mathbf{T}_\alpha^L$ the Lth row of the Cauchy stress tensor T_α^{LK}, we get

$$\begin{aligned}
\int_{\partial\Omega} [\mathbf{x} \times \mathbf{t}_\alpha]_I \, dS &= \int_\Omega \frac{\partial \mathcal{A}^{LI}}{\partial x^L}\, dv \\
&= \int_\Omega \frac{\partial}{\partial x^L} (e_{IJK}\, x^J\, T_\alpha^{LK})\, dv \\
&= \int_\Omega \left(e_{IJK}\, \frac{\partial x^J}{\partial x^L}\, T_\alpha^{LK} + e_{IJK}\, x^J\, \frac{\partial T_\alpha^{LK}}{\partial x^L} \right) dv \\
&= \int_\Omega \left(e_{IJK}\, \delta^{JL}\, T_\alpha^{LK} + \left[\mathbf{x} \times \frac{\partial \mathbf{T}_\alpha^L}{\partial x^L} \right]_I \right) dv \\
&= \int_\Omega \left(e_{IJK}\, T_\alpha^{JK} + \left[\mathbf{x} \times \frac{\partial \mathbf{T}_\alpha^L}{\partial x^L} \right]_I \right) dv.
\end{aligned} \tag{2.56}$$

Combining equations (2.53), (2.54), and (2.56) gives, in component form,

$$\int_\Omega \left[\mathbf{x} \times \left(\rho_\alpha \mathbf{a}_\alpha + \tilde{\rho}_\alpha \mathbf{v}_\alpha - \frac{\partial \mathbf{T}_\alpha^L}{\partial x^L} - \rho_\alpha \mathbf{b}_\alpha - \tilde{\mathbf{p}}_\alpha \right) \right]_I dv = \int_\Omega e_{IJK}\, T_\alpha^{JK}\, dv.$$

The left-hand side vanishes by the linear momentum balance in its local form (2.43), so

$$\int_\Omega e_{IJK}\, T_\alpha^{JK}\, dv = 0.$$

The equation must be valid for any volume Ω, which implies that the integrand is zero

$$e_{IJK}\, T_\alpha^{JK} = 0. \tag{2.57}$$

Expanding the Einstein convention and rearranging the terms in the sums gives

$$\begin{aligned}
e_{IJK}\,T_\alpha^{JK} &= \sum_{I=1}^{3}\sum_{J=1}^{3}\sum_{K=1}^{3} e_{IJK}\,T_\alpha^{JK} \\
&= e_{111}\,T_\alpha^{11} + e_{112}\,T_\alpha^{12} + e_{113}\,T_\alpha^{13} + e_{121}\,T_\alpha^{21} + e_{122}\,T_\alpha^{22} + \dots \\
&\quad + e_{331}\,T_\alpha^{31} + e_{332}\,T_\alpha^{32} + e_{333}\,T_\alpha^{33} \\
&= e_{111}\,T_\alpha^{11} + e_{121}\,T_\alpha^{21} + e_{131}\,T_\alpha^{31} + e_{112}\,T_\alpha^{12} + e_{122}\,T_\alpha^{22} + \dots \\
&\quad + e_{313}\,T_\alpha^{13} + e_{323}\,T_\alpha^{23} + e_{333}\,T_\alpha^{33} \\
&= \sum_{I=1}^{3}\sum_{J=1}^{3}\sum_{K=1}^{3} e_{IKJ}\,T_\alpha^{KJ} \\
&= e_{IKJ}T_\alpha^{IKJ}.
\end{aligned}$$

Hence, equation (2.57) can be rewritten as

$$e_{IJK}\,T_\alpha^{JK} = \frac{1}{2}(e_{IJK}\,T_\alpha^{JK} + e_{IKJ}\,T_\alpha^{KJ}) = 0,$$

and using the antisymmetry property of the Levi-Civita symbol, we have

$$\frac{1}{2}e_{IJK}\,(T_\alpha^{JK} - T_\alpha^{KJ}) = 0.$$

It follows that the Cauchy stress tensor must be symmetric

$$\boxed{T_\alpha^{JK} = T_\alpha^{KJ}}. \tag{2.58}$$

As a consequence of (2.51), (2.52), the balance of angular momentum for micro-polar materials does not lead to (2.58). Thus, the Cauchy stress tensor is not symmetric. In this work, only non-polar materials will be considered. For extensions of the balance equations for mixtures to micro-polar materials, the interested reader is referred to the work of Ehlers [28].

2.3.4 Balance of Energy

The balance of energy (first law of thermodynamics) expresses the notion of conservation of energy and states that the sum of the material time derivatives of the

internal and kinetic energies equals the sum of the rates of the heating and the mechanical work of the surface and body forces. This principle is applied to each individual constituent

$$(E_\alpha)'_\alpha + (K_\alpha)'_\alpha = W_\alpha + Q_\alpha + \int_\Omega \tilde{\phi}_\alpha \, dv, \tag{2.59}$$

where $E_\alpha, K_\alpha, W_\alpha$, and Q_α are the internal energy, the kinetic energy, the *rate* of mechanical work and the rate of heating of constituent α, respectively. The term $\tilde{\phi}_\alpha$ is an energy supply per unit volume to α caused by all the other constituents. The internal energy is

$$E_\alpha = \int_\Omega \rho_\alpha \phi_\alpha \, dv, \tag{2.60}$$

where $\phi_\alpha = \phi_\alpha(\mathbf{x}, t)$ is the partial (averaged reduced) energy density per unit mass. From the transport theorem (2.34) and the balance of mass (2.37) it follows that

$$\begin{aligned}
(E_\alpha)'_\alpha &= \left(\int_\Omega \rho_\alpha \phi_\alpha \, dv \right)'_\alpha = \int_\Omega (\rho_\alpha \phi_\alpha dv)'_\alpha = \int_\Omega \left(\, (\rho_\alpha \phi_\alpha)'_\alpha \, dv + \rho_\alpha \phi_\alpha (dv)'_\alpha \, \right) \\
&= \int_\Omega \left(\, (\rho_\alpha)'_\alpha \phi_\alpha + \rho_\alpha (\phi_\alpha)'_\alpha + \rho_\alpha \phi_\alpha \nabla \cdot \mathbf{v}_\alpha \, \right) dv \\
&= \int_\Omega \left(\, ((\rho_\alpha)'_\alpha + \rho_\alpha \nabla \cdot \mathbf{v}_\alpha) \phi_\alpha + \rho_\alpha (\phi_\alpha)'_\alpha \, \right) dv \\
&= \int_\Omega (\tilde{\rho}_\alpha \phi_\alpha + \rho_\alpha (\phi_\alpha)'_\alpha) \, dv.
\end{aligned} \tag{2.61}$$

The kinetic energy is defined as

$$K_\alpha = \int_\Omega \frac{1}{2} \rho_\alpha \mathbf{v}_\alpha \cdot \mathbf{v}_\alpha \, dv. \tag{2.62}$$

From the transport theorem (2.34) and the balance of mass (2.37) it follows that

$$\begin{aligned}
(K_\alpha)'_\alpha &= \left(\int_\Omega \frac{1}{2} \rho_\alpha \mathbf{v}_\alpha \cdot \mathbf{v}_\alpha \, dv \right)'_\alpha = \int_\Omega \left(\left(\frac{1}{2} \rho_\alpha \mathbf{v}_\alpha \cdot \mathbf{v}_\alpha \right)'_\alpha dv + \frac{1}{2} \rho_\alpha \mathbf{v}_\alpha \cdot \mathbf{v}_\alpha (dv)'_\alpha \right) \\
&= \int_\Omega \left(\frac{1}{2} (\rho_\alpha)'_\alpha \mathbf{v}_\alpha \cdot \mathbf{v}_\alpha + \rho_\alpha \mathbf{a}_\alpha \cdot \mathbf{v}_\alpha + \frac{1}{2} \rho_\alpha \mathbf{v}_\alpha \cdot \mathbf{v}_\alpha (\nabla \cdot \mathbf{v}_\alpha) \right) dv \\
&= \int_\Omega \left(\frac{1}{2} \left((\rho_\alpha)'_\alpha + \rho_\alpha \nabla \cdot \mathbf{v}_\alpha \right) \mathbf{v}_\alpha \cdot \mathbf{v}_\alpha + \rho_\alpha \mathbf{a}_\alpha \cdot \mathbf{v}_\alpha \right) dv \\
&= \int_\Omega \left(\frac{1}{2} \tilde{\rho}_\alpha \mathbf{v}_\alpha \cdot \mathbf{v}_\alpha + \rho_\alpha \mathbf{a}_\alpha \cdot \mathbf{v}_\alpha \right) dv.
\end{aligned} \tag{2.63}$$

The rate of work of the surface forces and the body forces is

$$W_\alpha = \int_\Omega \mathbf{v}_\alpha \cdot \rho_\alpha \mathbf{b}_\alpha \, dv + \int_{\partial\Omega} \mathbf{v}_\alpha \cdot \mathbf{t}_\alpha \, dS. \tag{2.64}$$

From Cauchy's theorem (2.42), and using Einstein summation convention, we obtain

$$W_\alpha = \int_\Omega \mathbf{v}_\alpha \cdot \rho_\alpha \mathbf{b}_\alpha \, dv + \int_{\partial\Omega} v_\alpha^J T_\alpha^{IJ} n^I \, dS. \tag{2.65}$$

The divergence theorem applied to the vector $P^I = v_\alpha^J T_\alpha^{IJ}$ gives

$$\begin{aligned} W_\alpha &= \int_\Omega \mathbf{v}_\alpha \cdot \rho_\alpha \mathbf{b}_\alpha \, dv + \int_\Omega \frac{\partial P^I}{\partial x^I} \, dv \\ &= \int_\Omega (\mathbf{v}_\alpha \cdot \rho_\alpha \mathbf{b}_\alpha + \frac{\partial v_\alpha^J}{\partial x^I} T_\alpha^{IJ} + v_\alpha^J \frac{\partial T_\alpha^{IJ}}{\partial x^I}) \, dv, \\ &= \int_\Omega \left(\mathbf{v}_\alpha \cdot \left(\rho_\alpha \mathbf{b}_\alpha + \frac{\partial \mathbf{T}_\alpha^I}{\partial x^I} \right) + L_\alpha^{IJ} T_\alpha^{IJ} \right) dv, \end{aligned} \tag{2.66}$$

where $L_\alpha^{IJ} = \partial v_\alpha^J / \partial x^I$ is the spatial velocity gradient. Let D_α^{IJ} and W_α^{IJ} be the symmetric and the antisymmetric parts of L_α^{IJ}, respectively. By the symmetry of the Cauchy stress tensor (2.58), we get

$$W_\alpha^{IJ} T_\alpha^{IJ} = \frac{1}{2}(L_\alpha^{IJ} - L_\alpha^{JI}) T_\alpha^{IJ} = \frac{1}{2}(L_\alpha^{IJ} T_\alpha^{IJ} - L_\alpha^{JI} T_\alpha^{JI}) = 0.$$

Given two tensors $\underline{\underline{A}}$ and $\underline{\underline{B}}$, their *contraction* $\underline{\underline{A}} : \underline{\underline{B}}$ is the operation defined by

$$\underline{\underline{A}} : \underline{\underline{B}} = A^{IJ} B^{IJ}. \tag{2.67}$$

From the previous equation we get

$$\underline{\underline{L}}_\alpha : \underline{\underline{T}}_\alpha = (\underline{\underline{D}}_\alpha + \underline{\underline{W}}_\alpha) : \underline{\underline{T}}_\alpha = \underline{\underline{D}}_\alpha : \underline{\underline{T}}_\alpha + 0 = \underline{\underline{D}}_\alpha : \underline{\underline{T}}_\alpha. \tag{2.68}$$

The total rate of heating is

$$Q_\alpha = \int_\Omega \rho_\alpha r_\alpha \, dv - \int_{\partial\Omega} \mathbf{q}_\alpha \cdot \mathbf{n} \, dS, \tag{2.69}$$

where $r_\alpha = r_\alpha(\mathbf{x}, t)$ is the partial heat supply per unit partial mass, and $\mathbf{q}_\alpha = \mathbf{q}_\alpha(\mathbf{x}, t)$ the partial heat flux vector. The negative sign is chosen so that heat flows into the

body, $-\mathbf{q}_\alpha \cdot \mathbf{n} > 0$, when the flux vector $\mathbf{q}_\alpha$ is also directed into the body. From the divergence theorem it follows that

$$Q_\alpha = \int_\Omega (\rho_\alpha r_\alpha - \nabla \cdot \mathbf{q}_\alpha)\, dv. \tag{2.70}$$

From (2.59), (2.60), (2.62), (2.64), (2.69), it follows that the balance of energy has the same form of equation (2.29) with

$$f_\alpha = \rho_\alpha \phi_\alpha + \frac{1}{2}\rho_\alpha \mathbf{v}_\alpha \cdot \mathbf{v}_\alpha, \quad g_\alpha = \mathbf{v}_\alpha \cdot \mathbf{t}_\alpha - \mathbf{q}_\alpha \cdot \mathbf{n}, \quad h_\alpha = \mathbf{v}_\alpha \cdot \rho_\alpha \mathbf{b}_\alpha + \rho_\alpha r_\alpha, \quad \tilde{f}_\alpha = \tilde{\phi}_\alpha.$$

Combining equations (2.59), (2.61), (2.63), (2.66), and (2.70), we get the local statement

$$\begin{aligned} &\tilde{\rho}_\alpha \phi_\alpha + \rho_\alpha (\phi_\alpha)'_\alpha + \frac{1}{2}\tilde{\rho}_\alpha \mathbf{v}_\alpha \cdot \mathbf{v}_\alpha + \mathbf{v}_\alpha \cdot \rho_\alpha \mathbf{a}_\alpha \\ &\qquad = \mathbf{v}_\alpha \cdot \left(\rho_\alpha \mathbf{b}_\alpha + \frac{\partial \mathbf{T}^I_\alpha}{\partial x^I} \right) + \underline{\underline{T}}_\alpha : \underline{\underline{D}}_\alpha + \rho_\alpha r_\alpha - \nabla \cdot \mathbf{q}_\alpha + \tilde{\phi}_\alpha, \end{aligned}$$

or, equivalently,

$$\begin{aligned} &\tilde{\rho}_\alpha \phi_\alpha + \rho_\alpha (\phi_\alpha)'_\alpha + \frac{1}{2}\tilde{\rho}_\alpha \mathbf{v}_\alpha \cdot \mathbf{v}_\alpha \\ &\qquad = \mathbf{v}_\alpha \cdot \left(\rho_\alpha \mathbf{b}_\alpha + \frac{\partial \mathbf{T}^I_\alpha}{\partial x^I} - \rho_\alpha \mathbf{a}_\alpha \right) + \underline{\underline{T}}_\alpha : \underline{\underline{D}}_\alpha + \rho_\alpha r_\alpha - \nabla \cdot \mathbf{q}_\alpha + \tilde{\phi}_\alpha. \end{aligned}$$

By the balance of momentum (2.43), we obtain

$$\begin{aligned} &\tilde{\rho}_\alpha \phi_\alpha + \rho_\alpha (\phi_\alpha)'_\alpha + \frac{1}{2}\tilde{\rho}_\alpha \mathbf{v}_\alpha \cdot \mathbf{v}_\alpha \\ &\qquad = \mathbf{v}_\alpha \cdot (\tilde{\rho}_\alpha \mathbf{v}_\alpha - \tilde{\mathbf{p}}_\alpha) + \underline{\underline{T}}_\alpha : \underline{\underline{D}}_\alpha + \rho_\alpha r_\alpha - \nabla \cdot \mathbf{q}_\alpha + \tilde{\phi}_\alpha, \end{aligned}$$

and finally

$$\boxed{\tilde{\rho}_\alpha \phi_\alpha + \rho_\alpha (\phi_\alpha)'_\alpha = \frac{1}{2}\tilde{\rho}_\alpha \mathbf{v}_\alpha \cdot \mathbf{v}_\alpha - \mathbf{v}_\alpha \cdot \tilde{\mathbf{p}}_\alpha + \underline{\underline{T}}_\alpha : \underline{\underline{D}}_\alpha + \rho_\alpha r_\alpha - \nabla \cdot \mathbf{q}_\alpha + \tilde{\phi}_\alpha}. \tag{2.71}$$

2.3.5 The Entropy Inequality

The entropy inequality (second law of thermodynamics) tells that there is a physical limit to the rate at which heat can be absorbed by a body, but no limit to the

rate at which it can be released. In classical continuum mechanics, for a body made of a single material, the law states that

$$Q \leq \mathcal{B}, \tag{2.72}$$

where Q is the net heating of the body and $\mathcal{B}$ is its least upper bound. For a body at uniform temperature, denoted by θ, a quantity called *entropy*, denoted by $\mathcal{H}$, is introduced, such that

$$\mathcal{H}' = \frac{\mathcal{B}}{\theta}, \tag{2.73}$$

where $(\cdot)'$ denotes the material derivative in classical continuum mechanics for bodies made of a single constituent. The rate of change of entropy represents the ability of a particular material to absorb heat. Combining (2.72) and (2.73) gives

$$\theta \mathcal{H}' \geq Q.$$

More generally, for a continuum body, we assume that there exists a specific entropy η such that

$$\mathcal{H} = \int_\Omega \rho \eta \, dv.$$

Also, we suppose that the rate of change in total entropy is greater than or equal to the net heating per unit temperature

$$\mathcal{H}' \geq \int_\Omega \frac{\rho r}{\theta} \, dv - \int_{\partial\Omega} \frac{\mathbf{q} \cdot \mathbf{n}}{\theta} \, dS,$$

which is known as the *Clausius-Duhem inequality*. This inequality is transferred to the individual constituents in porous media theory. The assumption that the entropy inequality has to be satisfied for every single constituent α is a sufficient, but too restrictive, condition. A necessary and sufficient condition to describe the thermodynamics of a porous medium is that the *sum* of all the individual entropy inequalities has to be fulfilled

$$\sum_{\alpha=1}^{\kappa} (\mathcal{H}_\alpha)'_\alpha \geq \sum_{\alpha=1}^{\kappa} \left(\int_\Omega \frac{\rho_\alpha r_\alpha}{\theta_\alpha} \, dv - \int_{\partial\Omega} \frac{\mathbf{q}_\alpha \cdot \mathbf{n}}{\theta_\alpha} \, dS \right). \tag{2.74}$$

In equation (2.74), we consider the same volume of integration Ω for all the components. With the help of the transport theorem (2.34), the balance of mass (2.37), and the divergence theorem applied to the vector field $\mathbf{q}_\alpha/\theta_\alpha$, we get

$$\begin{aligned}
\sum_{\alpha=1}^{\kappa}(\mathcal{H}_\alpha)'_\alpha &= \sum_{\alpha=1}^{\kappa}\int_\Omega (\rho_\alpha\eta_\alpha\, dv)'_\alpha \\
&= \sum_{\alpha=1}^{\kappa}\int_\Omega (\,(\rho_\alpha)'_\alpha\eta_\alpha + \rho_\alpha(\eta_\alpha)'_\alpha + \rho_\alpha\eta_\alpha(\nabla\cdot\mathbf{v}_\alpha)\,)\, dv \\
&= \sum_{\alpha=1}^{\kappa}\int_\Omega (\rho_\alpha(\eta_\alpha)'_\alpha + \tilde{\rho}_\alpha\eta_\alpha)\, dv \\
&\geq \sum_{\alpha=1}^{\kappa}\left(\int_\Omega \frac{\rho_\alpha r_\alpha}{\theta_\alpha}\, dv - \int_{\partial\Omega}\frac{\mathbf{q}_\alpha\cdot\mathbf{n}}{\theta_\alpha}\, dS\right) = \sum_{\alpha=1}^{\kappa}\int_\Omega\left(\frac{\rho_\alpha r_\alpha}{\theta_\alpha} - \nabla\cdot\left(\frac{\mathbf{q}_\alpha}{\theta_\alpha}\right)\right)\, dv.
\end{aligned}$$

By linearity of the integral and sum operators, as well as the assumption that the domain of integration Ω is the same for every constituent, it follows that

$$\int_\Omega \sum_{\alpha=1}^{\kappa}\left(\rho_\alpha(\eta_\alpha)'_\alpha + \tilde{\rho}_\alpha\eta_\alpha - \frac{\rho_\alpha r_\alpha}{\theta_\alpha} + \nabla\cdot\left(\frac{\mathbf{q}_\alpha}{\theta_\alpha}\right)\right)\, dv \geq 0.$$

If the integral must be non-negative for any volume Ω, no matter how small, then the integrand must be non-negative

$$\sum_{\alpha=1}^{\kappa}\left(\rho_\alpha(\eta_\alpha)'_\alpha + \tilde{\rho}_\alpha\eta_\alpha - \frac{\rho_\alpha r_\alpha}{\theta_\alpha} + \nabla\cdot\left(\frac{\mathbf{q}_\alpha}{\theta_\alpha}\right)\right) \geq 0.$$

Expanding the divergence term and factoring $1/\theta_\alpha$, we obtain

$$\sum_{\alpha=1}^{\kappa}\frac{1}{\theta_\alpha}\left(\rho_\alpha\theta_\alpha(\eta_\alpha)'_\alpha + \tilde{\rho}_\alpha\theta_\alpha\eta_\alpha - \rho_\alpha r_\alpha + \nabla\cdot\mathbf{q}_\alpha - \frac{1}{\theta_\alpha}\mathbf{q}_\alpha\cdot\nabla\theta_\alpha\right) \geq 0,$$

or

$$\sum_{\alpha=1}^{\kappa}\frac{1}{\theta_\alpha}\left(\mathcal{D}_\alpha - \frac{1}{\theta_\alpha}\mathbf{q}_\alpha\cdot\nabla\theta_\alpha\right) \geq 0, \tag{2.75}$$

where

$$\begin{aligned}
\mathcal{D}_\alpha &= \rho_\alpha\theta_\alpha(\eta_\alpha)'_\alpha + \tilde{\rho}_\alpha\theta_\alpha\eta_\alpha - \rho_\alpha r_\alpha + \nabla\cdot\mathbf{q}_\alpha \\
&= \rho_\alpha\theta_\alpha(\eta_\alpha)'_\alpha + \tilde{\rho}_\alpha\theta_\alpha\eta_\alpha - (\rho_\alpha r_\alpha - \nabla\cdot\mathbf{q}_\alpha)
\end{aligned}$$

is called the *internal dissipation* of constituent α per unit deformed volume. The internal dissipation is the net increase in specific entropy that is not due to net heating. From the conservation of energy (2.71), we can rewrite the dissipation as

$$\begin{aligned}\mathcal{D}_\alpha = {} & \rho_\alpha \theta_\alpha (\eta_\alpha)'_\alpha + \tilde{\rho}_\alpha \theta_\alpha \eta_\alpha \\ & - \left(\tilde{\rho}_\alpha \phi_\alpha + \rho_\alpha (\phi_\alpha)'_\alpha - \frac{1}{2} \tilde{\rho}_\alpha \mathbf{v}_\alpha \cdot \mathbf{v}_\alpha + \mathbf{v}_\alpha \cdot \tilde{\mathbf{p}}_\alpha - \underline{\underline{T}}_\alpha : \underline{\underline{D}}_\alpha - \tilde{\phi}_\alpha \right).\end{aligned} \tag{2.76}$$

It is convenient to introduce the *Helmholtz free energy* per unit partial mass

$$\psi_\alpha(\mathbf{x}, t) = \phi_\alpha(\mathbf{x}, t) - \eta_\alpha(\mathbf{x}, t)\theta_\alpha(\mathbf{x}, t). \tag{2.77}$$

To have an idea of what the Helmholtz free energy represents, consider a non-dissipative system (i.e. $\mathcal{D}_\alpha = 0$), with no supply terms (i.e. $\tilde{\rho}_\alpha = 0$, $\tilde{\mathbf{p}}_\alpha = \mathbf{0}, \tilde{\phi}_\alpha = 0$), at constant temperature. Then

$$(\psi_\alpha)'_\alpha = (\phi_\alpha)'_\alpha - \theta_\alpha (\eta_\alpha)'_\alpha,$$

and

$$\mathcal{D}_\alpha = 0 = \rho_\alpha \theta_\alpha (\eta_\alpha)'_\alpha - \rho_\alpha (\phi_\alpha)'_\alpha + \underline{\underline{T}}_\alpha : \underline{\underline{D}}_\alpha,$$

which together imply

$$\rho_\alpha (\psi_\alpha)'_\alpha = \underline{\underline{T}}_\alpha : \underline{\underline{D}}_\alpha.$$

Hence, the Helmholtz free energy is the energy available to do mechanical work in a non-dissipative system, with no supply terms, at constant temperature. In other words, it is some sort of potential energy. Using definition (2.77) in (2.75) and (2.76), the entropy inequality can be rewritten as

$$\boxed{\begin{aligned}\sum_{\alpha=1}^{\kappa} \frac{1}{\theta_\alpha} \Bigg(& -\rho_\alpha (\psi_\alpha)'_\alpha - \rho_\alpha (\theta_\alpha)'_\alpha \eta_\alpha - \tilde{\rho}_\alpha \left(\psi_\alpha - \frac{1}{2} \mathbf{v}_\alpha \cdot \mathbf{v}_\alpha \right) \\ & - \mathbf{v}_\alpha \cdot \tilde{\mathbf{p}}_\alpha + \underline{\underline{T}}_\alpha : \underline{\underline{D}}_\alpha + \tilde{\phi}_\alpha - \frac{1}{\theta_\alpha} \mathbf{q}_\alpha \cdot \nabla \theta_\alpha \Bigg) \geq 0.\end{aligned}} \tag{2.78}$$

2.4 Constitutive Modeling

Based on the theory presented in the preceding sections, several different multiphasic models can be defined. In view of the applications in ophthalmology presented

in Chapter 4, a general mixture model with one solid phase and one fluid phase will be presented. Hence, here, $\alpha = S, F$. This binary model is subject to the following assumptions:

1. *Saturated solid-fluid mixture:* the control space shaped by the porous solid is completely filled by the solid and the fluid constituents. Hence, the solid and fluid volume fractions have to satisfy the saturation constraint

$$n_S + n_F = 1. \tag{2.79}$$

2. *Materially incompressible solid and fluid constituents:* we will be assuming that both the solid and the fluid phases cannot undergo volume changes at the microscale. As discussed in Section 2.2, the microscopic deformation behavior of a real constituent is transferred to the macroscale by the tensor $\underline{\underline{F}}_{\alpha R}$. The incompressibility constraint of constituent α is then expressed by requiring the determinant $J_{\alpha R}$ of $\underline{\underline{F}}_{\alpha R}$ to be 1. Moreover, it is assumed that any exchange of mass between the two constituents does not happen between the real materials, but rather it is accommodated through a change in the partial volume fractions. This means that the real mass of a constituent is conserved, or, equivalently, its total mass M_α remains constant under the mapping $\underline{\underline{F}}_{\alpha R}$ between the reference and the intermediate placements

$$M_\alpha = \int_{\tilde{B}_\alpha} \rho_{\alpha R}\, d\tilde{v}_\alpha = \int_{B_{0\alpha}} \rho_\alpha^{0\alpha}\, dv_{0\alpha},$$

where $B_{0\alpha}$ is a control volume in the reference placement at the position $\mathbf{X}_\alpha$, and $\tilde{B}_\alpha$ is the corresponding domain in the intermediate placement in the tangent space. Proceeding similarly to Section 2.3.1 gives

$$\rho_{\alpha R} = \rho_\alpha^{0\alpha} J_{\alpha R}^{-1},$$

and, since $J_{\alpha R} = 1$, we obtain that the incompressibility constraint for phase α can be expressed by

$$\rho_{\alpha R} = \rho_\alpha^{0\alpha} = \text{constant}. \tag{2.80}$$

3. *Viscous pore fluid streaming through a viscoelastic solid skeleton:* we are interested in studying the role played by viscoelasticity in the modeling of biological tissues. In Chapter 4, we will be discussing about influences of tissue viscoelasticity on the optic nerve head perfusion.

4. *Uniform body force:* $\mathbf{b}_\alpha = \mathbf{b}$.

5. *Quasi-static conditions:* solid and fluid accelerations are neglected, that is

$$\mathbf{a}_\alpha = \mathbf{0}. \tag{2.81}$$

This choice will be motivated in Chapter 4 in the context of mathematical modeling of the optic nerve head perfusion.

6. *Isothermal process:*

$$\theta_\alpha = \theta = \text{constant}.$$

7. *Constraints on the source/sink terms:*

$$\tilde{\rho}_S + \tilde{\rho}_F = 0, \qquad \tilde{\mathbf{p}}_S + \tilde{\mathbf{p}}_F = \mathbf{0}, \qquad \tilde{\phi}_S = \tilde{\phi}_F = 0.$$

The system is isothermal, which means that there can be no external sources of heat and the boundary of the porous medium is insulated. Therefore, $r_\alpha = 0, \mathbf{q}_\alpha = \mathbf{0}$. Under these assumptions, and neglecting energy supply terms, it follows that the balance of energy equation (2.71) is not independent of the linear momentum equation (2.43), even if accelerations are not neglected. In fact, if $r_\alpha = 0, \mathbf{q}_\alpha = \mathbf{0}$, and $\tilde{\phi}_\alpha = 0$, the balance of energy (2.71) simplifies to

$$\tilde{\rho}_\alpha \phi_\alpha + \rho_\alpha (\phi_\alpha)'_\alpha = \frac{1}{2}\tilde{\rho}_\alpha \mathbf{v}_\alpha \cdot \mathbf{v}_\alpha - \mathbf{v}_\alpha \cdot \tilde{p}_\alpha + \underline{\underline{T}}_\alpha : \underline{\underline{D}}_\alpha.$$

Integrating over a generic control volume Ω gives

$$\int_\Omega (\tilde{\rho}_\alpha \phi_\alpha + \rho_\alpha (\phi_\alpha)'_\alpha)\, dv = \int_\Omega \left(\frac{1}{2}\tilde{\rho}_\alpha \mathbf{v}_\alpha \cdot \mathbf{v}_\alpha - \mathbf{v}_\alpha \cdot \tilde{p}_\alpha + \underline{\underline{T}}_\alpha : \underline{\underline{D}}_\alpha \right) dv. \tag{2.82}$$

The integral on the left hand side is the material time derivative of the internal energy E_α (see equation (2.61)). By the balance of energy in integral form (2.59),

the material derivative of E_α is given by $W_\alpha - (K_\alpha)'_\alpha$, which represents the net rate of work, i.e. the total power exerted by external forces that is not used to produce motion. From equations (2.63) and (2.65), we get

$$\begin{aligned}(E_\alpha)'_\alpha &= W_\alpha - (K_\alpha)'_\alpha \\ &= \int_\Omega \mathbf{v}_\alpha \cdot \rho_\alpha \mathbf{b}\, dv + \int_{\partial\Omega} v_\alpha^J T_\alpha^{IJ} n^I\, dS - \int_\Omega \left(\frac{1}{2}\tilde{\rho}_\alpha \mathbf{v}_\alpha \cdot \mathbf{v}_\alpha + \rho_\alpha \mathbf{a}_\alpha \cdot \mathbf{v}_\alpha\right) dv.\end{aligned} \tag{2.83}$$

Comparing equations (2.82) and (2.83) gives

$$\begin{aligned}&\int_\Omega \mathbf{v}_\alpha \cdot \rho_\alpha \mathbf{b}\, dv + \int_{\partial\Omega} v_\alpha^J T_\alpha^{IJ} n^I\, dS - \int_\Omega \left(\frac{1}{2}\tilde{\rho}_\alpha \mathbf{v}_\alpha \cdot \mathbf{v}_\alpha + \rho_\alpha \mathbf{a}_\alpha \cdot \mathbf{v}_\alpha\right) dv \\ &\quad = \int_\Omega \left(\frac{1}{2}\tilde{\rho}_\alpha \mathbf{v}_\alpha \cdot \mathbf{v}_\alpha - \mathbf{v}_\alpha \cdot \tilde{p}_\alpha + \underline{\underline{T}}_\alpha : \underline{\underline{D}}_\alpha\right) dv.\end{aligned} \tag{2.84}$$

Equation (2.84) follows immediately from the balance of linear momentum (2.43). Taking the dot product of equation (2.43) with the velocity $\mathbf{v}_\alpha$, we obtain

$$\int_\Omega \left(\frac{\partial T_\alpha^{IJ}}{\partial x^I} v_\alpha^J + \rho_\alpha \mathbf{b} \cdot \mathbf{v}_\alpha + \tilde{\mathbf{p}}_\alpha \cdot \mathbf{v}_\alpha\right) dv = \int_\Omega (\, \rho_\alpha \mathbf{a}_\alpha \cdot \mathbf{v}_\alpha + \tilde{\rho}_\alpha \mathbf{v}_\alpha \cdot \mathbf{v}_\alpha\,)\, dv. \tag{2.85}$$

The first term on the left hand side can be integrated by parts using the divergence theorem on the vector $T_\alpha^{IJ} v_\alpha^J$

$$\begin{aligned}\int_\Omega \left(\frac{\partial T_\alpha^{IJ}}{\partial x^I} v_\alpha^J\right) dv &= \int_\Omega \left(\frac{\partial (T_\alpha^{IJ} v_\alpha^J)}{\partial x^I} - T_\alpha^{IJ} \frac{\partial v_\alpha^J}{\partial x^I}\right) dv \\ &= \int_{\partial\Omega} T_\alpha^{IJ} v_\alpha^J n^I\, dS - \int_\Omega T_\alpha^{IJ} \frac{\partial v_\alpha^J}{\partial x^I}\, dv.\end{aligned}$$

By equation (2.68), we have

$$\begin{aligned}\int_{\partial\Omega} T_\alpha^{IJ} v_\alpha^J n^I\, dS - \int_\Omega T_\alpha^{IJ} \frac{\partial v_\alpha^J}{\partial x^I}\, dv &= \int_{\partial\Omega} T_\alpha^{IJ} v_\alpha^J n^I\, dS - \int_\Omega T_\alpha^{IJ} L_\alpha^{IJ}\, dv \\ &= \int_{\partial\Omega} T_\alpha^{IJ} v_\alpha^J n^I\, dS - \int_\Omega T_\alpha^{IJ} D_\alpha^{IJ}\, dv\end{aligned}$$

Hence, equation (2.85) becomes

$$\begin{aligned}&\int_{\partial\Omega} T_\alpha^{IJ} v_\alpha^J n^I\, dS + \int_\Omega (\rho_\alpha \mathbf{b} \cdot \mathbf{v}_\alpha + \tilde{\mathbf{p}}_\alpha \cdot \mathbf{v}_\alpha - T_\alpha^{IJ} D_\alpha^{IJ})\, dv \\ &\quad = \int_\Omega (\, \rho_\alpha \mathbf{a}_\alpha \cdot \mathbf{v}_\alpha + \tilde{\rho}_\alpha \mathbf{v}_\alpha \cdot \mathbf{v}_\alpha\,)\, dv,\end{aligned}$$

and, after few manipulations,

$$\int_{\partial\Omega} T_\alpha^{IJ} v_\alpha^J n^I \, dS + \int_\Omega \rho_\alpha \mathbf{b} \cdot \mathbf{v}_\alpha \, dv - \int_\Omega \left(\frac{1}{2} \tilde{\rho}_\alpha \mathbf{v}_\alpha \cdot \mathbf{v}_\alpha + \rho_\alpha \mathbf{a}_\alpha \cdot \mathbf{v}_\alpha \right) dv$$
$$= \int_\Omega \left(\frac{1}{2} \tilde{\rho}_\alpha \mathbf{v}_\alpha \cdot \mathbf{v}_\alpha - \tilde{\mathbf{p}} \cdot \mathbf{v}_\alpha + \underline{\underline{T}}_\alpha : \underline{\underline{D}}_\alpha \right) dv,$$

which coincides with (2.84).

Thus far we have formulated four balance equations, an entropy inequality, and a collection of kinematic relationships. The overall set of governing equations for a binary porous media model satisfying assumptions 1–7 is shown in Table 2.1. This Table shows that there are more unknown variables than equations. Hence, additional equations are required to close the system. These additional equations are called *constitutive* equations and describe the nature of the continuum under consideration by characterizing its responses, such as stress and Helmholtz free energy, in terms of the kinematics of the porous medium.

There is not a unique approach to formulate constitutive equations. One approach could be starting from a simplified description of the molecular behavior and then averaging over all possible configurations to obtain the behavior at the macroscopic (continuum) level. Alternatively, one could use phenomenological models based on experiments. No matter how we obtain a constitutive model, it is important to be aware of the assumptions behind it and which regime of motion it is valid over.

Two basic principle that constitutive equations should always fulfill are:

Principle 1. They should be objective (i.e. not influenced by superimposed rigid body motions).

Principle 2. They should not violate the laws of thermodynamics.

2.4.1 Principle of Material Objectivity

The behavior of a material should not be influenced by superimposed rigid body motions of the observer. A quantity that is not affected by the observer is called

Table 2.1
The governing equations for a binary porous model with one solid phase $\alpha = S$ and one fluid phase $\alpha = F$ satisfying assumptions 1–7.

Physical Law	Eulerian Form	Number of Equations	Number of Unknowns
Kinematics	$\mathbf{v}_\alpha = (\varphi_\alpha)'_\alpha$, $\underline{\underline{D}}_\alpha = \frac{1}{2}(\nabla \mathbf{v}_\alpha + \nabla^T \mathbf{v}_\alpha)$	18	24 $(\varphi_\alpha, \mathbf{v}_\alpha, \underline{\underline{D}}_\alpha)$
Mass	$(n_\alpha \rho_{\alpha R})'_\alpha + n_\alpha \rho_{\alpha R} \nabla \cdot \mathbf{v}_\alpha = \tilde{\rho}_\alpha$	2	4 $(n_\alpha, \tilde{\rho}_\alpha)$
Linear momentum	$\tilde{\rho}_\alpha \mathbf{v}_\alpha = \frac{\partial \mathbf{T}^I_\alpha}{\partial x^I} + n_\alpha \rho_{\alpha R} \mathbf{b} + \tilde{\mathbf{p}}_\alpha$	6	24 $(\underline{\underline{T}}_\alpha, \tilde{\mathbf{p}}_\alpha)$
Angular momentum	$\underline{\underline{T}}_\alpha = (\underline{\underline{T}}_\alpha)^T$	6	0
Entropy	$\sum_{\alpha=S,F} \left(-\rho_\alpha (\psi_\alpha)'_\alpha - \tilde{\rho}_\alpha \left(\psi_\alpha - \frac{1}{2}\mathbf{v}_\alpha \cdot \mathbf{v}_\alpha\right) - \mathbf{v}_\alpha \cdot \tilde{\mathbf{p}}_\alpha + \underline{\underline{T}}_\alpha : \underline{\underline{D}}_\alpha\right) \geq 0$	0	2 (ψ_α)
Constraints	$n_S + n_F = 1$, $\tilde{\rho}_S + \tilde{\rho}_F = 0$, $\tilde{\mathbf{p}}_S + \tilde{\mathbf{p}}_F = \mathbf{0}$	5	0
Total		37	54

objective or *material frame independent*. According to Principle 1, constitutive laws need to be formulated in terms of objective quantities.

In classical continuum mechanics, relativistic effects are neglected, and, thus, any observer must measure the same spatial distances and time intervals. Consider an observer measuring spatial position and time by the pair $(\mathbf{x} = \varphi_\alpha(\mathbf{X}_\alpha, t), t)$, where $\mathbf{x}$ is given by

$$\begin{aligned} \varphi_\alpha \colon B_{0\alpha} \times [0, T) &\to B \\ (\mathbf{X}_\alpha, t) \qquad &\to \mathbf{x} = \varphi_\alpha(\mathbf{X}_\alpha, t), \end{aligned}$$

and another one by $(\breve{\mathbf{x}}, \breve{t})$, where $\breve{\mathbf{x}}$ is given by

$$\begin{aligned} \breve{\varphi}_\alpha \colon B_{0\alpha} \times [-t_0, \breve{T}) &\to \breve{B} \\ (\mathbf{X}_\alpha, \breve{t}) \qquad &\to \breve{\mathbf{x}} = \breve{\varphi}_\alpha(\mathbf{X}_\alpha, \breve{t}), \end{aligned}$$

and $\breve{t} = t - t_0$, t_0 being a constant time shift. Since $\breve{t}$ and t differ only by a constant amount and a change of (Eulerian) observer does not affect the Lagrangian coordinates, the material (total) derivative with respect to t and $\breve{t}$, i.e. $(\cdot)'_\alpha$ and $(\cdot)'_{\breve{\alpha}}$, respectively, coincide. More precisely, given an Eulerian function

$$f(\mathbf{x}, t) = \breve{f}(\breve{\mathbf{x}}(\mathbf{x}), \breve{t}),$$

we have

$$(f)'_\alpha = (\breve{f})'_{\breve{\alpha}}.$$

The most general transformation between the two observers is a rigid body motion

$$\breve{\mathbf{x}} = \underline{\underline{Q}}(t)\mathbf{x} + \mathbf{c}(t), \tag{2.86}$$

where $\underline{\underline{Q}} \colon [0, T) \to \mathbf{R}^3 \times \mathbf{R}^3$ is an orthogonal matrix, and $\mathbf{c} \colon [0, T) \to \mathbf{R}^3$ a translation vector.

Given a scalar function $w(\mathbf{x}, t) = \breve{w}(\breve{\mathbf{x}}(\mathbf{x}, t), \breve{t})$, its value must not change due to a superimposed rigid body motion, that is

$$\breve{w}(\breve{\mathbf{x}}, \breve{t}) = w(\breve{\mathbf{x}}, t). \tag{2.87}$$

Hence, w is invariant under an Eulerian observer transformation, i.e., it is *observer invariant*. For a vector $\mathbf{u}$, to be objective, its length must not change under the observer transformation

$$\breve{\mathbf{u}} \cdot \breve{\mathbf{u}} = \mathbf{u} \cdot \mathbf{u}.$$

Writing vector $\mathbf{u}$ as a difference of two points in space, $\mathbf{u} = \mathbf{x} - \mathbf{y}$, we get

$$\breve{\mathbf{u}} = \breve{\mathbf{x}} - \breve{\mathbf{y}} = \underline{\underline{Q}}\mathbf{x} + \mathbf{c} - \underline{\underline{Q}}\mathbf{y} - \mathbf{c} = \underline{\underline{Q}}(\mathbf{x} - \mathbf{y}) = \underline{\underline{Q}}\mathbf{u},$$

and then

$$\breve{\mathbf{u}} \cdot \breve{\mathbf{u}} = \breve{u}^I \breve{u}^I = Q_{IJ} u^I Q_{IK} u^K = Q^T_{JI} Q_{IK} u^J u^K = \delta_{JK} u^J u^K = u^J u^J = \mathbf{u} \cdot \mathbf{u},$$

because $\underline{\underline{Q}}$ is orthogonal. Thus, a vector $\mathbf{u}$ is observer independent (or objective *in the Eulerian sense*) if

$$\breve{\mathbf{u}} = \underline{\underline{Q}}\mathbf{u}. \tag{2.88}$$

From equation (2.88), for a tensor of order two, $\underline{\underline{A}}$, to remain invariant under observer rigid motions, it must be

$$\underline{\underline{\breve{A}}}\breve{\mathbf{u}} = \underline{\underline{Q}}(\underline{\underline{A}}\mathbf{u}),$$

that we can rewrite as

$$\underline{\underline{\breve{A}}}\breve{\mathbf{u}} = \underline{\underline{Q}}(\underline{\underline{A}}\mathbf{u}) = \underline{\underline{Q}}(\underline{\underline{A}}(\underline{\underline{Q}}^T\breve{\mathbf{u}})) = \underline{\underline{Q}}\,\underline{\underline{A}}\,\underline{\underline{Q}}^T\breve{\mathbf{u}}.$$

Hence, in order to be objective in the Eulerian sense, $\underline{\underline{A}}$ must obey the following transformation rule

$$\underline{\underline{\breve{A}}} = \underline{\underline{Q}}\,\underline{\underline{A}}\,\underline{\underline{Q}}^T. \tag{2.89}$$

The transformations for the velocity and the acceleration are obtained by taking the material derivative of equation (2.86). Since, the material derivatives $(\cdot)'_{\breve{\alpha}}$ and $(\cdot)'_{\alpha}$ coincide, as observed before, we have, for the velocity

$$\breve{\mathbf{v}}_\alpha = (\breve{\mathbf{x}})'_{\breve{\alpha}} = (\underline{\underline{Q}}\mathbf{x} + \mathbf{c})'_\alpha = (\underline{\underline{Q}})'_\alpha\mathbf{x} + \underline{\underline{Q}}(\mathbf{x})'_\alpha + (\mathbf{c})'_\alpha = \underline{\underline{Q}}\mathbf{v}_\alpha + (\underline{\underline{Q}})'_\alpha\mathbf{x} + (\mathbf{c})'_\alpha,$$

and, for the acceleration

$$\breve{\mathbf{a}}_\alpha = (\breve{\mathbf{v}}_\alpha)'_{\breve{\alpha}} = (\,\underline{\underline{Q}}\mathbf{v}_\alpha + (\underline{\underline{Q}})'_\alpha\mathbf{x} + (\mathbf{c})'_\alpha\,)'_\alpha = \underline{\underline{Q}}\mathbf{a}_\alpha + 2(Q)'_\alpha\mathbf{v}_\alpha + (\underline{\underline{Q}})''_\alpha\mathbf{x} + (\mathbf{c})''_\alpha.$$

Hence, the velocity and acceleration do not transform according to (2.88) unless $\underline{\underline{Q}}$ and $\mathbf{c}$ are both constant. Thus, they are not objective and depend on the motion of the observer.

The deformation gradient tensor $\underline{\underline{F}}_\alpha$ transforms via

$$\breve{F}^{IJ}_\alpha = \frac{\partial \breve{x}^I}{\partial X^J_\alpha} = \frac{\partial}{\partial X^J_\alpha}(\, Q^{IK}(t)x^K + c^I(t)\,) = Q^{IK}F^{KJ}_\alpha,$$

or

$$\underline{\underline{\breve{F}}}_\alpha = \underline{\underline{Q}}\,\underline{\underline{F}}_\alpha, \tag{2.90}$$

so that the deformation gradient tensor is not objective, as it does not transform according to equation (2.89). The right Cauchy-Green tensor is invariant under a change of observer as

$$\underline{\underline{\breve{C}}}_\alpha = \underline{\underline{\breve{F}}}^T_\alpha \underline{\underline{\breve{F}}}_\alpha = (\underline{\underline{Q}}\,\underline{\underline{F}}_\alpha)^T \underline{\underline{Q}}\,\underline{\underline{F}}_\alpha = \underline{\underline{F}}^T_\alpha \underline{\underline{Q}}^T \underline{\underline{Q}}\,\underline{\underline{F}}_\alpha = \underline{\underline{F}}^T_\alpha \underline{\underline{F}}_\alpha = \underline{\underline{C}}_\alpha, \tag{2.91}$$

Therefore, the same holds for the Green-Lagrange strain tensor

$$\underline{\underline{\breve{E}}}_\alpha = \frac{1}{2}(\underline{\underline{\breve{C}}}_\alpha - \underline{\underline{\breve{I}}}) = \frac{1}{2}(\underline{\underline{\breve{C}}}_\alpha - \underline{\underline{\breve{I}}}) = \frac{1}{2}(\underline{\underline{C}}_\alpha - \underline{\underline{I}}) = \underline{\underline{E}}_\alpha, \tag{2.92}$$

where we used the fact that $\underline{\underline{\breve{I}}} = \underline{\underline{I}}$ since the Lagrangian identity tensor $\underline{\underline{I}}\colon B_{0\alpha} \to B_{0\alpha}$ is invariant under an Eulerian observer transformation. Thus, $\underline{\underline{C}}_\alpha$ and $\underline{\underline{E}}_\alpha$, which are based on the Lagrangian coordinates, do not transform according to (2.89), so they are not observer independent. Rather, they are observer invariant, or objective in a Lagrangian sense. The Eulerian (Almansi) strain tensor is based on the Eulerian coordinates and does transform objectively. In fact, from equation (2.90) and since

$$\underline{\underline{Q}}(t)\colon B \to \breve{B}, \qquad \underline{\underline{Q}}^T(t)\colon \breve{B} \to B, \qquad \underline{\underline{Q}}^{-1}(t) = \underline{\underline{Q}}^T(t),$$

we obtain

$$\underline{\underline{\breve{A}}}_\alpha = \frac{1}{2}(\underline{\underline{\breve{\mathcal{I}}}} - \underline{\underline{\breve{\mathcal{C}}}}_\alpha) = \frac{1}{2}(\underline{\underline{Q}}\,\underline{\underline{Q}}^T - \underline{\underline{\breve{F}}}^{-T}_\alpha \underline{\underline{\breve{F}}}^{-1}_\alpha) = \frac{1}{2}(\underline{\underline{Q}}\,\underline{\underline{Q}}^T - \underline{\underline{Q}}\,\underline{\underline{F}}^{-T}_\alpha \underline{\underline{F}}^{-1}_\alpha \underline{\underline{Q}}^T) = \underline{\underline{Q}}\,\underline{\underline{A}}_\alpha \underline{\underline{Q}}^T. \tag{2.93}$$

The spatial velocity gradient $\underline{\underline{L}}_\alpha$ does not transform objectively. In fact, by equations (2.16), (2.90), and the remark about the material derivatives $(\cdot)'_{\breve{\alpha}}, (\cdot)'_\alpha$, we get

$$\begin{aligned} \underline{\underline{\breve{L}}}_\alpha &= (\underline{\underline{\breve{F}}}_\alpha)'_{\breve{\alpha}} \underline{\underline{\breve{F}}}^{-1}_\alpha = (\underline{\underline{Q}}\,\underline{\underline{F}}_\alpha)'_\alpha (\underline{\underline{Q}}\,\underline{\underline{F}}_\alpha)^{-1} \\ &= ((\underline{\underline{Q}})'_\alpha \underline{\underline{F}}_\alpha + \underline{\underline{Q}}(\underline{\underline{F}}_\alpha)'_\alpha)\underline{\underline{F}}^{-1}_\alpha \underline{\underline{Q}}^T = (\underline{\underline{Q}})'_\alpha \underline{\underline{Q}}^T + \underline{\underline{Q}}\,\underline{\underline{L}}_\alpha \underline{\underline{Q}}^T. \end{aligned} \tag{2.94}$$

The symmetric part of $\underline{\underline{L}}_\alpha$, the Eulerian rate of deformation tensor $\underline{\underline{D}}_\alpha$, transforms objectively. In order to prove this, take the material derivative of the identity tensor $\underline{\underline{\breve{I}}} = \underline{\underline{QQ^T}}$ to get

$$\underline{\underline{0}} = (\underline{\underline{QQ^T}})'_{\breve{\alpha}} = (\underline{\underline{Q}})'_\alpha \underline{\underline{Q}}^T + \underline{\underline{Q}}[(\underline{\underline{Q}})'_\alpha]^T,$$

which shows that

$$(\underline{\underline{Q}})'_\alpha \underline{\underline{Q}}^T = -\underline{\underline{Q}}[(\underline{\underline{Q}})'_\alpha]^T. \tag{2.95}$$

Hence, from equations (2.94) and (2.95), we have

$$\begin{aligned} \underline{\underline{\breve{D}}}_\alpha &= \frac{1}{2}(\underline{\underline{\breve{L}}}_\alpha + \underline{\underline{\breve{L}}}^T_\alpha) = \frac{1}{2}((\underline{\underline{Q}})'_\alpha \underline{\underline{Q}}^T + \underline{\underline{QL}}_\alpha \underline{\underline{Q}}^T + \underline{\underline{Q}}[(\underline{\underline{Q}})'_\alpha]^T + \underline{\underline{QL}}^T_\alpha \underline{\underline{Q}}^T) \\ &= \underline{\underline{Q}}\frac{1}{2}(\underline{\underline{L}}_\alpha + \underline{\underline{L}}^T_\alpha)\underline{\underline{Q}}^T = \underline{\underline{QD}}_\alpha \underline{\underline{Q}}^T, \end{aligned} \tag{2.96}$$

so $\underline{\underline{D}}_\alpha$ transforms according to (2.89). Conversely, the antisymmetric pat of $\underline{\underline{L}}_\alpha$, $\underline{\underline{W}}_\alpha$, does not transform objectively

$$\begin{aligned} \underline{\underline{\breve{W}}}_\alpha &= \frac{1}{2}(\underline{\underline{\breve{L}}}_\alpha - \underline{\underline{\breve{L}}}^T_\alpha) = \frac{1}{2}((\underline{\underline{Q}})'_\alpha \underline{\underline{Q}}^T + \underline{\underline{QL}}_\alpha \underline{\underline{Q}}^T - \underline{\underline{Q}}[(\underline{\underline{Q}})'_\alpha]^T - \underline{\underline{QL}}^T_\alpha \underline{\underline{Q}}^T) \\ &= \underline{\underline{Q}}\frac{1}{2}(\underline{\underline{L}}_\alpha - \underline{\underline{L}}^T_\alpha)\underline{\underline{Q}}^T + (\underline{\underline{Q}})'_\alpha \underline{\underline{Q}}^T = \underline{\underline{QW}}_\alpha \underline{\underline{Q}}^T + (\underline{\underline{Q}})'_\alpha \underline{\underline{Q}}^T. \end{aligned}$$

Let us summarize this section about the principle of material objectivity. We found that constitutive laws should be formulated using:

- either quantities objective in a Lagrangian sense, i.e. observer invariant, like the Cauchy-Green tensor $\underline{\underline{C}}_\alpha$ and the Green-Lagrange strain tensor $\underline{\underline{E}}_\alpha$, together with its material time derivative $(\underline{\underline{E}}_\alpha)'_\alpha$ (see equations (2.91), (2.92));

- or quantities objective in the Eulerian sense, i.e. observer independent, like the Almansi strain tensor $\underline{\underline{A}}_\alpha$ and the Eulerian rate of deformation tensor $\underline{\underline{D}}_\alpha$ (see equations (2.93), (2.96)).

2.4.2 The Saturation and Incompressibility Constraints

As described in Section 2.3.5, the entropy inequality is a constraint on the evolution of a physical system. Its essence is that there is a physical limit to the rate at

which heat can be absorbed by a body, but no limit to the rate at which it can be released. The entropy inequality can be used to gain restrictions for the constitutive equations, according to Principle 2.

There are many possibilities to satisfy this inequality. Some evaluations may be less restrictive than others. The entropy inequality has to be manipulated in order to include fundamental physical phenomena known from experience, test observations, and theories. Similarly to what is done in constraint optimization theory in finite [29] and infinite [30] dimensional problems, all additional constraints, like the saturation (2.79) and the incompressibility (2.80) conditions, have to be put in a stress-power like form by taking their material derivative and multiplying each of them by a Lagrange multiplier, and finally added to the entropy inequality. A constraint is then formulated is such a way that its stress-power like form provides an easy and physical meaningful interpretation of its Lagrange multiplier. We will illustrate this last point in the following.

Differentiating the saturation constraint (2.79) with respect to the solid phase gives

$$0 = (n_S)'_S + (n_F)'_S,$$

which, using the definition of the total derivatives $(\cdot)'_\alpha, \alpha = S, F$, as well as adding and subtracting $\nabla n_F \cdot \mathbf{v}_F$, can be rewritten as

$$\begin{aligned} 0 &= (n_S)'_S + (n_F)'_S \\ &= (n_S)'_S + \frac{\partial n_F}{\partial t} + \nabla n_F \cdot \mathbf{v}_S + \nabla n_F \cdot \mathbf{v}_F - \nabla n_F \cdot \mathbf{v}_F \\ &= (n_S)'_S + (n_F)'_F - \nabla n_F \cdot (\mathbf{v}_F - \mathbf{v}_S), \end{aligned}$$

or, equivalently

$$\boxed{0 = -(n_S)'_S - (n_F)'_F + \nabla n_F \cdot (\mathbf{v}_F - \mathbf{v}_S)}. \tag{2.97}$$

The same result can be obtained by taking the derivative with respect to the fluid phase

$$\begin{aligned} 0 &= (n_S)'_F + (n_F)'_F \\ &= \frac{\partial n_S}{\partial t} + \nabla n_S \cdot \mathbf{v}_F + (n_F)'_F + \nabla n_S \cdot \mathbf{v}_S - \nabla n_S \cdot \mathbf{v}_S \\ &= (n_S)'_S + (n_F)'_F + \nabla n_S \cdot (\mathbf{v}_F - \mathbf{v}_S). \end{aligned}$$

Taking the gradient of the saturation constraint gives

$$\nabla n_S = \nabla(1 - n_F) = -\nabla n_F,$$

which, together with the previous equation, implies (2.97). Observe that the unit of measure of each term in equation (2.97) is $[\mathrm{s}^{-1}]$. Multiplying (2.97) by a Lagrange multiplier λ and comparing it with the units of the entropy inequality in Table 2.1 ($[\mathrm{N}\cdot \mathrm{m}^{-2}\cdot\mathrm{s}^{-1}]$), reveals that λ has the same units of a pressure $[\mathrm{N}\cdot\mathrm{m}^{-2}]$. In fact, since the saturation constraint in the rate formulation restricts the rates of volumetric changes of both the solid and fluid phases, its multiplier λ is understood as an unknown hydrostatic interface pressure acting on both the constituents. Hence, we expect the evaluation of the entropy inequality to provide us with two constitutive equations for λ, one containing properties of the smeared solid constituent, and another one with properties of the smeared fluid constituent.

From the incompressibility constraints

$$\rho_{SR} = \text{constant}, \qquad \rho_{FR} = \text{constant},$$

we get

$$(\rho_{SR})'_S = (\rho_{FR})'_F = 0. \tag{2.98}$$

Rather than using equation (2.98), multiplied by an appropriate Lagrange multiplier, in the evaluation of the entropy inequality, we rewrite it with the help of the balance of

mass (2.37). Using the definition of the partial density $\rho_\alpha = n_\alpha \rho_{\alpha R}$ in equations (2.37) and (2.98), we have

$$\begin{aligned}\tilde{\rho}_\alpha &= (\rho_\alpha)'_\alpha + \rho_\alpha \nabla \cdot \mathbf{v}_\alpha \\ &= (n_\alpha)'_\alpha \rho_{\alpha R} + n_\alpha (\rho_{\alpha R})'_\alpha + \rho_\alpha \nabla \cdot \mathbf{v}_\alpha \\ &= (n_\alpha)'_\alpha \rho_{\alpha R} + \rho_\alpha \nabla \cdot \mathbf{v}_\alpha,\end{aligned}$$

and, dividing through by $\rho_{\alpha R}$, we obtain

$$\boxed{(n_\alpha)'_\alpha + n_\alpha \nabla \cdot \mathbf{v}_\alpha = \frac{\tilde{\rho}_\alpha}{\rho_{\alpha R}}}, \qquad \text{or} \qquad \boxed{\frac{\partial n_\alpha}{\partial t} + \nabla \cdot (n_\alpha \mathbf{v}_\alpha) = \frac{\tilde{\rho}_\alpha}{\rho_{\alpha R}}}. \tag{2.99}$$

Let us stress that equation (2.99) is the incompressibility constraint (2.98) rewritten with the help of the balance of mass. This form can now be readily used in the evaluation of the entropy inequality. In fact, its units are $[s^{-1}]$, so that its Lagrange multiplier $\lambda_{\alpha R}$ has the same units of a pressure, i.e. $[\mathrm{N} \cdot \mathrm{m}^{-2}]$, similarly to the case of the saturation constraint. Thus, $\lambda_{\alpha R}$ can be interpreted as an hydrostatic pressure reflecting the incompressibility of the *real* (not the smeared) material.

Finally, observe that the divergence of the velocity field $\mathbf{v}_\alpha$ can be written as the contraction (see equation (2.67)) of the identity tensor $\underline{\underline{\mathcal{I}}}$ with the Eulerian rate of deformation tensor $\underline{\underline{D}}_\alpha$

$$\nabla \cdot \mathbf{v}_\alpha = \frac{\partial v_\alpha^I}{\partial x^I} = D_\alpha^{II} = \underline{\underline{\mathcal{I}}} : \underline{\underline{D}}_\alpha.$$

Now we are ready to start manipulating the entropy inequality. Multiply equations (2.97) and (2.99) by their corresponding Lagrange multipliers, λ, λ_{SR}, and λ_{FR}, respectively, and add them to the entropy inequality in Table 2.1 to obtain

$$\begin{aligned}&\sum_{\alpha=S,R} \left(-\rho_\alpha (\psi_\alpha)'_\alpha - \tilde{\rho}_\alpha \left(\psi_\alpha - \frac{1}{2} \mathbf{v}_\alpha \cdot \mathbf{v}_\alpha \right) + \underline{\underline{T}}_\alpha : \underline{\underline{D}}_\alpha - \tilde{\mathbf{p}}_\alpha \cdot \mathbf{v}_\alpha \right) \\ &+ \lambda \left(-(n_S)'_S - (n_F)'_F + \nabla n_F \cdot (\mathbf{v}_F - \mathbf{v}_S) \right) \\ &+ \lambda_{SR} \left((n_S)'_S + n_S \nabla \cdot \mathbf{v}_S - \frac{\tilde{\rho}_S}{\rho_{SR}} \right) \\ &+ \lambda_{FR} \left((n_F)'_F + n_F \nabla \cdot \mathbf{v}_F - \frac{\tilde{\rho}_F}{\rho_{FR}} \right) \geq 0.\end{aligned}$$

Manipulating the last inequality and using the constraint $\tilde{\mathbf{p}}_S + \tilde{\mathbf{p}}_F = \mathbf{0}$ in Table 2.1, we obtain

$$\begin{aligned}
&- \rho_S(\psi_S)'_S - \rho_F(\psi_F)'_F \\
&- \tilde{\rho}_S \left(\psi_S - \frac{1}{2}\mathbf{v}_S \cdot \mathbf{v}_S + \frac{\lambda_{SR}}{\rho_{SR}} \right) - \tilde{\rho}_F \left(\psi_F - \frac{1}{2}\mathbf{v}_F \cdot \mathbf{v}_F + \frac{\lambda_{FR}}{\rho_{FR}} \right) \\
&+ (\underline{\underline{T}}_S + \lambda_{SR} n_S \underline{\underline{\mathcal{I}}}) : \underline{\underline{D}}_S + (\underline{\underline{T}}_F + \lambda_{FR} n_F \underline{\underline{\mathcal{I}}}) : \underline{\underline{D}}_F \\
&- (\tilde{\mathbf{p}}_F - \lambda \nabla n_F) \cdot (\mathbf{v}_F - \mathbf{v}_S) - (n_S)'_S(\lambda - \lambda_{SR}) - (n_F)'_F(\lambda - \lambda_{FR}) \geq 0.
\end{aligned} \tag{2.100}$$

To concisely rewrite the above inequality, it is common practice [13] to define the *chemical potential functions*

$$\mu_\alpha := \psi_\alpha - \frac{1}{2}\mathbf{v}_\alpha \cdot \mathbf{v}_\alpha + \frac{\lambda_{\alpha R}}{\rho_{\alpha R}}, \tag{2.101}$$

and the *effective* or *extra field quantities*

$$\underline{\underline{T}}^E_\alpha := \underline{\underline{T}}_\alpha + \lambda_{\alpha R} n_\alpha \underline{\underline{\mathcal{I}}}, \qquad \tilde{\mathbf{p}}^E_F = \tilde{\mathbf{p}}_F - \lambda \nabla n_F. \tag{2.102}$$

The word *effective* is used to denote the total stress tensors $\underline{\underline{T}}_\alpha$ and interaction term $\tilde{\mathbf{p}}_F$ minus the effects of the hydrostatic pressure λ. This is in full agreement with the classical concept of effective stress, which presumes that the effective soil stress in a geophysical consolidation problem is determined by the total stress minus the excess pore pressure [13, 31]. With the help of $\mu_\alpha, \underline{\underline{T}}^E_\alpha$, and $\tilde{\mathbf{p}}^E_F$, and using the constraint $\tilde{\rho}_F + \tilde{\rho}_S = 0$ from Table 2.1, we can rewrite (2.100) as follows

$$\boxed{\begin{aligned}
&- \rho_S(\psi_S)'_S - \rho_F(\psi_F)'_F - \tilde{\rho}_F (\mu_F - \mu_S) + \underline{\underline{T}}^E_S : \underline{\underline{D}}_S + \underline{\underline{T}}^E_F : \underline{\underline{D}}_F \\
&- \tilde{\mathbf{p}}^E_F \cdot (\mathbf{v}_F - \mathbf{v}_S) - (n_S)'_S(\lambda - \lambda_{SR}) - (n_F)'_F(\lambda - \lambda_{FR}) \geq 0.
\end{aligned}} \tag{2.103}$$

In the following, we will introduce constitutive relations for $\underline{\underline{T}}^E_S, \underline{\underline{T}}^E_F, \tilde{\mathbf{p}}^E_F, \psi_S, \psi_F$, and $\tilde{\rho}_F$. This will allow us to close the poro-visco-elastic system of equations listed in Table 2.1.

2.4.3 Constitutive Variables and Evaluation of the Entropy Inequality

The goal of this section is to provide constitutive relations for the quantities

$$\mathcal{R} = \{\underline{\underline{T}}^E_S, \underline{\underline{T}}^E_F, \tilde{\mathbf{p}}^E_F, \psi_S, \psi_F, \tilde{\rho}_F\}, \tag{2.104}$$

in order to close the system of equations shown in Table 2.1. Since porous media theory proceeds from the assumption that each point of the space shaped by the porous solid is occupied by both the fluid and solid phases simultaneously, the response functions (2.104) may depend on a common set $\mathcal{U}$ of constitutive or process variables (see [13, 22, 32]):

$$\mathcal{U} = \left\{ n_S, \underline{\underline{E}}_S, \nabla_S \underline{\underline{E}}_S, \{\underline{\underline{\mathcal{Q}}}^n_S, \nabla_S \underline{\underline{\mathcal{Q}}}^n_S\}^N_{n=1}, \mathbf{v}_F - \mathbf{v}_S, \underline{\underline{D}}_F \right\} \tag{2.105}$$

The choice of process variables is justified as follows:

- The solid volume fraction n_S affects the unknown hydrostatic pressure λ, which is the Lagrange multiplier of the saturation constraint in the rate formulation, see equation (2.97). Observe that n_F does not appear in $\mathcal{U}$ as it is coupled to n_S via the saturation constraint (2.79). Being a scalar function, n_S is observer invariant (see equation (2.87)).

- The partial solid Green-Lagrange strain tensor $\underline{\underline{E}}_S$ and its gradient $\nabla_S \underline{\underline{E}}_S$, together with the internal state variables $\underline{\underline{\mathcal{Q}}}^n_S$ and their gradients $\nabla_S \underline{\underline{\mathcal{Q}}}^n_S$ represent the deformations of the partial solid. The solid free energy ψ_S is a scalar function and must be invariant under a change in Eulerian observer in order for the material behavior to be objective (see equation (2.87)). Since ψ_S depends on the deformation measure d, d must also remain invariant under a change in Eulerian observer, i.e. $\breve{d} = d$. From this argument, the choice of the Green-Lagrange strain tensor follows, since we know it is observer invariant, as shown in Section 2.4.1. The internal state variables $\{\underline{\underline{\mathcal{Q}}}^n_S\}^N_{n=1}$ are variables that represent the *memory* of the material, and are introduced to characterize the viscoelasticity of the solid phase [33, 34]. A viscoelastic solid material exhibits both elastic and viscous, i.e. rate-dependent, material responses, so that the current state of stress (or strain) depends on the whole strain (or stress) history [35,36]. Therefore, $\{\underline{\underline{\mathcal{Q}}}^n_S\}^N_{n=1}$ need to be observer invariant variables defined via evolution equations

$$(\underline{\underline{\mathcal{Q}}}^n_S)'_S = \mathcal{G}_n(\mathcal{U}), \qquad n = 1, \ldots, N.$$

- The velocity difference $\mathbf{v}_F - \mathbf{v}_S$ and the symmetric part of the fluid velocity gradient tensor, $\underline{\underline{D}}_F$, govern dissipative effects in the fluid. In fact, if there is relative motion between the solid and fluid phases ($\mathbf{v}_F - \mathbf{v}_S \neq \mathbf{0}$), we can expect boundary layers at the wall of the pore channels to occur and lead to dissipation. Also, shear stresses in the fluid lead to dissipation. These stresses develop when the fluid is in motion; thus, we expect them to be a function of the Eulerian rate of deformation tensor $\underline{\underline{D}}_F$. Observe that $\underline{\underline{D}}_F$ is objective, whereas $\mathbf{v}_F - \mathbf{v}_S$ is not, as shown in Section 2.4.1. This is not an actual issue, as we will show that $\mathbf{v}_F - \mathbf{v}_S$ is not an independent constitutive variable, so it can be removed from the set $\mathcal{U}$ (2.105).

We are now ready to use the entropy inequality to gain restrictions for constitutive equations. This procedure is known as *evaluation of the entropy inequality*. The analysis will be performed in the case of *small deviations from the equilibrium state of the mixture* [13, 32].

Definition. The *equilibrium state of a mixture* is the state characterized by

$$\mathcal{U} = \left\{ n_S, \underline{\underline{E}}_S, \nabla_S \underline{\underline{E}}_S = \overset{3}{0}, \{ \underline{\underline{\mathcal{Q}}}^n_S, \nabla_S \underline{\underline{\mathcal{Q}}}^n_S = \overset{3}{0} \}_{n=1}^N, \mathbf{v}_F - \mathbf{v}_S = \mathbf{0}, \underline{\underline{D}}_F = \underline{\underline{0}} \right\}, \tag{2.106}$$

where $\overset{3}{(\cdot)}$ denotes a tensor of order 3, i.e. a tensor with 3 associated directions (for example, the Levi-Civita symbol defined in (2.55) is a tensor of order 3).

Thus, considering small deviations from the equilibrium state refers to small values of $\nabla_S \underline{\underline{E}}_S, \nabla_S \underline{\underline{\mathcal{Q}}}_S, \mathbf{v}_F - \mathbf{v}_S, \underline{\underline{D}}_F$. The evaluation of the entropy inequality around the mixture equilibrium state is described in great details by de Boer [13] and Bowen [32]. The main results of their analysis are the following functional dependencies for the solid and fluid free energies

$$\psi_S = \psi_S(n_S, \underline{\underline{E}}_S, \{ \underline{\underline{\mathcal{Q}}}^n_S \}_{n=1}^N), \qquad \psi_F = \text{constant}. \tag{2.107}$$

In equation (2.107), the free energy ψ_α of a given constituent α only depends on the variables included into the process by the respective constituent (actually, ψ_F is a

constant in our case, so this observation is trivially true for ψ_F). This situation is also known as *principle of phase separation* [37]. Rather than repeating the extremely detailed analysis of Bowen [32] and de Boer [13], we will illustrate the evaluation of the entropy inequality giving the functional dependencies (2.107) for granted.

Using the chain rule on (2.107), the material time derivatives of ψ_S and ψ_F are

$$(\psi_S)'_S = \frac{\partial \psi_S}{\partial n_S}(n_S)'_S + \frac{\partial \psi_S}{\partial \underline{\underline{E}}_S} : (\underline{\underline{E}}_S)'_S + \sum_{n=1}^{N} \frac{\partial \psi_S}{\partial \underline{\underline{\mathcal{Q}}}^n_S} : (\underline{\underline{\mathcal{Q}}}^n_S)'_S, \tag{2.108}$$

$$(\psi_F)'_F = 0. \tag{2.109}$$

From the definition of the Green-Lagrange strain tensor $\underline{\underline{E}}_\alpha$ (2.20) and equation (2.16), it follows that

$$\begin{aligned}(E^{IJ}_S)'_S &= \frac{1}{2}(F^{KI}_S F^{KJ}_S - \delta^{IJ})'_S = \frac{1}{2}(\,(F^{KI}_S)'_S F^{KJ}_S + F^{KI}_S (F^{KJ}_S)'_S\,) \\ &= \frac{1}{2}(\,(L^{KM}_S F^{MI}_S) F^{KJ}_S + F^{KI}_S (L^{KM}_S F^{MJ}_S)\,),\end{aligned}$$

and then

$$\begin{aligned}\frac{\partial \psi_S}{\partial \underline{\underline{E}}_S} : (\underline{\underline{E}}_S)'_S &= \frac{\partial \psi_S}{\partial E^{IJ}_S}(E^{IJ}_S)'_S = \frac{1}{2}\frac{\partial \psi_S}{\partial E^{IJ}_S}(L^{KM}_S F^{MI}_S F^{KJ}_S + F^{KI}_S L^{KM}_S F^{MJ}_S) \\ &= \frac{1}{2}\left(F^{MI}_S \frac{\partial \psi_S}{\partial E^{IJ}_S} F^{KJ}_S\right) L^{KM}_S + \frac{1}{2}\left(F^{KI}_S \frac{\partial \psi_S}{\partial E^{IJ}_S} F^{MJ}_S\right) L^{KM}_S \\ &= \frac{1}{2}\left(\underline{\underline{F}}_S \frac{\partial \psi_S}{\partial \underline{\underline{E}}_S} \underline{\underline{F}}^T_S\right) : \underline{\underline{L}}^T_S + \frac{1}{2}\left(\underline{\underline{F}}_S \frac{\partial \psi_S}{\partial \underline{\underline{E}}_S} F^T_S\right) : \underline{\underline{L}}_S \\ &= \left(\underline{\underline{F}}_S \frac{\partial \psi_S}{\partial \underline{\underline{E}}_S} \underline{\underline{F}}^T_S\right) : \underline{\underline{D}}_S,\end{aligned} \tag{2.110}$$

where $\underline{\underline{D}}_S$ is the symmetric part of $\underline{\underline{L}}_S$. Inserting (2.108), (2.109), and (2.110)

$$\begin{aligned}&\left(\underline{\underline{T}}^E_S - \rho_S \underline{\underline{F}}_S \frac{\partial \psi_S}{\partial \underline{\underline{E}}_S} \underline{\underline{F}}^T_S\right) : \underline{\underline{D}}_S - \rho_S \sum_{n=1}^{N} \frac{\partial \psi_S}{\partial \underline{\underline{\mathcal{Q}}}^n_S} : (\underline{\underline{\mathcal{Q}}}^n_S)'_S - \tilde{\rho}_F\,(\mu_F - \mu_S) + \underline{\underline{T}}^E_F : \underline{\underline{D}}_F \\ &- \tilde{\mathbf{p}}^E_F \cdot (\mathbf{v}_F - \mathbf{v}_S) - (n_S)'_S \left(\lambda - \lambda_{SR} + \rho_S \frac{\partial \psi_S}{\partial n_S}\right) - (n_F)'_F (\lambda - \lambda_{FR}) \geq 0,\end{aligned} \tag{2.111}$$

which has to be true for all valid thermodynamic processes. These processes are identified by all possible combinations of the variables

$$\underline{\underline{D}}_S, \quad (\underline{\underline{\mathcal{Q}}}^n_S)'^{\,N}_{S\,n=1}, \quad \mu_F - \mu_S, \quad \underline{\underline{D}}_F, \quad \mathbf{v}_F - \mathbf{v}_S, \quad (n_S)'_S, \quad (n_F)'_F. \tag{2.112}$$

One such process is the instantaneous elastic deformation of the real solid material, which is represented by an arbitrary change in $\underline{\underline{D}}_S$, whereas all the other variables in (2.112) are fixed. Inequality (2.111) is then satisfied only if

$$\boxed{\underline{\underline{T}}^E_S - \rho_S \underline{\underline{F}}_S \frac{\partial \psi_S}{\partial \underline{\underline{E}}_S} \underline{\underline{F}}^T_S = \underline{\underline{0}}}, \quad \text{or} \quad \boxed{\underline{\underline{T}}^E_S = \rho_S \underline{\underline{F}}_S \frac{\partial \psi_S}{\partial \underline{\underline{E}}_S} \underline{\underline{F}}^T_S}. \tag{2.113}$$

In addition, considering a process that only involves a change in the volume fractions, either $(n_S)'_S$ or $(n_F)'_F$, independently, we deduce that

$$\boxed{\lambda - \lambda_{SR} + \rho_S \frac{\partial \psi_S}{\partial n_S} = 0}, \quad \text{or} \quad \boxed{\lambda = \lambda_{SR} - \rho_S \frac{\partial \psi_S}{\partial n_S}}, \tag{2.114}$$

and

$$\boxed{\lambda - \lambda_{FR} = 0}, \quad \text{or} \quad \boxed{\lambda = \lambda_{FR}}. \tag{2.115}$$

As expected, we gain two expressions for the interface pressure λ, because λ acts on both the solid and fluid constituents. Equation (2.115) implies that, within the assumptions we made to develop our constitutive model, λ coincides with the Lagrange multiplier of the fluid incompressibility, λ_{FR}, which is understood as the fluid pressure, in analogy with classical fluid mechanics.

The remainder of the entropy inequality (2.111), the so-called *residual* inequality is

$$-\rho_S \sum_{n=1}^{N} \frac{\partial \psi_S}{\partial \underline{\underline{\mathcal{Q}}}^n_S} : (\underline{\underline{\mathcal{Q}}}^n_S)'_S + \underline{\underline{T}}^E_F : \underline{\underline{D}}_F - \tilde{\rho}_F(\mu_F - \mu_S) - \tilde{\mathbf{p}}^E_F \cdot (\mathbf{v}_F - \mathbf{v}_S) \geq 0. \tag{2.116}$$

This inequality cannot be further reduced because the following variables

$$\{(\underline{\underline{\mathcal{Q}}}^n_S)'_S\}_{n=1}^N, \quad \underline{\underline{D}}_F, \quad \mu_F - \mu_S, \quad \mathbf{v}_F - \mathbf{v}_S$$

are not free, i.e. they cannot assume arbitrary values independently from one another:

- The rates of the internal variables $\{(\underline{\underline{\mathcal{Q}}}^n_S)'_S\}_{n=1}^N$ have to be defined by evolution equations associated with the intrinsic dissipation mechanisms of the solid phase.

- According to classic continuum mechanics, the stress for a general fluid does depend on the rate of deformation. In other words, $\underline{\underline{D}}_F$ cannot vary independently of $\underline{\underline{T}}_F^E$.

- The chemical potentials μ_F and μ_S are related to the fluid and solid velocities, $\mathbf{v}_F$ and $\mathbf{v}_S$, respectively.

- The velocity difference $\mathbf{v}_F - \mathbf{v}_S$ is coupled to the free variables $(n_F)'_F$ and $(n_S)'_S$ via equation (2.97), so it is not an independent variable.

Comparing inequality (2.116) with the definition of equilibrium state of the mixture (2.106), we get that (2.116) represents the irreversible or dissipative parts responsible for the non-equilibrium states of the binary model. Constitutive laws for

$$\{(\underline{\underline{\mathcal{Q}}}_S^n)'_S\}_{n=1}^N, \quad \underline{\underline{T}}_F^E, \quad \tilde{\rho}_F, \quad \tilde{\mathbf{p}}_F^E,$$

can be obtained assuming that each expression of the residual inequality (2.116) yields a positive definite quadratic form, which can accomplished by assuming the following proportionalities

$$-\rho_S \frac{\partial \psi_S}{\partial \underline{\underline{\mathcal{Q}}}_S^n} \propto (\underline{\underline{\mathcal{Q}}}_S^n)'_S, \quad \underline{\underline{T}}_F^E \propto \underline{\underline{D}}_F, \quad \tilde{\rho}_F \propto -(\mu_F - \mu_S), \quad \tilde{\mathbf{p}}_F^E \propto -(\mathbf{v}_F - \mathbf{v}_S). \tag{2.117}$$

2.4.4 Linear Viscoelastic Models for the Solid Constituent

The goal of this section is to provide constitutive laws for the effective stress tensor $\underline{\underline{T}}_S^E$ of the solid constituent. The main references used here are the books of Fung [35] and Findley et al. [36].

Many materials, included the living tissues our bodies are made of, exhibit both elastic and viscous behaviors in response to applied loads. When stressed, elastic materials undergo instantaneous deformation, whereas viscous materials exhibit time-dependent strain effects. Materials that exhibit both these behaviors are called *viscoelastic*, and, as such, have strain rate effects in response to applied loads. These time-dependent phenomena may have a considerable effect on the stress and strain

distributions. In this section, few basic concepts of linear viscoelasticity will be provided within a one dimensional framework, which yields a mathematically tractable representation for stress-strain-time relationships and leads to reasonably simple models for the biomechanical applications we are interested in. Linear viscoelasticity is based on the *Boltzmann superposition principle*:

Proposition 2.4.1 (Boltzmann superposition principle) *The sum of the strain outputs resulting from each component of stress input is the same as the strain output resulting from the combined stress input [36].*

The behavior of most materials is linear, or approximately linear, under small strain and stress levels. Three dimensional linear viscoelastic behavior will be described by formal extension of the governing scalar equations. Finally, these findings will be brought in accordance with the entropy inequality (2.111), in order to formulate constitutive laws for the effective stress tensor $\underline{\underline{T}}_S^E$.

There are some phenomena that are common to many viscoelastic materials, as illustrated in Figure 2.7:

- *Instantaneous elasticity*: the material instantaneously deforms in response to an applied load and instantaneously recovers once the load is removed.
- *Creep under constant stress*: if the material is suddenly stressed and then the stress is maintained constant afterwards, the body continues to deform.
- *Stress relaxation under constant strain*: when a body is suddenly strained and then the strain is maintained constant afterwards, the corresponding stresses induced in the body decrease with time.
- *Delayed recovery*: following stress removal, the material does not recover immediately, but rather at a decreasing rate.
- *Permanent set*: following recovery, a permanent nonzero strain remains in the material.

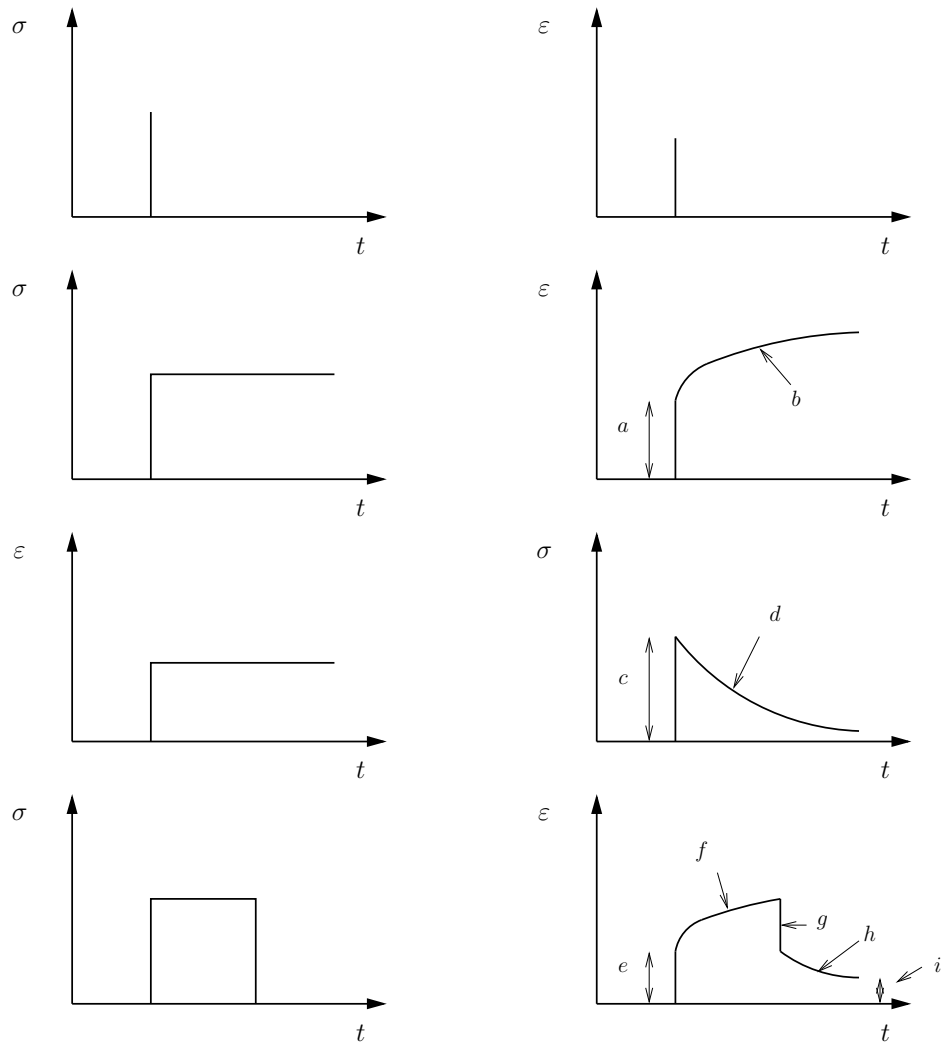

Figure 2.7. Phenomena common to many viscoelastic materials. For each row, the graph on the left represents a particular stress (σ) or strain (ε) input, whereas the graph on the right represents the corresponding strain or stress output: (first row) instantaneous elasticity; (second row) instantaneous elasticity (a) and creep (b) under constant stress; (third row) instantaneous elasticity (c) and stress relaxation (d) under constant strain; (fourth row) instantaneous elasticity (e), creep (f), instantaneous recovery (g), delayed recovery (h), and permanent set (i).

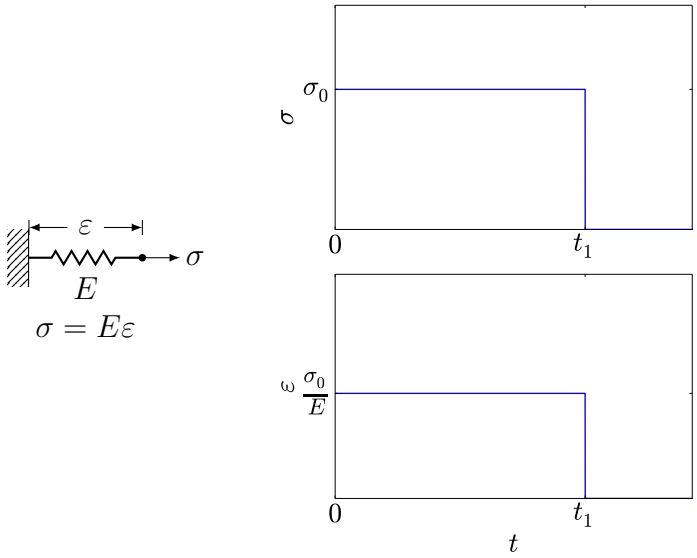

Figure 2.8. Behavior of a linear spring.

- *Hysteresis*: if the material is subject to a cyclic loading, the stress-strain relationship in the loading process is usually different from that in the unloading process.

One Dimensional Models for Linear Viscoelasticity

Mechanical models are often used to discuss the viscoelastic behavior of materials. These models are composed of combinations of linear springs with spring constant E and linear dashpots with constant coefficient of viscosity η. A *linear spring* is supposed to produce an instantaneous deformation proportional to the load (see Figure 2.8). If $\sigma\colon [0,T) \to \mathbb{R}$ is the stress acting on a spring and $\varepsilon\colon [0,T) \to \mathbb{R}$ is the induced strain, we have

$$\sigma(t) = E\varepsilon(t). \tag{2.118}$$

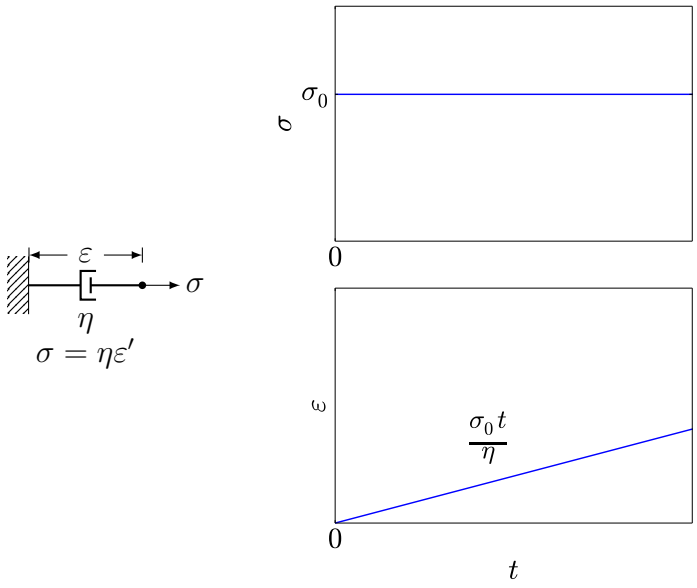

Figure 2.9. Behavior of a linear dashpot.

A *linear dashpot* is supposed to produce a strain rate proportional to the load (see Figure 2.9). Dashpots are commonly used in shock absorbers for cars and airplanes. For a dashpot, we have

$$\sigma(t) = \eta\varepsilon'(t), \tag{2.119}$$

where $(\cdot)'$ denotes time differentiation within the current one dimensional framework. Equation (2.119) is equivalent to

$$\varepsilon(t) = \frac{1}{\eta}\int_0^t \sigma(s)\, ds.$$

According to (2.119), the strain rate $\varepsilon'(t)$ is proportional to the stress, i.e. the dashpot will be deformed continuously at a constant rate when it is subject to a step of constant stress (see Figure 2.9). On the other hand, if it was possible to impose a step of constant strain on the dashpot, the strain rate $\varepsilon'(0)$, and so $\sigma(0)$, should have an infinite value, whereas it would be $\varepsilon'(t) = 0$ and $\sigma(t) = 0$ for $t > 0$. This behavior can be modeled by the so called *Dirac measure at the origin*, denoted by the symbol

δ. The Dirac measure is not a function in the usual sense of analysis; if it were, it should have the following properties:

$$\begin{aligned} &\delta(0) = \infty, \quad \delta(t) = 0 \text{ for } t \neq 0, \\ &\int_{\mathbb{R}} \delta(t)\, dt = 1, \end{aligned} \tag{2.120}$$

clearly incompatible with any concept of classical function or integral. A rigorous definition of the Dirac measure requires the theory of *generalized functions* or *distributions* [38]. Thus, the stress resulting from a step change in strain is indicated as follows

$$\sigma(t) = \eta\delta(t).$$

Since an infinite stress is impossible in reality, it is impossible to impose any finite deformation on a dashpot instantaneously.

Maxwell Model

The Maxwell model is a two-element model consisting of a linear spring and a linear dashpot connected in series, as shown in Figure 2.10. In a Maxwell model, the same stress σ is transmitted from the spring to the dashpot. This stress produces a strain

$$\varepsilon_1 = \frac{\sigma}{E} \tag{2.121}$$

in the spring, and a strain rate

$$\varepsilon_2' = \frac{\sigma}{\eta} \tag{2.122}$$

in the dashpot. Since both elements are connected in series, the total strain ε is

$$\varepsilon = \varepsilon_1 + \varepsilon_2,$$

so that the total strain rate is

$$\varepsilon' = \varepsilon_1' + \varepsilon_2'. \tag{2.123}$$

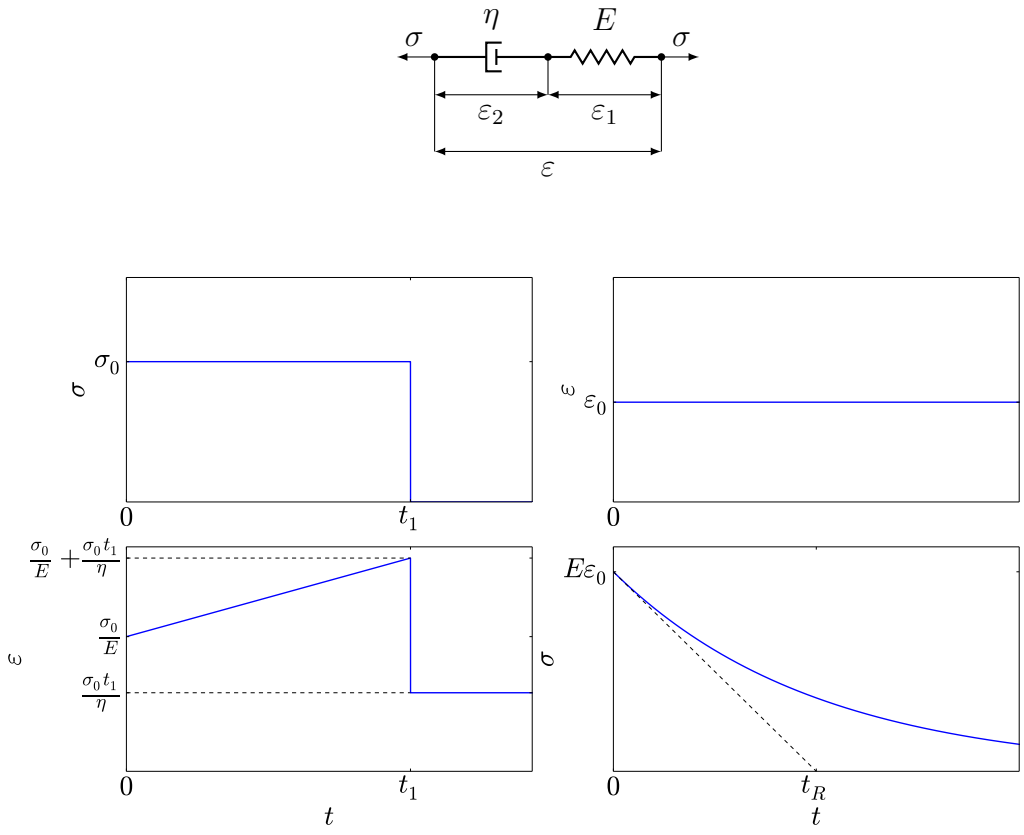

Figure 2.10. Behavior of a Maxwell model: (top) Maxwell model; (graphs on the left) creep and recovery; (graphs on the right) stress relaxation.

Substituting the time derivative of equations (2.121) and (2.122) into (2.123), we obtain the following relationship between σ and ε for the Maxwell model

$$\boxed{\varepsilon' = \frac{\sigma'}{E} + \frac{\sigma}{\eta}, \quad t > 0}. \tag{2.124}$$

Equation (2.124) can be solved for the strain $\varepsilon(t)$ given a stress condition $\sigma(t)$, or for the stress $\sigma(t)$ given a strain $\varepsilon(t)$ input.

For example, applying a constant stress $\sigma = \sigma(0)$ at $t = 0$, equation (2.124) becomes a first order differential equation for ε

$$\varepsilon' = \frac{\sigma(0)}{\eta}, \tag{2.125}$$

which describes the *creep response* of the Maxwell model. If the stress is suddenly applied at $t = 0$, the spring will be suddenly deformed to $\varepsilon_1 = \sigma(0)/E$, but the initial dashpot deflection ε_2 would be zero, because there is no time to deform. Thus the initial condition for (2.125) is

$$\varepsilon(0) = \frac{\sigma(0)}{E}.$$

The solution of (2.125) is then

$$\boxed{\varepsilon(t) = \sigma(0)\left(\frac{1}{E} + \frac{1}{\eta}t\right)}, \tag{2.126}$$

which is represented in Figure 2.10. According to the last equation, the sudden application of a load induces an immediate deflection by the elastic spring, which is followed by *creep* of the dashpot. If the stress is removed at time t_1, the elastic strain $\sigma(0)/E$ in the spring returns to zero at the instant the stress is removed (instantaneous recovery), whereas $\sigma(0)t_1/\eta$ is a permanent stress that does not go away. If the Maxwell model is subject to a constant strain $\varepsilon(0)$ at time $t = 0$, then equation (2.124) becomes

$$\sigma' = -\frac{E}{\eta}\sigma,$$

with initial condition $\sigma(0) = E\varepsilon(0)$, whose solution is

$$\boxed{\sigma(t) = E\varepsilon(0)e^{-Et/\eta}}, \tag{2.127}$$

which is represented in Figure 2.10. Equation (2.127) describes the *stress relaxation* phenomenon for a Maxwell model under constant strain. The initial stress rate of change is

$$\sigma'(t)|_{t=0} = -\frac{\sigma(0)E}{\eta}.$$

If the stress was decreasing linearly at this initial rate, the relaxation would follow the straight line

$$\sigma(t) = -\frac{\sigma(0)E}{\eta}t + \sigma(0),$$

so that the stress would be zero when $t = t_R = \eta/E$, which is called the *relaxation time* of the Maxwell model. The relaxation time is one of the viscoelastic properties of the material. When $t = t_R$, most of the relaxation has already occurred, since $\sigma(t_R) = \sigma(0)/e \approx 0.37\sigma(0)$. Thus, about 37% of the initial stress remains at $t = t_R$.

Voigt Model

In the Voigt model, a linear spring and a linear dashpot are connected in parallel (see Figure 2.11). Since they are connected in parallel, they undergo the same strain ε. The spring and the dashpot will produce stresses

$$\sigma_1 = E\varepsilon \quad \text{and} \quad \sigma_2 = \eta\varepsilon', \tag{2.128}$$

respectively. Since both elements are connected in parallel, the total stress σ is

$$\sigma = \sigma_1 + \sigma_2. \tag{2.129}$$

Combining equations (2.128) and (2.129), we get the following relation between stress σ and strain ε

$$\boxed{\varepsilon' + \frac{E}{\eta}\varepsilon = \frac{\sigma}{\eta}, \quad t > 0}. \tag{2.130}$$

The creep curve for the Voigt model can be obtained by solving (2.130) under a constant stress $\sigma = \sigma(0)$ applied at $t = 0$. A sudden application of a stress will produce no immediate deflection, because the dashpot, arranged in parallel with the spring, will not move instantaneously. Therefore, the appropriate initial condition is

$$\varepsilon(0) = 0.$$

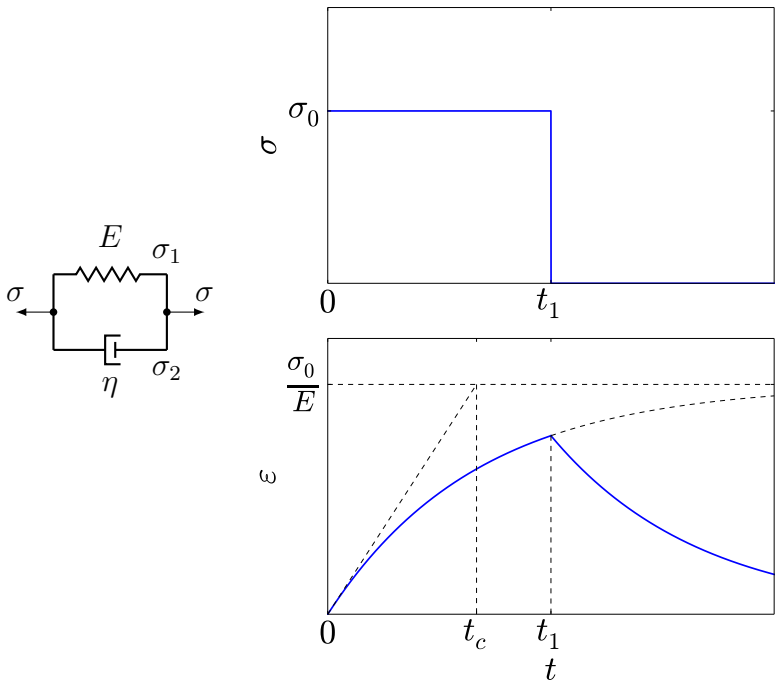

Figure 2.11. Behavior of a Voigt model: (left) Voigt model; (right) creep and recovery.

The solution of equation (2.130) is then

$$\boxed{\varepsilon(t) = \frac{\sigma(0)}{E}(1 - e^{-Et/\eta})}. \tag{2.131}$$

As illustrated in Figure 2.11, the strain described by (2.131) decreases with a decreasing rate and approaches asymptotically the value $\sigma(0)/E$. Initially, for the Voigt model, a suddenly applied stress is carried entirely by the dashpot. Under the constant stress $\sigma(0)$, the dashpot elongates and gradually transfers the load to the spring. Finally, i.e. when $e^{-Et/\eta} \to 0$ for $t \to \infty$, the entire stress is carried by the spring. This behavior is called *delayed elasticity*.

The initial strain rate is

$$\varepsilon'(t)|_{t=0} = \frac{\sigma(0)}{\eta}.$$

If the strain ε increased linearly at this initial rate, it would cross the horizontal asymptote at time $t = t_C = \eta/E$, called the *retardation time*. Most of the total strain $\sigma(0)/E$ occurs before the retardation time, since

$$\varepsilon(t_C) = \frac{\sigma(0)}{E}\left(1 - \frac{1}{e}\right) \approx 0.63\frac{\sigma(0)}{E}.$$

Hence, after $t = t_C$, only about 37% of the asymptotic strain remains to be accomplished. The recovery behavior of the Voigt model can be obtained from equation (2.131) and the superposition principle (Proposition 2.4.1) by considering that at time $t = t_1$ a constant stress $-\sigma(0)$ is added. Therefore, the recovery strain $\varepsilon(t), t > t_1$ is the sum of two independent actions

$$\begin{aligned}\varepsilon(t) &= \frac{\sigma(0)}{E}(1 - e^{-Et/\eta}) - \frac{\sigma(0)}{E}(1 - e^{-E(t-t_1)/\eta}) \\ &= \frac{\sigma(0)}{E}e^{-Et/\eta}(e^{Et_1/\eta} - 1), \qquad t > t_1.\end{aligned}$$

When $t \to \infty$, $\varepsilon(t) \to 0$: the Voigt model exhibits full recovery. In reality, some materials show full recovery, whereas others only partial recovery.

The Voigt model cannot be used to study the stress relaxation phenomenon in response to a step change in strain $\varepsilon(0)$. As noted above, a sudden application of a strain cannot produce immediate deflection due to the dashpot, which is arranged

in parallel with the spring. A step change in strain would correspond to an infinite stress at $t = 0$. For $t > 0$, due to the constant strain $\varepsilon = \varepsilon(0)$, the stress carried by the dashpot would immediately drop to zero

$$\sigma_2(t) = \eta(\varepsilon)' = 0,$$

but a constant stress $E\varepsilon(0)$ would remain in the spring. This can be modeled by using the Dirac distribution δ, heuristically defined in (2.120)

$$\boxed{\sigma(t) = \eta\delta(t) + E\varepsilon(0)}. \tag{2.132}$$

Neither the Maxwell nor the Voigt models are able to describe the behavior of all possible viscoelastic materials. For example, the Voigt model does not exhibit instantaneous elasticity, and it cannot be used to study stress relaxation under constant strain, as we just discussed, nor does it describe a permanent strain after unloading. The Maxwell model does not show either time-dependent recovery or the decreasing strain rate under constant stress that is typical of primary creep. Therefore, sometimes, more complex mechanical models need to be formulated.

Kelvin model

The Kelvin model (also called the *standard linear solid model*) is shown in Figure 2.12, where a spring and a Maxwell model are connected in parallel. Since they are connected in parallel, the strain ε in the spring and the strain $\varepsilon_1 + \varepsilon_2$ in the Maxwell element are the same

$$\varepsilon = \varepsilon_1 + \varepsilon_2. \tag{2.133}$$

The total stress σ is the sum of the stress σ_0 from the spring and σ_1 from the Maxwell element:

$$\sigma = \sigma_0 + \sigma_1, \tag{2.134}$$

$$\sigma_0 = E_0\varepsilon, \tag{2.135}$$

$$\sigma_1 = E_1\varepsilon_1 = \eta_1\varepsilon_2'. \tag{2.136}$$

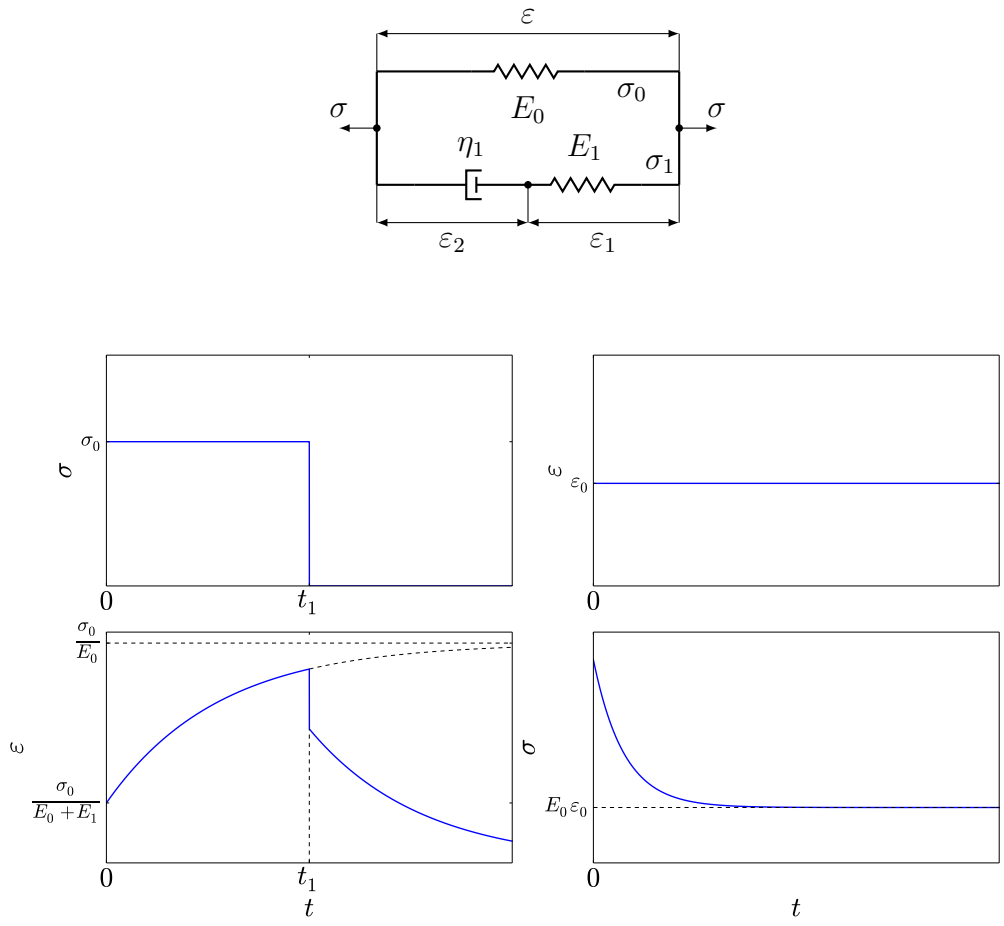

Figure 2.12. Behavior of a Kelvin model: (top) Kelvin model; (graphs on the left) creep and recovery; (graphs on the right) stress relaxation.

A constitutive equation between σ and ε for the Kelvin model can be obtained in the following way:

- Combine the time derivative of equation (2.133), $\varepsilon' = \varepsilon_1' + \varepsilon_2'$, with (2.136) to get
$$\varepsilon' = \varepsilon_1' + \varepsilon_2' = \frac{\sigma_1'}{E_1} + \frac{\sigma_1}{\eta_1}. \tag{2.137}$$

- Solve for σ_1 and its time derivative σ_1' from (2.134) and combine it with (2.135)
$$\sigma_1 = \sigma - \sigma_0 = \sigma - E_0\varepsilon, \qquad \sigma_1' = \sigma' - \sigma_0' = \sigma' - E_0\varepsilon'.$$

- Combine the last two equations with (2.137)
$$\varepsilon' = \frac{\sigma' - E_0\varepsilon'}{E_1} + \frac{\sigma - E_0\varepsilon}{\eta_1},$$
which can be rewritten in the form
$$\eta_1\left(1 + \frac{E_0}{E_1}\right)\varepsilon' + E_0\varepsilon = \frac{\eta_1}{E_1}\sigma' + \sigma,$$
or, equivalently,
$$\boxed{E_0(\tau_\sigma\varepsilon' + \varepsilon) = \tau_\varepsilon\sigma' + \sigma, \qquad t > 0}, \tag{2.138}$$
where
$$\tau_\sigma = \frac{\eta_1}{E_0}\left(1 + \frac{E_0}{E_1}\right), \qquad \tau_\varepsilon = \frac{\eta_1}{E_1}.$$

For a suddenly applied stress $\sigma(0)$ and strain $\varepsilon(0)$, the initial dashpot strain ε_2 would be zero, because there is no time to deform. Thus, the two springs have the same strain $\varepsilon = \varepsilon_1 = \varepsilon(0)$, and the appropriate initial condition for equation (2.138) is

$$\sigma(0) = E_0\varepsilon(0) + E_1\varepsilon(0) = (E_0 + E_1)\varepsilon(0) = E_0\frac{\tau_\sigma}{\tau_\varepsilon}\varepsilon(0). \tag{2.139}$$

The creep behavior of the Kevin model under constant stress $\sigma = \sigma(0)$ can be obtained by solving (2.138) with initial condition (2.139), which gives

$$\boxed{\varepsilon(t) = \frac{\sigma(0)}{E_0}\left(1 - \left(1 - \frac{\tau_\varepsilon}{\tau_\sigma}\right)e^{-t/\tau_\sigma}\right)}, \tag{2.140}$$

which is illustrated in Figure 2.12. At $t = 0$, there is an instantaneous elastic response from the two springs. Then, the dashpot starts elongating, transferring a greater and greater portion of σ_1 to the spring E_0. As a result, the strain approaches $\sigma(0)/E_0$ asymptotically. The recovery behavior can be obtained from equation (2.140) and the superposition principle (Proposition 2.4.1) by considering that at $t = t_1$ a constant stress $\sigma = -\sigma_0$ is added. Hence, the recovery strain $\varepsilon(t), t > t_1$ is

$$\begin{aligned}\varepsilon(t) = &\frac{\sigma(0)}{E_0}\left(1 - \left(1 - \frac{\tau_\varepsilon}{\tau_\sigma}\right)e^{-t/\tau_\sigma}\right) \\ &- \frac{\sigma(0)}{E_0}\left(1 - \left(1 - \frac{\tau_\varepsilon}{\tau_\sigma}\right)e^{-(t-t_1)/\tau_\sigma}\right),\end{aligned}$$

or

$$\varepsilon(t) = \frac{\sigma(0)}{E_0}\left(1 - \frac{\tau_\varepsilon}{\tau_\sigma}\right)\left(e^{t_1/\tau_\sigma} - 1\right)e^{-t/\tau_\sigma}. \tag{2.141}$$

Recovery is also shown in Figure 2.12. The recovery exhibits an instantaneous elastic decrease (equal to $(\sigma(0)\tau_\varepsilon)/(E_0\tau_\sigma)$), then tends towards zero as $t \to \infty$.

From equations (2.138) and (2.139), the stress relaxation behavior of the Kelvin model can also be obtained

$$\sigma(t) = E_0\varepsilon(0)\left(1 - \left(1 - \frac{\tau_\sigma}{\tau_\varepsilon}\right)e^{-t/\tau_\varepsilon}\right), \tag{2.142}$$

which is illustrated in Figure 2.12. From (2.142), it follows that $\sigma(t) \to E_0\varepsilon(0)$ as $t \to \infty$, so that the Kelvin model prescribes a nonzero permanent stress from a relaxation process with infinite duration.

In conclusion, the behavior of the Kelvin model shows similarities with both the Maxwell and the Voigt models. Nevertheless, it cannot describe the behavior of many viscoelastic materials. For example, from (2.141), it follows that it cannot be used for those materials that exhibit partial recovery after stress unloading.

Another limitation of the Maxwell, Voigt and Kelvin models is that they have only one relaxation or retardation time, whereas real materials often behave as if they have several relaxation times. To deal with this situation and be able to describe more materials, several complex models have been proposed.

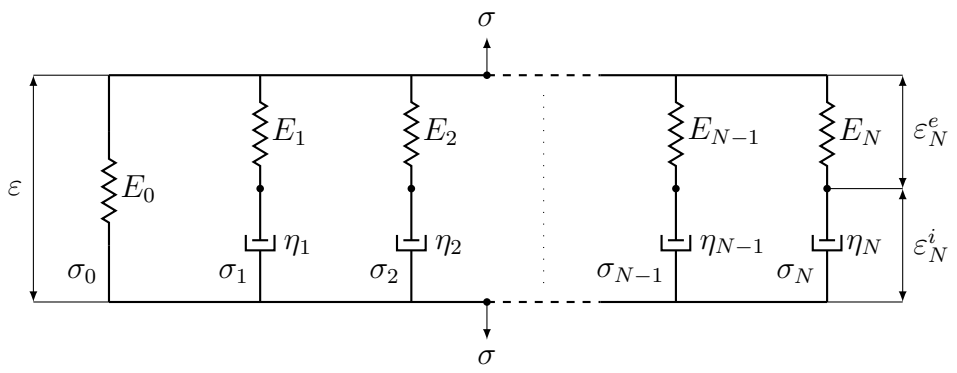

Figure 2.13. Generalized Maxwell model.

Generalized Linear Viscoelastic Models

In order to account for several relaxation mechanisms within a single body, each of which characterized by a different relaxation time, several spring and dashpot elements could be combined together. For example, several Maxwell models connected in parallel with a spring, as shown in Figure 2.13, are able to represent instantaneous elasticity, delayed elasticity with various retardation times, and stress relaxation with various relaxation times. The generalized Maxwell model is rather convenient to predict the stress associated with a prescribed strain variation, because the same prescribed strain is applied to each individual element. The resulting stress σ is the sum of the individual contributions. Denoting by N the number of Maxwell elements, constitutive equations of this model are:

$$\begin{aligned}
\varepsilon &= \varepsilon_n^e + \varepsilon_n^i, \\
\sigma &= \sigma_0 + \sum_{n=1}^{N} \sigma_n, \\
\sigma_0 &= E_0 \varepsilon, \\
\sigma_n &= E_n \varepsilon_n^e = \eta_n (\varepsilon_n^i)'.
\end{aligned}$$

The order of the differential equation relating σ and ε is increased by one for each additional Maxwell branch [36]. Another generalized form of the basic models may

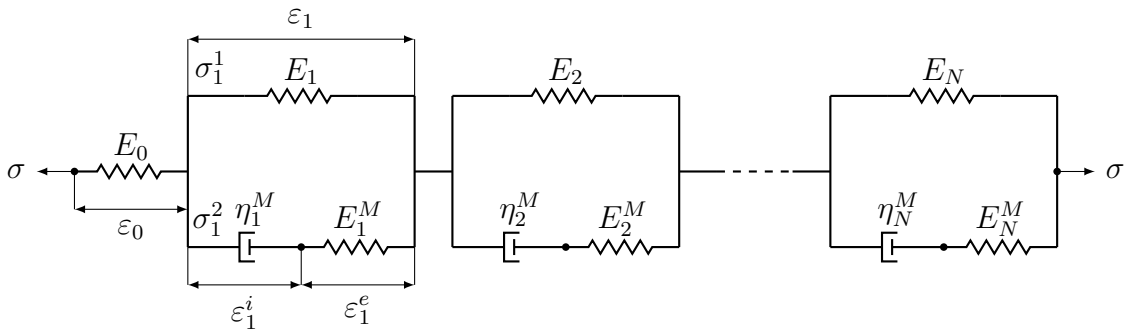

Figure 2.14. Generalized Kelvin model.

be obtained by considering various Kelvin models in series with a spring as in Figure 2.14 [35].

The same stress σ is transmitted to the spring E_0 and to each Kelvin unit. In analogy with (2.133)–(2.136), the constitutive equations of this model are:

$$\begin{aligned}
\varepsilon &= \varepsilon_0 + \sum_{n=1}^{N} \varepsilon_n, \\
\varepsilon_n &= \varepsilon_n^e + \varepsilon_n^i, \\
\sigma &= \sigma_n^1 + \sigma_n^2, \\
\sigma_n^1 &= E_n \varepsilon_n, \\
\sigma_n^2 &= E_n^M \varepsilon_n^e = \eta_n^M (\varepsilon_n^i)'.
\end{aligned}$$

The generalized Kelvin model (see Figure 2.14) is more convenient than the generalized Maxwell model (see Figure 2.13) for viscoelastic analysis in cases where the stress history is prescribed. Because of the range of different relaxation times that can be brought into play, both of these models permit a close description of real behavior over a wider time span than with simpler models.

The most general formulation of a linear viscoelastic law is the integral representation due to Boltzmann (1844–1906). Let the origin of time be taken at the beginning of motion and loading. We introduce two functions:

- The *creep compliance*, $J\colon [0,T) \to \mathbb{R}$. For each $t \in [0,T)$, $J(t)$ represents the creep strain per unit of applied stress at time t.

- The *relaxation modulus*, $E\colon [0,T) \to \mathbb{R}$. For each $t \in [0,T)$, $E(t)$ represents the stress per unit of applied strain at time t.

In general, $J(t)$ and $E(t)$ are different for each material. Also, let

$$H(t) = \begin{cases} 1 & \text{if } t \geq 0, \\ 0 & \text{if } t < 0, \end{cases} \tag{2.143}$$

be the characteristic function of the interval $[0,\infty)$, known as the Heaviside function. If a constant stress is applied at $t = \tau_1$, then $\sigma(t) = \sigma_1 H(t-\tau_1)$ and the corresponding strain will be

$$\varepsilon(t) = \sigma_1 J(t-\tau_1)H(t-\tau_1).$$

If the stress input $\sigma(t)$ is variable with time, the strain output $\varepsilon(t)$ can be expressed using the superposition principle (Proposition 2.4.1). If the function $\sigma(t)$ is continuous and differentiable, Taylor's theorem can be used to write the increment of loading $d\sigma(\tau)$ in a small time interval $d\tau$ at time τ

$$d\sigma(\tau) = \frac{d\sigma(\tau)}{d\tau} d\tau.$$

This stress increment will induce a strain increment $d\varepsilon$

$$d\varepsilon = J(t-\tau)H(t-\tau)d\sigma(\tau) = J(t-\tau)H(t-\tau)\frac{d\sigma(\tau)}{d\tau}d\tau.$$

Thus, summing over the entire stress history, which is allowed under the superposition principle (Proposition 2.4.1), we get

$$\varepsilon(t) = \int_0^t J(t-\tau)H(t-\tau)\frac{d\sigma(\tau)}{d\tau}d\tau = \int_0^t J(t-\tau)\frac{d\sigma(\tau)}{d\tau}d\tau. \tag{2.144}$$

To get the last equality, we used the fact that $H(t-\tau) = 1$, $\forall \tau \in [0,t]$. Similar arguments apply when arbitrary changes in strain are applied and the resulting change

in stress is determined. Thus, the current stress $\sigma(t)$ due to a constant strain ε_1 applied at $t = \tau_1$ is

$$\sigma(t) = E(t - \tau_1)\varepsilon(t) = \varepsilon_1 E(t - \tau_1)H(t - \tau_1),$$

whereas, if the strain input $\varepsilon(t)$ is variable with time, we have

$$\sigma(t) = \int_0^t E(t - \tau)H(t - \tau)\frac{d\varepsilon(\tau)}{d\tau}d\tau = \int_0^t E(t - \tau)\frac{d\varepsilon(\tau)}{d\tau}d\tau. \tag{2.145}$$

Equations (2.144) and (2.145) are known as *Boltzmann integral representation* of $\varepsilon(t)$ and $\sigma(t)$, respectively. All the models examined so far, from the Maxwell model to the generalized Kelvin model, are special cases of the Boltzmann formulation. For example, from equations (2.126) and (2.127), we infer that the creep and relaxation functions for the Maxwell model are given by

$$J(t) = \frac{1}{E} + \frac{1}{\eta}t \quad \text{and} \quad E(t) = Ee^{-Et/\eta},$$

respectively. These models have a relaxation function of the form

$$E(t) = \sum_{n=0}^{N} \alpha_n e^{-t\nu_n}, \tag{2.146}$$

for a proper integer N, where α_n denotes the *amplitude* associated with the *characteristic frequency* ν_n. Plotting a vertical line of length α_n at each ν_n on a frequency axis, we obtain the *discrete spectrum of the relaxation function* (2.146), as shown in Figure 2.15.

Sometimes, for example in the case of a living tissue such as mesentery [35], a discrete spectrum does not reproduce experimental results on relaxation accurately enough. Thus, not even a generalized Maxwell or generalized Kelvin model with a finite number of units would be appropriate. In these cases, a generalization to a *continuum spectrum* has to be introduced.

Response of a Viscoelastic Material to a Harmonic Input

In order to characterize the mechanical behavior of a viscoelastic material and choose the right model to fit the experimental data, the response to an oscillatory

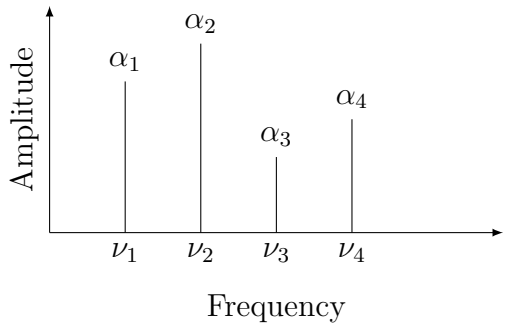

Figure 2.15. A discrete spectrum of the relaxation function.

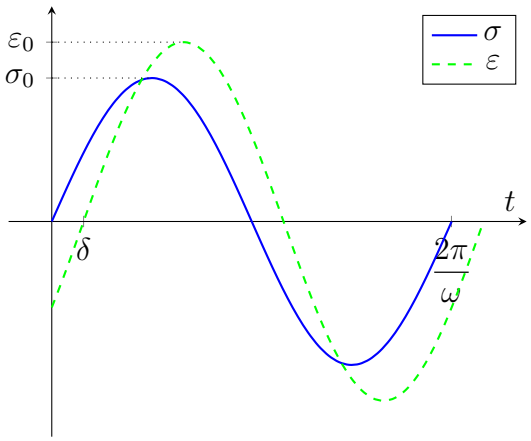

Figure 2.16. Oscillating stress σ, strain ε and loss angle δ.

input should be considered, in addition to creep and relaxation experiments. Suppose the material is subject to an oscillating stress σ:

$$\begin{aligned} \sigma\colon [0,T) &\to \mathbb{R} \\ t \qquad &\to \sigma(t) = \sigma_0 \cos(\omega t). \end{aligned} \tag{2.147}$$

Using Euler's formula

$$e^{i\omega t} = \cos(\omega t) + i \sin(\omega t),$$

σ can be represented by a complex number with magnitude σ_0 and argument ωt

$$\sigma = \sigma_0 e^{i\omega t}.$$

The stress input will induce a strain ε oscillating at the same frequency, but lagging behind by a phase angle γ (see Figure 2.16):

$$\begin{aligned} \varepsilon\colon [0,T) &\to \mathbb{R} \\ t \qquad &\to \varepsilon(t) = \varepsilon_0 \cos(\omega t - \gamma), \end{aligned}$$

or, equivalently,

$$\varepsilon = \varepsilon_0 e^{i(\omega t - \gamma)},$$

where ε_0 is the strain amplitude. The phase angle γ is often called the *loss angle*. Both ε_0 and γ are functions of the internal friction of the material, which causes energy dissipation. In general, the energy dissipated is different for each value of the angular frequency ω. Thus, ε_0 and γ depend on ω.

Using the complex representation for σ and ε, the *complex creep compliance* J^* is the complex function defined as:

$$\begin{aligned} J^*\colon \mathbb{R} &\to \mathbb{C} \\ \omega &\to J^*(\omega), \end{aligned}$$

with

$$\begin{aligned} J^*(\omega) = \frac{\varepsilon}{\sigma} &= \frac{\varepsilon_0(\omega) e^{i(\omega t - \gamma(\omega))}}{\sigma_0 e^{i\omega t}} = \frac{\varepsilon_0(\omega)}{\sigma_0} e^{-i\gamma(\omega)} \\ &= \frac{\varepsilon_0(\omega)}{\sigma_0} (\cos\gamma(\omega) - i \sin\gamma(\omega)) \\ &= J_1(\omega) - i J_2(\omega) = |J^*(\omega)| e^{-i\gamma(\omega)}, \end{aligned} \tag{2.148}$$

where:

- J_1 is called the *storage compliance* and is associated with the elastic behavior of a material;
- J_2 is called the *loss compliance* and is associated with dissipation of energy;
- $|J^*|$ is the magnitude of the complex compliance.

Similarly, if the input is an oscillatory strain

$$\varepsilon = \varepsilon_0 e^{i\omega t}, \tag{2.149}$$

the stress response σ will lead the strain by a phase angle γ. Using the complex representation, we can write

$$\sigma = \sigma_0(\omega) e^{i(\omega t + \gamma(\omega))}. \tag{2.150}$$

The *complex relaxation modulus* E^* is then the complex function defined as:

$$\begin{aligned} E^* \colon \mathbb{R} &\to \mathbb{C} \\ \omega &\to E^*(\omega), \end{aligned}$$

with

$$\begin{aligned} E^*(\omega) = \frac{\sigma}{\varepsilon} &= \frac{\sigma_0(\omega) e^{i(\omega t + \gamma(\omega))}}{\varepsilon_0 e^{i\omega t}} = \frac{\sigma_0(\omega)}{\varepsilon_0} e^{i\gamma(\omega)} \\ &= \frac{\sigma_0(\omega)}{\varepsilon_0} (\cos\gamma(\omega) + i \sin\gamma(\omega)) = E_1(\omega) + iE_2(\omega) = |E^*(\omega)| e^{i\gamma(\omega)}, \end{aligned} \tag{2.151}$$

where:

- E_1 is called the *storage modulus* and, like J_1, is associated with the elastic behavior of a material;
- E_2 is called the *loss modulus* and, like J_2, is associated with dissipation of energy;
- $|E^*|$ is the magnitude of the complex modulus.

Using the same values for σ_0 and ε_0 to define the complex compliance J^* and complex modulus E^*, equations (2.148) and (2.151) imply that

$$|J^*| = \frac{1}{|E^*|} \quad \text{and} \quad \tan\gamma = \frac{E_2}{E_1} = \frac{J_2}{J_1}.$$

As an illustrative example, let us compute the relaxation modulus for the Kelvin model. By plugging the complex representations for the strain (2.149) and the stress (2.150) and their time derivatives into the constitutive equation of the Kelvin model (2.138), we get

$$E_0(i\omega\tau_\sigma\varepsilon + \varepsilon) = i\omega\tau_\varepsilon\sigma + \sigma,$$

which, after few manipulations, provides

$$E^*(\omega) = \frac{\sigma}{\varepsilon} = E_0\frac{1 + i\omega\tau_\sigma}{1 + i\omega\tau_\varepsilon} = \frac{E_0}{1 + \omega^2\tau_\varepsilon^2}(1 + \omega^2\tau_\sigma\tau_\varepsilon + i\omega(\tau_\sigma - \tau_\varepsilon)),$$

with

$$|E^*| = E_0\sqrt{\frac{1 + \omega^2\tau_\sigma^2}{1 + \omega^2\tau_\varepsilon^2}}, \qquad \tan\gamma = \frac{\omega(\tau_\sigma - \tau_\varepsilon)}{1 + \omega^2\tau_\sigma\tau_\varepsilon}.$$

In a similar manner, the complex relaxation modulus for any viscoelastic model can be obtained. The quantities $|E^*|$ and $\tan\gamma$ are usually plotted against the logarithm of ω (see Figure 2.17).

Having determined the experimental curves of relaxation, creep, frequency response, and internal friction of the material being studied, a scientist can compare them with those of the theoretical models and choose the most appropriate model for the problem at hand.

Reconciling Linear Viscoelastic Models with the Entropy Inequality

The goal of this section is to show that, under appropriate assumptions, linear viscoelastic models can be brought in accordance with the entropy inequality (2.111), and so can be used to describe the viscoelastic behavior of the solid phase. In the following discussion, we shall eliminate both geometrical and material nonlinearities

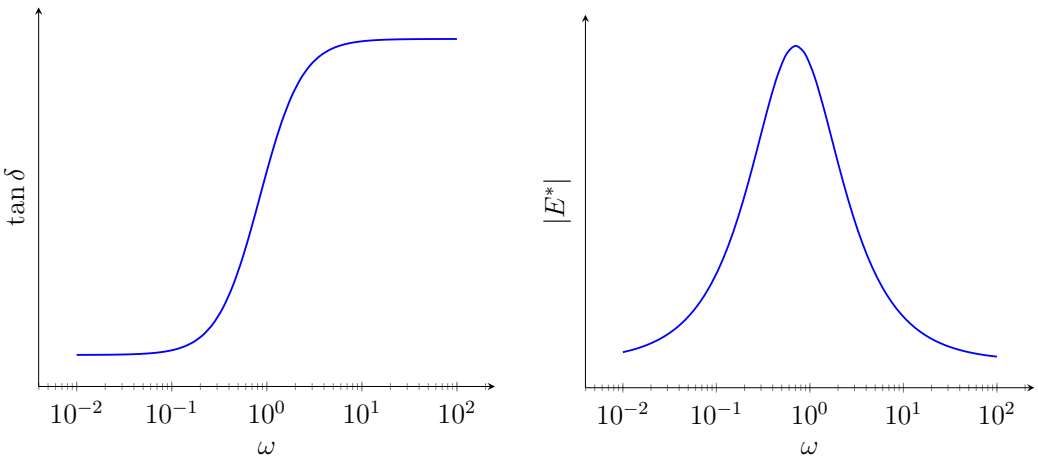

Figure 2.17. Magnitude of the complex modulus $|E^*|$ and internal damping $\tan\delta$ with a logarithmic scale for the frequency ω for a Kelvin model.

by assuming both that the deformations are infinitesimal and that constitutive laws are linear. According to (2.9) and the hypothesis of infinitesimal deformations, the current position $\mathbf{x}$ can be written as follows

$$\mathbf{x} = \mathbf{X}_\alpha + \mathbf{u}_\alpha = \mathbf{X}_\alpha + \epsilon \check{\mathbf{u}}_\alpha, \tag{2.152}$$

where $\epsilon \ll 1$ and the norm of $\check{\mathbf{u}}_\alpha$ is $\mathcal{O}(1)$. We will also assume small mass production

$$|\tilde{\rho}_\alpha| \ll 1. \tag{2.153}$$

From (2.152) and (2.153), it follows that [22, 24]:

1. There is little point making a distinction between Lagrangian and Eulerian coordinates, that is between reference and current configurations. As a consequence, partial derivatives with respect to the coordinates $\mathbf{X}_\alpha$ in the reference configuration, denoted by ∇_α, are approximately the same as partial derivatives with respect to the current position $\mathbf{x}$, denoted by ∇. Thus we can replace ∇_α with ∇. Also, the material derivative $(\cdot)'_\alpha$ reduces to a partial derivative with respect to time t, which we will denote by $(\cdot)'$ or $\partial(\cdot)/\partial t$, interchangeably.

2. From equation (2.21) and point 1, the deformation gradient $\underline{\underline{F}}_\alpha$ is given by

$$\underline{\underline{F}}_\alpha = \underline{\underline{I}} + \nabla \mathbf{u}_\alpha = \underline{\underline{I}} + \epsilon \nabla \check{\mathbf{u}}_\alpha,$$

where $\underline{\underline{I}}$ denotes the identity tensor. It follows that the determinant J_α of $\underline{\underline{F}}_\alpha$ is approximately equal to $1 + \nabla \cdot \mathbf{u}_\alpha$. In fact, using the definition of determinant, we get

$$\begin{aligned} J_\alpha &= \det \underline{\underline{F}}_\alpha = \det(\underline{\underline{I}} + \nabla \mathbf{u}_\alpha) = \det(\underline{\underline{I}} + \epsilon \nabla \check{\mathbf{u}}_\alpha) \\ &= 1 + \epsilon \frac{\partial \check{u}^1_\alpha}{\partial x} + \epsilon \frac{\partial \check{u}^2_\alpha}{\partial y} + \epsilon \frac{\partial \check{u}^3_\alpha}{\partial z} + \mathcal{O}(\epsilon^2) \\ &\approx 1 + \epsilon \frac{\partial \check{u}^1_\alpha}{\partial x} + \epsilon \frac{\partial \check{u}^2_\alpha}{\partial y} + \epsilon \frac{\partial \check{u}^3_\alpha}{\partial z} \\ &= 1 + \nabla \cdot \mathbf{u}_\alpha. \end{aligned} \tag{2.154}$$

3. From the assumption of small mass production (2.153), in accordance with the conservation of mass in Lagrangian form (2.38), we get

$$\rho_S \approx \rho_S^0 J_S^{-1},$$

which, by the incompressibility assumption (2.80) and the relation between partial and real densities (2.5), implies that

$$n_S \approx n_S^0 J_S^{-1}, \tag{2.155}$$

where n_S^0 is the volume fraction of the solid constituent in the reference configuration. Note that, according to our remarks in point 1, we are not distinguishing between the reference configuration of the solid and fluid phases. Equation (2.155) implies that n_S is determined by the solid state of deformation. Thus, n_S can be dropped from the list of independent constitutive variables (2.105) and the functional dependencies of the solid Helmholtz free energy (2.107). Moreover, combining equations (2.154) and (2.155), it follows that

$$n_S \approx n_S^0 (1 + \nabla \cdot \mathbf{u}_S)^{-1},$$

and then, by the saturation constraint (2.79),

$$\begin{aligned} n_F = 1 - n_S &\approx 1 - \frac{n_S^0}{1 + \nabla \cdot \mathbf{u}_S} \\ &= \frac{1 + \nabla \cdot \mathbf{u}_S - n_S^0}{1 + \nabla \cdot \mathbf{u}_S} \\ &= \frac{n_F^0 + \nabla \cdot \mathbf{u}_S}{1 + \nabla \cdot \mathbf{u}_S} \\ &\approx n_F^0 + \nabla \cdot \mathbf{u}_S, \end{aligned} \tag{2.156}$$

where n_F^0 is the fluid volume fraction in the reference configuration.

4. The nonlinear term $\left(\nabla^T \mathbf{u}_\alpha\right)\left(\nabla \mathbf{u}_\alpha\right)$ in the Green-Lagrange strain tensor $\underline{\underline{E}}_\alpha$ (see equation (2.22)) is negligible. Thus, $\underline{\underline{E}}_\alpha$ is approximately equal to the infinitesimal strain tensor $\underline{\underline{\varepsilon}}_\alpha$, which is defined as follows:

$$\begin{aligned} \underline{\underline{\varepsilon}}_\alpha \colon B \times [0,T) &\to \mathbb{R}^3 \times \mathbb{R}^3 \\ (\mathbf{x}, t) \qquad &\to \underline{\underline{\varepsilon}}_\alpha = \frac{1}{2}(\nabla \mathbf{u}_\alpha + \nabla^T \mathbf{u}_\alpha). \end{aligned} \tag{2.157}$$

According to point 1, the material derivative of $\underline{\underline{\varepsilon}}_\alpha$ is approximately equal to the symmetric part $\underline{\underline{D}}_\alpha$ of the spatial velocity gradient, that is

$$(\underline{\underline{\varepsilon}}_\alpha)'_\alpha \approx (\underline{\underline{\varepsilon}}_\alpha)' \approx \underline{\underline{D}}_\alpha.$$

5. The Taylor expansions of all the stress tensors (e.g. the Cauchy stress tensor, body stress tensor, first and second Piola-Kirchhoff stress tensors) about the reference configuration coincide up to $\mathcal{O}(\epsilon)$. Therefore, there is no distinction between them in linear viscoelasticity. In the following, we will denote the single solid stress tensor by $\underline{\underline{\sigma}}$. Moreover, we will assume that the solid phase is not pre-stressed in the reference configuration, that is the $\mathcal{O}(0)$ term of the Taylor expansion of $\underline{\underline{\sigma}}_S$ is zero.

According to the above five points, the functional dependencies of the solid Helmholtz free energy (2.107) can be reduced to

$$\psi_S = \psi_S(\underline{\underline{\varepsilon}}_S, \{\underline{\underline{\mathcal{Q}}}^n_S\}_{n=1}^N). \tag{2.158}$$

Moreover, the entropy inequality (2.111) can be rewritten as follows

$$\begin{aligned}&\left(\underline{\underline{\sigma}}^E_S - \rho_S \frac{\partial \psi_S}{\partial \underline{\underline{\varepsilon}}_S}\right) : \underline{\underline{\varepsilon}}'_S - \rho_S \sum_{n=1}^{N} \frac{\partial \psi_S}{\partial \underline{\underline{\mathcal{Q}}}^n_S} : (\underline{\underline{\mathcal{Q}}}^n_S)'_S - \tilde{\rho}_F\,(\mu_F - \mu_S) + \underline{\underline{T}}^E_F : \underline{\underline{D}}_F \\ &- \tilde{\mathbf{p}}^E_F \cdot (\mathbf{v}_F - \mathbf{v}_S) - (n_S)'_S(\lambda - \lambda_{SR}) - (n_F)'_F(\lambda - \lambda_{FR}) \geq 0,\end{aligned} \tag{2.159}$$

where $\underline{\underline{\sigma}}^E_S$ denotes the linear solid effective stress tensor of the infinitesimal theory.

Linear viscoelastic models can be brought in accordance with (2.159). We will show how this can be done for one of the viscoelastic models presented before, the Voigt model, which has been analyzed by Bociu et al. [39] within the framework of porous media viscoelasticity. In Chapter 3 of this thesis, a novel numerical method for the solution of their poro-viscoelastic model is proposed. In Chapter 4, this method will be used to theoretically investigate the perfusion of the optic nerve head, a region of the eye that is believed to play an important role in ocular pathologies, including glaucoma [11].

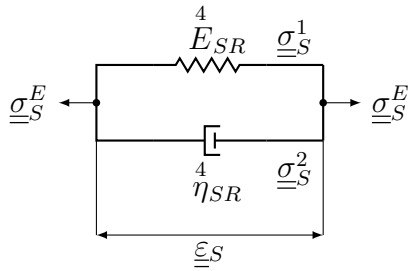

Figure 2.18. Extension of the Voigt model (see Figure 2.11) to three dimensions.

By formal extension of the constitutive equations (2.128) and (2.129) of the Voigt model to three dimensions, we get (see Figure 2.18):

$$\underline{\underline{\sigma}}_S^E = \underline{\underline{\sigma}}_S^1 + \underline{\underline{\sigma}}_S^2, \tag{2.160}$$

$$\underline{\underline{\sigma}}_S^1 = \overset{4}{E}_{SR}\,\underline{\underline{\varepsilon}}_S, \tag{2.161}$$

$$\underline{\underline{\sigma}}_S^2 = \overset{4}{\eta}_{SR}\,\underline{\underline{\varepsilon}}'_S, \tag{2.162}$$

where:

- $\underline{\underline{\sigma}}_S^E$ and $\underline{\underline{\varepsilon}}_S$ have the same meaning as in (2.159).
- The spring and dashpot elements are connected in parallel, so they undergo the same strain $\underline{\underline{\varepsilon}}_S$.
- $\underline{\underline{\sigma}}_S^1$ is a stress due to the linear spring and so is determined by a linear elasticity law with the positive definite fourth order *elasticity tensor* $\overset{4}{E}_{SR}$. The subscript SR refers to macroscopic real parameters of the solid phase. In the case of a Hooke-type elasticity law, we have

  $$\underline{\underline{\sigma}}_S^1 = \overset{4}{E}_{SR}\,\underline{\underline{\varepsilon}}_S = 2\mu_{SR}^e\underline{\underline{\varepsilon}}_S + \lambda_{SR}^e(\nabla\cdot\mathbf{u}_S)\underline{\underline{I}}, \tag{2.163}$$

  where μ_{SR}^e and λ_{SR}^e are the solid macroscopic real elastic parameters.
- $\underline{\underline{\sigma}}_S^2$ is a stress due to the linear dashpot and so is determined by another linear law with the positive definite fourth order *viscosity tensor* $\overset{4}{\eta}_{SR}$. In the case of isotropic tensor functions, $\overset{4}{\eta}$ assumes a form similar to $\overset{4}{E}_{SR}$. Thus

  $$\underline{\underline{\sigma}}_S^2 = \overset{4}{\eta}_{SR}\,(\underline{\underline{\varepsilon}}_S)' = 2\mu_{SR}^v\underline{\underline{\varepsilon}}'_S + \lambda_{SR}^v(\nabla\cdot\mathbf{u}'_S)\underline{\underline{I}},$$

  with μ_{SR}^v and λ_{SR}^v being the viscosity parameters and $\mathbf{u}'_S = \mathbf{v}_S$, i.e. the velocity of the solid phase.

In order to bring Voigt model (2.160)–(2.162), or any other viscoelastic model, in accordance with (2.159), it is assumed that the Helmholtz free energy ψ_S can be

decomposed into the sum of an *equilibrium part* ψ_S^{EQ} and a *non equilibrium part* ψ_S^{NEQ}, also known as *pseudo-potential* or *dissipative potential* (see [22, 40])

$$\psi_S = \psi_S^{EQ} + \psi_S^{NEQ}. \tag{2.164}$$

The equilibrium part ψ_S^{EQ} is exclusively associated with equilibrium stress states obtained from a relaxation process with infinite duration at constant strain [41]. It does not include strain rate effects. Hence, ψ_S^{EQ} can depend on the total solid strain $\underline{\underline{\varepsilon}}_S$, but not on the internal state variables $\underline{\underline{\mathcal{Q}}}_S^n$, which represent strain rate effects. Thus, we can have

$$\psi_S^{EQ} = \psi_S^{EQ}(\underline{\underline{\varepsilon}}_S).$$

The non equilibrium part ψ_S^{NEQ} is associated with strain rate effects causing dissipation in the material. Thus we can have

$$\psi_S^{NEQ} = \psi_S^{NEQ}(\{\underline{\underline{\mathcal{Q}}}_S\}_{n=1}^N).$$

Observe that the terms

$$\frac{\partial \psi_S}{\partial \underline{\underline{\varepsilon}}_S} \quad \text{and} \quad \frac{\partial \psi_S}{\partial \underline{\underline{\mathcal{Q}}}_S^n},$$

provide *distinct* contributions to the entropy inequality (2.159). Thus, following our discussion about ψ_S^{EQ} and ψ_S^{NEQ}, we can write

$$\frac{\partial \psi_S}{\partial \underline{\underline{\varepsilon}}_S} = \frac{\partial \psi_S^{EQ}}{\partial \underline{\underline{\varepsilon}}_S} \quad \text{and} \quad \frac{\partial \psi_S}{\partial \underline{\underline{\mathcal{Q}}}_S^n} = \frac{\partial \psi_S^{NEQ}}{\partial \underline{\underline{\mathcal{Q}}}_S^n}. \tag{2.165}$$

Now we wish to find an expression for ψ_S^{EQ} and ψ_S^{NEQ} in the case of the Voigt model. In every linear viscoelastic model, the internal variables $\underline{\underline{\mathcal{Q}}}_S^n$ are identified with deformations of dashpot elements, which, by definition, are not elastic. In the Voigt model (see Figure 2.18), there is only one dashpot and, thus, only one internal variable $\underline{\underline{\mathcal{Q}}}_S$. Since the spring and the dashpot are in parallel, dashpot deformations coincide with the total solid strain $\underline{\underline{\varepsilon}}_S$. It follows that

$$\underline{\underline{\mathcal{Q}}}_S \equiv \underline{\underline{\varepsilon}}_S, \tag{2.166}$$

and thus

$$\psi_S^{NEQ} = \psi_S^{NEQ}(\underline{\underline{\mathcal{Q}}}_S) = \psi_S^{NEQ}(\underline{\underline{\varepsilon}}_S), \qquad \frac{\partial \psi_S^{NEQ}}{\partial \underline{\underline{\mathcal{Q}}}_S} = \frac{\partial \psi_S^{NEQ}}{\partial \underline{\underline{\varepsilon}}_S}. \tag{2.167}$$

Moreover, as discussed at the beginning of this Section, the Voigt model cannot undergo instantaneous elastic deformations when subject to a step change in stress nor it can be used to study stress relaxation in response to constant strain (see equations (2.131) and (2.132)). We can conclude that

$$\psi_S^{EQ} = 0. \tag{2.168}$$

Observe that, due to (2.166) and (2.168), the evaluation of the entropy inequality will be slightly different from what described in Section 2.4.3. Concerning ψ_S^{NEQ}, since:

- the Helmholtz free energy is a form of potential energy (see the discussion in Section 2.3.5 about the entropy inequality);
- energy can only be stored in the spring element;
- the deformation of the spring element coincides with $\underline{\underline{\varepsilon}}_S$;

we can write

$$\psi_S^{NEQ} = \frac{1}{2\rho_{SR}} \underline{\underline{\varepsilon}}_S : \overset{4}{E}_{SR}\, \underline{\underline{\varepsilon}}_S,$$

and then

$$\frac{\partial \psi_S^{NEQ}}{\partial \underline{\underline{\varepsilon}}_S} = \frac{1}{\rho_{SR}} \overset{4}{E}_{SR}\, \underline{\underline{\varepsilon}}_S. \tag{2.169}$$

Combining (2.159), (2.165), (2.167), (2.168), and (2.169), we get

$$\begin{aligned} &\left(\underline{\underline{\sigma}}_S^E - \frac{\rho_S}{\rho_{SR}} \overset{4}{E}_{SR}\, \underline{\underline{\varepsilon}}_S \right) : \underline{\underline{\varepsilon}}'_S - \tilde{\rho}_F \left(\mu_F - \mu_S \right) + \underline{\underline{T}}_F^E : \underline{\underline{D}}_F \\ &- \tilde{\mathbf{p}}_F^E \cdot (\mathbf{v}_F - \mathbf{v}_S) - (n_S)'_S (\lambda - \lambda_{SR}) - (n_F)'_F (\lambda - \lambda_{FR}) \geq 0. \end{aligned} \tag{2.170}$$

Evaluation of the above inequality provides

$$\lambda = \lambda_{SR} \quad \text{and} \quad \lambda = \lambda_{FR}, \tag{2.171}$$

i.e. the interface pressure λ coincides with the Lagrange multiplier of the fluid incompressibility λ_{FR}, which is understood as the fluid pressure, and the Lagrange multiplier of the solid incompressibility λ_{SR}. The residual inequality is

$$\left(\underline{\underline{\sigma}}_S^E - \overset{4}{E}_S\, \underline{\underline{\varepsilon}}_S\right) : \underline{\underline{\varepsilon}}'_S - \tilde{\rho}_F\,(\mu_F - \mu_S) + \underline{\underline{T}}_F^E : \underline{\underline{D}}_F - \tilde{\mathbf{p}}_F^E \cdot (\mathbf{v}_F - \mathbf{v}_S) \geq 0.$$

where $\overset{4}{E}_S$ is the partial macroscopic, i.e. smeared, elasticity tensor obtained as follows

$$\frac{\rho_S}{\rho_{SR}} \overset{4}{E}_{SR} = \frac{n_S \rho_{SR}}{\rho_{SR}} \overset{4}{E}_{SR} = n_S \overset{4}{E}_{SR} = \overset{4}{E}_S. \tag{2.172}$$

In analogy with (2.117), in order to satisfy the residual inequality, we require

$$\underline{\underline{\sigma}}_S^E - \overset{4}{E}_S\, \underline{\underline{\varepsilon}}_S \propto \underline{\underline{\varepsilon}}'_S, \quad \tilde{\rho}_F \propto -(\mu_F - \mu_S), \quad \underline{\underline{T}}_F^E \propto \underline{\underline{D}}_F, \quad \tilde{\mathbf{p}}_F^E \propto -(\mathbf{v}_F - \mathbf{v}_S). \tag{2.173}$$

Dimensional analysis reveals that the proportionality tensor in

$$\underline{\underline{\sigma}}_S^E - \overset{4}{E}_S\, \underline{\underline{\varepsilon}}_S \propto \underline{\underline{\varepsilon}}'_S,$$

has the units of a viscosity parameter, i.e. [Pa · s]. Hence, denoting by $\overset{4}{\eta}_S$ a partial (smeared) positive definite fourth order viscosity tensor, we can write

$$\boxed{\underline{\underline{\sigma}}_S^E - \overset{4}{E}_S\, \underline{\underline{\varepsilon}}_S = \overset{4}{\eta}_S\, \underline{\underline{\varepsilon}}'_S} \qquad \text{or} \qquad \boxed{\underline{\underline{\sigma}}_S^E = \overset{4}{E}_S\, \underline{\underline{\varepsilon}}_S + \overset{4}{\eta}_S \underline{\underline{\varepsilon}}'_S}, \tag{2.174}$$

which coincides with the constitutive equations of the Voigt model (2.160)–(2.162). We can finally conclude that the Voigt model provides a constitutive law for the effective stress tensor $\underline{\underline{\sigma}}_S^E$ of the solid constituent that allows to satisfy the entropy inequality.

Let us stress that the elasticity tensor $\overset{4}{E}_S$ and the viscosity tensor $\overset{4}{\eta}_S$ in (2.174) are macroscopic partial quantities, i.e they represent average properties of the solid constituent after being smeared over the volume shaped by the porous solid. However, they are determined by physical quantities at the microscale. Similarly to what we discussed in Section 2.2.1, in order to transfer the microscopic behavior of the real solid phase to the macroscale, $\overset{4}{E}_S$ and $\overset{4}{\eta}_S$ should be expressed using quantities representative of the real solid material and of the empty porous solid [20, 42–44].

For example, in the case of a Hooke-type elasticity law like (2.163), the partial elastic parameter λ_S^e can be expressed as

$$\lambda_S^e = K_S^e - \frac{2}{3}\mu_S^e,$$

where K_S^e is the partial compression modulus that depends on the solid volume fraction n_S and the compression moduli K_{SR}^e and K_{SN}^e of the real solid material and the empty porous solid, respectively,

$$K_S^e = \frac{n_S K_{SR}^e K_{SN}^e}{K_{SR}^e + K_{SN}^e}, \tag{2.175}$$

as described by de Boer [44]. In the case of incompressible solid phase,

$$K_{SR}^e \to \infty,$$

and therefore

$$K_S^e \to n_S K_{SN}^e < \infty. \tag{2.176}$$

From (2.176), we get that, unlike classic linear elasticity, the hypothesis of solid incompressibility does not cause the partial compression modulus K_S^e to blow up. Four types of tests are commonly used to determine poroelastic parameters: drained, undrained, jacketed, and unjacketed tests. A thorough discussion about these tests is presented by Coussy [20], Terragni [42], and Detournay [43].

Here we conclude our discussion about constitutive laws for the viscoelastic solid constituent. In the next section, we will be formulating constitutive laws for the effective fluid stress tensor $\underline{\underline{T}}_F^E$ and the fluid-solid interaction force $\tilde{\mathbf{p}}_E^F$ in (2.173).

2.4.5 Darcy Law for the Fluid Constituent

In accordance with the sufficient conditions (2.173), the following constitutive law can be given for the effective stress tensor $\underline{\underline{T}}_F^E$

$$\underline{\underline{T}}_F^E = 2\mu_F \underline{\underline{D}}_F + \lambda_F (\nabla \cdot \mathbf{v}_F)\underline{\underline{I}} = 2\mu_F \underline{\underline{D}}_F + \lambda_F \,\mathrm{trace}(\underline{\underline{D}}_F)\,\underline{\underline{I}}, \tag{2.177}$$

where μ_F is the partial *dynamic viscosity* and λ_F is the partial *dilatational viscosity*. In equation (2.177), $\underline{\underline{T}}_F^E$ is linearly related to the rate of deformation $\underline{\underline{D}}_F$, just like a Newtonian fluid. Concerning the interaction term $\tilde{\mathbf{p}}_F^E$, in accordance with (2.173) and the analysis of Whitaker for fluid flows in homogeneous porous media [21], it is assumed that

$$\tilde{\mathbf{p}}_F^E = -(n_F)^2 \underline{\underline{K}}_F^{-1}(\mathbf{v}_F - \mathbf{v}_S) = -n_F \underline{\underline{K}}_F^{-1}\mathbf{v}, \tag{2.178}$$

where:

- $\underline{\underline{K}}_F^{-1}$ represents a positive definite inverse *permeability tensor*, which is a measure of the capability of a porous material to transmit fluid. A constitutive equation for $\underline{\underline{K}}_F$ has to be provided and will depend on properties of both the fluid and solid phases, in general. The components of $\underline{\underline{K}}_F$ can be calculated by considering a representative unit cell in a spatially periodic model of the porous medium and then solving a *closure problem* on such representative cell [21]. A constitutive equation for $\underline{\underline{K}}_F$ dependent on the local state of stress and strain is proposed in Chapter 4 to study the ONH perfusion.

- $\mathbf{v} = n_F(\mathbf{v}_F - \mathbf{v}_S)$ is known as *discharge* (or *Darcy*) *velocity*.

According to the quasi-static approximation (2.81) and considering a uniform body force $\mathbf{b}$, the balance of linear momentum for the fluid phase (2.43) can be rewritten as follows

$$\tilde{\rho}_F \mathbf{v}_F = \nabla \cdot \underline{\underline{T}}_F + \rho_F \mathbf{b} + \tilde{\mathbf{p}}_F. \tag{2.179}$$

By neglecting fluid accelerations in (2.179), we are assuming that fluid viscosity dominates over inertial effects and the fluid flow is laminar [24, 45]. By definition of the effective quantities $\underline{\underline{T}}_F^E, \tilde{\mathbf{p}}_F^E$ (2.102) and equation (2.171), we obtain

$$\begin{aligned}
\tilde{\rho}_F \mathbf{v}_F &= \nabla \cdot \underline{\underline{T}}_F + \rho_F \mathbf{b} + \tilde{\mathbf{p}}_F \\
&= \nabla \cdot \underline{\underline{T}}_F^E - \nabla(\lambda\, n_F) + \rho_F \mathbf{b} + \tilde{\mathbf{p}}_F^E + \lambda \nabla n_F \\
&= \nabla \cdot \underline{\underline{T}}_F^E - n_F \nabla \lambda + \rho_F \mathbf{b} + \tilde{\mathbf{p}}_F^E.
\end{aligned}$$

Plugging (2.177) and (2.178) into the last equation gives

$$\begin{aligned}\tilde{\rho}_F\mathbf{v}_F &= \nabla\cdot\left(2\mu_F\underline{\underline{D}}_F+\lambda_F(\nabla\cdot\mathbf{v}_F)\underline{\underline{I}}\right)-n_F\nabla\lambda+\rho_F\mathbf{b}-n_F\underline{\underline{K}}_F^{-1}\mathbf{v}\\ &= \nabla\cdot\left(\mu_F(\nabla\mathbf{v}_F+\nabla^T\mathbf{v}_F)+\lambda_F(\nabla\cdot\mathbf{v}_F)\underline{\underline{I}}\right)-n_F\nabla\lambda+\rho_F\mathbf{b}-n_F\underline{\underline{K}}_F^{-1}\mathbf{v}\\ &= \mu_F\nabla^2\mathbf{v}_F+(\mu_F+\lambda_F)\nabla(\nabla\cdot\mathbf{v}_F)-n_F\nabla\lambda+\rho_F\mathbf{b}-n_F\underline{\underline{K}}_F^{-1}\mathbf{v},\end{aligned}\tag{2.180}$$

where we have assumed that μ_F and λ_F do not depend on space. Applying the procedure of length scale analysis by Whitaker [21], it is possible to prove that

$$||\mu_F\nabla^2\mathbf{v}_F+(\mu_F+\lambda_F)\nabla(\nabla\cdot\mathbf{v}_F)||\ll||n_F\underline{\underline{K}}_F^{-1}\mathbf{v}||.\tag{2.181}$$

In (2.181), the term on the left hand side represents dissipative terms acting within the fluid flow, whereas the term on the right hand side represents terms acting at the fluid-solid interface. Thus, according to equation (2.181), we are assuming that dissipation mainly occurs at the wall boundary layers of the pore channels, whereas the fluid is almost inviscid at the pore interior, that is

$$\underline{\underline{T}}_F^E\approx\underline{\underline{0}}.\tag{2.182}$$

Inserting (2.181) and (2.182) into (2.180), we get the *Darcy law*

$$\tilde{\rho}_F\mathbf{v}_F\approx-n_F\nabla\lambda+\rho_F\mathbf{b}-n_F\underline{\underline{K}}_F^{-1}\mathbf{v},$$

or, equivalently,

$$\boxed{\mathbf{v}\approx-\underline{\underline{K}}_F\left(\nabla\lambda-\rho_{FR}\mathbf{b}+\frac{\tilde{\rho}_F}{n_F}\mathbf{v}_F\right)}.\tag{2.183}$$

2.5 A Poro-Viscoelastic Model

In accordance with the residual inequality (2.172), we have determined constitutive laws for $\underline{\underline{\sigma}}_S^E$ (2.174), $\underline{\underline{T}}_F^E$ (2.182), and $\tilde{\mathbf{p}}_F^E$ (2.178). From (2.173), it follows that a constitutive law for the fluid mass supply $\tilde{\rho}_F$ is still needed. In this section, since a discussion of possible constitutive laws for $\tilde{\rho}_F$ is outside the scope of this thesis, we will assume such a law to be given in terms of the fluid chemical potential μ_F and

the solid chemical potential μ_S, defined in equation (2.101). The interested reader is referred to, e.g., Ricken and Blum [46].

From the results of the previous sections, a model describing the coupled behavior of a viscous fluid streaming through a viscoelastic solid constituent is obtained and summarized in Table 2.2. Constitutive laws allowed us to close the system of governing equations shown in Table 2.1.

The number of unknowns can be reduced by combining equations in Table 2.2. Adding the balance of mass equations of the fluid and solid phases and using the constraints

$$n_S + n_F = 1, \qquad \tilde{\rho}_S + \tilde{\rho}_F = 0, \tag{2.184}$$

together with the definition of discharge velocity

$$\mathbf{v} = n_F(\mathbf{v}_F - \mathbf{v}_S),$$

we get

$$\begin{aligned}\tilde{\rho}_F \left(\frac{1}{\rho_{FR}} - \frac{1}{\rho_{SR}}\right) &= \frac{\partial(n_S + n_F)}{\partial t} + \nabla \cdot (n_F \mathbf{v}_F + n_S \mathbf{v}_S) \\ &= 0 + \nabla \cdot (n_F \mathbf{v}_F - n_F \mathbf{v}_S + n_F \mathbf{v}_S + n_S \mathbf{v}_S) \\ &= \nabla \cdot (\mathbf{v}_S + \mathbf{v}),\end{aligned}$$

which, assuming sufficient regularity of spatial and time derivatives so that they can be interchanged, is equivalent to

$$(\nabla \cdot \mathbf{u}_S)' + \nabla \cdot \mathbf{v} = \tilde{\rho}_F \left(\frac{1}{\rho_{FR}} - \frac{1}{\rho_{SR}}\right).$$

The last equation represents the balance of mass for the overall mixture. As shown in Section 2.4.4, under the hypothesis of small mass supply $\tilde{\rho}_S \ll 1$, the balance of mass for the solid phase and the incompressibility constraint can be manipulated to obtain

$$n_F = n_F^0 + \nabla \cdot \mathbf{u}_S.$$

Adding the balance equations of linear momentum and using

$$\tilde{\mathbf{p}}_F + \tilde{\mathbf{p}}_S = \mathbf{0},$$

Table 2.2
The closed system of governing equations for a viscous fluid ($\alpha = F$) streaming through a viscoelastic solid constituent ($\alpha = S$).

Physical Law	Linearized Form	Number of Equations	Number of Unknowns
Kinematics	$\mathbf{v}_S = \mathbf{u}'_S, \quad \mathbf{v} = n_F(\mathbf{v}_F - \mathbf{v}_S)$	6	13 $(n_F, \mathbf{u}_S, \mathbf{v}_F, \mathbf{v}_S, \mathbf{v})$
	$\underline{\underline{\varepsilon}}_S = \frac{1}{2}(\nabla \mathbf{u}_S + \nabla^T \mathbf{u}_S)$	6	6 $(\underline{\underline{\varepsilon}}_S)$
Mass	$\frac{\partial n_\alpha}{\partial t} + \nabla \cdot (n_\alpha \mathbf{v}_\alpha) = \frac{\tilde{\rho}_\alpha}{\rho_{\alpha R}}$	2	3 $(n_S, \tilde{\rho}_\alpha)$
Linear momentum	$\tilde{\rho}_S \mathbf{v}_S = \nabla \cdot \underline{\underline{\sigma}}_S + n_S \rho_{SR} \mathbf{b} + \tilde{\mathbf{p}}_S$	3	9 $(\underline{\underline{\sigma}}_S, \tilde{\mathbf{p}}_S)$
	$\tilde{\rho}_F \mathbf{v}_F = \nabla \cdot \underline{\underline{T}}_F + n_F \rho_{FR} \mathbf{b} + \tilde{\mathbf{p}}_F$	3	9 $(\underline{\underline{T}}_F, \tilde{\mathbf{p}}_F)$
Constraints	$n_S + n_F = 1$, $\tilde{\rho}_S + \tilde{\rho}_F = 0$, $\tilde{\mathbf{p}}_S + \tilde{\mathbf{p}}_F = \mathbf{0}$	5	0
Constitutive modeling	$\underline{\underline{\sigma}}_S = \overset{4}{E}_S \underline{\underline{\varepsilon}}_S + \overset{4}{\eta}_S \underline{\underline{\varepsilon}}'_S - n_S \lambda \underline{\underline{I}}$	6	1 (λ)
	$\underline{\underline{T}}_F = \underline{\underline{0}} - \lambda n_F \underline{\underline{I}} = -\lambda n_F \underline{\underline{I}}$	6	0
	$\tilde{\mathbf{p}}_F = -n_F \underline{\underline{K}}_F^{-1} \mathbf{v}$	3	6 $(\underline{\underline{K}}_F)$
	$\tilde{\rho}_F, \underline{\underline{K}}_F$ problem specific	7	0
Total		47	47

together with (2.184) and the constitutive equations

$$\underline{\underline{\sigma}}_S = \overset{4}{E}_S\,\underline{\underline{\varepsilon}}_S + \overset{4}{\eta}_S\underline{\underline{\varepsilon}}'_S - n_S\lambda\underline{\underline{I}}, \qquad \underline{\underline{T}}_F = -\lambda n_F\underline{\underline{I}},$$

we get

$$\begin{aligned}\tilde{\rho}_F(\mathbf{v}_F - \mathbf{v}_S) &= \nabla\cdot\left(\overset{4}{E}_S\,\underline{\underline{\varepsilon}}_S + \overset{4}{\eta}_S\underline{\underline{\varepsilon}}'_S - (n_F+n_S)\lambda\underline{\underline{I}}\right) + (n_F\rho_{FR} + n_S\rho_{SR})\mathbf{b}\\ &= \nabla\cdot\left(\overset{4}{E}_S\,\underline{\underline{\varepsilon}}_S + \overset{4}{\eta}_S\underline{\underline{\varepsilon}}'_S - \lambda\underline{\underline{I}}\right) + (n_F\rho_{FR} + (1-n_F)\rho_{SR})\mathbf{b}.\end{aligned} \tag{2.185}$$

Defining the total stress tensor $\underline{\underline{\sigma}}$ and the mixture partial density ρ as

$$\underline{\underline{\sigma}} = \overset{4}{E}_S\,\underline{\underline{\varepsilon}}_S + \overset{4}{\eta}_S\underline{\underline{\varepsilon}}'_S - \lambda\underline{\underline{I}}, \qquad \rho = n_F\rho_{FR} + (1-n_F)\rho_{SR},$$

respectively, equation (2.185) can be rewritten as

$$\nabla\cdot\underline{\underline{\sigma}} + \rho\mathbf{b} = \frac{\tilde{\rho}_F}{n_F}\mathbf{v},$$

which represents the balance of linear momentum for the overall mixture. In accordance with Section 2.4.5, combining the balance of linear momentum for the fluid phase with the constitutive law

$$\tilde{\mathbf{p}}_F^E = -n_F\underline{\underline{K}}_F^{-1}\mathbf{v},$$

we obtain Darcy's law

$$\mathbf{v} = -\underline{\underline{K}}_F\left(\nabla\lambda - \rho_{FR}\mathbf{b} + \frac{\tilde{\rho}_F}{n_F}\mathbf{v}_F\right).$$

To summarize, the coupled behavior of a viscous fluid streaming through a viscoelastic solid is described by:

$$\underline{\underline{\sigma}} = \overset{4}{E}_S\,\underline{\underline{\varepsilon}}_S(\mathbf{u}_S) + \overset{4}{\eta}_S\underline{\underline{\varepsilon}}_S(\mathbf{u}'_S) - p\underline{\underline{I}}, \tag{2.186}$$

$$\rho = n_F\rho_{FR} + (1-n_F)\rho_{SR}, \tag{2.187}$$

$$\nabla\cdot\underline{\underline{\sigma}} + \rho\mathbf{b} = \frac{\tilde{\rho}_F}{n_F}\mathbf{v}, \tag{2.188}$$

$$\mathbf{v} = n_F(\mathbf{v}_F - \mathbf{u}'_S) = -\underline{\underline{K}}_F\left(\nabla p - \rho_{FR}\mathbf{b} + \frac{\tilde{\rho}_F}{n_F}\mathbf{v}_F\right), \tag{2.189}$$

$$n_F = n_F^0 + \nabla\cdot\mathbf{u}_S, \tag{2.190}$$

$$(\nabla\cdot\mathbf{u}_S)' + \nabla\cdot\mathbf{v} = \tilde{\rho}_F\left(\frac{1}{\rho_{FR}} - \frac{1}{\rho_{SR}}\right), \tag{2.191}$$

where the fluid pressure λ has been denoted by p. Note that, in (2.186) and (2.191), spatial and time derivatives have been interchanged, under the assumption of sufficient regularity. The mass supply $\tilde{\rho}_F$ and the permeability tensor $\underline{\underline{K}}_F$ are assumed to be known functions of the other variables. Thus, equations (2.186)–(2.191) are a system of 18 scalar equations in the 18 scalar unknowns

$$n_F, \rho, \mathbf{u}_S, p, \mathbf{v}_F, \mathbf{v}, \underline{\sigma}.$$

These equations have to be equipped by proper initial and boundary conditions in order to be solved, as we will be discussing in Chapter 3.

3. A HYBRIDIZABLE DISCONTINUOUS GALERKIN METHOD FOR POROUS MEDIA VISCOELASTICITY

This chapter is concerned with the numerical treatment of the biphasic solid fluid model (2.186)–(2.191) discussed in Chapter 2. We propose a novel numerical method based on HDG finite elements for the direct approximation of the dual variables, i.e. the total stress $\underline{\underline{\sigma}}$ and the discharge velocity $\mathbf{v}$, which involve gradients of the primal unknowns, i.e. the solid displacement $\mathbf{u}$ and the fluid pressure p. Gradients often represent quantities of primary interest in engineering, and, therefore, it is very important to approximate them accurately. Numerical differentiation is a particularly delicate procedure that usually suffers from a loss in approximation accuracy [47]. The HDG method proposed in this work computes both primal and dual variables simultaneously with optimal order of accuracy. In other words, if polynomials of degree k are used to approximate a variable and the variable itself meets sufficient regularity requirements, then the approximation error behaves like $\mathcal{O}(h^{k+1})$, where h is the maximum diameter of a mesh.

The HDG methods can be understood as mixed finite element methods [16] stemming from the Local Discontinuous Galerkin method, one of the many discontinuous Galerkin (DG) schemes covered in a paper by Arnold, Brezzi, Cockburn and Marini [48]. DG schemes are praised for their ability to handle all sorts of complicated meshes and discontinuous data, to provide high-order accurate solutions, to perform h/p adaptivity, and to retain very good scalability properties. However, they have been criticized because, for the same mesh and same polynomial degree, the number of globally coupled degrees of freedom is much larger than those of continuous Galerkin methods.

Certain DG methods, however, including the one proposed in this work, have the key property of being *hybridizable*, i.e., the global system can be recast in terms of (statically condensed onto) a single *hybrid* variable that represents the trace of the solution on the boundaries of the mesh elements [49]. These form a family of methods that are called the HDG methods [19]. The main guidelines for devising these methods are:

- Use a characterization of the associated exact solution in terms of solutions of Dirichlet boundary-value problems on each element of the mesh.
- Use DG methods to approximate the local Dirichlet problems. This can be done in parallel over the mesh elements.
- Patch all the local problems together by weakly imposing transmission conditions representing the continuity of normal flux and stress on inter-element faces [50]. The hybrid variable we introduced before coincides with the Lagrange multiplier associated with the transmission conditions.

The procedure just described is called *hybridization* or *static condensation* [19], and creates a global linear system for the hybrid variable only, whose dimension is much smaller than what it would be obtained from standard DG methods. After solving the global system, the unknowns are recovered locally on each element, again in parallel. This is similar to the hybridized implementation of mixed methods such as the Raviart-Thomas elements (see [19, 51]), except that the HDG method has the very interesting feature of using different (and simpler) polynomial spaces and a stabilization function (which does *not* need tuning) instead of a stable mixed finite element pair.

Therefore, HDG methods retain all the advantages of DG methods and, thanks to hybridization, become computationally competitive with traditional continuous Galerkin approaches [52]. However, hybridization is not just an implementation trick. Rather, it endows HDG methods with some attractive convergence properties that allow to enhance the accuracy of the approximate solution by local postprocessing [53].

Due to their attractive features, scientists are constantly pushing limits of applicability of HDG ideas to many problems in continuum mechanics and physics. Below, an absolutely not exhaustive list of applications of HDG methods and related references is given:

- steady-state diffusion [49];
- convection-diffusion [54–56];
- linear and nonlinear elasticity [57, 58];
- Stokes flow [59];
- compressible and incompressible Navier-Stokes [60, 61];
- wave and Maxwell's equations [62–64];
- fluid-structure interaction [65].

In this chapter, we present a novel numerical approach for solving porous media viscoelasticity. The key feature of this approach is the use of a new HDG method for spatial discretization of the poro-viscoelastic system, which is obtained by carefully blending the approaches by Cockburn et al. [19] and Qiu et al. [55,57] for the diffusion equation and linear elasticity with a fixed-point map for the nonlinear dependence of the permeability on the volumetric solid strain.

3.1 Problem Setting

Let $\Omega \subset \mathbb{R}^3$ be an open subset of $\mathbb{R}^3$ representing the spatial domain occupied by the fluid-solid mixture with boundary $\partial\Omega$ and let $[0, T), T > 0$ be the time domain.

The model problem we will be discussing in this chapter is a modified version of system (2.186)–(2.191) presented at the end of Chapter 2, namely:

$$\underline{\underline{\sigma}} = \underline{\underline{\sigma}}_e + \delta\underline{\underline{\sigma}}_v - p\underline{\underline{I}} \qquad \text{in } \Omega \times (0,T), \tag{3.1}$$

$$\nabla \cdot \underline{\underline{\sigma}} = \mathbf{F} \qquad \text{in } \Omega \times (0,T), \tag{3.2}$$

$$\mathbf{v} = -\mathcal{K}(\nabla \cdot \mathbf{u})\nabla p \qquad \text{in } \Omega \times (0,T), \tag{3.3}$$

$$(\nabla \cdot \mathbf{u})' + \nabla \cdot \mathbf{v} = S \qquad \text{in } \Omega \times (0,T), \tag{3.4}$$

where $\underline{\underline{\sigma}}_e$ and $\underline{\underline{\sigma}}_v$ are the elastic and viscoelastic stress contributions, respectively, for which Hooke-type laws are assumed:

$$\underline{\underline{\sigma}}_e = \overset{4}{E}\,\underline{\underline{\varepsilon}}(\mathbf{u}) = 2\mu^e\underline{\underline{\varepsilon}}(\mathbf{u}) + \lambda^e(\nabla \cdot \mathbf{u})\underline{\underline{I}}, \tag{3.5}$$

$$\underline{\underline{\sigma}}_v = \overset{4}{\eta}\,\underline{\underline{\varepsilon}}(\mathbf{u}') = 2\mu^v\underline{\underline{\varepsilon}}(\mathbf{u}') + \lambda^v(\nabla \cdot \mathbf{u}')\underline{\underline{I}}, \tag{3.6}$$

where μ^e and λ^e are the smeared elastic parameters, and μ^v and λ^v are the smeared viscous parameters. The parameter $\delta \geq 0$ in (3.1) indicates the extent to which the model includes viscoelastic effects for the solid constituent, with $\delta = 0$ corresponding to the purely elastic case. In equations (3.1)–(3.4), with respect to the poro-viscoelastic system presented at the end of Chapter 2, we have that:

- The subscript S has been dropped when referring to physical quantities of the solid phase.
- In the balance of linear momentum for the overall mixture (3.2), the divergence of the total stress $\nabla \cdot \underline{\underline{\sigma}}$ is set equal to $\mathbf{F}$, which is assumed to be a given function.
- In the Darcy's law (3.3), only the effect of the fluid pressure is retained. Moreover, the permeability tensor $\underline{\underline{K}}_F$ is an isotropic tensor depending on the size of the interconnected pore volume, which is represented by the fluid volume fraction n_F:

$$\underline{\underline{K}}_F = \kappa\underline{\underline{I}}, \quad \text{with } \kappa = \kappa(n_F).$$

From now on, n_F will be simply denoted by n. Using equation (2.190), the dependency of $\kappa(n)$ can be rewritten in terms of $\nabla \cdot \mathbf{u}$ as

$$\kappa(n) = \mathcal{K}(\nabla \cdot \mathbf{u}), \tag{3.7}$$

as it appears in (3.3).

- In the balance of mass for the overall mixture (3.4), the right hand side is denoted by S and is assumed to be a given function.

Let $\partial\Omega$ denote the boundary of Ω. We consider two partitions of $\partial\Omega$: one for the solid phase

$$\partial\Omega = \overline{\Gamma}_S^D \cup \overline{\Gamma}_S^N \cup \overline{\Gamma}_S^{xy} \cup \overline{\Gamma}_S^{xz} \cup \overline{\Gamma}_S^{yz} \cup \overline{\Gamma}_S^{x} \cup \overline{\Gamma}_S^{y} \cup \overline{\Gamma}_S^{z}, \tag{3.8}$$

with $\Gamma_S^i \cap \Gamma_S^j = \emptyset$, $i, j \in \{D, N, xy, xz, yz, x, y, z\}$, $i \neq j$; and another one for the fluid phase

$$\partial\Omega = \overline{\Gamma}_F^D \cup \overline{\Gamma}_F^N, \tag{3.9}$$

with $\Gamma_F^D \cap \Gamma_F^N = \emptyset$. We consider the following boundary conditions:

$$\mathbf{u} = \mathbf{g}_S^D \qquad \text{on } \Gamma_S^D, \tag{3.10}$$

$$\underline{\underline{\sigma}}\mathbf{n} = \mathbf{g}_S^N \qquad \text{on } \Gamma_S^N, \tag{3.11}$$

$$\mathbf{e}_1 \cdot \mathbf{u} = g_{S,1}^{xy}, \quad \mathbf{e}_2 \cdot \mathbf{u} = g_{S,2}^{xy}, \quad \mathbf{e}_3 \cdot \underline{\underline{\sigma}}\mathbf{n} = g_{S,3}^{xy} \qquad \text{on } \Gamma_S^{xy}, \tag{3.12}$$

$$\mathbf{e}_1 \cdot \mathbf{u} = g_{S,1}^{xz}, \quad \mathbf{e}_2 \cdot \underline{\underline{\sigma}}\mathbf{n} = g_{S,2}^{xz}, \quad \mathbf{e}_3 \cdot \mathbf{u} = g_{S,3}^{xz} \qquad \text{on } \Gamma_S^{xz}, \tag{3.13}$$

$$\mathbf{e}_1 \cdot \underline{\underline{\sigma}}\mathbf{n} = g_{S,1}^{yz}, \quad \mathbf{e}_2 \cdot \mathbf{u} = g_{S,2}^{yz}, \quad \mathbf{e}_3 \cdot \mathbf{u} = g_{S,3}^{yz} \qquad \text{on } \Gamma_S^{yz}, \tag{3.14}$$

$$\mathbf{e}_1 \cdot \mathbf{u} = g_{S,1}^{x}, \quad \mathbf{e}_2 \cdot \underline{\underline{\sigma}}\mathbf{n} = g_{S,2}^{x}, \quad \mathbf{e}_3 \cdot \underline{\underline{\sigma}}\mathbf{n} = g_{S,3}^{x} \qquad \text{on } \Gamma_S^{x}, \tag{3.15}$$

$$\mathbf{e}_1 \cdot \underline{\underline{\sigma}}\mathbf{n} = g_{S,1}^{y}, \quad \mathbf{e}_2 \cdot \mathbf{u} = g_{S,2}^{y}, \quad \mathbf{e}_3 \cdot \underline{\underline{\sigma}}\mathbf{n} = g_{S,3}^{y} \qquad \text{on } \Gamma_S^{y}, \tag{3.16}$$

$$\mathbf{e}_1 \cdot \underline{\underline{\sigma}}\mathbf{n} = g_{S,1}^{z}, \quad \mathbf{e}_2 \cdot \underline{\underline{\sigma}}\mathbf{n} = g_{S,2}^{z}, \quad \mathbf{e}_3 \cdot \mathbf{u} = g_{S,3}^{z} \qquad \text{on } \Gamma_S^{z}, \tag{3.17}$$

$$p = g_F^D \qquad \text{on } \Gamma_F^D, \tag{3.18}$$

$$\mathbf{v} \cdot \mathbf{n} = g_F^N \qquad \text{on } \Gamma_F^N, \tag{3.19}$$

where $\mathbf{g}_S^D, \mathbf{g}_S^N, \{g_{S,i}^{xy}, g_{S,i}^{xz}, g_{S,i}^{yz}, g_{S,i}^{x}, g_{S,i}^{y}, g_{S,i}^{z}, i = 1,2,3\}, g_F^D, g_F^N$ are given functions of space and time. In some cases, it may be useful to express Neumann boundary conditions involving the total stress $\underline{\underline{\sigma}}$ or the discharge velocity $\mathbf{v}$ in the following way

$$\underline{\underline{\sigma}}\mathbf{n} = \underline{\underline{g}}_S\mathbf{n} \qquad \text{and} \qquad \mathbf{v}\cdot\mathbf{n} = \mathbf{g}_F\cdot\mathbf{n},$$

respectively. The HDG method proposed in this thesis does not require any simplifying assumption on the boundary partitions (3.8) and (3.9) (i.e. we include cases when $\Gamma_S^i \cap \Gamma_F^j \neq \emptyset$, for any i, j) and the associated boundary conditions. In the boundary conditions (3.12)–(3.17), the solid displacement is specified along one or two coordinate directions, whereas the total normal traction $\underline{\underline{\sigma}}\mathbf{n}$ is specified along the other one(s). A boundary condition of type (3.17) will be used in Chapter 4 to describe the anchorage between the sclera and the lamina cribrosa in the ONH.

In order to specify the initial conditions, it is useful to distinguish between the viscoelastic case, i.e. $\delta > 0$, and the purely elastic case, i.e. $\delta = 0$. When $\delta > 0$, time derivatives appear both in (3.1) and (3.4), requiring an initial condition on the whole displacement field, namely

$$\mathbf{u} = \mathbf{u}^0 \quad \text{in } \Omega \quad \text{at } t = 0 \qquad (\text{case } \delta > 0). \tag{3.20}$$

When $\delta = 0$, only the divergence of the displacement $\nabla\cdot\mathbf{u}$ undergoes time differentiation, see equation (3.4). Therefore, only a condition on $\nabla\cdot\mathbf{u}$ is required, namely

$$\nabla\cdot\mathbf{u} = d_0 \quad \text{in } \Omega \quad \text{at } t = 0 \qquad (\text{case } \delta = 0). \tag{3.21}$$

3.1.1 Existence of Solutions

Several theoretical approaches have been developed to study poroelastic systems [66–73]. However, Bociu et al. [39] present the first study that addresses the solution of system (3.1)–(3.4), simultaneously accounting for non-zero, mixed boundary data, nonlinear dependence of the permeability on the volumetric solid strain, and elastic and viscoelastic effects in the solid constituent. Their existence results are particularly relevant to our discussion and will be reported below.

Let us begin by introducing some notations and conventions. Norms $\|\cdot\|_D$ are taken to be $L^2(D)$ for a domain D. For functions u, v in $L^2(D)$ we write $(u,v)_D = \int_D uv\,dx$ if D is a domain of $\mathbb{R}^3$ and $\langle u,v\rangle_D = \int_D uv\,dx$ if D is a domain of $\mathbb{R}^2$. The subscript denoting the domain in norms and inner products will be dropped where the context does not lead to confusion. The Sobolev space of order s defined on a domain D will be denoted by $H^s(D)$, with $H_0^s(D)$ denoting the closure of $C_0^\infty(D)$ in the $H^s(D)$ norm (which we denote by $\|\cdot\|_{H^s(D)}$ or $\|\cdot\|_{s,D}$). When $s=0$, we may further abbreviate the notation to $\|\cdot\|$ (as described above). We make use of the standard notation for the trace of functions $\gamma[w]$ as the map from $H^1(D)$ to $H^{1/2}(\partial D)$. We will make use of the spaces $L^2(0,T;U)$ and $H^s(0,T;U)$, where U is a topological vector space. These norms (and their associated inner products) will be denoted with the appropriate subscript, e.g., $||\cdot||_{L^2(0,T;U)}$.

The principal spaces we consider are of the form

$$H^1_{\Gamma_*}(\Omega) = \left\{ f \in H^1(\Omega) \;\middle|\; \gamma[f]\big|_{\Gamma_*} = 0 \right\}.$$

In this case we have $H^1_{\Gamma_*}(\Omega) \supset H^1_0(\Omega)$ for any $\Gamma_* \subset \Gamma \equiv \partial\Omega$. The norms in these spaces are inherited from $H^1(\Omega)$. In this section, we will provide existence results in the case of boundary conditions of type (3.10) with $\mathbf{g}_S^D = \mathbf{0}$, (3.11), (3.18) with $g_F^D = 0$, and (3.19), with no simplifying assumptions on the boundary partitions

$$\partial\Omega = \overline{\Gamma}_S^D \cup \overline{\Gamma}_S^N \qquad \text{and} \qquad \partial\Omega = \overline{\Gamma}_F^D \cup \overline{\Gamma}_F^N,$$

i.e. we include cases when $\Gamma_S^i \cap \Gamma_F^j \neq \emptyset$, for $i,j = D,N$. Let us introduce the following bilinear forms

$$a_e(\mathbf{u},\mathbf{w}) = \lambda^e(\nabla\cdot\mathbf{u}, \nabla\cdot\mathbf{w})_\Omega + \mu^e(\nabla\mathbf{u}, \nabla\mathbf{w})_\Omega + \mu^e(\nabla\mathbf{u}, \nabla^T\mathbf{w})_\Omega, \tag{3.22}$$

$$a_v(\mathbf{u},\mathbf{w}) = \lambda^v(\nabla\cdot\mathbf{u}, \nabla\cdot\mathbf{w})_\Omega + \mu^v(\nabla\mathbf{u}, \nabla\mathbf{w})_\Omega + \mu^v(\nabla\mathbf{u}, \nabla^T\mathbf{w})_\Omega. \tag{3.23}$$

In this notation, we utilize

$$(\underline{\underline{A}}, \underline{\underline{B}})_\Omega = \int_\Omega (A_{ij}B_{ij})\,dv,$$

sometimes also denoted by $(\underline{\underline{A}} : \underline{\underline{B}})$ (see equation (2.67)).

In both cases $\delta > 0$ (viscoelastic case, or VE) and $\delta = 0$ (elastic case, or E), solutions will satisfy a weak form of (3.1)–(3.4), (3.10), (3.11), (3.18), and (3.19). Bociu et al. [39] notion of an E-solution ($\delta = 0$) follows that in [66] (and it is closely related to the notion in [71]). For a VE-solution ($\delta > 0$), they extend this notion in a natural way as specified below.

Definition 3.1.1 *[VE-Solution] A solution to* (3.1)–(3.4), (3.10), (3.11), (3.18), *and* (3.19) *(with $\delta > 0$) is represented by the pair of functions $\mathbf{u} \in H^1(0,T;[H^1_{\Gamma_S^D}(\Omega)]^3)$ and $p \in L^2(0,T;H^1_{\Gamma_F^D}(\Omega))$ such that:*

1. *the following relations are satisfied for any $\mathbf{w} \in [H^1_{\Gamma_S^D}(\Omega)]^3$, $q \in H^1_{\Gamma_F^D}(\Omega)$, and $f \in C^\infty([0,T])$:*

$$\delta \int_0^T a_v(\mathbf{u}', \mathbf{w}) f \, dt + \int_0^T a_e(\mathbf{u},\mathbf{w}) f \, dt - \int_0^T (p, \nabla \cdot \mathbf{w}) f \, dt = \int_0^T \langle \mathbf{g}_S^N, \mathbf{w} \rangle_{\Gamma_S^N} f \, dt + \int_0^T (\mathbf{F}, \mathbf{w}) f \, dt, \tag{3.24}$$

$$\int_0^T (\mathcal{K}(\nabla \cdot \mathbf{u}) \nabla p, \nabla q) f \, dt + \int_0^T (\nabla \cdot \mathbf{u}', q) f \, dt = -\int_0^T \langle g_F^N, q \rangle_{\Gamma_F^N} f \, dt + \int_0^T (S, q) f \, dt \tag{3.25}$$

2. *the initial conditions $\mathbf{u}(\mathbf{x}, 0) = \mathbf{u}^0 \in [H^1_{\Gamma_S^D}(\Omega)]^3$ and $\nabla \cdot \mathbf{u}(\mathbf{x}, 0) = d_0 \in L^2(\Omega)$ are given, and we require $\nabla \cdot \mathbf{u}^0 = d_0$ (in the $L^2(\Omega)$ sense).*

Definition 3.1.2 *[E-Solution] A solution to* (3.1)–(3.4), (3.10), (3.11), (3.18), *and* (3.19) *(with $\delta = 0$) is represented by the pair of functions $\mathbf{u} \in L^2(0,T;[H^1_{\Gamma_S^D}(\Omega)]^3)$ and $p \in L^2(0,T;H^1_{\Gamma_F^D}(\Omega))$ such that:*

1. *the following relations are satisfied for any* $\mathbf{w} \in [H^1_{\Gamma_S^D}(\Omega)]^3$, $q \in H^1_{\Gamma_F^D}(\Omega)$, *and* $f \in C_0^\infty((0,T))$*:*

$$\int_0^T a_e(\mathbf{u},\mathbf{w}) f \, dt - \int_0^T (p, \nabla\cdot\mathbf{w}) f \, dt = \int_0^T \langle \mathbf{g}_N^S, \mathbf{w}\rangle_{\Gamma_S^N} f \, dt + \int_0^T (\mathbf{F}, \mathbf{w}) f \, dt \tag{3.26}$$

$$\int_0^T (\mathcal{K}(\nabla\cdot\mathbf{u})\nabla p, \nabla q) f \, dt - \int_0^T (\nabla\cdot\mathbf{u}, q) f' \, dt = -\int_0^T \langle g_F^N, q\rangle_{\Gamma_F^N} f \, dt + \int_0^T (S, q) f \, dt \tag{3.27}$$

2. *for every* $q \in H^1_{\Gamma_F^D}(\Omega)$, *the term* $(\nabla\cdot\mathbf{u}(t), q)$ *uniquely defines an absolutely continuous function on* $[0,T]$ *and the initial condition* $(\nabla\cdot\mathbf{u}(0), q) = (d_0, q)$ *is satisfied.*

Definition 3.1.3 *[Energies] Energy functionals for solutions are defined as follows:*

$$E_e(\mathbf{u}(t)) = \frac{1}{2}\left[\lambda^e ||\nabla\cdot\mathbf{u}(t)||^2 + \mu^e ||\nabla\mathbf{u}||^2 + \mu^e(\nabla\mathbf{u}, \nabla^T\mathbf{u})\right], \tag{3.28}$$

$$E_v(\mathbf{u}(t)) = \frac{1}{2}\left[\lambda^v ||\nabla\cdot\mathbf{u}(t)||^2 + \mu^v ||\nabla\mathbf{u}||^2 + \mu^v(\nabla\mathbf{u}, \nabla^T\mathbf{u})\right], \tag{3.29}$$

$$W(p(t)) = (\mathcal{K}(\nabla\cdot\mathbf{u})\nabla p, \nabla p), \tag{3.30}$$

where E_e *is the* integrated elastic energy*,* E_v *is the* integrated viscous energy*, and* W *is the* integrated rate of change of fluid kinetic energy*.*

Let us consider the following assumptions on the domain Ω and the permeability κ:

Assumption 3.1.1 *We assume:*

1. Γ_S^D *is a set of positive measure, so by Korn's inequality [16] there exists a constant* $C_{\text{Korn}} = C_{\text{Korn}}(\Omega) > 0$ *such that*

$$||\underline{\underline{\varepsilon}}(\mathbf{w})||^2_{[L^2(\Omega)]^{3\times 3}} \geq C_{\text{Korn}} ||\nabla\mathbf{w}||^2_{[L^2(\Omega)]^{3\times 3}} \qquad \forall\, \mathbf{w} \in [H^1_{\Gamma_S^D}(\Omega)]^3. \tag{3.31}$$

2. Γ_F^D *is a set of positive measure, so by Poincare's inequality [38] there exists a constant* $C_P = C_P(\Omega) > 0$ *such that*

$$||q||_{L^2(\Omega)} \leq C_P ||\nabla q||_{L^2(\Omega)} \qquad \forall\, q \in H^1_{\Gamma_F^D}(\Omega). \tag{3.32}$$

3. *The scalar function* $\mathcal{K} : \mathbb{R} \to \mathbb{R}$ *is continuous on* $\mathbb{R}$. *We assume* $\mathcal{K}(s) \geq \mathcal{K}_{\min} > 0 \ \forall s \in \mathbb{R}$, *so there is a constant* C_κ *such that*

$$||p||^2_{1,\Omega} \leq C_\kappa W(p(t)).$$

Additionally, we assume: $\mathcal{K}(s) \leq \mathcal{K}_{\max} < \infty \ \forall s \in \mathbb{R}$.

4. *The boundary* Γ *is sufficiently regular [39].*

We can now state the two main existence results [39].

Theorem 3.1.1 *[Existence of VE-Solutions] Consider equations* (3.1)–(3.4), (3.10), (3.11), (3.18), *and* (3.19) *with* $\delta > 0$. *Let Assumption 3.1.1 hold, and consider data of the form:*

$$\mathbf{F} \in L^2\left(0,T;\left[L^2(\Omega)\right]^3\right), \qquad S \in L^2(0,T;L^2(\Omega)), \tag{3.33}$$

$$\mathbf{g}_S^N \in L^2\left(0,T;[H^{1/2}(\Gamma_S^N)]^3\right), \qquad g_F^N \in L^2\left(0,T;L^2(\Gamma_F^N)\right). \tag{3.34}$$

Then, there exists a VE-solution *(in the sense of* (3.24)–(3.25)*) satisfying*

$$\begin{aligned}\sup_{t\in[0,T]}\left[E_e(\mathbf{u}(t)) + \delta E_v(\mathbf{u}(t))\right] + \int_0^T \left[E_e(\mathbf{u}) + \delta E_v(\mathbf{u}_t)\right] dt + \int_0^T W(p)\, dt \\ \leq \mathscr{C}[e^{\mathscr{K}_1 T} + e^{\mathscr{K}_2 T}],\end{aligned} \tag{3.35}$$

where:

$$\begin{aligned}\mathscr{C} \equiv\ & \left[CE_e(\mathbf{u}(0)) + \delta CE_v(\mathbf{u}(0))\right] \\ & + C(c_\gamma, C_P, \mathcal{K}_{\min}^{-1}) \int_0^T \left[||\mathbf{F}||_0^2 + ||\mathbf{g}_S^N||^2_{L^2(\Gamma_S^N)} + ||S||_0^2 + ||g_F^N||^2_{L^2(\Gamma_F^N)}\right],\end{aligned} \tag{3.36}$$

$$\mathscr{K}_1 \equiv C(c_\gamma, C_{\text{Korn}}, \mu^e, \lambda^e), \tag{3.37}$$

$$\mathscr{K}_2 \equiv C(c_\gamma, C_{\text{Korn}}, \mu^v, \lambda^v, \delta^{-1}), \tag{3.38}$$

and $c_\gamma, C_{\text{Korn}}$ *and* $C_P 0$ *are the constants associated with the trace theorem [38], the Korn's inequality* (3.31), *and the Poincare's inequality* (3.32), *respectively.*

Theorem 3.1.2 *[Existence of E-Solutions] Consider equations* (3.1)–(3.4), (3.10), (3.11), (3.18), *and* (3.19) *with* $\delta = 0$. *Let Assumption 3.1.1 hold, and consider data of the form:*

$$\mathbf{F} \in H^1\left(0,T;\left(L^2(\Omega)\right)^3\right), \qquad S \in L^2(0,T;L^2(\Omega)), \tag{3.39}$$

$$\mathbf{g}_S^N \in H^1\left(0,T;(H^{1/2}(\Gamma_S^N))^3\right), \qquad g_F^N \in L^2\left(0,T;L^2(\Gamma_F^N)\right). \tag{3.40}$$

Then there exists an E-solution *(in the sense of* (3.26)–(3.27)*) satisfying*

$$\sup_{t\in[0,T]} E_e(\mathbf{u}(t)) + \int_0^T \left[W(p) + E_e(\mathbf{u})\right] dt \leq \mathscr{C} e^{\mathscr{K} T}, \tag{3.41}$$

where

$$\begin{aligned}
\mathscr{C} \equiv\ & C(c_\gamma, C_{\text{Korn}}, \mu^e, \lambda^e) E_e(\mathbf{u}(0)) \\
& + C(c_\gamma, C_{\text{Korn}}, \mu^e, \lambda^e) \sup_{[0,T]} \left(||\mathbf{g}_S^N(t)||^2_{L^2(\Gamma_S^N)} + ||\mathbf{F}(t)||_0^2 \right) \\
& + C(c_\gamma, C_P, \mathcal{K}_{\min}^{-1}) \int_0^T \left(||\mathbf{g}_S^N||^2_{L^2(\Gamma_S^N)} + ||\mathbf{g}_{S\,t}^N||^2_{L^2(\Gamma_S^N)} + ||g_F^N||^2_{L^2(\Gamma_F^N)} \right) \\
& + C(c_\gamma, C_P, \mathcal{K}_{\min}^{-1}) \int_0^T \left(||\mathbf{F}||_0^2 + ||\mathbf{F}_t||_0^2 + ||S||_0^2 \right),
\end{aligned} \tag{3.42}$$

and

$$\mathscr{K} \equiv C(c_\gamma, C_{\text{Korn}}, C_P, \mu^e, \lambda^e, \mathcal{K}_{\min}^{-1}), \tag{3.43}$$

and $c_\gamma, C_{\text{Korn}}$ *and* C_P *are the constants associated with the trace theorem [38], the Korn's inequality* (3.31), *and the Poincare's inequality* (3.32), *respectively.*

In Theorem 3.1.1 and Theorem 3.1.2, different time regularities of the volumetric source of linear momentum $\mathbf{F}$ and the boundary source of traction $\mathbf{g}_S^N$ are required, namely L^2 time regularity for the viscoelastic case and H^1 for the elastic case. Interestingly, numerical experiments described in Chapter 4 show that the Darcy velocity and the related fluid energy might become unbounded in the purely elastic case if data do not exhibit sufficient time regularity.

3.2 Numerical Algorithm

In this section, we propose a novel numerical approach based on HDG finite elements for the solution of system (3.1)–(3.6) in the computational domain Ω with boundary $\partial\Omega = \Gamma$, subject to boundary conditions of the form (3.10)–(3.19) and initial conditions (3.20) (viscoelastic case, $\delta > 0$) or (3.21) (purely elastic case, $\delta = 0$). Without loss of generality, we will present the method considering boundary conditions of type (3.10), (3.11), (3.18), and (3.19), corresponding to the following partitions of the boundary $\partial\Omega$

$$\partial\Omega = \overline{\Gamma}_S^D \cup \overline{\Gamma}_S^N = \overline{\Gamma}_F^D \cup \overline{\Gamma}_F^N.$$

Boundary conditions of mixed type (3.12)–(3.17) simply require a projection on the coordinates axes. We define the computational time domain $t \in (t_{\text{start}}, t_{\text{end}})$ of length $T = t_{\text{end}} - t_{\text{start}}$. Thus, in the space-time domain $Q = \Omega \times (t_{\text{start}}, t_{\text{end}})$, the following system has to be solved:

$$\underline{\underline{\sigma}} = 2\mu^e \underline{\underline{\varepsilon}}(\mathbf{u}) + \lambda^e(\nabla\cdot\mathbf{u})\underline{\underline{I}} + \delta(2\mu^v \underline{\underline{\varepsilon}}(\mathbf{u}') + \lambda^v(\nabla\cdot\mathbf{u}')\underline{\underline{I}}) - p\underline{\underline{I}} \qquad \text{in } Q, \tag{3.44}$$

$$\nabla\cdot\underline{\underline{\sigma}} = \mathbf{F} \qquad \text{in } Q, \tag{3.45}$$

$$\mathbf{v} = -\kappa(n)\nabla p \qquad \text{in } Q, \tag{3.46}$$

$$(\nabla\cdot\mathbf{u})' + \nabla\cdot\mathbf{v} = S \qquad \text{in } Q, \tag{3.47}$$

$$n = \nabla\cdot\mathbf{u} + n^0 \qquad \text{in } Q, \tag{3.48}$$

$$\mathbf{u} = \mathbf{g}_S^D \qquad \text{on } \Gamma_S^D, \tag{3.49}$$

$$\underline{\underline{\sigma}}\mathbf{n} = \mathbf{g}_S^N \qquad \text{on } \Gamma_S^N, \tag{3.50}$$

$$p = g_F^D \qquad \text{on } \Gamma_F^D, \tag{3.51}$$

$$\mathbf{v}\cdot\mathbf{n} = g_F^N \qquad \text{on } \Gamma_F^N, \tag{3.52}$$

subject to the following initial conditions:

$$\mathbf{u} = \mathbf{u}^0 \quad \text{in } \Omega \quad \text{at } t = t_{\text{start}} \qquad (\text{case } \delta > 0), \tag{3.53}$$

$$\nabla\cdot\mathbf{u} = d_0 \quad \text{in } \Omega \quad \text{at } t = t_{\text{start}} \qquad (\text{case } \delta = 0). \tag{3.54}$$

Observe that we used equation (3.7) and (2.156) to rewrite the permeability coefficient as a function of the fluid volume fraction n, i.e. $\kappa(n) = \mathcal{K}(\nabla \cdot \mathbf{u})$. In (3.48), n^0 represents the initial value of the fluid volume fraction.

The computational method proposed by Bociu et al. [39] for a one dimensional version of system (3.44)–(3.48) is composed of three main steps:

1. Backward Euler method for discretization in time [47];

2. a fixed-point iteration for the nonlinearity in the permeability that couples balance and constitutive equations (3.44)–(3.48);

3. a dual mixed finite element method for the discretization in space.

In this thesis, we extend their numerical approach to multidimensional geometries and validate it against available data in a living tissue, i.e. the lamina cribrosa in the ONH [1]. The details of each step are given in the following subsections.

3.2.1 Temporal Semi-Discretization

We divide $[t_{\text{start}}, t_{\text{end}}]$ into a finite number $r \geq 1$ of sub-intervals $[t^i, t^{i+1}], i = 0, \ldots, r-1$, of uniform length $\Delta t = T/r$. For any smooth function (in time) $\mathcal{Y} = \mathcal{Y}(\mathbf{x}, t)$, we let $\mathcal{Y}^i := \mathcal{Y}(\mathbf{x}, t^i)$; otherwise, if $\mathcal{Y}$ is discontinuous (in time) at $t = t^i$, we let $\mathcal{Y}^i := \mathcal{Y}(\mathbf{x}, t^{i-})$. Using the Backward Euler method for the time discretization, we get a sequence of r non linearly coupled boundary value problems, as shown in Algorithm 3.2.1.

3.2.2 Fixed-Point Iteration

We adopt a Picard iteration to numerically deal with the nonlinear dependence of the permeability κ on $n = \nabla \cdot \mathbf{u} + n^0$ in equation (3.57). This approach has also been used by Cao et al. [73]. The complete fixed point iteration is described in Algorithm 3.2.2. The limiter Π in equation (3.66) is a function $\Pi \colon \mathbb{R} \to [n_{\min}, n_{\max}]$,

Algorithm 3.2.1 Temporal Semi-Discretization of system (3.44)–(3.52)

Input: $\mathbf{u}^0$ and n^0.

1: **for** $i = 0, \ldots, r-1$ **do**

2: Given $\mathbf{u}^i$, solve the following *nonlinear* problem:

$$\begin{aligned}
\underline{\underline{\sigma}}^{i+1} &= 2\mu^{ve}\underline{\underline{\varepsilon}}(\mathbf{u}^{i+1}) + \lambda^{ve}(\nabla\cdot\mathbf{u}^{i+1})\underline{\underline{I}} \\
&\quad - \frac{\delta}{\Delta t}(2\mu^{v}\underline{\underline{\varepsilon}}(\mathbf{u}^{i}) + \lambda^{v}(\nabla\cdot\mathbf{u}^{i})\underline{\underline{I}}) - p^{i+1}\underline{\underline{I}}, && (3.55)\\
\nabla\cdot\underline{\underline{\sigma}}^{i+1} &= \mathbf{F}^{i+1}, && (3.56)\\
\mathbf{v}^{i+1} &= -\kappa(n^{i+1})\nabla p^{i+1}, && (3.57)\\
\frac{1}{\Delta t}\nabla\cdot\mathbf{u}^{i+1} + \nabla\cdot\mathbf{v}^{i+1} &= S^{i+1} + \frac{1}{\Delta t}\nabla\cdot\mathbf{u}^{i}, && (3.58)\\
n^{i+1} &= \nabla\cdot\mathbf{u}^{i+1} + n^0, && (3.59)\\
& && (3.60)
\end{aligned}$$

for $\mathbf{x} \in \Omega$, with:

$$\begin{aligned}
\mathbf{u}^{i+1} &= \mathbf{g}_S^{D,i+1} && \text{on } \Gamma_S^D, && (3.61)\\
\underline{\underline{\sigma}}^{i+1}\mathbf{n} &= \mathbf{g}_S^{N,i+1} && \text{on } \Gamma_S^N, && (3.62)\\
p^{i+1} &= g_F^{D,i+1} && \text{on } \Gamma_F^D, && (3.63)\\
\mathbf{v}^{i+1}\cdot\mathbf{n} &= g_F^{N,i+1} && \text{on } \Gamma_F^N, && (3.64)
\end{aligned}$$

where $\mu^{ve} = \mu^e + \frac{\delta}{\Delta t}\mu^v, \lambda^{ve} = \lambda^e + \frac{\delta}{\Delta t}\lambda^v$.

3: **end for**

where $0 < n_{\min} < n_{\max} < 1$ are prescribed bounds on the fluid volume fraction n. This step is important to ensure that n remains within its physical admissible range, i.e. $n \in (0, 1)$. We do not allow either $n = 0$ (no fluid phase) or $n = 1$ (no solid phase). Several different choices are possible for Π. However, it is important to let Π be a sufficiently smooth mapping in order to avoid limit cycles in the iterative method. For example, a mapping that is only only Lipschitz-continuous on $\mathbb{R}$ and could lead to limit cycles is given below (see Figure 3.1):

$$\Pi_{\text{Lip}}(n) = \begin{cases} n_{\min} & \text{if } n \leq n_{\min}, \\ n & \text{if if } n_{\min} < n \leq n_{\max}, \\ n_{\max} & \text{if } n > n_{\max}. \end{cases}$$

On the other hand, a $C^1(\mathbb{R})$ mapping that should be able to suppress limit cycles is the following (see Figure 3.1):

$$\Pi_{C^1}(n) = \begin{cases} h_1(n) & \text{if } n \leq n_{\min} + \Delta, \\ n & \text{if if } n_{\min} + \Delta < n \leq n_{\max} - \Delta, \\ h_2(n) & \text{if } n > n_{\max} - \Delta, \end{cases} \tag{3.65}$$

where $\Delta = c(n_{\max} - n_{\min})$ and $0 < c < 1$. The functions $h_1 \colon \mathbb{R} \to \mathbb{R}$ and $h_2 \colon \mathbb{R} \to \mathbb{R}$ in (3.65) have to meet some reasonable criteria, such as:

$$\begin{aligned} &\lim_{n \to -\infty} h_1(n) = n_{\min}, \\ &h_1(n) \geq n_{\min} \text{ if } n \leq n_{\min} + \Delta, \\ &h_1(n_{\min} + \Delta) = n_{\min} + \Delta, \\ &\left. \frac{dh_1}{dn} \right|_{n = n_{\min} + \Delta} = 1, \end{aligned}$$

and, similarly,

$$\begin{aligned}
&\lim_{n\to\infty} h_2(n) = n_{\max},\\
&h_2(n) \leq n_{\max} \text{ if } n \geq n_{\max} - \Delta,\\
&h_2(n_{\max} - \Delta) = n_{\max} - \Delta,\\
&\left.\frac{dh_2}{dn}\right|_{n=n_{\max}-\Delta} = 1.
\end{aligned}$$

In this work, we let h_1 and h_2 be branches of hyperbolas satisfying the above conditions:

$$\begin{aligned}
h_1(n) &= \frac{-\Delta^2}{n - (n_{\min} + 2\Delta)} + n_{\min},\\
h_2(n) &= \frac{-\Delta^2}{n - (n_{\max} - 2\Delta)} + n_{\max}.
\end{aligned}$$

Depending on the functional dependence of the permeability κ on n, bounding n also causes κ to be bounded, thus ensuring that Assumption 3.1.1, introduced by Bociu et al. [39] to prove the existence theorems 3.1.1 and 3.1.2, is satisfied.

Algorithm 3.2.2 is a semi-implicit variant of the staggered (or loosely coupled) algorithm proposed and successfully used by Causin et al. [74] for the numerical study of a problem similar to that considered in Chapter 4. Algorithm 3.2.2 is convergent if the following map:

$$\begin{aligned}
\Pi_{\text{tot}} \colon \mathbb{R} &\to [n_{\min}, n_{\max}]\\
n^{(j)} &\to n^{(j+1)} = \Pi_{\text{tot}}(n^{(j)}),
\end{aligned}$$

which is a composition of the limiter Π introduced in (3.66) with the solution map of system (3.55)–(3.64), admits a fixed point. In this work, we do not provide an analytic study of the conditions under which this holds. Nevertheless, the sensitivity analysis provided in Section 3.3.2 suggests that the convergence of Algorithm 3.2.2 is strongly affected by the physical and geometrical parameters characterizing the problem.

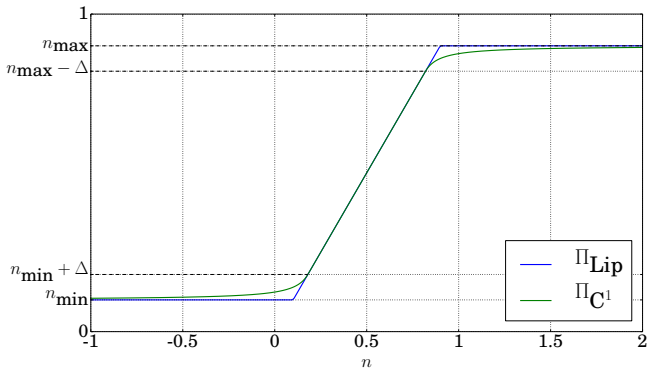

Figure 3.1. Examples of limiter functions that can be used in Algorithm 3.2.2 to ensure that the fluid volume fraction n is within physical limits, i.e. $0 < n < 1$. The limiter Π_{Lip} is only Lipschitz continuous and leads to limit cycles in the fixed-point iterations, whereas Π_{C^1} is $C^1(\mathbb{R})$ and does not cause such behavior.

Finally, the divergence of the solid displacement $\nabla \cdot \mathbf{u}^{j+1}$ has to be updated, as mentioned in line 4 of Algorithm 3.2.2. This point will be addressed in the next section.

3.2.3 Spatial Discretization by the HDG Method

In many engineering applications, it is extremely delicate to choose a proper spatial discretization. This is due to the fact that gradients often represent quantities of primary interest. For example, stresses drive the non-uniform growth and remodeling of the collagen within the lamina cribrosa [75], whereas discharge velocities are related to the blood perfusion of the laminar tissue.

This thesis presents a novel numerical method for porous media viscoelasticity based on HDG finite elements for the direct approximation of both the primal unknowns, i.e. the solid displacement $\mathbf{u}$ and the fluid pressure p, and the dual unknowns, i.e. the total stress $\underline{\underline{\sigma}}$ and the discharge velocity $\mathbf{v}$.

Algorithm 3.2.2 Fixed-Point Iteration for the Nonlinear Problem (3.55)–(3.64).

Input: $\mathbf{u}^{(0)} = \mathbf{u}^i$ and $n^{(0)} = n^i, j = 0$.

1: **while** termination criterion is not met **do**

2: Apply a limiter to the fluid volume fraction $n^{(j+1/2)}$

$$n^{(j+1/2)} = \Pi(n^{(j)}). \tag{3.66}$$

3: Solve the following *linear* problem:

$$\begin{aligned}
\underline{\underline{\sigma}}^{(j+1)} &= 2\mu^{ve}\underline{\underline{\varepsilon}}(\mathbf{u}^{(j+1)}) + \lambda^{ve}(\nabla\cdot\mathbf{u}^{(j+1)})\underline{\underline{I}} \\
&\quad - \frac{\delta}{\Delta t}(2\mu^{v}\underline{\underline{\varepsilon}}(\mathbf{u}^{i}) + \lambda^{v}(\nabla\cdot\mathbf{u}^{i})\underline{\underline{I}}) - p^{(j+1)}\underline{\underline{I}}, && (3.67)\\
\nabla\cdot\underline{\underline{\sigma}}^{(j+1)} &= \mathbf{F}^{i+1}, && (3.68)\\
\mathbf{v}^{(j+1)} &= -\kappa(n^{(j+1/2)})\nabla p^{(j+1)}, && (3.69)\\
\frac{1}{\Delta t}\nabla\cdot\mathbf{u}^{(j+1)} + \nabla\cdot\mathbf{v}^{(j+1)} &= S^{i+1} + \frac{1}{\Delta t}\nabla\cdot\mathbf{u}^{i}, && (3.70)
\end{aligned}$$

for $\mathbf{x}\in\Omega$, with

$$\begin{aligned}
\mathbf{u}^{(j+1)} &= \mathbf{g}_S^{D,i+1} && \text{on } \Gamma_S^D, && (3.71)\\
\underline{\underline{\sigma}}^{(j+1)}\mathbf{n} &= \mathbf{g}_S^{N,i+1} && \text{on } \Gamma_S^N, && (3.72)\\
p^{(j+1)} &= g_F^{D,i+1} && \text{on } \Gamma_F^D, && (3.73)\\
\mathbf{v}^{(j+1)}\cdot\mathbf{n} &= g_F^{N,i+1} && \text{on } \Gamma_F^N. && (3.74)
\end{aligned}$$

4: Update $\nabla\cdot\mathbf{u}^{(j+1)}$ by using equation (3.67).

5: Update the fluid volume fraction

$$n^{(j+1)} = \nabla\cdot\mathbf{u}^{(j+1)} + n^0. \tag{3.75}$$

6: $j = j + 1$.

7: **end while**

Similarly to other HDG methods devised for other applications, the approach considered here has some very interesting features, partially inherited by DG methods, which make it particularly well-suited for solving poro-viscoelastic models compared to other finite element approaches, like those mentioned in Chapter 1:

- It can handle any type of mesh and basis functions and is ideally suited for h/p-adaptivity [52].

- It obtains optimal order of convergence for all the variables on stationary problems. In other words, if polynomials of degree k are used to approximate a variable and the variable itself meets sufficient regularity requirements, then the approximation error behaves like $\mathcal{O}(h^{k+1})$, where h is the maximum diameter of a mesh.

- It has a stabilization mechanism that does not degrade its high order accuracy and does not need any tuning.

- It is obtained by discretizing a characterization of the exact solution written in terms of many local problems, one for each element of the triangulation Ω_h of the domain Ω, with suitably chosen data, and in terms of a single global problem that actually determines them. This is what makes this method, like other HDG methods, efficiently implementable since it inherits the above-mentioned structure of the exact solution. With respect to other DG methods of comparable accuracy, HDG methods require less degrees of freedom in the solution of the global system, since this is written in terms of (statically condensed onto) *hybrid* variables that represent the trace of the solution on the boundaries of the elements.

Let us now describe the HDG discretization for system (3.67)–(3.74) in details. The method we use combines Cockburn et al.'s [19] and Qiu et al.'s [55, 57]. We will then use their notation. Let Ω_h be a conforming triangulation of a polyhedral domain $\Omega \subset \mathbb{R}^d, d = 2, 3$, made of shape-regular polyhedral elements K. An interior *face* of

Ω_h is any set F of positive $(d-1)$-Lebesgue measure of the form $F = \partial K^+ \cap \partial K^-$ for some two elements K^+ and K^- of Ω_h. We say that F is a boundary face if there is an element $K \in \Omega_h$ such that $F = \partial K \cap \Gamma$ and the $(d-1)$-Lebesgue measure of F is not zero. We recall that $\partial\Omega_h = \{\, \partial K \mid K \in \Omega_h \,\}$, and $\mathcal{E}_h$ denotes the set of all faces F of all the elements. Let also $\mathcal{E}_h^o$ denote the set of interior faces of Ω_h. If $V(D)$ denotes a space of scalar-valued functions defined on D, the corresponding space of vector-valued functions is $\mathbf{V}(D) := (V(D))^d$ and the corresponding space of matrix-valued functions is $\underline{\underline{V}}(D) := (V(D))^{d\times d}$. Finally, $\underline{\underline{V}}(S, D)$ denotes the symmetric subspace of $\underline{\underline{V}}(D)$. We will also write

$$(v, w)_{\Omega_h} = \sum_{K\in\Omega_h} (v, w)_K, \qquad \langle \mu, \lambda\rangle_{\partial\Omega_h} = \sum_{K\in\Omega_h} \langle \mu, \lambda\rangle_{\partial K}. \tag{3.76}$$

We seek an approximation $(\underline{\underline{\sigma}}_h, \mathbf{u}_h, \hat{\mathbf{u}}_h, \mathbf{v}_h, p_h, \hat{p}_h)$ to

$$(\underline{\underline{\sigma}}^{(j+1)}, \mathbf{u}^{(j+1)}, \mathbf{u}^{(j+1)}|_{\mathcal{E}_h}, \mathbf{v}^{(j+1)}, p^{(j+1)}, p^{(j+1)}|_{\mathcal{E}_h}),$$

in the finite dimensional space

$$\underline{\underline{V}}_h^u \times \mathbf{W}_h^u \times \mathbf{M}_h^u \times \mathbf{V}_h^p \times W_h^p \times M_h^p,$$

defined by:

$$\underline{\underline{V}}_h^u = \left\{\, \underline{\underline{\mu}}_1 \in \underline{\underline{L}}^2(S, \Omega) \;\middle|\; \underline{\underline{\mu}}_1|_K \in \underline{\underline{P}}^k(S, K) \quad \forall\, K \in \Omega_h \,\right\}, \tag{3.77}$$

$$\mathbf{W}_h^u = \left\{\, \boldsymbol{\mu}_2 \in \mathbf{L}^2(\Omega) \;\middle|\; \boldsymbol{\mu}_2|_K \in \mathbf{P}^{k+1}(K) \quad \forall\, K \in \Omega_h \,\right\}, \tag{3.78}$$

$$\mathbf{M}_h^u = \left\{\, \boldsymbol{\mu}_5 \in \mathbf{L}^2(\mathcal{E}_h) \;\middle|\; \boldsymbol{\mu}_5|_F \in \mathbf{P}^k(F) \quad \forall\, F \in \mathcal{E}_h \,\right\}, \tag{3.79}$$

$$\mathbf{V}_h^p = \left\{\, \boldsymbol{\mu}_3 \in \mathbf{L}^2(\Omega) \;\middle|\; \boldsymbol{\mu}_3|_K \in \mathbf{P}^k(K) \quad \forall\, K \in \Omega_h \,\right\}, \tag{3.80}$$

$$W_h^p = \left\{\, \mu_4 \in L^2(\Omega) \;\middle|\; \mu_4|_K \in P^{k^*}(K) \quad \forall\, K \in \Omega_h \,\right\}, \tag{3.81}$$

$$M_h^p = \left\{\, \mu_6 \in L^2(\mathcal{E}_h) \;\middle|\; \mu_6|_F \in P^k(F) \quad \forall\, F \in \mathcal{E}_h \,\right\}, \tag{3.82}$$

where k^* could be either k or $k+1$ in equation (3.81). Observe that all the spaces introduced above are element-wise, or face-wise, discontinuous. Moreover, by definition of $\underline{\underline{V}}_h^u$, the symmetry of the stress tensor is imposed *strongly*, rather than in a weak sense [76–78].

For any discontinuous (scalar, vector or tensor) function u in $\underline{\underline{V}}_h^u$, $\mathbf{W}_h^u$, $\mathbf{V}_h^p$, or W_h^p, the trace $u|_F$ on an interior face $F = \partial K^+ \cap \partial K^-$ is a double value function, whose two branches are denoted by $(u|_F)_{K^+}$ and $(u|_E)_{K^-}$. For any double-valued scalar (u), vector ($\mathbf{v}$), or tensor ($\underline{\underline{w}}$) function, we define the *jump* of its normal component across an interior face F by

$$\begin{aligned}
[\![u]\!]_F &= u_{K^+} - u_{K^-}, \\
[\![\mathbf{v}]\!]_F &= \mathbf{v}_{K^+} \cdot \mathbf{n}_{K^+} + \mathbf{v}_{K^-} \cdot \mathbf{n}_{K^-}, \\
[\![\underline{\underline{w}}]\!]_F &= \underline{\underline{w}}_{K^+}\mathbf{n}_{K^+} + \underline{\underline{w}}_{K^-}\mathbf{n}_{K^-},
\end{aligned}$$

respectively. On any face F of K lying on the boundary, we set

$$\begin{aligned}
[\![\mathbf{v}]\!]_F &= \mathbf{v}_K \cdot \mathbf{n}_K, \\
[\![\underline{\underline{w}}]\!]_F &= \underline{\underline{w}}_K \mathbf{n}_K.
\end{aligned}$$

A Characterization of the Exact Solution

Let us rewrite system (3.67)–(3.74) in mixed form:

$$c_1\underline{\underline{\sigma}}^{(j+1)} + c_2(\operatorname{tr}\underline{\underline{\sigma}}^{(j+1)})\underline{\underline{I}} - \underline{\underline{\varepsilon}}(\mathbf{u}^{(j+1)}) + P_T p^{(j+1)}\underline{\underline{I}} = -c_3\underline{\underline{\varepsilon}}(\mathbf{u}^i) - c_4(\nabla\cdot\mathbf{u}^i)\underline{\underline{I}}, \tag{3.83}$$

$$\nabla\cdot\underline{\underline{\sigma}}^{(j+1)} = \mathbf{F}^{i+1}, \tag{3.84}$$

$$\kappa^{-1}(n^{(j+1/2)})\mathbf{v}^{(j+1)} + \nabla p^{(j+1)} = \mathbf{0}, \tag{3.85}$$

$$\frac{1}{\Delta t}\nabla\cdot\mathbf{u}^{(j+1)} + \nabla\cdot\mathbf{v}^{(j+1)} = S^{i+1} + \frac{1}{\Delta t}\nabla\cdot\mathbf{u}^i, \tag{3.86}$$

for $\mathbf{x}\in\Omega$, where $\operatorname{tr}\underline{\underline{\sigma}} = \sigma_{ii}$, $n^{(j+1/2)}$ depends on $\nabla\cdot\mathbf{u}^{(j)}$ according to (3.66), (3.75), and

$$\begin{aligned}
c_1 &= \frac{1}{2\mu^{ve}}, & c_2 &= -\frac{\lambda^{ve}}{2\mu^{ve}(2\mu^{ve}+3\lambda^{ve})} = -\frac{1}{2\mu^{ve}\left(\dfrac{2\mu^{ve}}{\lambda^{ve}}+3\right)}, \\
c_3 &= \frac{\delta}{\Delta t}(2\mu^v c_1), & c_4 &= \frac{\delta}{\Delta t}(2\mu^v c_2 + \lambda^v P_T), \\
P_T &= c_1 + 3c_2.
\end{aligned}$$

In Appendix A, it is shown how equation (3.67) can be manipulated to obtain its mixed form (3.83) and the functional expressions of coefficients $c_1, c_2, c_3,$ and c_4. Boundary conditions are:

$$\mathbf{u}^{(j+1)} = \mathbf{g}_S^{D,i+1} \qquad \text{on } \Gamma_S^D, \tag{3.87}$$

$$\underline{\underline{\sigma}}^{(j+1)}\mathbf{n} = \mathbf{g}_S^{N,i+1} \qquad \text{on } \Gamma_S^N, \tag{3.88}$$

$$p^{(j+1)} = g_F^{D,i+1} \qquad \text{on } \Gamma_F^D, \tag{3.89}$$

$$\mathbf{v}^{(j+1)} \cdot \mathbf{n} = g_F^{N,i+1} \qquad \text{on } \Gamma_F^N, \tag{3.90}$$

Four functions $\underline{\underline{\sigma}}, \mathbf{u}, \mathbf{v}, p$ are exact solutions of (3.83)–(3.90) if and only if they satisfy the following conditions [19]:

- equations (3.83)–(3.86) are satisfied on each element K of the mesh Ω_h;
- *transmission conditions* are satisfied on each interior face $F \in \mathcal{E}_h^o$:

$$[\![\hat{\mathbf{u}} \cdot \mathbf{e}_1]\!]_F = 0, [\![\hat{\mathbf{u}} \cdot \mathbf{e}_2]\!]_F = 0, [\![\hat{\mathbf{u}} \cdot \mathbf{e}_3]\!]_F = 0, \tag{3.91}$$

$$[\![\underline{\underline{\hat{\sigma}}}]\!]_F = \mathbf{0}, \tag{3.92}$$

$$[\![\hat{p}]\!]_F = 0, \tag{3.93}$$

$$[\![\hat{\mathbf{v}}]\!]_F = 0; \tag{3.94}$$

- boundary conditions:

$$\hat{\mathbf{u}}|_F = \mathbf{g}_S^{D,i+1}|_F \qquad \text{if } F \in \Gamma_S^D,$$

$$\underline{\underline{\hat{\sigma}}}\mathbf{n}|_F = \mathbf{g}_S^{N,i+1}|_F \qquad \text{if } F \in \Gamma_S^N,$$

$$\hat{p}|_F = g_F^{D,i+1}|_F \qquad \text{if } F \in \Gamma_F^D,$$

$$\hat{\mathbf{v}} \cdot \mathbf{n}|_F = g_F^{N,i+1}|_F \qquad \text{if } F \in \Gamma_F^N;$$

where $\hat{\mathbf{u}}, \underline{\underline{\hat{\sigma}}}, \hat{p}$, and $\hat{\mathbf{v}}$ are the traces of the displacement, the stress, the fluid pressure and the discharge velocity on the boundary of the elements, respectively. The transmission conditions (3.91)–(3.94) imply that $\hat{\mathbf{u}}, \underline{\underline{\hat{\sigma}}}\mathbf{n}, \hat{p}$, and $\hat{\mathbf{v}} \cdot \mathbf{n}$ are single-valued on

the interior faces of the mesh. In every mesh element K, we can obtain $(\underline{\underline{\sigma}}, \mathbf{u}, \mathbf{v}, p)$ in terms of $\hat{\mathbf{u}}, \hat{p}$ on ∂K and $\mathbf{u}^i, \mathbf{F}^{i+1}, S^{i+1}$ by solving the following *local* Dirichlet problem

$$c_1\underline{\underline{\sigma}} + c_2(\operatorname{tr}\underline{\underline{\sigma}})\underline{\underline{I}} - \underline{\underline{\varepsilon}}(\mathbf{u}) + P_T p\underline{\underline{I}} = -c_3\underline{\underline{\varepsilon}}(\mathbf{u}^i) - c_4(\nabla\cdot\mathbf{u}^i)\underline{\underline{I}} \qquad \text{in } K, \tag{3.95}$$

$$\nabla\cdot\underline{\underline{\sigma}} = \mathbf{F}^{i+1} \qquad \text{in } K, \tag{3.96}$$

$$\kappa^{-1}(n^{(j+1/2)})\mathbf{v} + \nabla p = \mathbf{0} \qquad \text{in } K, \tag{3.97}$$

$$\frac{1}{\Delta t}\nabla\cdot\mathbf{u} + \nabla\cdot\mathbf{v} = S^{i+1} + \frac{1}{\Delta t}\nabla\cdot\mathbf{u}^i \qquad \text{in } K, \tag{3.98}$$

$$\mathbf{u} = \hat{\mathbf{u}} \qquad \text{on } \partial K, \tag{3.99}$$

$$p = \hat{p} \qquad \text{on } \partial K. \tag{3.100}$$

The functions $\hat{\mathbf{u}}$ and $\hat{p}$ can now be determined on $\mathcal{E}_h$ as the solutions of the following *global* problem:

$$[\![\underline{\underline{\hat{\sigma}}}]\!]_F = \mathbf{0} \qquad \text{if } F \in \mathcal{E}_h^o, \tag{3.101}$$

$$[\![\hat{\mathbf{v}}]\!]_F = 0 \qquad \text{if } F \in \mathcal{E}_h^o, \tag{3.102}$$

$$\hat{\mathbf{u}}|_F = \mathbf{g}_S^{D,i+1}|_F \qquad \text{if } F \in \Gamma_S^D, \tag{3.103}$$

$$\underline{\underline{\hat{\sigma}}}\mathbf{n}|_F = \mathbf{g}_S^{N,i+1}|_F \qquad \text{if } F \in \Gamma_S^N, \tag{3.104}$$

$$\hat{p}|_F = g_F^{D,i+1}|_F \qquad \text{if } F \in \Gamma_F^D, \tag{3.105}$$

$$\hat{\mathbf{v}}\cdot\mathbf{n}|_F = g_F^{N,i+1}|_F \qquad \text{if } F \in \Gamma_F^N. \tag{3.106}$$

The HDG method is obtained by constructing *discrete* versions of (3.95)–(3.106). In this way, the *only* globally coupled degrees of freedom will be those of the global formulations (3.101)–(3.106).

The HDG Formulation

Using notation (3.76), equations (3.95)–(3.106) are discretized with:

$$(c_1\underline{\underline{\sigma}}_h, \underline{\underline{\mu}}_1)_{\Omega_h} + (c_2 \operatorname{tr}\underline{\underline{\sigma}}_h, \operatorname{tr}\mu_1)_{\Omega_h} - \langle \hat{\mathbf{u}}_h, \underline{\underline{\mu}}_1\mathbf{n}\rangle_{\partial\Omega_h} + (\mathbf{u}_h, \nabla\cdot\underline{\underline{\mu}}_1)_{\Omega_h} + (P_T p_h, \operatorname{tr}\underline{\underline{\mu}}_1)_{\Omega_h} = -(c_3\underline{\underline{\varepsilon}}(\mathbf{u}_h^i), \underline{\underline{\mu}}_1)_{\Omega_h} - (c_4(\nabla\cdot\mathbf{u}_h^i), \operatorname{tr}\underline{\underline{\mu}}_1)_{\Omega_h}, \tag{3.107}$$

$$-(\underline{\underline{\sigma}}_h, \nabla\boldsymbol{\mu}_2)_{\Omega_h} + \langle \underline{\underline{\hat{\sigma}}}_h\mathbf{n}, \boldsymbol{\mu}_2\rangle_{\partial\Omega_h} = (\mathbf{F}^{i+1}, \boldsymbol{\mu}_2)_{\Omega_h}, \tag{3.108}$$

$$(\kappa^{-1}\mathbf{v}_h, \boldsymbol{\mu}_3)_{\Omega_h} + \langle \hat{p}_h, \boldsymbol{\mu}_3\cdot\mathbf{n}\rangle_{\partial\Omega_h} - (p_h, \nabla\cdot\boldsymbol{\mu}_3)_{\Omega_h} = 0, \tag{3.109}$$

$$\frac{1}{\Delta t}(\nabla\cdot\mathbf{u}_h, \mu_4)_{\Omega_h} - (\mathbf{v}_h, \nabla\mu_4)_{\Omega_h} + \langle \hat{\mathbf{v}}_h\cdot\mathbf{n}, \mu_4\rangle_{\partial\Omega_h} = (S^{i+1}, \mu_4)_{\Omega_h} + \frac{1}{\Delta t}(\nabla\cdot\mathbf{u}_h^i, \mu_4)_{\Omega_h}, \tag{3.110}$$

$$\langle \underline{\underline{\hat{\sigma}}}_h\mathbf{n}, \boldsymbol{\mu}_5\rangle_{\partial\Omega_h\setminus\Gamma_S^D} = \langle \mathbf{g}_S^{N,i+1}, \boldsymbol{\mu}_5\rangle_{\Gamma_S^N}, \tag{3.111}$$

$$\langle \hat{\mathbf{u}}_h, \boldsymbol{\mu}_5\rangle_{\Gamma_S^D} = \langle \mathbf{g}_S^{D,i+1}, \boldsymbol{\mu}_5\rangle_{\Gamma_S^D}, \tag{3.112}$$

$$\langle \hat{\mathbf{v}}_h\cdot\mathbf{n}, \mu_6\rangle_{\partial\Omega_h\setminus\Gamma_F^D} = \langle g_F^{N,i+1}, \mu_6\rangle_{\Gamma_F^N}, \tag{3.113}$$

$$\langle \hat{p}_h, \mu_6\rangle_{\Gamma_F^D} = \langle g_F^{D,i+1}, \mu_6\rangle_{\Gamma_F^D}, \tag{3.114}$$

for all $(\underline{\underline{\mu}}_1, \boldsymbol{\mu}_2, \boldsymbol{\mu}_3, \mu_4, \boldsymbol{\mu}_5, \mu_6) \in \underline{\underline{V}}_h^u \times \mathbf{W}_h^u \times \mathbf{V}_h^p \times W_h^p \times \boldsymbol{M}_h^u \times M_h^p$, where the numerical normal fluxes $\underline{\underline{\hat{\sigma}}}_h$ and $\hat{\mathbf{v}}_h$ are defined as:

$$\underline{\underline{\hat{\sigma}}}_h\mathbf{n} = \underline{\underline{\sigma}}_h\mathbf{n} - \tau_S(P_{\mathbf{M}^u}\mathbf{u}_h - \hat{\mathbf{u}}_h), \qquad \text{on } \partial\Omega_h, \tag{3.115}$$

$$\hat{\mathbf{v}}_h\cdot\mathbf{n} = \begin{cases} \mathbf{v}_h\cdot\mathbf{n} + \tau_F(p_h - \hat{p}_h) & \text{if } p_h|_K \in P^k(K), \\ \mathbf{v}_h\cdot\mathbf{n} + \tau_F(P_{M^p}p_h - \hat{p}_h) & \text{if } p_h|_K \in P^{k+1}(K), \end{cases} \qquad \text{on } \partial\Omega_h. \tag{3.116}$$

In (3.115), (3.116), $P_{\mathbf{M}^u}$ and P_{M^p} denote the standard L^2-orthogonal projections from $\mathbf{L}^2(\mathcal{E}_h)$ onto $\mathbf{M}_h^u$ and from $L^2(\mathcal{E}_h)$ onto M_h^p, respectively. These projection operators have been introduced by Lehrenfeld [79] to define the numerical normal fluxes for diffusion problems. The parameters τ_S and τ_F are called *stabilization parameters*. They only need to satisfy few requirements in order to get optimal convergence rates:

- τ_S is allowed to be double valued on $\mathcal{E}_h^o$, with two branches $\tau_S^- = \tau_S^{K^-} > 0$ and $\tau_S^+ = \tau_S^{K^+} > 0$ defined on the face F shared by the elements K^- and K^+, such that

$$\tau_S^- = \mathcal{O}(h_{K^-}^{-1}), \qquad \tau_S^+ = \mathcal{O}(h_{K^+}^{-1}), \tag{3.117}$$

  where h_K is the diameter of the K-th element. We can also let τ_S be a fixed positive number on all faces, with $\tau_S = \mathcal{O}(h^{-1})$ [57].

- Similarly to τ_S, τ_F is allowed to be double valued on $\mathcal{E}_h^o$. However, its definition depends on the choice of the space W_h^p for the fluid pressure (see equation (3.81)). If $p_h|_K \in P^k(K)$, i.e. $k^* = k$ in (3.81), τ_F is a *non negative* function that does not vanish identically on the boundary ∂K of each element, that is $\forall\, K \in \Omega_h$, $\exists\, F \in \partial K$ such that $\tau_F^K|_F > 0$ [54]. Instead, if $p_h|_K \in P^{k+1}(K)$, i.e. $k^* = k+1$ in (3.81), τ_F must be strictly positive on all the faces. In particular

$$\tau_F^- = \mathcal{O}(h_{K^-}^{-1}) > 0, \qquad \tau_F^+ = \mathcal{O}(h_{K^+}^{-1}) > 0. \tag{3.118}$$

  In this case, we can also let τ_F be a fixed positive number on all the faces, with $\tau_F = \mathcal{O}(h^{-1})$ [55].

Equations (3.111) and (3.113) combine the flux equilibrium on internal faces (3.101), (3.102) and the Neumann boundary conditions (3.105), (3.106) written in weak form:

- *Flux equilibrium*: for all $F \in \mathcal{E}_h^o, F = K^- \cap K^+$, we impose:

$$\langle [\![\hat{\underline{\sigma}}_h]\!], \boldsymbol{\mu}_5 \rangle_F = \langle (\hat{\underline{\sigma}}_h \mathbf{n})|_{K^-}, \boldsymbol{\mu}_5 \rangle_F + \langle (\hat{\underline{\sigma}}_h \mathbf{n})|_{K^+}, \boldsymbol{\mu}_5 \rangle_F = 0, \tag{3.119}$$

$$\langle [\![\hat{\mathbf{v}}_h]\!], \mu_6 \rangle_F = \langle (\hat{\mathbf{v}}_h \cdot \mathbf{n})|_{K^-}, \mu_6 \rangle_F + \langle (\hat{\mathbf{v}}_h \cdot \mathbf{n})|_{K^+}, \mu_6 \rangle_F = 0. \tag{3.120}$$

  These last two equations also provide an intuitive explanation of the important role played by the projection operators $P_{\mathbf{M}^u}$ and P_{M^p} in the definition of the normal numerical fluxes (3.115), (3.116). By (3.115) and (3.116), the (extension by zero to $\mathcal{E}_h$ of the functions) $[\![\hat{\underline{\sigma}}_h]\!]|_{\mathcal{E}_h^o}$ and $[\![\hat{\mathbf{v}}_h]\!]|_{\mathcal{E}_h^o}$ belong to $\mathbf{M}_h^u$ and M_h^p, respectively. Thus, equations (3.119) and (3.120) are stating that

$$[\![\hat{\underline{\sigma}}_h]\!]|_{\mathcal{E}_h^o} = 0, \qquad [\![\hat{\mathbf{v}}_h]\!]|_{\mathcal{E}_h^o} = 0$$

pointwise, i.e. the normal numerical fluxes $\hat{\underline{\underline{\sigma}}}_h\mathbf{n}$ and $\hat{\mathbf{v}}_h \cdot \mathbf{n}$ are single-valued. This means that $\hat{\underline{\underline{\sigma}}}_h$ and $\hat{\mathbf{v}}_h$ are *conservative* numerical fluxes [19, 48]. Without the projections $P_{\mathbf{M}^u}$ and P_{M^p}, by (3.119) and (3.120) the normal components of $\hat{\underline{\underline{\sigma}}}_h$ and $\hat{\mathbf{v}}_h$ are only weakly continuous across the interfaces.

- *Neumann boundary conditions*:

$$\langle \hat{\underline{\underline{\sigma}}}_h\mathbf{n}, \boldsymbol{\mu}_5\rangle_F = \langle \mathbf{g}_S^{N,i+1}, \boldsymbol{\mu}_5\rangle_F \qquad \forall\, F \in \Gamma_S^N,$$
$$\langle \hat{\mathbf{v}}_h \cdot \mathbf{n}, \mu_6\rangle_F = \langle g_F^{N,i+1}, \mu_6\rangle_F \qquad \forall\, F \in \Gamma_F^N.$$

Dirichlet boundary conditions are represented by (3.112) and (3.114).

Note that equations (3.107)–(3.110) are completely local and, consequently, for each element $K \in \Omega_h$, the internal variables $\underline{\underline{\sigma}}_h, \mathbf{u}_h, \mathbf{v}_h$, and p_h can be eliminated in favor of $\hat{\mathbf{u}}_h, \hat{p}_h$ and the problem data, i.e. $\mathbf{u}_h^i, \mathbf{F}^{i+1}$, and S^{i+1}. The solutions of the local problems can then be plugged into (3.111)–(3.114) to get a system whose globally coupled degrees of freedom are those of the numerical traces $\hat{\mathbf{u}}_h$ and $\hat{p}_h$. This elimination procedure is referred to as *static condensation* and is the fundamental step that makes the hybridized method efficient and computationally competitive with standard displacement-based approaches.

After solving problem (3.107)–(3.114), which corresponds to the spatial discretization of the linear problem in Algorithm 3.2.2, the divergence of the solid displacement has to be updated. By applying the trace operator to (3.83), we get the following equation

$$c_1 \operatorname{tr} \underline{\underline{\sigma}}_h^{(j+1)} + 3c_2 \operatorname{tr} \underline{\underline{\sigma}}_h^{(j+1)} - \nabla \cdot \mathbf{u}_h^{(j+1)} + 3P_T p_h^{(j+1)} = -c_3 \nabla \cdot \mathbf{u}_h^i - 3c_4 \nabla \cdot \mathbf{u}_h^i,$$

which can be solved for $\nabla \cdot \mathbf{u}_h^{(j+1)}$, yielding

$$\nabla \cdot \mathbf{u}_h^{(j+1)} = (c_1 + 3c_2) \operatorname{tr} \underline{\underline{\sigma}}_h^{(j+1)} + 3P_T p_h^{(j+1)} + (c_3 + 3c_4)\nabla \cdot \mathbf{u}^i. \tag{3.121}$$

We notice that the evaluation of (3.121) does not require numerical differentiation, but only quantities that are directly computed by the HDG method. Thus it is expected that the high accuracy provided by the HDG scheme in the approximation

of the stress, the solid displacement and the fluid pressure reflects into the evaluation of $\nabla \cdot \mathbf{u}_h^{(j+1)}$.

3.3 Numerical Experiments

In this section we provide experiments to numerically validate our HDG method. For any function $u(\mathbf{x}, t)$, either scalar or vectorial, defined in the space-time domain

$$Q = \Omega \times [t_{\text{start}}, t_{\text{end}}]$$

we consider the norm

$$\|u\|_Q := \sup_{t \in [t_{\text{start}}, t_{\text{end}}]} \|u(\mathbf{x}, t)\|_{L^2(\Omega)}.$$

If u does not depend on time, we have

$$\|u\|_Q := \|u(\mathbf{x})\|_{L^2(\Omega)},$$

For any function $w(\mathbf{x}, t)$, either scalar or vectorial, defined on the set of faces $\mathcal{E}_h$ of a mesh, we consider

$$\|w\|_h := \sup_{t \in [t_{\text{start}}, t_{\text{end}}]} \|w(\mathbf{x}, t)\|_h, \quad \text{with} \quad \|w(\mathbf{x}, t)\|_h := \left(\sum_{F \in \mathcal{E}_h} |F| \|w(\mathbf{x}, t)\|_F^2 \right)^{1/2}.$$

If w does not depend on time, we have

$$||w||_h := \left(\sum_{F \in \mathcal{E}_h} |F| \|w(\mathbf{x})\|_F^2 \right)^{1/2}.$$

To estimate the accuracy of the HDG method on time dependent problems, the following errors are computed

$$e_h^{\sigma} = ||\underline{\underline{\sigma}} - \underline{\underline{\sigma}}_h||_Q, \quad e_h^{u} = ||\mathbf{u} - \mathbf{u}_h||_Q, \quad e_h^{v} = ||\mathbf{v} - \mathbf{v}_h||_Q, \quad e_h^{p} = ||p - p_h||_Q, \quad (3.122)$$

and

$$e_h^{\overline{u}} = ||\bar{\mathbf{u}} - \bar{\mathbf{u}}_h||_Q, \quad e_h^{\overline{p}} = ||\bar{p} - \bar{p}_h||_Q, \quad e_h^{\hat{u}} = ||\mathbf{u} - \hat{\mathbf{u}}_h||_h, \quad e_h^{\hat{p}} = ||p - \hat{p}_h||_h, \quad (3.123)$$

Table 3.1
Data for the eight meshes used in the experiments.

Number of triangles	8	32	128	512	2048	8192	32768	131072
Number of edges	16	56	208	800	3136	12416	49408	197120

where $\bar{\mathbf{u}}_h, \bar{p}_h$ represent the local averages of the solid displacement and fluid pressure, respectively. On stationary problems, relative errors are computed, instead:

$$e^{\underline{\underline{\sigma}}}_{h,\text{rel}} = \frac{||\underline{\underline{\sigma}} - \underline{\underline{\sigma}}_h||_\Omega}{||\underline{\underline{\sigma}}||_\Omega}, \quad e^{u}_{h,\text{rel}} = \frac{||\mathbf{u} - \mathbf{u}_h||_\Omega}{||\mathbf{u}||_\Omega}, \quad e^{v}_{h,\text{rel}} = \frac{||\mathbf{v} - \mathbf{v}_h||_\Omega}{||\mathbf{v}||_\Omega}, \quad e^{p}_{h,\text{rel}} = \frac{||p - p_h||_\Omega}{||p||_\Omega}, \tag{3.124}$$

$$e^{\bar{u}}_{h,\text{rel}} = \frac{||\bar{\mathbf{u}} - \bar{\mathbf{u}}_h||_Q}{||\bar{\mathbf{u}}||_Q}, \quad e^{\bar{p}}_{h,\text{rel}} = \frac{||\bar{p} - \bar{p}_h||_Q}{||\bar{p}||_Q}, \quad e^{\hat{u}}_{h,\text{rel}} = \frac{||\mathbf{u} - \hat{\mathbf{u}}_h||_h}{||\mathbf{u}||_h}, \quad e^{\hat{p}}_{h,\text{rel}} = \frac{||p - \hat{p}_h||_h}{||p||_h}. \tag{3.125}$$

Estimates of the order of convergence for a generic quantity e_h are computed using the formula $\log_2(e_{h/2}/e_h)$.

3.3.1 Convergence Tests in 2D

In this section we reproduce in a two-dimensional setting the convergence tests provided by Bociu et al. in the one-dimensional case for their dual mixed hybridized method for poro-viscoelasticity [39]. We perform tests for several values of the degree k of the local basis functions, $k = 1, 2, 3$. The global coupled HDG system coming from the flux equilibrium conditions (3.119), (3.120) is solved on 64 cores using the SuperLU library, a general purpose library for the direct solution of large, sparse, non-symmetric systems of linear equations [80, 81].

Validation Test Case 1

First, we consider a linear stationary test case with $\delta = 0$ in (3.44)–(3.52). We take the domain Ω to be the square $[0,1] \times [0,1]$. Boundary conditions (BCs) are as follows:

- on $0 \leq x < 1, y = 0$: Dirichlet BCs on both the displacement $\mathbf{u}$ and the fluid pressure p;
- on $x = 1, 0 \leq y < 1$: Neumann BCs on the total stress $\underline{\underline{\sigma}}$ and Dirichlet BCs on p;
- on $0 < x \leq 1, y = 1$: Dirichlet BCs on $\mathbf{u}$ and Neumann BCs on the Darcy velocity $\mathbf{v}$;
- on $x = 0, 0 < y \leq 1$: Neumann BCs on both $\underline{\underline{\sigma}}$ and $\mathbf{v}$.

The coarsest triangulation contains 8 elements. Seven nested refinements of this partition are used. The main triangulation data are given in Table 3.1. We use a constant permeability coefficient $\kappa = \kappa_{\text{ref}} = 1\,\text{m}^2\text{Pa}^{-1}\text{s}^{-1}$ and choose the data so that the exact solution is

$$\mathbf{u} = U_{\text{ref}} \begin{bmatrix} \cos(\pi x)\sin(\pi y) \\ \sin(\pi x)\cos(\pi y) \end{bmatrix}, \qquad p = P_{\text{ref}} \sin(\pi x)\sin(\pi y),$$

with $U_{\text{ref}} = 1\,\text{m}, P_{\text{ref}} = 1\,\text{Pa}$. We use the formulation with $p_h|_K \in P^{k+1}(K)$, for $K \in \Omega_h$, and test for several values of the polynomial degree k on the eight meshes.

As shown in Tables C.1–C.3, the errors $e^{\sigma}_{h,\text{rel}}, e^{v}_{h}, e^{\hat{u}}_{h,\text{rel}}, e^{\hat{p}}_{h,\text{rel}}$ behave like $\mathcal{O}(h^{k+1})$ whereas errors $e^{u}_{h,\text{rel}}, e^{p}_{h,\text{rel}}, e^{\overline{u}}_{h,\text{rel}}, e^{\overline{p}}_{h,\text{rel}}$ behave like $\mathcal{O}(h^{k+2})$. The reduced convergence rates for $k = 2, 3$ on the finest meshes are due to round-off errors. Hence, the HDG method is able to achieve optimal convergence for both the dual variables, $\underline{\underline{\sigma}}_h$ and $\mathbf{v}_h$, and the primal variables, $\mathbf{u}_h$ and p_h. Note that due to the disparity of polynomial degrees for the stress and displacement, and for the Darcy velocity and fluid pressure, optimal convergence of this method yields the same quality of

the solution as a postprocessed method based on a superconvergent scheme. This is extremely important in any application where gradients have to be approximated accurately and high order accuracy is also required for the primal variables.

Validation Test Case 2

Here, we consider a nonlinear test case. We consider the same domain, boundary conditions and mesh data as in test case 1. The porosity n is now allowed to vary according to

$$n = \nabla \cdot \mathbf{u} + 0.5, \tag{3.126}$$

within the range $[n_{\min}, n_{\max}]$, where $0 < n_{\min} < n_{\max}$, so that the permeability κ, expressed by the Carman-Kozeny law [21]

$$\kappa(n) = \kappa_{\text{ref}} \frac{n^3}{(1-n)^2}, \tag{3.127}$$

satisfies

$$0 < \kappa_{\text{ref}} \frac{n_{\min}^3}{(1-n_{\min})^2} \leq \kappa(n) \leq \kappa_{\text{ref}} \frac{n_{\max}^3}{(1-n_{\max})^2}.$$

We set $n_{\min} = 0.1, n_{\max} = 0.9, \kappa_{\text{ref}} = 1\,\text{m}^2\text{Pa}^{-1}\text{s}^{-1}$. Figure 3.2 shows the graph of $\kappa(n)$ for $n \in [n_{\min}, n_{\max}] = [0.1, 0.9]$. Observe that

$$\kappa(n_{\min}) \approx 0.0012\,\text{m}^2\text{Pa}^{-1}\text{s}^{-1}, \qquad \kappa(n_{\max}) \approx 73\,\text{m}^2\text{Pa}^{-1}\text{s}^{-1},$$

so that variations in κ range over almost 5 orders of magnitude.

Data are taken so that the exact solution is

$$\mathbf{u} = U_{\text{ref}} \begin{bmatrix} \cos(\pi x)\sin(\pi y) \\ \sin(\pi x)\cos(\pi y) \end{bmatrix}, \qquad p = P_{\text{ref}} \sin(\pi x)\sin(\pi y),$$

with $U_{\text{ref}} = 0.1/\pi\,\text{m}, P_{\text{ref}} = 0.1\,\text{Pa}$. The fixed point algorithm terminates when

$$\frac{||\hat{\mathbf{U}}_j - \hat{\mathbf{U}}_{j-1}||_\infty}{||\hat{\mathbf{U}}_{j-1}||_\infty} < \varepsilon \tag{3.128}$$

where $\varepsilon = \cdot 10^{-10}$ and $\hat{\mathbf{U}}_j$ and $\hat{\mathbf{U}}_{j-1}$ are the vectors with all the Lagrange multipliers $\hat{\mathbf{u}}, \hat{p}$ at the current and the previous fixed point iterations, respectively. Interestingly,

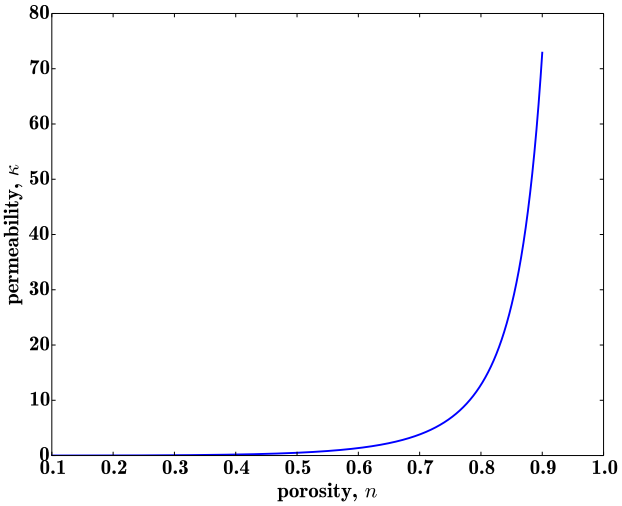

Figure 3.2. Carman-Kozeny law for the permeability coefficient.

the fixed point algorithm converges in 11 iterations for *all* the values of k on all the meshes (besides the case $k = 1$ on the first mesh where convergence is achieved in 12 iterations).

Tables C.4–C.6 show that the errors $e^{\sigma}_{h,\mathrm{rel}}, e^{v}_{h,\mathrm{rel}}, e^{\hat{u}}_{h,\mathrm{rel}}, e^{\hat{p}}_{h,\mathrm{rel}}$ behave like $\mathcal{O}(h^{k+1})$ whereas errors $e^{u}_{h,\mathrm{rel}}, e^{p}_{h,\mathrm{rel}}, e^{\overline{u}}_{h,\mathrm{rel}}, e^{\overline{p}}_{h,\mathrm{rel}}$ behave like $\mathcal{O}(h^{k+2})$. Again, the reduced convergence rates for $k = 2, 3$ on the finest meshes are due to round-off errors. Thus, even in this nonlinear test case, the HDG method coupled with the fixed point algorithm has the very interesting feature of achieving optimal convergence for both the dual variables, $\underline{\underline{\sigma}}_h$ and $\mathbf{v}_h$, and the primal variables, $\mathbf{u}_h$ and $\mathbf{p}_h$.

Validation Test Case 3

Here we consider a time dependent version of test case 1. We consider problem (3.44)–(3.53) with $\delta = 1$ in the unit square $\Omega = [0, 1] \times [0, 1]$ and the time interval $[0, T]$, with $T = 1\,\mathrm{s}$. A constant permeability coefficient $\kappa = \kappa_{\mathrm{ref}} = 1\,\mathrm{m^2Pa^{-1}s^{-1}}$ is used and data are taken so that the exact solution is

$$\mathbf{u} = U_{\mathrm{ref}} \begin{bmatrix} \cos(\pi x)\sin(\pi y)\sin(2\pi t) \\ \sin(\pi x)\cos(\pi y)\sin(2\pi t) \end{bmatrix}, \qquad p = P_{\mathrm{ref}} \sin(\pi x)\sin(\pi y)\sin(2\pi t),$$

with $U_{\mathrm{ref}} = 1\,\mathrm{m}$, $P_{\mathrm{ref}} = 1\,\mathrm{Pa}$. We take the same meshes used in test case 1 and temporal step sizes $\Delta t = T/r$, with $r \in \{5, 10, 20, 40, 80, 160, 320, 640\}$. Tables C.7–C.9 show the absolute errors. The approximate variables converge to the corresponding exact ones with linear rate with respect to the mesh diameter h, spoiling the convergence property of the HDG method achieved in the stationary test case 1. The degradation of the convergence rate of the HDG method is due to the choice of the Backward Euler method as time-advancing scheme, which is first-order accurate in time [47]. Observe that increasing the polynomial degree of the HDG spaces (p-refinement) is effective in reducing the errors for any pair of mesh and time step.

Validation Test Case 4

Here we consider a time dependent version of test case 2. Let us consider again problem (3.44)–(3.53) with $\delta = 1$ in the unit square $\Omega = [0,1] \times [0,1]$ and the time interval $[0,T]$, with $T = 1\,\mathrm{s}$. Porosity and permeability are nonlinear functions of the solution, as described in test case 2. Data are taken so that the exact solution is

$$\mathbf{u} = U_{\mathrm{ref}} \begin{bmatrix} \cos(\pi x)\sin(\pi y)\sin(2\pi t) \\ \sin(\pi x)\cos(\pi y)\sin(2\pi t) \end{bmatrix}, \qquad p = P_{\mathrm{ref}} \sin(\pi x)\sin(\pi y)\sin(2\pi t),$$

with $U_{\mathrm{ref}} = 0.1/\pi\,\mathrm{m}$, $P_{\mathrm{ref}} = 0.1\,\mathrm{Pa}$. We take the same meshes used in test case 2 and temporal step sizes $\Delta t = T/r$, with $r \in \{5, 10, 20, 40, 80, 160, 320, 640\}$. Tables C.10–C.12 show the absolute errors. Unlike the stationary nonlinear case 2, the convergence of the approximate variables reduces to linear rate due to the Backward Euler method. Increasing the polynomial degree effectively reduces the errors also in this test case.

3.3.2 Sensitivity Analysis

The goal of this section is to determine how variations in the poro-visco-elastic model parameters affect the performance of our HDG method. Variations in the following physical parameters will be considered:

- permeability κ;
- elastic and viscous parameters: $\lambda^e, \mu^e, \lambda^v, \mu^v$;
- different scaling of the fluid pressure and the solid displacement;
- time step Δt.

In 2D, the sensitivity analysis is carried out by repeating the four validation test cases with updated parameters on the first seven meshes in Table 3.1 with polynomial degree $k = 1$. The results shown below illustrate that, in some cases, it may be beneficial to scale problem (3.44)–(3.54) and reformulate it in terms of dimensionless

variables in order to restore the accuracy provided by the HDG scheme. However, care is needed when using this approach, as the choice of characteristic scales may be a non trivial issue for the problem at hand [82]. In Appendix B, we show how problem (3.44)–(3.54) can be reformulated in terms of dimensionless variables.

Effect of Permeability

- Solving the validation test case 1 in 2D for a smaller value of the permeability κ ($\kappa = \kappa_{\text{ref}} = 1 \times 10^{-4}\,\text{m}^2\text{Pa}^{-1}\text{s}^{-1}$), we observe a full order drop in the convergence rate of $\bar{p}_h$ on the seventh mesh when using the formulation with $p_h|_K \in P^{k+1}(K)$. Instead, when taking $p_h|_K \in P^k(K)$, there is no convergence rate drop for $\bar{p}_h$, but errors for p_h are one order of magnitude bigger, as expected. Using a smaller value for the permeability κ ($\kappa = \kappa_{\text{ref}} = 1 \times 10^{-6}\,\text{m}^2\text{Pa}^{-1}\text{s}^{-1}$), the errors for p_h and $\bar{p}_h$ actually increase from the sixth to the seventh mesh with $p_h|_K \in P^{k+1}(K)$, whereas this does not occur with $p_h|_K \in P^k(K)$.

- By setting $\kappa_{\text{ref}} = 1 \times 10^{-2}\,\text{m}^2\text{Pa}^{-1}\text{s}^{-1}$ in the validation test case 2 in 2D, relative errors for the two different formulations for p_h exhibit a similar trend to those obtained in test case 1 for $\kappa_{\text{ref}} = 1 \times 10^{-4}\,\text{m}^2\text{Pa}^{-1}\text{s}^{-1}$. Also, the numbers of fixed point iterations needed by both formulations to converge are not affected. Conversely, when taking $\kappa_{\text{ref}} = 1 \times 10^{-4}\,\text{m}^2\text{Pa}^{-1}\text{s}^{-1}$, the formulation with $p_h|_K \in P^{k+1}(K)$ does not converge within the maximum number of fixed point iterations (500) on the last three meshes. The relative inf norm of the increments defined in (3.128) oscillates between 1×10^{-10} and 1×10^{-9}. With $p_h|_K \in P^k(K)$, the algorithm converges in 11 iterations on every mesh (except the first one where it takes 14 iterations to converge). By comparing relative errors, we observe that the formulation with $p_h|_K \in P^{k+1}(K)$ provides smaller approximation errors, even if it does not always achieve convergence.

Working with the poro-viscoelastic equations in dimensionless form (see Appendix B) may be beneficial in the following situations:

- in test case 1, setting all the characteristic parameters but v_c (the characteristic Darcy velocity) equal to 1 and $v_c = \kappa p_c / x_c$, restores the accuracy of the formulation with $p_h|_K \in P^{k+1}(K)$.

- in test case 2, with $v_c = \kappa_{\text{ref}} = 1 \times 10^{-4}\,\text{ms}^{-1}$ and all the other characteristic parameters set equal to 1, the fixed point algorithm converges in 11 iterations on every mesh, and its accuracy is restored for $p_h|_K \in P^{k+1}(K)$.

Conclusion: the formulation with $p_h|_K \in P^k(K)$ looks more stable when the permeability κ gets small. On the other hand, the formulation with $p_h|_K \in P^{k+1}(K)$ always provides smaller errors on stationary problems as expected, even when it does not converge. This may indicate that using too strict tolerances in the fixed point algorithm is not beneficial or that a better alternative to the fixed point algorithm should be used.

Effect of Elastic and Viscous Parameters

Here we consider three pairs of values for the elastic parameters μ^e and λ^e:

$$\mu^e = 5 \times 10^4\,\text{Pa}, \lambda^e = 1 \times 10^4\,\text{Pa},$$
$$\mu^e = 3 \times 10^4\,\text{Pa}, \lambda^e = 2 \times 10^6\,\text{Pa},$$
$$\mu^e = 6 \times 10^6\,\text{Pa}, \lambda^e = 1 \times 10^8\,\text{Pa}.$$

The first two pairs correspond to the elastic parameters used by Phillips to study locking, or the nonphysical pressure oscillations, which sometimes arise in numerical algorithms for poroelasticity [17]. The last pair is used in this work in a later section to characterize the elastic behavior of the lamina cribrosa [83,84]. For stationary test cases, we considered relative rather than absolute errors as in (3.122), (3.123).

- All the three pairs have similar effects on the performance of the HDG method in the validation test case 1. The higher the elastic parameters, the bigger the relative errors for $\mathbf{u}_h$ and $\hat{u}_h$. Also, relative errors for p_h are 1 to 2 orders of

magnitude smaller when taking $p_h|_K \in P^{k+1}(K)$ rather than $p_h|_K \in P^k(K)$. Interestingly, convergence rates for *all* the variables are just as expected (see Table C.13), except for $\hat{\mathbf{u}}_h$, which decreases much faster.

- Similar relative errors and convergence rates to those shown in Table C.13 are found in the validation test case 2 as the elastic parameters get bigger. Moreover, with the first two pairs of elastic parameters, the fixed point algorithm converges just in 4 iterations on each mesh, whereas, with the last pair, it fails to converge on all the meshes but the two coarsest ones. The performance of our method is still very good, as the relative inf norm of the increments defined in (3.128) oscillates between 1×10^{-9} and 1×10^{-8}.

Working with the poro-viscoelastic equations in dimensionless form (see Appendix B) may be beneficial in the following situations:

- Setting the characteristic total stress $\sigma_c = 2\mu^e$ and all the other characteristic parameters to 1 restores the accuracy of $\mathbf{u}_h$ and $\hat{\mathbf{u}}_h$ in test case 1 and 2, even for the biggest pair of elastic parameters, $\mu^e = 6 \times 10^6\,\text{Pa}, \lambda^e = 1 \times 10^8\,\text{Pa}$ (see Table C.14 and Table C.15). In test case 2, even with this last pair, the fixed point algorithm converges in 4 iterations on all the meshes.

Conclusion: as the values of the elastic parameters increase, fine meshes might be needed in order to get reasonable errors for the solid displacement. The HDG method seems *not to suffer* from locking arising in linear elasticity for nearly incompressible materials, as all the variables retain optimal convergence rates even for the biggest pair of elastic parameters. The convergence of the fixed point method is affected by the elastic parameters, but this could be tackled by working with dimensionless equations. Taking $p_h|_K \in P^{k+1}(K)$ provides smaller approximation errors than $p_h|_K \in P^k(K)$ as expected.

Table 3.2
Combinations of U_{ref} and P_{ref} tested in the sensitivity analysis.

Pair	U_{ref} [m]	P_{ref} [Pa]
1	1	100
2	1	10000
3	0.01	1
4	0.0001	1
5	0.01	0.01
6	0.0001	0.0001

Effect of Pressure and Solid Displacement Scaling

In this section, we consider the effect of changing the scaling of $\mathbf{u}_h$ and p_h by tuning U_{ref} and P_{ref}, as shown in Table 3.2. Choosing $P_{\text{ref}}/U_{\text{ref}} \geq 1\,\text{Pa}\,\text{m}^{-1}$ is based on the fact that the model proposed by Bociu et al. [39] is valid under the assumption of small solid deformations and displacements, whereas the fluid pressure is allowed to vary greatly.

- In the validation test case 1, as long as $P_{\text{ref}}/U_{\text{ref}} = 1\,\text{Pa}\,\text{m}^{-1}$, the performance of the HDG method is not affected and the same approximation errors corresponding to $U_{\text{ref}} = 1\,\text{m}, P_{\text{ref}} = 1\,\text{Pa}$ are obtained (see Table C.1). Conversely, the bigger the ratio $P_{\text{ref}}/U_{\text{ref}}$, the worse the effect on the convergence of the HDG method. In particular, if $P_{\text{ref}}/U_{\text{ref}} = 1 \times 10^4\,\text{Pa}\,\text{m}^{-1}$, approximation errors for $\mathbf{u}_h$ and $\bar{\mathbf{u}}_h$ are 3 orders of magnitude bigger than the case $P_{\text{ref}}/U_{\text{ref}} = 1\,\text{Pa}\,\text{m}^{-1}$ on all the meshes (see Table C.16). Using $p_h|_K \in P^k(K)$ rather than $p_h|_K \in P^{k+1}(K)$ provides bigger errors, but with the same order of magnitude.

- In the validation test case 2, only the first 6 meshes shown in Table 3.1 were used. Similarly to test case 1, as long as $P_{\text{ref}}/U_{\text{ref}} = 1\,\text{Pa}\,\text{m}^{-1}$, the accuracy of the HDG method does not degrade and the same approximation errors corresponding to $U_{\text{ref}} = 1\,\text{m}, P_{\text{ref}} = 1\,\text{Pa}$ are obtained (see Table C.4). Instead, in the other four cases shown in Table 3.2, the HDG method does not perform well. With the third and the fourth pairs, the fixed point algorithm converges, even faster than in the original test case 2, but errors show the same trend as in the linear test case (see Table C.16). The first two pairs $U_{\text{ref}}, P_{\text{ref}}$ shown in Table 3.2 have a detrimental effect on the fixed point algorithm: there is no convergence on any mesh, as the relative increments defined in equation (3.128) oscillate between 1×10^{-3} and 1×10^{-1}. Errors are several orders of magnitude bigger than those in the original test case 2 and decrease very slowly (compare Table C.4 and Table C.17).

The use of dimensionless equations (see Appendix B) is tested only for the first two pairs $(U_{\text{ref}}, P_{\text{ref}})$ shown in Table 3.2, as they involve scaling of the fluid pressure, not of the displacement field. Conversely, when considering the third and the fourth pairs, the displacement field $\mathbf{u}_h$ should be scaled, but this would be problematic in the nonlinear test case 2, as $\nabla \cdot \mathbf{u}_h$ could become close to 1, thereby making the Carman-Kozeny formula blow up. We take

$$p_c = P_{\text{ref}}, \qquad \sigma_c = P_{\text{ref}}, \qquad v_c = \kappa p_c / x_c = 1 \cdot P_{\text{ref}}/1 = P_{\text{ref}} \cdot 1\,\text{m}\,\text{s}^{-1}\,\text{Pa}^{-1},$$

and set all the other characteristic parameters to 1. Scaling is not very effective either in test case 1 or 2, as there is only a slight improvement in the approximation errors in test case 1 and the fixed point algorithm still fails to converge on any mesh in test case 2. Looking at the definition of the total stress in dimensionless form (see equation (B.1)) and observing that relative errors for $\mathbf{u}_h, \hat{\mathbf{u}}_h$ are small on finer meshes in Table C.16, we guess that it is necessary to take very small spatial step sizes in order for the strain tensor $\underline{\underline{\varepsilon}}_h^*(\mathbf{u}_h^*)$ to balance the scaling of the total stress and the fluid pressure.

Conclusion: the relative scaling of the solid displacement $\mathbf{u}_h$ and the fluid pressure p_h has a strong effect on the performance of the HDG algorithm. Unlike the results obtained in previous sections, scaling does not help here. This should warn the reader against thinking that scaling is a panacea in any situation. Instead, our results suggest that, depending on the regime of motion, it might be necessary to use a different preconditioning strategy or a different iterative method than the fixed point approach used in this work.

Effect of Time Step

We study the effect of reducing the time step Δt of the Backward Euler method used to discretize test case 3 in time. We fix the triangulation (the fourth one in Table 3.1), use temporal step sizes $\Delta t = T/r$, with

$$r \in \{20, 40, 80, 160, 320, 640, 1280, 2560\},$$

and test for different values of the degree k of the local polynomial bases, $k = 1, 2, 3, 4$. Interestingly, for $k = 1$, the smaller the time step, the higher the approximation errors (see Table C.18). Even more interestingly, higher order bases have a stabilization effect on the errors: the higher the degree, the more stabilized the errors. For example, for $k = 2$, errors start increasing only for $\Delta t \leq 1/320$s, whereas, for $k = 4$, errors always decrease linearly with Δt (see Table C.19).

Conclusion: using a small temporal step size has a negative effect on the convergence of the HDG method. However, this can be countered by using high order basis functions, which the HDG method is ideally suited for.

3.3.3 The Problem of Locking

Phillips and Wheeler [85] provided evidence that numerical methods for poroelasticity may suffer from locking, or nonphysical pressure oscillations. They used the famous problem of Barry and Mercer as test case [86]. This problem has a couple of interesting features: first, it provides an exact solution in 2D to the poro-elastic system (3.44)–(3.52), (3.54), where viscous effects have been neglected ($\delta = 0$); second, both the dimensionless deformation and pressure solutions do not depend on the dimensionless parameter $m = 1 + \lambda^e/\mu^e$.

Domain and boundary conditions are shown in Figure 3.3. We use $a = b = 1\,\mathrm{m}$, $x_0 = 0.23\,\mathrm{m}$ and $y_0 = 0.22\,\mathrm{m}$. There is no source term in the balance of momentum, whereas on the right side of the balance of mass (3.47), we have

$$s_f(t) = 2\beta F(\beta t), \tag{3.129}$$

with $\beta = a^{-1}b^{-1}(\lambda^e + 2\mu^e)\kappa = (\lambda^e + 2\mu^e)\kappa$, and

$$F(s) = \delta(x - x_0, y - y_0)\sin(s),$$

δ being the Dirac delta function. Equation (3.129) represents an oscillating point source. Denoting by P_i^K the i-th basis function for the approximate fluid pressure in

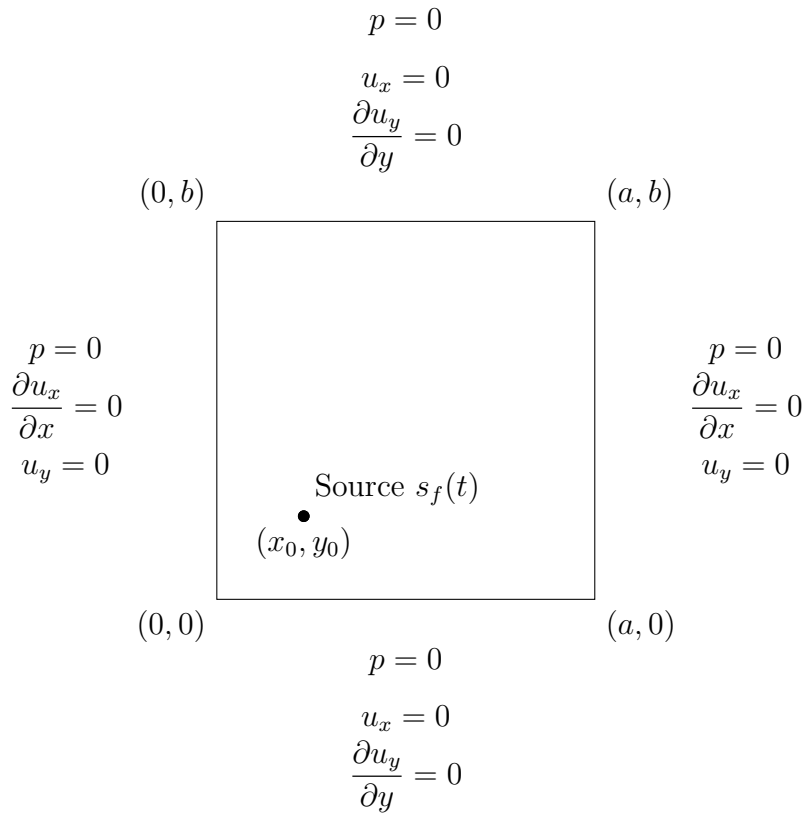

Figure 3.3. Domain and boundary conditions for the Barry and Mercer problem [86].

element $K \in \Omega_h$, the local contribution of s_f to the discrete balance of mass (3.110) is

$$\begin{aligned}\int_K s_f P_i^K d\mathbf{x} &= \int_K 2\beta\delta(x - x_0, y - y_0)\sin(\beta t) P_i^K d\mathbf{x} \\ &= 2\beta\sin(\beta t)\int_K \delta(x - x_0, y - y_0) P_i^K d\mathbf{x} \\ &= 2\beta\sin(\beta t) P_i^K(x_0, y_0).\end{aligned}$$

Barry and Mercer provide a solution for the fluid pressure and the solid displacement for this problem [86]. Let:

$$\gamma_n = n\pi, \qquad \gamma_q = q\pi, \qquad \gamma_{nq} = \gamma_n^2 + \gamma_q^2,$$

$$\hat{p}(n, q, t) = -\frac{2\sin(\gamma_n x_0)\sin(\gamma_q y_0)}{\gamma_{nq}^2 + 1}(\gamma_{nq}\sin(\beta t) - \cos(\beta t) + e^{-\gamma_{nq}\beta t}),$$

$$\hat{u}(n, q, t) = \frac{\gamma_n}{\gamma_{nq}}\hat{p}(n, q, t), \qquad \hat{w}(n, q, t) = \frac{\gamma_q}{\gamma_{nq}}\hat{p}(n, q, t).$$

The solution is then:

$$p(x, y, t) = -4(\lambda^e + 2\mu^e)\sum_{n=1}^{\infty}\sum_{q=1}^{\infty}\hat{p}(n, q, t)\sin(\gamma_n x)\sin(\gamma_q y), \tag{3.130}$$

$$u_x(x, y, t) = 4\sum_{n=1}^{\infty}\sum_{q=1}^{\infty}\hat{u}(n, q, t)\cos(\gamma_n x)\sin(\gamma_q y), \tag{3.131}$$

$$u_y(x, y, t) = 4\sum_{n=1}^{\infty}\sum_{q=1}^{\infty}\hat{w}(n, q, t)\sin(\gamma_n x)\cos(\gamma_q y). \tag{3.132}$$

We approximate the series in equations (3.130)–(3.132) with finite sums using the first 30×30 terms. Taking more terms does not affect the values of p, u_x, and u_y noticeably.

We consider the same set of material parameters used by Phillips and Wheeler [17, 18,85] to numerically validate their scheme using continuous or discontinuous elements for displacement and a mixed formulation for the fluid pressure

$$E = 1 \times 10^5\,\mathrm{Pa}, \qquad \nu = 0.1, \qquad \kappa = 1 \times 10^{-2}\,\mathrm{m}^2\,\mathrm{Pa}^{-1}\,\mathrm{s}^{-1}. \tag{3.133}$$

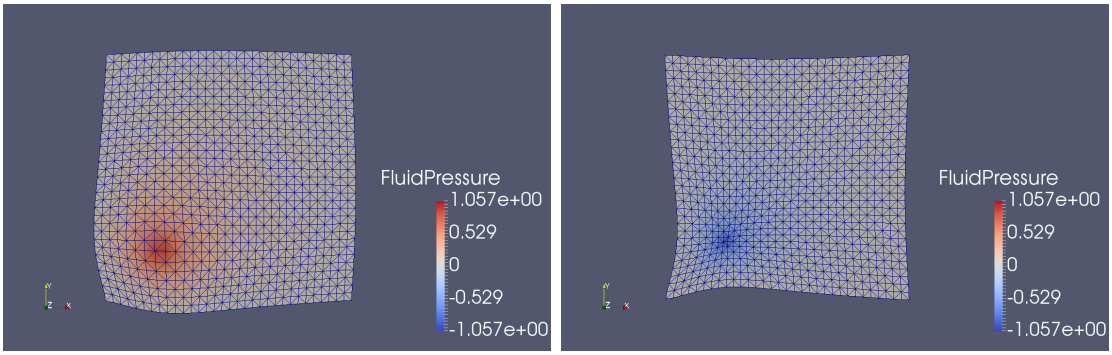

Figure 3.4. The problem of Barry and Mercer: dimensionless fluid pressure computed by the HDG method at time $t^* = \pi/2$ (left) and $t^* = 3\pi/2$ (right), plotted on the deformed meshes. The solid displacement field has not been amplified.

The HDG formulation with $k = 1$ and $p_h|_K \in P^k(K)$ is applied to the dimensionless form of the poro-elastic system (see Appendix B), where characteristic parameters are chosen as follows:

$$x_c = 1\,\mathrm{m}, \qquad u_c = 1\,\mathrm{m}, \qquad p_c = \lambda^e + 2\mu^e, \tag{3.134}$$

$$\sigma_c = 2\mu^e, \qquad v_c = \frac{\kappa p_c}{x_c} = \kappa p_c \cdot 1\,\mathrm{m}^{-1}, \qquad t_c = \frac{u_c}{v_c} = \frac{1}{\kappa p_c} = \frac{1}{\beta}. \tag{3.135}$$

Let $t^* = t/t_c = \beta t$ be the *dimensionless time*. A normalized time step of $\Delta t^* = 0.1\pi/2$ is used for this test case. Figure 3.4 shows the HDG solution obtained for the parameter set (3.133) at two relevant values of t^*. At $t^* = \pi/2$ (left), the source s_f is at a positive maximum; this fluid injection causes an expansion of the poro-elastic medium. At $t^* = 3\pi/2$ (right), the source is at a negative minimum; the fluid is withdrawing and this makes the medium contract.

Figure 3.5 illustrates the effect of element size on the errors of the normalized pressure (top) and displacement (bottom). A smaller step size leads to a reduction in error at most times. The initial overshooting of the errors for the displacement is also reported by Phillips [17]. Taking smaller values for the permeability and the time step, i.e. $\kappa = 1 \times 10^{-6}\,\mathrm{m}^2\,\mathrm{Pa}^{-1}\,\mathrm{s}^{-1}$ and $\Delta t^* = 1 \times 10^{-5}\pi/2$, Phillips and Wheeler [18]

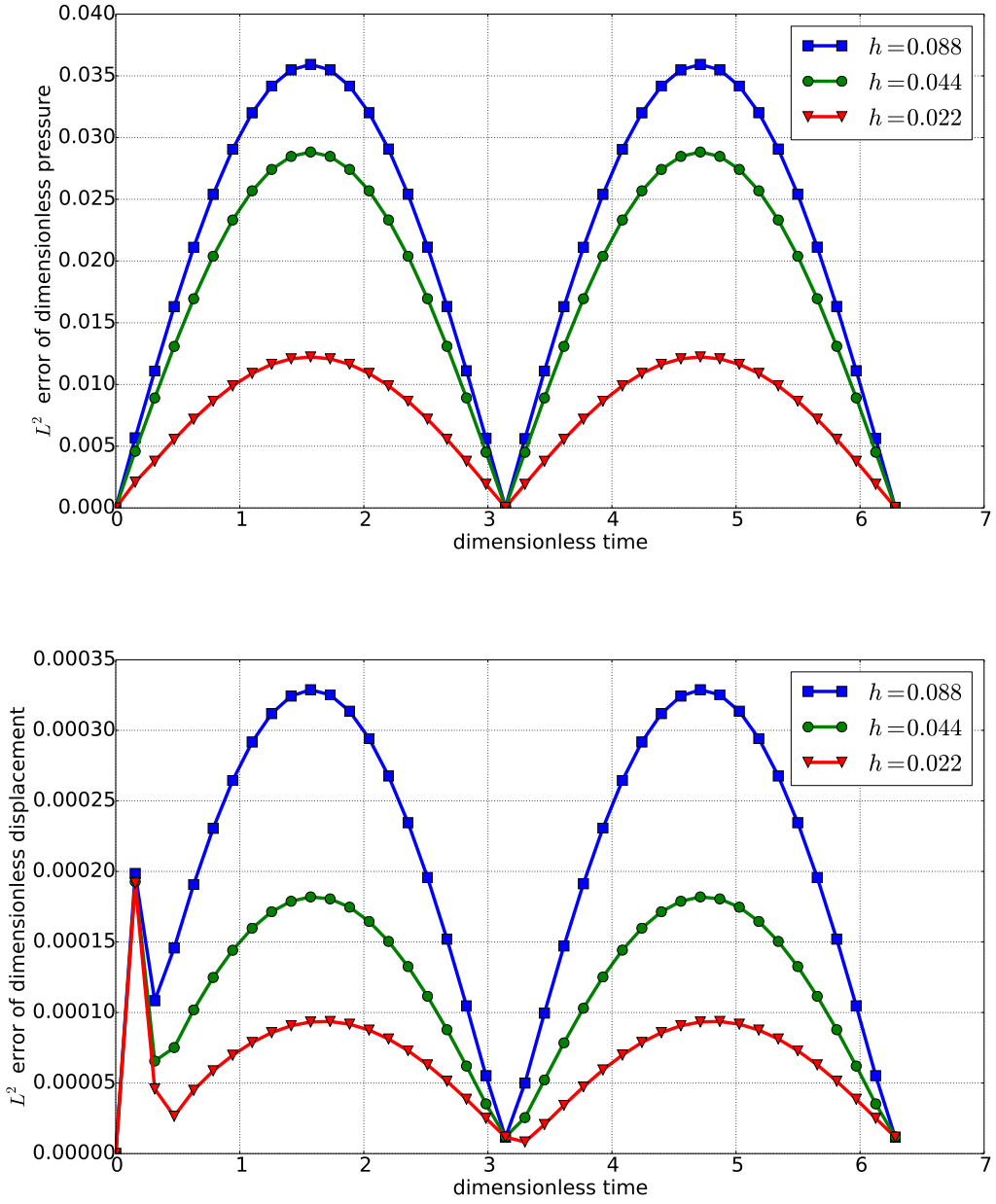

Figure 3.5. HDG errors in Barry and Mercer's problem. The displacement error contains a kink at the initial time step.

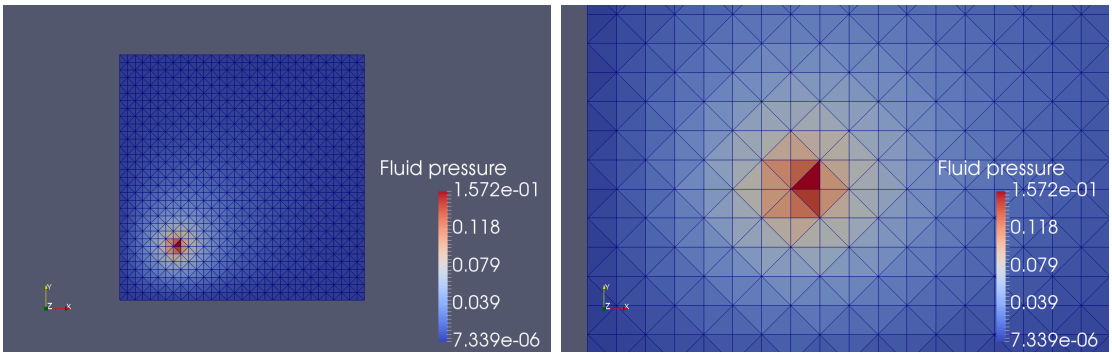

Figure 3.6. Fluid pressure computed by the HDG method at the first time step using the time interval $\Delta t^* = 0.1\pi/2$ and permeability $\kappa = 1 \times 10^{-2}\,\mathrm{m}^2\,\mathrm{Pa}^{-1}\,\mathrm{s}^{-1}$. The solution does not exhibit nonphysical oscillations.

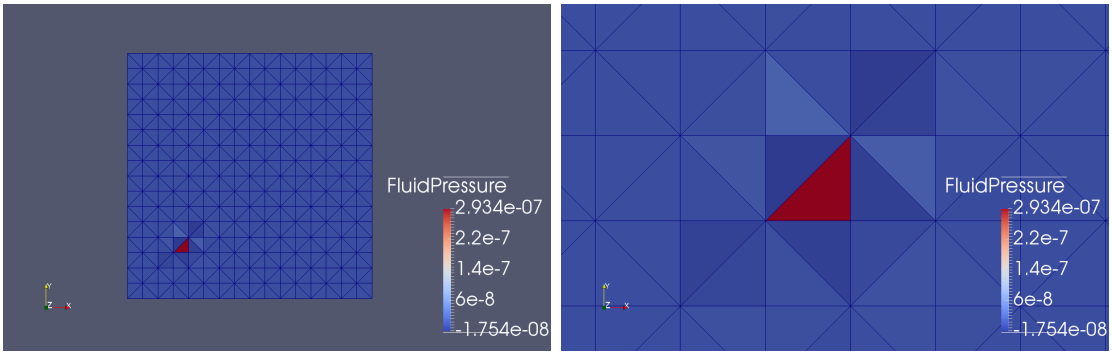

Figure 3.7. Fluid pressure computed by the HDG method at the first time step using a short time interval $\Delta t^* = 1 \times 10^{-5}\pi/2$ and low permeability $\kappa = 1 \times 10^{-6}\,\mathrm{m}^2\,\mathrm{Pa}^{-1}\,\mathrm{s}^{-1}$. Pressure oscillations are suppressed to a very good degree.

show that their numerical scheme using continuous elements for displacement suffers from nonphysical pressure oscillations for the initial time step solution, whereas the one using discontinuous elements suppresses them to a fair degree. Figure 3.7 shows the HDG solution at the initial time step. The average fluid pressure at the red-colored cell, where the fluid source is placed, is 2.934×10^{-7}, whereas for all the other cells the pressure is bounded between -1.754×10^{-8} and 1.691×10^{-8}, more than one order of magnitude smaller. Hence, also the HDG method is able to counter pressure oscillations and combat locking.

Finally, we address the dependence of the HDG solution on the elastic parameters, μ^e and λ^e. At the beginning of this section, we mentioned that the normalized analytic pressure and deformation solutions are independent of $m = 1 + \lambda^e/\mu^e$. Since $1 + \lambda^e/\mu^e = 1/(1 - 2\nu)$, this implies an independence of Poisson's ratio, ν, over its admissible range. To study whether this independence carries over to the HDG method, we consider the parameter set (3.133) and take $\nu = 0.1$ in one case, and $\nu = 0.49$ in the other case. Characteristic parameters are chosen as in (3.134) and (3.135). Figure 3.8 shows that the errors for the normalized pressure are not affected by ν, whereas the errors for the normalized displacement decrease as ν gets bigger.

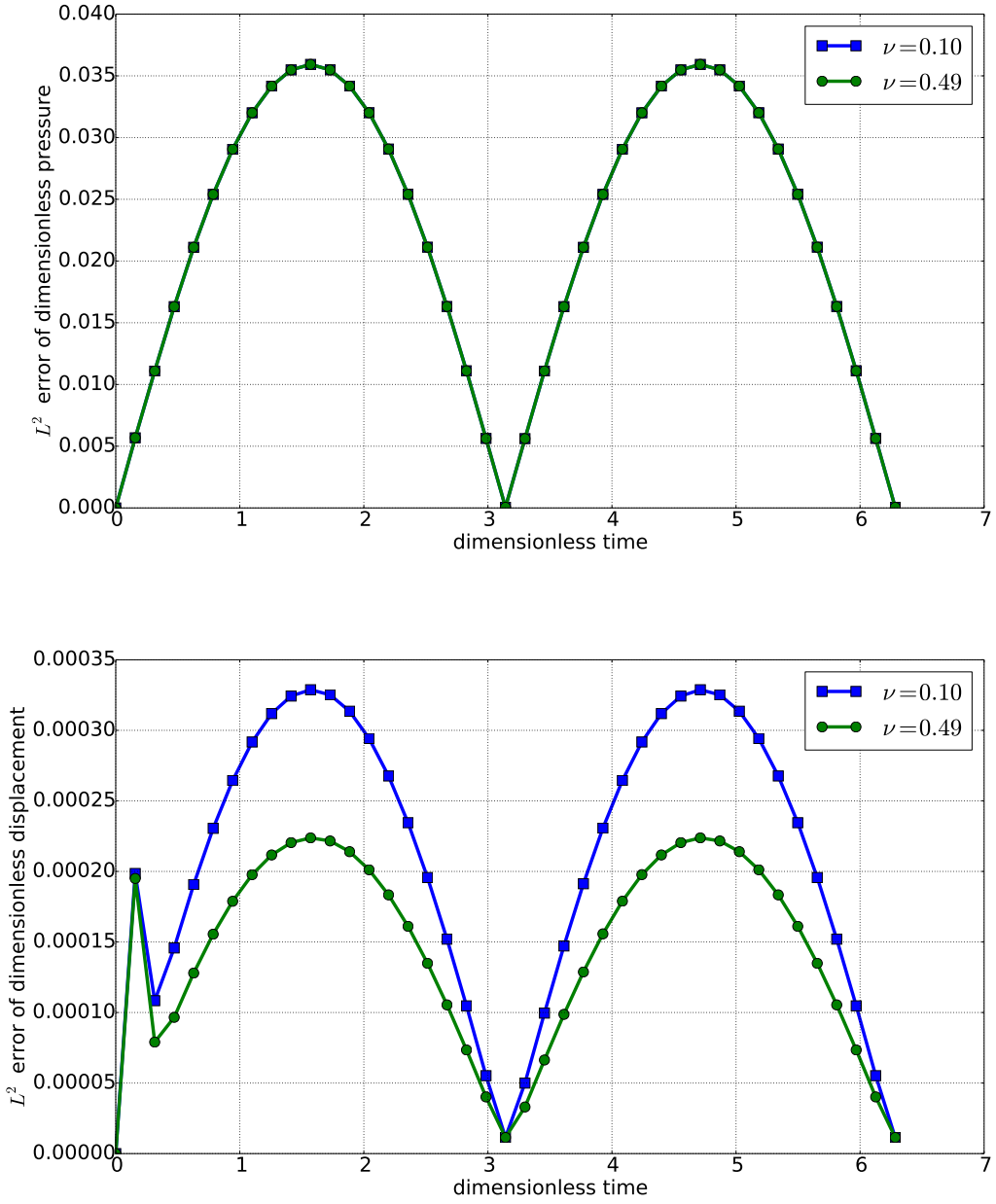

Figure 3.8. Dependence of the HDG solution on the Poisson's ratio in Barry and Mercer's problem.

Table 3.3
Data for the seven meshes used in the 3D experiments.

Mesh	1	2	3	4	5	6	7
Number of tetrahedra	6	48	384	3072	24576	196608	1572864
Number of faces	18	120	864	6528	50688	399360	3170304

3.3.4 Convergence tests in 3D

In this Section, we reproduce the convergence tests provided in Section 3.3.1 in a three-dimensional setting. The main triangulation data are given in Table 3.3. We test for three values of the polynomial degree k, $k = 1, 2, 3$. In each of the four following tests, the formulation with $p_h|_K \in P^{k+1}(K)$, $K \in \Omega_h$, is used. The global HDG system coming from the flux equilibrium conditions (3.119), (3.120) is solved on 64 cores using an iterative method, the restarted Generalized Minimal Residual method (GMRES) [87], preconditioned with the block Jacobi method (with one block per process) [88].

Validation Test Case 1

We consider a stationary linear test case with $\delta = 0$ in (3.44)–(3.48). We take the domain Ω to be the unit cube $[0,1] \times [0,1] \times [0,1]$. Boundary conditions are described in Table 3.4. The coarsest triangulation contains 6 elements. Six nested refinements of this partition are used. We use a constant permeability coefficient $\kappa = \kappa_{\text{ref}} = 1\,\text{m}^2\,\text{Pa}^{-1}\,\text{s}^{-1}$ and choose the data so that the exact solution is

$$\mathbf{u} = U_{\text{ref}} \begin{bmatrix} \sin(\pi x)\cos(\pi y)\sin(\pi z) \\ \cos(\pi x)\sin(\pi y)\cos(\pi z) \\ x^2yz + xy^2z + xyz^2 \end{bmatrix}, \qquad p = P_{\text{ref}} \sin(\pi x)\sin(\pi y)\sin(\pi z),$$

Table 3.4
Boundary conditions in the 3D validation test cases.

Boundary	Boundary Conditions (momentum)	Boundary conditions (mass)
$x = 0, 0 \leq y \leq 1, 0 \leq z \leq 1$	Dirichlet on u_x, u_y, Neumann on $[\underline{\underline{\sigma}}\mathbf{n}]_z$	Dirichlet on p
$x = 1, 0 \leq y \leq 1, 0 \leq z \leq 1$	Dirichlet on u_x, Neumann on $[\underline{\underline{\sigma}}\mathbf{n}]_y, [\underline{\underline{\sigma}}\mathbf{n}]_z$	Neumann on $\mathbf{v}$
$0 < x < 1, y = 0, 0 < z < 1$	Dirichlet on u_y, u_z, Neumann on $[\underline{\underline{\sigma}}\mathbf{n}]_x$	Dirichlet on p
$0 < x < 1, y = 1, 0 < z < 1$	Dirichlet on u_y, Neumann on $[\underline{\underline{\sigma}}\mathbf{n}]_x, [\underline{\underline{\sigma}}\mathbf{n}]_z$	Neumann on $\mathbf{v}$
$0 < x < 1, 0 \leq y \leq 1, z = 0$	Dirichlet on u_x, u_z, Neumann on $[\underline{\underline{\sigma}}\mathbf{n}]_y$	Neumann on $\mathbf{v}$
$0 < x < 1, 0 \leq y \leq 1, z = 1$	Dirichlet on u_z, Neumann on $[\underline{\underline{\sigma}}\mathbf{n}]_x, [\underline{\underline{\sigma}}\mathbf{n}]_y$	Neumann on $\mathbf{v}$

with $U_{\text{ref}} = 1\,\text{m}, P_{\text{ref}} = 1\,\text{Pa}$. We use the formulation with $p_h|_K \in P^{k+1}(K)$, for $K \in \Omega_h$, and test for $k = 1, 2$ on the seven meshes in Table 3.3. Polynomial basis functions of degree $k = 3$ are tested on the first six meshes.

Tables C.20–C.22 confirm the excellent performance of the HDG method we have in the 2D case: the errors achieve optimal convergence rates. As observed before, note that due to the disparity of polynomial degrees for the stress and displacement, optimal convergence of this method yields the same quality of the solution as a post-processed method based on a superconvergent scheme. Unfortunately, most variables suffer from a huge drop or even an inversion in convergence rate on the finest mesh, the average fluid pressure $\bar{p}_h$ being affected the worst (see Tables C.20–C.21 for the cases $k = 1$ and $k = 2$). This issue is not due to the HDG method itself, but rather to the loss of performance of the global solver when the condition number of the global matrix becomes very large as the spatial step size shrinks. Preconditioning strategies other than the block Jacobi approach used here should definitely be investigated.

Validation Test Case 2

Here, we consider a stationary nonlinear test case. We use the same domain and boundary conditions as in test case 1. The finest mesh in Table 3.3 is not included in this analysis. Similarly to the validation test case 2 in 2D, the porosity n and the permeability coefficient κ are allowed to vary according to

$$n = \nabla \cdot \mathbf{u} + 0.5, \qquad \text{with } n \in [n_{\min}, n_{\max}],$$

and the Carman-Kozeny law

$$\kappa(n) = \kappa_{\text{ref}} \frac{n^3}{(1-n)^2}.$$

Table 3.5
Number of fixed point iterations in the nonlinear test case 2 in 3D.

Mesh	$k=1$	$k=2$	$k=3$
1	7	6	6
2	6	6	6
3	6	6	6
4	6	6	6
5	6	6	6
6	6	9	6

We take $n_{\min} = 0.1, n_{\max} = 0.9, \kappa_{\text{ref}} = 1\,\text{m}^2\,\text{Pa}^{-1}\,\text{s}^{-1}$. Data are taken so that the exact solution is

$$\mathbf{u} = U_{\text{ref}} \begin{bmatrix} \sin(\pi x)\cos(\pi y)\sin(\pi z) \\ \cos(\pi x)\sin(\pi y)\cos(\pi z) \\ x^2yz + xy^2z + xyz^2 \end{bmatrix}, \qquad p = P_{\text{ref}} \sin(\pi x)\sin(\pi y)\sin(\pi z),$$

with $U_{\text{ref}} = 0.01\,\text{m}, P_{\text{ref}} = 0.01\,\text{Pa}$. For the fixed point iterations, we use the same stopping criterion as in 2D (3.128). Interestingly, the fixed point algorithm converges very quickly and with a number of iterations independent of the mesh size (see Table 3.5).

Tables C.23–C.25 shows that, similarly to the linear test case, the relative errors are achieving optimal convergence, suggesting that the fixed point algorithm is performing well. On the finest mesh considered in this analysis (mesh number 6), both $e^{\overline{u}}_{h,\text{rel}}$ and $e^{\overline{p}}_{h,\text{rel}}$ show huge losses of convergence rate, $e^{\overline{p}}_{h,\text{rel}}$ being affected the worst.

Validation Test Case 3

Here we consider a time dependent linear test case. We consider problem (3.44)–(3.53) with $\delta = 1$ defined on the unit cube $\Omega = [0,1] \times [0,1] \times [0,1]$ and the time

interval $[0, T]$, with $T = 1\,\mathrm{s}$. with the same boundary conditions as in Table 3.4. A constant permeability coefficient $\kappa = \kappa_{\mathrm{ref}} = 1\,\mathrm{m}^2\,\mathrm{Pa}^{-1}\,\mathrm{s}^{-1}$ is used and data are taken so that the exact solution is

$$\mathbf{u} = U_{\mathrm{ref}} \begin{bmatrix} (\cos(\pi x) + yz)\sin(2\pi t) \\ (\cos(\pi y) + xz)\sin(2\pi t) \\ (\cos(\pi z) + xy)\sin(2\pi t) \end{bmatrix}, \qquad p = P_{\mathrm{ref}} \sin(\pi(x + y + z))\sin(2\pi t),$$

with $U_{\mathrm{ref}} = 1\,\mathrm{m}, P_{\mathrm{ref}} = 1\,\mathrm{Pa}$. We take the five coarsest meshes in Table 3.3 and temporal step sizes $\Delta t = T/r$, with $r \in \{5, 10, 20, 40, 80\}$. Tables C.26–C.28 show the absolute errors. For most combinations of meshes and polynomial degree k, the approximate variables converge to the corresponding exact ones with linear rate with respect to the mesh diameter h, due to the choice of the Backward Euler method as time-advancing scheme, thereby spoiling the convergence property of the HDG method achieved in the stationary test case 1. Interestingly, for $k = 1$, the approximation errors literally explode on the finest mesh (see Table C.26), whereas higher order bases have a stabilization effect on the errors (see Tables C.27–C.28). The degradation of the convergence rates of $e_h^{\sigma}, e_h^{u}, e_h^{\overline{u}}, e_h^{\hat{u}}$ on the finest mesh, for $k = 3$, should be further investigated to understand whether it is due to our particular choice of mesh and time step, or to something else. This behavior resembles the effect of reducing the time step in 2D as it is described in Section 3.3.2 about sensitivity analysis.

Validation Test Case 4

Here we consider a time dependent nonlinear test case. Let us consider problem (3.44)–(3.53) with $\delta = 1$, defined in the same spatial-time domain as in test case 3, with the same boundary conditions as in Table 3.4. The porosity n and the per-

meability coefficient κ are allowed to vary as in test case 2. Data are taken so that the exact solution is

$$\mathbf{u} = U_{\text{ref}} \begin{bmatrix} \cos(\pi x)\sin(2\pi t) \\ \cos(\pi y)\sin(2\pi t) \\ \cos(\pi z)\sin(2\pi t) \end{bmatrix}, \qquad p = P_{\text{ref}} \sin(\pi x)\sin(\pi y)\sin(\pi z)\sin(2\pi t),$$

with $U_{\text{ref}} = 0.01\,\text{m}$ and $P_{\text{ref}} = 0.01\,\text{Pa}$. We take the five coarsest meshes in Table 3.3 and temporal step sizes $\Delta t = T/r$, with $r \in \{5, 10, 20, 40, 80\}$. The polynomial degree k is set to 1, the tolerance ε of the stopping criterion (3.128) and the maximum number of fixed point iterations per time step are set to 1×10^{-9} and 40, respectively. The performance of the fixed point algorithm is summarized in Table 3.6. Observe that no convergence is achieved on the finest mesh for most time iterations, neither if the maximum number of fixed point iterations is increased to 500 (experiment not shown). Table C.29 shows the absolute errors $e_h^{\sigma}, e_h^{u}, e_h^{v}, e_h^{p}, e_h^{\overline{u}}, e_h^{\overline{p}}, e_h^{\hat{u}}$ and $e_h^{\hat{p}}$. Even if convergence rates are far from reaching their asymptotic values, it is clear that the optimal convergence of the HDG method is spoiled by the choice of the Backward Euler method as time-advancing technique. Moreover, the errors blow up on the finest mesh, most probably due to the lack of convergence of the fixed point algorithm. As discussed in previous test cases, this implies that preconditioning and/or alternative nonlinear algorithms might be useful in these situations.

3.3.5 The Sponge's Problem

In order to further motivate the use of the HDG method in poroelastic problems, we test it using an exact three dimensional solution proposed by Kaasschieter and Frijns [89]. This solution has the interesting property of having a clear physical meaning. Consider a cubic sponge with edges of length $2L$ being saturated with water. The origin of the frame of reference is placed in the center of the sponge and the coordinate axes parallel to its edges. It is assumed that the the solid skeleton behaves like a homogeneous isotropic linear elastic material and that the flow of water

Table 3.6
Performance of the fixed point algorithm on test case 4 in 3D for $k = 1$ on the five coarsest meshes shown in Table 3.3.

Mesh	Time iterations	Converging time iterations
1	5	3
2	10	10
3	20	20
4	40	40
5	80	31

through the pores can be described by Darcy's law. Therefore, the set of governing equations is obtained by taking $\delta = 0$ in (3.44)–(3.48). These equations are completed with suitable initial and boundary conditions:

- *Initial conditions*: at time $t = 0$ all unknowns are equal to zero, except for the fluid pressure p that can be taken equal to some arbitrary constant value. In particular, we have

$$(\nabla \cdot \mathbf{u})(\mathbf{x}, 0) = 0. \tag{3.136}$$

- *Boundary conditions*: at $t = 0^+$, an instantaneous compression is applied and water is squeezed out of the pores. After this instantaneous compression, the faces of the sponge are fixed in their compressed position and sealed. Kaasschieter and Frijns [89] show how this experiment can be described analytically. Denoting by $\mathbf{n}, \boldsymbol{\tau}_1$ and $\boldsymbol{\tau}_2$ the outward unit normal vector and the two tangential unit vectors to each face F of the cubic sponge, we obtain the following set of boundary conditions on F:

$$\mathbf{u} \cdot \mathbf{n} = u_0, \tag{3.137}$$

$$\boldsymbol{\tau} \cdot \underline{\underline{\sigma}}_S^E \mathbf{n} = 0, \tag{3.138}$$

$$\mathbf{v} \cdot \mathbf{n} = 0, \tag{3.139}$$

  where $u_0 < 0$ is a given constant value and $\underline{\underline{\sigma}}_S^E$ is the effective stress tensor of the solid phase. Equation (3.138) means that perfect slip applies, whereas, by equation (3.139), an impervious boundary is assumed.

As shown by Kaasschieter and Frijns [89], the solution to this poroelastic problem is given by:

$$\mathbf{u}(\mathbf{x},t) = \frac{u_0}{L}\mathbf{x} + L\sum_{n=1}^{\infty}\gamma_n \sin\left(\frac{n\pi\mathbf{x}}{L}\right)\exp\left(-\frac{n^2\pi^2 t}{C}\right), \tag{3.140}$$

$$\begin{aligned}\underline{\underline{\sigma}}_S^E(\mathbf{x},t) = {} & (2\mu^e + 3\lambda^e)\frac{u_0}{L}\underline{\underline{I}} + 2\mu^e\sum_{n=1}^{\infty}\gamma_n n\pi\exp\left(-\frac{n^2\pi^2 t}{C}\right) \\ & \cdot \operatorname{diag}\left(\cos\left(\frac{n\pi x_1}{L}\right), \cos\left(\frac{n\pi x_2}{L}\right), \cos\left(\frac{n\pi x_3}{L}\right)\right) \\ & + \lambda^e\sum_{n=1}^{\infty}\gamma_n n\pi\sum_{I=1}^{3}\cos\left(\frac{n\pi x_I}{L}\right)\exp\left(-\frac{n^2\pi^2 t}{C}\right)\underline{\underline{I}},\end{aligned} \tag{3.141}$$

$$p(\mathbf{x},t) = (2\mu^e + \lambda^e)\sum_{n=1}^{\infty}\gamma_n n\pi\sum_{I=1}^{3}\cos\left(\frac{n\pi x_I}{L}\right)\exp\left(-\frac{n^2\pi^2 t}{C}\right), \tag{3.142}$$

$$\mathbf{v}(\mathbf{x},t) = L\sum_{n=1}^{\infty}\gamma_n\frac{n^2\pi^2}{C}\sin\left(\frac{n\pi\mathbf{x}}{L}\right)\exp\left(-\frac{n^2\pi^2 t}{C}\right), \tag{3.143}$$

where:

- $\gamma_n = \dfrac{2u_0}{n\pi L}(-1)^n$;
- $C = \dfrac{L^2}{(2\mu^e + \lambda^e)\kappa}$ is a characteristic time; μ^e and λ^e are the smeared elastic parameters, and κ is a constant permeability coefficient;
- $\operatorname{diag}(a,b,c)$ denotes the 3×3 diagonal matrix with the entries a, b, and c on the main diagonal

$$\operatorname{diag}(a,b,c) = \begin{bmatrix} a & 0 & 0 \\ 0 & b & 0 \\ 0 & 0 & c \end{bmatrix}.$$

Since the analytic solution (3.140)–(3.143) involves series, the results in this section are intended only to provide an indication of the agreement between the analytical and numerical solutions. According to equations (3.136), (3.137) and (3.140), the normal component of the solid displacement $\mathbf{u}\cdot\mathbf{n}$ on each face of the sponge is not time-differentiable at $t = 0\,\mathrm{s}$. In order to avoid this discontinuity, numerical simulations are performed in the time interval $[0.005C, C]$, where C is the characteristic time

introduced before. By plotting the analytic solution in this time interval, we observe that it can be very well approximated taking the first 100 terms in the series (3.140)–(3.143). We choose the following parameters

$$L = 1\,\mathrm{m}, \quad u_0 = -0.2\,\mathrm{m}, \quad \mu^e = 1 \times 10^7\,\mathrm{Pa}, \quad \lambda^e = 2 \times 10^8\,\mathrm{Pa}, \quad \kappa = 1\,\mathrm{m}^2\,\mathrm{Pa}^{-1}\,\mathrm{s}^{-1}.$$

The HDG formulation with $k = 1$ and $p_h|_K \in P^{k+1}(K)$ is applied to the dimensionless form of the poro-elastic system (see Appendix B), where characteristic parameters are chosen as follows:

$$x_c = L, \qquad u_c = |u_0|, \qquad p_c = \lambda^e + 2\mu^e, \tag{3.144}$$

$$\sigma_c = 2\mu^e, \qquad v_c = \frac{\kappa p_c}{x_c}, \qquad t_c = C. \tag{3.145}$$

Let $t^* = t/t_C$ be the dimensionless time. A normalized time step of $\Delta t^* = 0.995/100$ and a mesh with 24576 tetrahedra is used for this test case. Figure 3.9 shows the fluid pressure and Darcy velocity computed by the HDG method at the first and last time steps. After the sponge is reduced to a smaller cube by an instantaneous compression, the water in the pores redistribute to a stationary situation characterized by $\mathbf{v} = \mathbf{0}$ and $p = 0$.

Figure 3.10 illustrates the effect of element size on the errors of some normalized variables: total stress, solid displacement, Darcy velocity, and fluid pressure. A smaller step size leads to a reduction in error at most times.

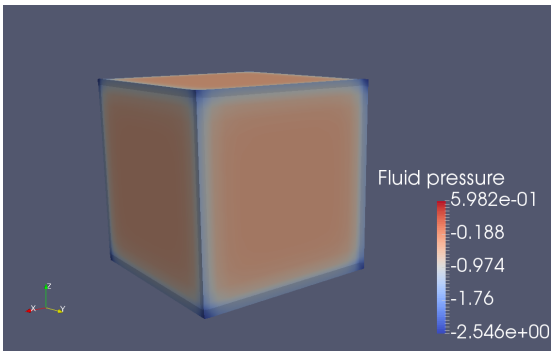

(a) Fluid pressure at $t^* = 0.005 + \Delta t^*$.

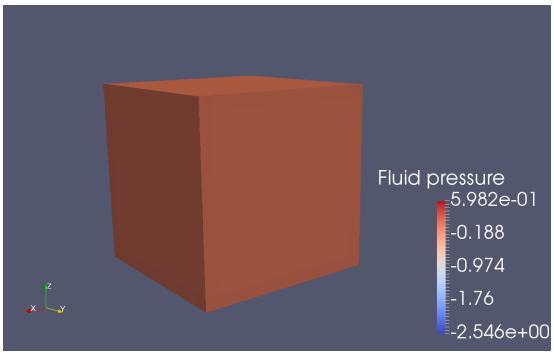

(b) Fluid pressure at $t^* = 1$.

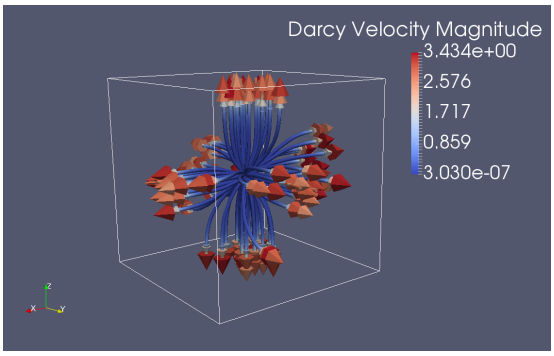

(c) Darcy velocity at $t^* = 0.005 + \Delta t^*$.

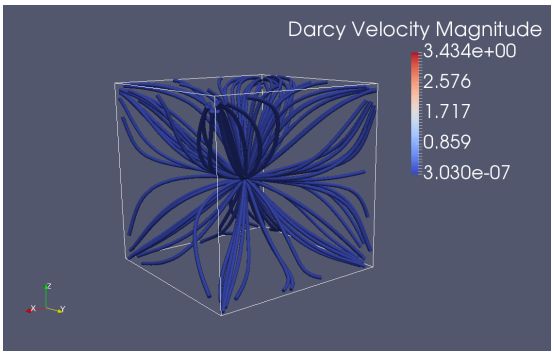

(d) Darcy velocity at $t^* = 1$.

Figure 3.9. The sponge problem: dimensionless fluid pressure and dimensionless Darcy velocity computed by the HDG method at the first and last time steps, i.e. $t^* = 0.005 + \Delta t^*$ and $t^* = 1$, respectively. In Figures 3.9(c) and 3.9(d), the Darcy velocity is characterized with streamlines, colored with the magnitude of the vector field. The streamlines are augmented with little pointers. The pointers face in the direction of the velocity, and their size is proportional to the magnitude of the velocity.

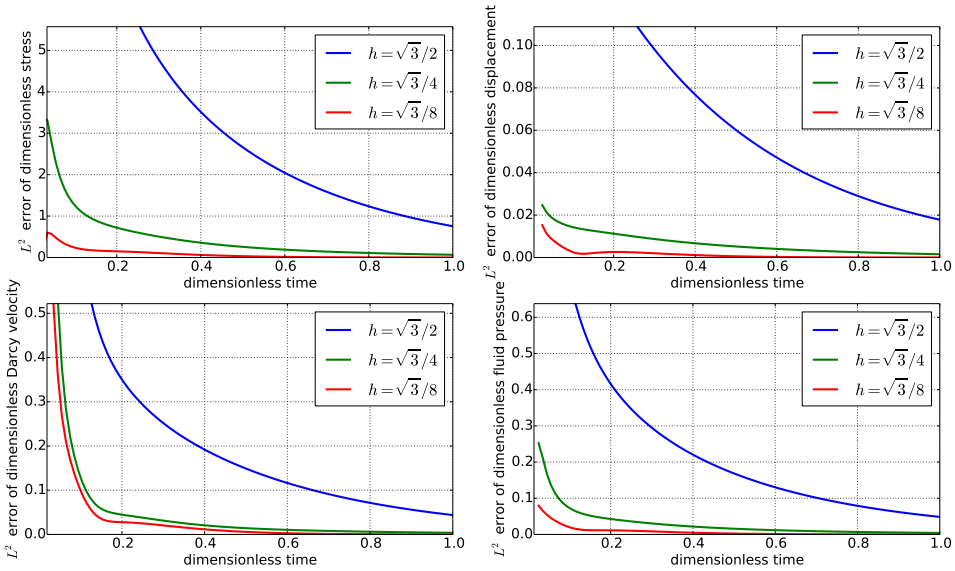

Figure 3.10. Effect of element size on the error of the HDG solution: (top-left) total stress; (top-right) solid displacement; (bottom-left) Darcy velocity; (bottom-right) fluid pressure. The element sizes $h = \sqrt{3}/2, \sqrt{3}/4$, and $\sqrt{3}/8$ correspond to a mesh with $384, 3072$, and 24576 tetrahedra, respectively.

4. MATHEMATICAL MODELING OF THE OPTIC NERVE HEAD PERFUSION

Glaucoma is an optic neuropathy characterized by progressive death of RGCs and irreversible visual loss. Glaucoma is the second leading cause of blindness worldwide [2], and yet its etiology and treatment remain unclear. The main modifiable risk factor in glaucoma patients is elevated IOP [3–7]; however, a high percentage of individuals with elevated IOP (a condition called ocular hypertension) never develop glaucoma [8], and many glaucoma patients continue to experience disease progression despite lowering IOP to target levels or have no history of elevated IOP - a condition called normal tension glaucoma [9].

Several studies suggest correlations between impaired ocular blood flow and glaucoma [90–96]. In healthy conditions, vascular beds exhibit an intrinsic ability to maintain relatively constant blood flow over a large range of arterial pressures. This *autoregulatory* behavior is recognized in most vascular beds - including the eye [97,98], brain [99], heart [100], kidney [101], skeletal muscle [102], and gut [103] - but the effectiveness of autoregulation differs among these vascular beds according to importance of function. For example, the brain and kidney receive stable flow over a range of arterial pressure [99, 104] whereas autoregulation in other beds such as the gut is less effective. In the eye, the retinal and ONH vascular beds are known to exhibit autoregulation, though to differing extents [1]. Details and experimental measures of autoregulation are better established in the retina than in the ONH. In experiments assessing hemodynamic responses to light stimulation [105–108], blood flow in the retina and ONH seems to be highly correlated to increased neural activity. This phenomenon is called *neurovascular coupling* [109].

In glaucoma the location of damage to nerve cells is hypothesized to be predominantly in the ONH [11], and thus a clearer understanding of the factors affecting the blood supply to the ONH is necessary to determine how this may be compromised and potentially contribute to the pathophysiology of glaucoma. In this chapter, we first describe the complex anatomy and vascular supply of the ONH, laying down the anatomical foundations of our modeling efforts to describe the perfusion of the lamina cribrosa in the ONH. In the second part of the chapter, we use modeling and numerical approaches described in Chapters 2 and 3 to theoretically investigate the influence of viscoelasticity on the mechanics and hemodynamics of the lamina cribrosa.

4.1 Anatomy and Vascular Supply of the ONH

4.1.1 Anatomy

The ONH is where RGC axons leave the eye through the scleral portion of the neural canal, forming bundles separated by astrocytes, a particular type of glial cell [110]. For the purpose of description, the anatomy and vascular supply of the ONH is best divided into 4 regions, from anterior to posterior segments (see Figure 4.1).

The most anterior part of the ONH is the *superficial nerve fiber layer* (SNFL). Some vascular details of this layer can be resolved on ophthalmoscopy examination or angiography. A part of the appearance of the SNFL comes from light back-scattered from deeper tissue [111]. Immediately behind the SNFL is the *prelaminar region*, which lies adjacent to the peripapillary choroid. Posterior to the prelaminar region, the *laminar region* is composed of the lamina cribrosa, a structure consisting of fenestrated connective tissue beams through which the RGC axons pass on their path from the retina to the optic nerve. Finally, the *retrolaminar region* lies posterior to the lamina cribrosa. It is marked by the beginning of axonal myelination and is surrounded by meninges.

The lamina cribrosa bears the translaminar pressure difference: the difference between the IOP, which is the pressure in the intraocular space, and the retrolaminar

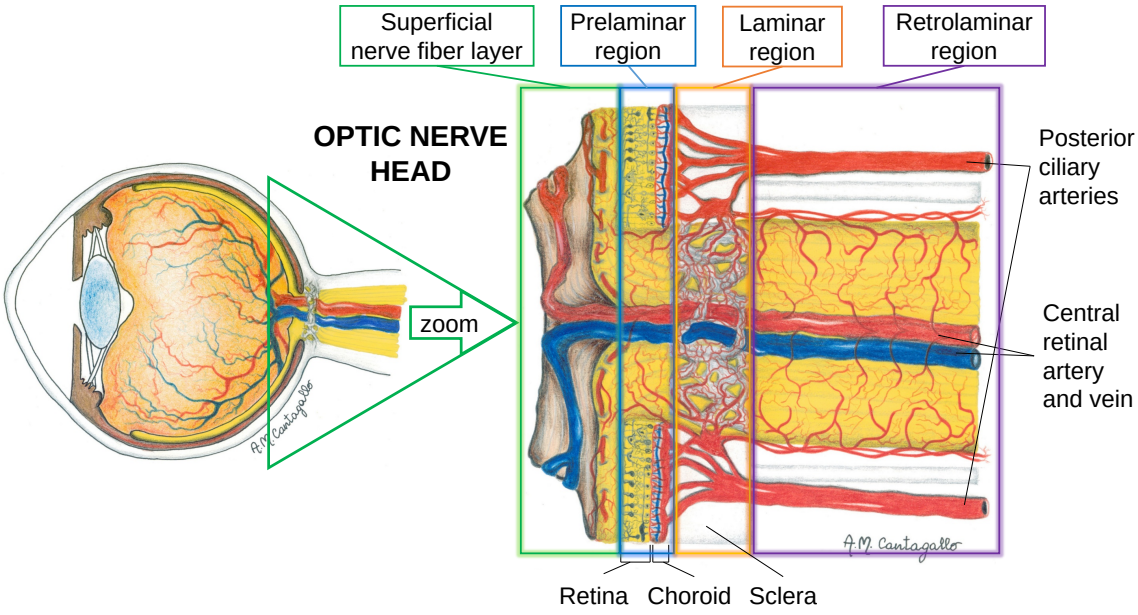

Figure 4.1. Anatomy and vascular supply of the optic nerve head (ONH). The ONH includes the superficial nerve fiber layer, the prelaminar region, the laminar region, and the retrolaminar region [1].

tissue pressure (RLTp), which is the pressure in the retrolaminar region. The RLTp is usually lower than the IOP and is strongly correlated to the cerebrospinal fluid pressure and the pressure in the subarachnoid space of the optic nerve when cerebrospinal fluid pressure $> 2\,\mathrm{mmHg}$ ($1\,\mathrm{mmHg} \approx 133.3224\,\mathrm{Pa}$) [112, 113]. A hoop stress is also transferred to the lamina by the sclera [110]. There is evidence that an annulus of collagen fibrils exists around the scleral canal in the peripapillary sclera. These fibrils appear to be oriented mostly radially in the periphery of the lamina [114–116]. The peripapillary annulus significantly reduces the IOP-related expansion of the scleral canal and shields the lamina from high-tensile stress. The radially oriented fibrils in the lamina periphery reinforce the lamina against transverse shear stresses and reduce laminar bending deformations [114]. The lamina cribrosa remodels into a thicker, more posterior structure, which incorporates more connective tissue after chronic IOP elevation [75, 115].

In the prelaminar, laminar, and retrolaminar regions, RGC axons are surrounded by astrocytes, which are believed to maintain the homeostasis of the extracellular environment. In particular, astrocytes remove potassium and glutamate from the extracellular space, provide cellular support to the axons, and synthesize extracellular matrix macromolecules [110, 117]. In the prelaminar and retrolaminar region, it is presumed that nutrient delivery to the axons occurs both via diffusion and advection [110]. In the laminar region, the extracellular matrix of laminar beams lies in between capillaries and astrocytes. Consequently, nutrients likely diffuse from laminar capillaries, across the endothelial and pericyte basement membranes, through the extracellular matrix of the laminar beams, across the basement membranes of astrocytes. From there, they may go into the astrocytes or percolate in the extracellular space between them, ultimately reaching the adjacent axons.

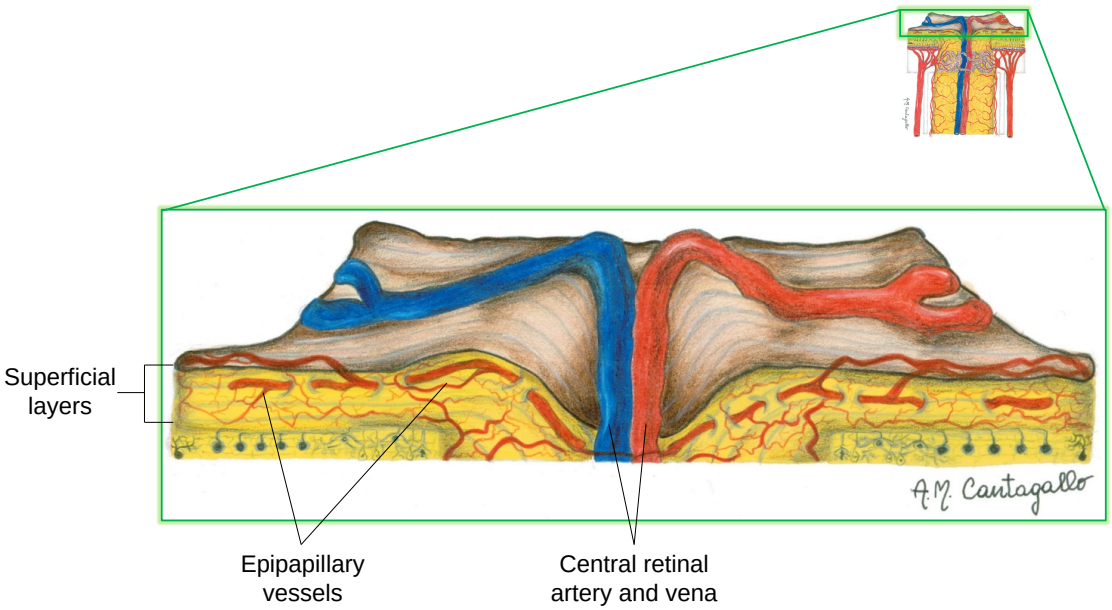

Figure 4.2. Superficial nerve fiber layer (SNFL). The SNFL receives oxygenated blood primarily from retinal arterioles. These small vessels, called epipapillary vessels, originate in the peripapillary SNFL and run toward the center of the ONH [1].

4.1.2 Vascular Supply

The vascular system nourishing the ONH is quite complex [118, 119] and shows high inter-individual and intra-individual variability [120–122]. A critical anatomic distinction between the different portions of the ONH is that blood flow to the ONH is primarily supplied by the posterior ciliary arteries (PCAs), whereas the SNFL receives oxygenated blood primarily from retinal arterioles [123]. These small vessels, called *epillary vessels*, originate in the peripapillary SNFL and run toward the center of the ONH (see Figure 4.2).

In approximately 30% of all people, a cilioretinal artery may be present and supply the temporal SNFL. This artery, if present, may be a direct branch of the ciliary or

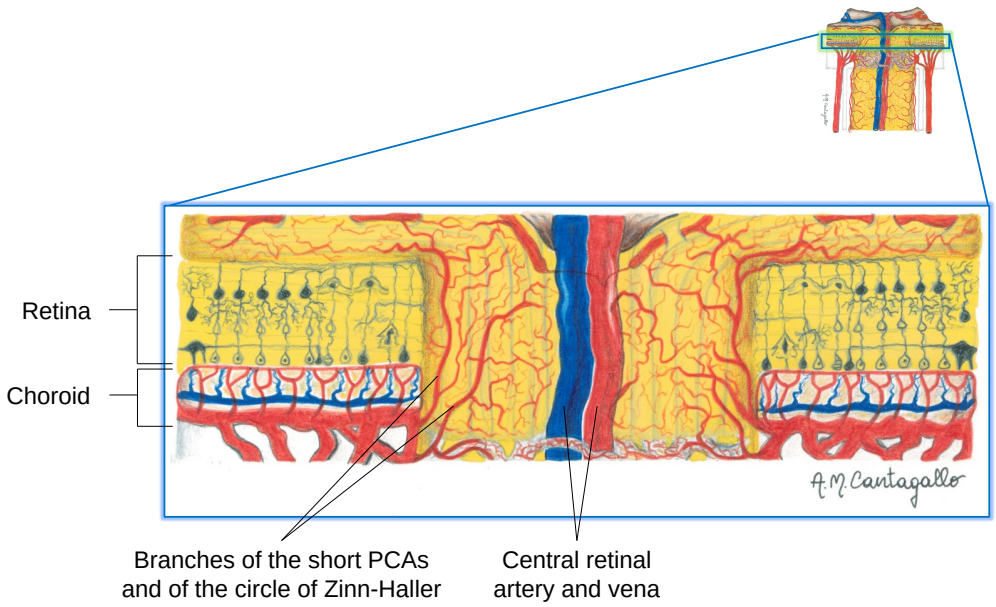

Figure 4.3. Prelaminar region. The prelaminar region is mainly supplied by direct branches of the short posterior ciliary arteries (PCAs) and by branches of the circle of Zinn-Haller. The circle of Zinn-Haller, if present, is a complete or incomplete ring of arterioles within the perineural sclera formed by the confluence of branches of the short PCAs [1].

choroidal arteries, emerging from the temporal SNFL of the ONH and extending laterally along the papillomacular bundle. The retinal arteries and the cilioretinal arteries lack anastomotic blood exchange in the case of an artery occlusion, leading to an ischemic infarct in the area supplied by the artery or its branches [124].

The prelaminar region is mainly supplied by direct branches of the short PCAs and by branches from the circle of Zinn-Haller (see Figure 4.3).

The circle of Zinn-Haller, if present, is a complete or incomplete ring of arterioles within the perineural sclera formed by the confluence of branches of the short PCAs. The arterial circle branches into the prelaminar region, lamina cribrosa, and retrolaminar pial system and supplies the peripapillary choroid. This vascular ring

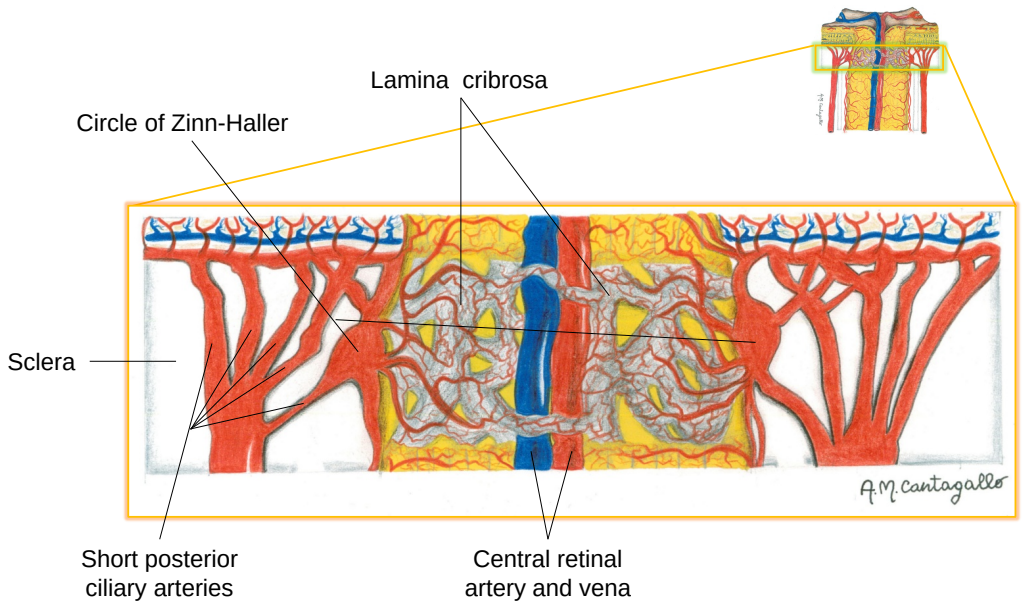

Figure 4.4. Laminar region. Blood flow to the laminar region is provided by centripetal branches of the short PCAs. The centripetal branches arise either directly from the short PCAs or from the circle of Zinn-Haller. The lamina cribrosa is shown as a 3D network, as suggested in recent *in vivo* imaging studies based on optical coherence tomography (OCT) [127–130], and in finite element modeling studies [115,131,132] of the lamina cribrosa microarchitecture [1].

can be recognized *in vivo* using indocynanine green videoangiography in highly myopic eyes [125]. These vessels exhibit an anastomotic blood exchange [126], but it is unclear whether this exchange can counterbalance an insufficiency of a single PCA. There is also evidence of direct arterial supply to the prelaminar layer arising from the choroidal vasculature [119], even though the extent to which it contributes to the perfusion of the region is still a matter of debate [118]. Blood flow to the laminar region is provided by centripetal branches of the short PCAs (see Figure 4.4).

Such a 3D architecture differs from, without effectively denying, what is proposed in some histology studies, where the lamina is viewed as a set of stacked perforated

sheets containing vessels, with pores in each sheet aligned to create tunnel for bundles of nerve fibers to exit from the eye [133,134]. Unlike *in vivo* imaging, histology imaging suffers from distortions because of the loss of pressure (IOP, intracranial pressure, and blood pressure), distortions during tissue preparation, and tissue degradation after death. Nevertheless, care is needed when comparing optical coherence tomography (OCT) results to histology because of differences in optical resolution and sampling density. OCT has significantly worse lateral resolution when compared with electron microscopy or other forms of microscopy used to study the lamina cribrosa, and it likely overemphasizes beams, compared to histology [130]. Hence, many questions still need to be answered to characterize the 3D geometry of the lamina cribrosa accurately [135].

The centripetal branches arise either directly from the short PCAs or from the circle of Zinn-Haller. These precapillary branches perforate the outer boundary of the lamina and then branch into an intraseptal capillary network, which runs inside the laminar beams. It is still unclear whether there are anastomoses between the capillary or precapillary bed of the laminar region, the prelaminar region, and the SNFL region. If these anastomoses exist, it is unclear whether they play a role when a sudden (or slowly progressive) vascular occlusion on the precapillary or intracapillary level happens [124]. The retrolaminar region is supplied by the central retinal artery (CRA) and the pial system (see Figure 4.5). The pial system is an anastomosing network of capillaries located immediately within the pia mater. The pial system originates from the circle of Zinn-Haller and may also be fed directly by the short PCAs. The branches of the pial system extend centripetally to nourish the axons of the optic nerve. The CRA may supply several small intraneural branches in the retrolaminar region. Some of these branches may also anastomose with the pial system.

In the ONH the capillaries form a continuous network throughout its entire length, being continuous posteriorly with those in the rest of the optic nerve and anteriorly with the adjacent retinal capillaries [133, 136]. It is unclear whether this implies that

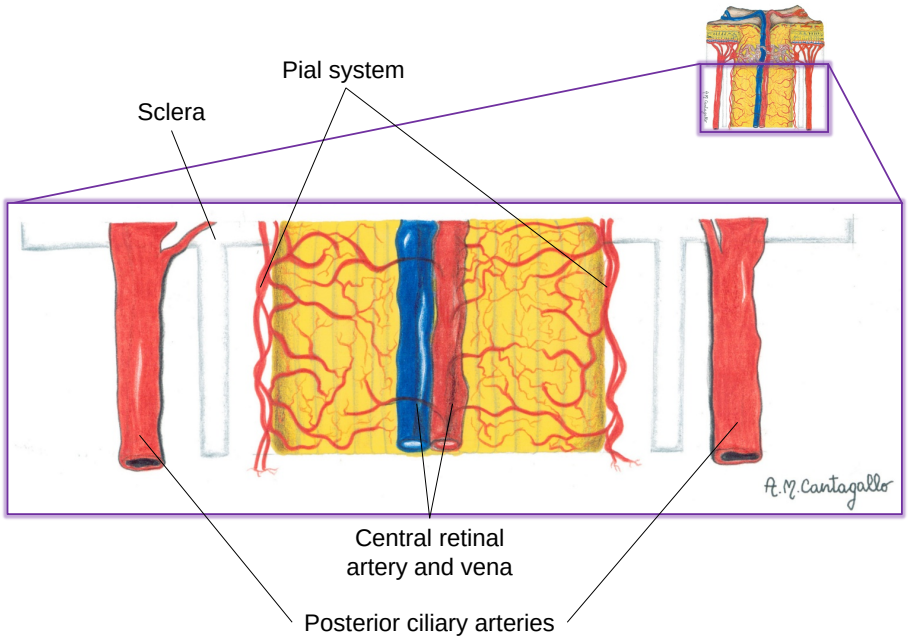

Figure 4.5. Retrolaminar region. The retrolaminar region is supplied by the central retinal artery (CRA) and the pial system. The pial system is an anastomosing network of capillaries located immediately within the pia mater [1].

blood flow regulation is similar [136] or not [119] in both vascular regions, independent of the arterial source.

Critical questions remain unanswered. The CRA within the intraorbital optic nerve is innervated, but innervation stops (at least) anterior to the lamina cribrosa, and it does not follow the branches of the CRA inside the eye [137]. Neurotransmitter receptors, however, are present on the surface of retinal vessels [138,139]. In addition, normal retinal vessels lack fenestrations [124]. Hence, vasoactive hormones cannot leak from capillaries and reach the muscular coat of nearby arterioles where they can influence blood flow. The branches of the PCA that feed the intrascleral portion of the optic nerve may or may not be innervated and/or fenestrated. Such knowledge is crucial to understand how blood flow is regulated in the ONH.

Venous drainage of the ONH occurs primarily through the central retinal vein (CRV). In the SNFL, blood is drained directly into the retinal veins, which then join to form the CRV. In the prelaminar, laminar, and retrolaminar regions, venous drainage occurs via the CRV or axial tributaries to the CRV.

4.2 Techniques for *In Vivo* Studies of ONH Hemodynamics

As described in Section 4.1, the complex vasculature of the ONH is comprised of small diameter vessels arranged in an intricate 3D geometry. At present, no technology allows a noninvasive measurement of volumetric blood flow in absolute units; however, some hemodynamic measurement techniques provide surrogates for ONH blood flow in arbitrary units. Four of these measurement techniques for *in vivo* studies of ONH hemodynamics are discussed and compared in the following sections. Table 4.1 summarizes their main features, advantages, and limitations.

4.2.1 Laser Doppler Flowmetry

Laser Doppler flowmetry (LDF) is a noninvasive method of assessing blood flow and perfusion in the ONH. LDF is based on the Doppler effect. It measures the shift

Table 4.1
Techniques for *in vivo* studies of ONH hemodynamics

Technique	Measurements	Location of mesurement	Advantages	Limitations
Laser Doppler flowmetry	Velocity, volume, and flow in arbitrary units	ONH	Multiple hemodynamic parameters	No absolute measurements; no interindividual comparisons
OCT angiography	Flow in arbitrary units	ONH	High quality images, fast	No absolute measurements; difficult to localize measurements
Doppler Color imaging	Velocity	Ophthalmic artery, CRA, and short PCAs	Vessel selective, no need for pupil dilation, clear media, or fixation	No absolute measurements; velocity measurements only; expert operator required
Laser speckle flowgraphy	Velocity, flow in arbitrary units	ONH	Time evolution of velocity at the same site of the same eye	No absolute measurements; no interindividual comparisons

in frequency that occurs when light is scattered by the red blood cells moving through capillaries. LDF uses a fundus camera and a computer system to detect these changes in frequency. This information is used to calculate three hemodynamic parameters: velocity, blood volume, and blood flow within the ONH. Velocity is defined as the average speed of red blood cells traveling through capillaries and is proportional to the mean change in Doppler shift frequency. Blood volume is defined as the number of red blood cells in the given sample. Blood flow or flux is defined as the flux of red blood cells through a specific part of a capillary at a given time. The main advantage of LDF is its ability to measure three different hemodynamic parameters; however, LDF only provides measurements of blood perfusion in arbitrary (and not absolute) units, which limits its usefulness in a clinical setting [140]. Moreover, LDF measurements depend significantly on the depth of the sampled tissue. This depth determines the relative contribution to the Doppler signal of the superficial layers, the layers supplied by the CRA, and the deeper layers supplied by the short PCAs. Blood flow autoregulation may or may not differ within these vascular beds. In a study on monkey eyes, LDF appeared to be more heavily influenced by blood flow changes in the more superficial layers of the ONH than in deeper ones, but to what extent remains uncertain [141].

4.2.2 OCT Angiography

OCT angiography, a combination of high speed OCT and a new 3D angiography system called split-spectrum amplitude-decorrelation angiography, is a noninvasive method used to estimate blood flow in the ONH, especially within the microcirculation [142]. It computes the flow index, which is a surrogate for blood flow in arbitrary units.

OCT is a technique that takes cross-sectional images of a biologic tissue using a low-coherence interferometer. These cross-section images are captured using a low-coherence beam directed at the target tissue. The light signals reflect off of the

tissue back to the interferometer, which stacks a series of longitudinal tomographic b-scans to derive a three dimensional image. Doppler OCT, a commonly used subtype of OCT, can detect the Doppler frequency shift of the reflected light, providing additional information on blood flow. The split-spectrum amplitude-decorrelation angiography algorithm allows three dimensional angiography to be done four times faster than previous algorithms and also improves blood flow detection, creates better visualization of the microvasculature, and removes motion errors automatically [143].

OCT angiography has many advantages over Doppler OCT. Doppler OCT can only quantify blood flow in large superficial vessels of the ONH and cannot visualize the microvasculature [143]. OCT angiography minimizes the pulsatory bulk motion noise along the axial direction and optimizes flow detection along the transverse direction [142]. As with all measuring techniques, OCT angiography has limitations. One of the main disadvantages is that blood flow from superficial layers can be projected to deeper layers, thereby incorrectly indicating that the imaged blood flow is a few layers deeper than its location *in vivo* [142]. Also, split-spectrum amplitude-decorrelation angiography cannot distinguish between perfusion defects caused by damaged tissue or ischemia [144], and ONH blood flow estimates are provided in arbitrary units. Despite these limitations, OCT angiography is a very useful tool to measure blood flow in the ONH.

4.2.3 Color Doppler Imaging

Color Doppler imaging (CDI), also known as color Doppler ultrasound, is a noninvasive procedure that allows the user to visualize a color-coded image of blood velocity against a gray-scale image of the surrounding structures. This technique uses the principle of Doppler frequency shift to measure blood flow velocity in absolute units. Various transducers are used to measure the Doppler frequency shift, which produces color pixels [145]. The color red represents blood flowing toward the ultrasound probe, whereas blue represents blood flowing away from the probe [146]. CDI is most com-

monly used to measure the peak systolic velocity (PSV) and end diastolic velocity (EDV), which are then used to measure the resistive index (RI = (PSV − EDV)/PSV) and pulsatility index (PI = (PSV − EDV)/$T_{\max}$, where $T_{\max}$ is the time averaged peak velocity). These values estimate resistance to blood flow caused by the microvasculature distal to the site of measurement. The RI is particularly suitable for investigating the low resistance retrobulbar vasculature [145]. The major advantages of CDI are that it is noninvasive, vessel selective, reproducible, and does not require pupil dilation, clear media, or fixation. CDI is limited in its ability to measure only velocity (not flow) and calculate vascular resistance and requires an experienced operator to obtain accurate results [147]. CDI has particular difficulty in imaging and interpreting small vessels, and the PCAs are close to the size limit that can be studied.

4.2.4 Laser Speckle Flowgraphy

Laser speckle flowgraphy (LSFG) is a noninvasive method of measuring blood flow and velocity in the ONH. LSFG measures blood flow by using the laser speckle phenomenon, which is an interference event that occurs when laser light scatters off of a diffusing tissue. This creates a speckle pattern that varies in proportion to the velocity of red blood cells and thus represents capillary blood flow. The faster the velocity of the red blood cells, the greater the rate of pattern variation. Although the velocity cannot be measured directly, the normalized blur and square blur ratio values can be calculated as quantitative indicators of blood velocity. Normalized blur values are well correlated with blood flow measurements simultaneously taken with the hydrogen gas clearance method, colored microspheres technique, and other methods in the ONH, iris, choroid, and retina [148–155]. The distribution of blood flow can be displayed in a two dimensional color-coded map, which reflects the time variation of the speckles at each pixel point [156]. This allows for visualization of blood flow in real time.

LSFG uses a diode laser, image sensor, infrared charge-coupled device camera, and digital charge-coupled device camera. The diode laser and image sensor are used for laser speckle measurements. The laser is focused on the image sensor and creates a speckle pattern, which is scanned at 512 scans/second [156]. The digital charge-coupled device camera measures vessel diameter and takes pictures of the fundus.

The advantages of LSFG are that its results are adequately reproducible and that the change in velocity at the same site of the same eye can be followed over time. A major disadvantage of LSFG is that the meaning of its measurement is not clearly understood and does not allow for intereye or interindividual comparisons [147].

4.3 Mathematical Modeling of ONH Mechanics and Hemodynamics

Despite significant recent advances in the understanding of ONH blood flow and the techniques to study it, important questions still remain unanswered concerning the identification of the geometrical, material and fluid dynamical parameters that have the strongest influence on the blood supply to the ONH and how these may be compromised and potentially contribute to the pathophysiology of glaucoma.

The quest for answers to these questions is hindered by limitations in both the technological and scientific tools currently available to the community. Major limitations in the current technologies for ONH measurements include the fact that LDF, LSFG, and OCT angiography only provide ONH blood flow estimates in arbitrary units and intereye comparison is problematic. LDF appears to be mainly influenced by blood flow changes in the more superficial layers of the ONH than deeper ones, but to what extent remains uncertain. OCT angiography provides measurements for the ONH deeper layers which may contain spurious projections from the superficial layers. In addition to the difficulties related to structural and functional imaging of the ONH, there are scientific challenges in designing experimental and clinical studies capable of disentangling the complex interplay between chemical, mechanical, and hemodynamic factors that contribute to the pathogenesis of optic neuropathies.

Given these challenges, mathematical modeling provides a unique tool that can play a significant role in advancing the understanding of ONH physiology in health and disease. A mathematical model can serve as a virtual laboratory where the influence of each factor acting on the system can be singled out and investigated, from a theoretical viewpoint, in isolation or in relation with other factors. In the following, we review the main contributions to the modeling of the biomechanics and perfusion in the ONH. Finally, we show how the models and numerical approaches discussed in Chapters 2 and 3 can be used to investigate the mechanics and hemodynamics of the lamina cribrosa in the ONH. In particular, we will investigate how changes in lamina viscoelasticity may compromise lamina perfusion in response to sudden variations of IOP, possibly leading to disc hemorrhages.

4.3.1 Mechanics of the ONH

Alterations in the ONH biomechanical response to changes in IOP have been identified as a major factor in the pathogenesis of glaucoma [110, 157]. Particular attention has been devoted to the mathematical description of the mechanical stresses and strains arising within the lamina cribrosa, which is thought to be a primary site of axonal injury in glaucoma [11]. A linear model of elastic mechanics theory on the bending of thin circular plate was developed for the lamina cribrosa [158]. Such an idealization allowed quantitative estimates to be obtained of the extent to which the degree of fixity offered by the connection with the sclera, the pretension caused by scleral expansion, and the ratio between flexural and in-plane stiffness influence the mechanical response of the lamina cribrosa to IOP. An idealized, analytical microstructural model of the ONH load bearing tissues based on an octagonal cellular solid description of the porosity within the lamina identified the material and geometrical properties of the sclera as major determinants in the strain distributions within the lamina [159]. The analysis also showed that much larger strains are developed perpendicular to the major axis of an elliptical canal rather than in a circular canal.

Eye-specific finite element models based on experimentally reconstructed geometries have been used recently [115, 160, 161]. These models are used to study in depth influences of geometry and material properties of the ONH to changes in IOP and to investigate growth and remodeling mechanisms in glaucoma, including adaptation of tissue anisotropy, tissue thickening/thinning, tissue elongation/shortening, and tissue migration. Macro- and micro-scale strains are proposed as potential control mechanisms governing mechanical homeostasis [75, 114, 162–164]. Further development of these sophisticated finite element models may benefit from the recent advances in OCT imaging aimed at providing a more accurate characterization of the architectural microstructure within the lamina cribrosa [135].

4.3.2 Hemodynamics of the ONH

Perfusion of the ONH results from the complex interplay between blood pressure, which provides the driving force for the blood through the vasculature, *mechanical stress*, which acts as external forces on the vessels, and *vascular regulation*, which mediates vessel dilation/constriction to compensate for changes in the system. Using idealized networks to describe the vasculature nourishing the lamina cribrosa in the ONH (see Figure 4.4), Girard et al. found that the lamina hemodynamics and oxygen concentration is influenced by the shape of the lamina and the blood pressure in the circle of Zinn-Haller and in the CRV [165].

To the best of our knowledge, only the model by Causin et al. [74] combines mechanics and hemodynamics in the lamina cribrosa. In this model, which is the first novel contribution of this thesis, the lamina cribrosa is treated as a two dimensional poroelastic material, where blood vessels are viewed as isotropically distributed pores in a solid matrix comprising collagen, elastin, extracellular matrix and neural tissue (see Figure 4.6). The presence of blood vessels in the tissue defines a vascular porosity n that changes with the local state of stress and strain. The vascular permeability,

which defines the ability of the porous material to allow fluid passing through it, is described by an isotropic tensor $\underline{\underline{K}}$ that depends on n

$$\underline{\underline{K}} = \underline{\underline{K}}(n) = \kappa(n)\underline{\underline{I}}. \tag{4.1}$$

Using Poiseuille's law to model the blood flow within a capillary, we derive the following constitutive relationship for κ

$$\kappa = \kappa(n) = \frac{\beta}{8\mu_b} n^2, \tag{4.2}$$

where β is a constant depending on the geometry of the lamina and μ_b is the dynamic viscosity of blood. Equation (4.2) can be obtained as follows. In view of Poiseuille's law, the velocity v of blood moving through a cylindrical capillary of radius R_c and length L_c is

$$v = \frac{1}{4\mu_b}(R_c^2 - r^2)\frac{\Delta p}{L_c}, \tag{4.3}$$

where r is the distance from the center of the capillary and Δp is the blood pressure drop across the capillary. From (4.3), the average velocity on the capillary cross-section is given by

$$v_{\text{avg}} = \frac{R_c^2}{8\mu_b}\frac{\Delta p}{L_c}. \tag{4.4}$$

According to Darcy's law (2.189), we have

$$n v_{\text{avg}} = \kappa \frac{\Delta p}{L_c}. \tag{4.5}$$

Comparing (4.4) and (4.5), we obtain

$$\kappa = \kappa(n) = \frac{n R_c^2}{8\mu_b}. \tag{4.6}$$

The radius R_c of a laminar capillary and the blood volume fraction n are related. Let Vol_B be the total volume occupied by blood in laminar capillaries, N_c be the total number of capillaries, vol_B be the volume of a single laminar capillary, and Vol_{LC} be the total volume of the lamina excluding the opening for the central retinal vessels. Thus, by definition of n, we have

$$n = \frac{\text{Vol}_B}{\text{Vol}_{\text{LC}}} = \frac{N_c \text{vol}_B}{\text{Vol}_{\text{LC}}} = \frac{N_c \pi R_c^2 L_c}{\text{Vol}_{\text{LC}}},$$

from which it follows that

$$R_c^2 = \frac{\mathrm{Vol_{LC}}}{N_c \pi L_c} n = \beta n, \tag{4.7}$$

where

$$\beta = \frac{\mathrm{Vol_{LC}}}{N_c \pi L_c},$$

is assumed to be a constant. By combining (4.6) and (4.7), equation (4.2) is obtained.

Concerning the solid matrix, we model it as a *nonlinear* isotropic elastic material. Blood flow is driven by the difference between the arterial pressure in the short PCAs (P_a) and the venous pressure in the CRV (P_v). The lamina cribrosa deforms under the combined action of IOP, RLTp and scleral tension. This exploratory two dimensional analysis suggested that the degree of fixity at the conjunction with the sclera has a strong influence on the distributions of stresses and strains, as suggested by other studies [158, 159], but also on the blood flow within the lamina. In particular, the inner surface of the lamina was found to be more susceptible to experiencing reduced blood supply following IOP elevation. Despite the many simplifying assumptions adopted in the model, most importantly the choice of a two dimensional geometry, the satisfactory qualitative agreement between experimental data and numerical simulations encouraged us to further investigate the use of poroelastic models to describe the complex mechanisms governing ONH perfusion.

4.4 Mathematical Modeling of Tissue Viscoelasticity and its Influence on the ONH Hemodynamics

Studies have suggested that the development and progression of glaucoma are associated with changes in the viscoelastic properties of collagen fibers embedded into the laminar tissue [166, 167]. We hypothesize that changes in lamina viscoelasticity may compromise lamina perfusion in response to sudden variations of IOP, possibly leading to disc hemorrhages. Isolating these factors experimentally is difficult, and mathematical modeling provides an approach to address these limitations.

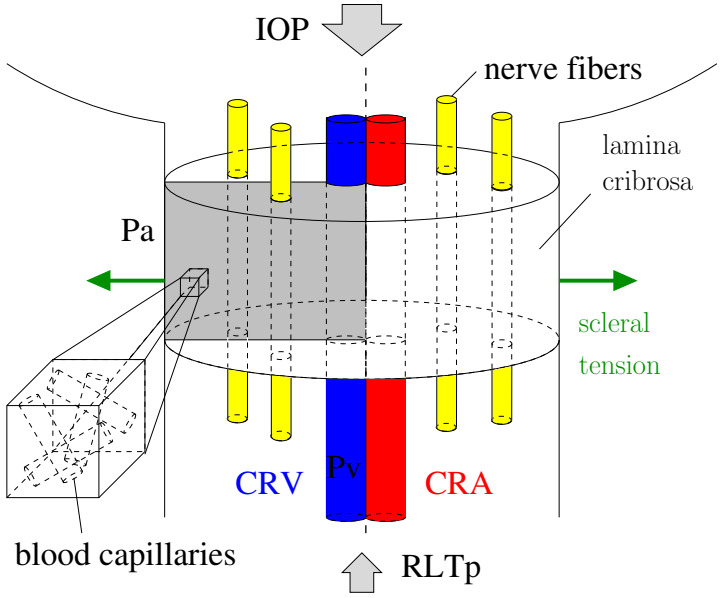

Figure 4.6. Schematic representation of the mathematical model describing the lamina cribrosa in the ONH [74].

4.4.1 Methods

Extending the approach in Causin et al. [74], the LC is modeled as a three dimensional poro-viscoelastic material [39, 74], where blood vessels are viewed as isotropically distributed pores in a solid matrix comprising collagen, elastin, neural tissue and extracellular matrix. The vascular porosity n, defined by the presence of blood vessels in the tissue, changes with the local state of stress and strain. The vascular permeability is assumed to be proportional to the square of n according to equations (4.1), (4.2); in this section, the solid matrix is assumed to behave as a *linear* isotropic elastic material. Both blood and the solid matrix are assumed to be separately incompressible. As discussed in Chapter 2, this does not imply that the overall fluid-solid mixture is incompressible, as the pores are still allowed to change in size and shape.

Let $\Omega \subset \mathbb{R}^3$ be the spatial domain occupied by the lamina cribrosa and $(t_{\text{start}}, t_{\text{end}})$ be the time domain. The spatial domain used in the numerical experiments is sketched in Figure 4.7 and its geometrical parameters listed in Table 4.2. As discussed in Chapters 2 and 3, the lamina can be described by the following poro-viscoelastic system in the space-time domain $Q = \Omega \times (t_{\text{start}}, t_{\text{end}})$:

$$\underline{\underline{\sigma}} = 2\mu^e \underline{\underline{\varepsilon}}(\mathbf{u}) + \lambda^e (\nabla \cdot \mathbf{u}) \underline{\underline{I}} + \delta(2\mu^v \underline{\underline{\varepsilon}}(\mathbf{u}') + \lambda^v (\nabla \cdot \mathbf{u}') \underline{\underline{I}}) - p \underline{\underline{I}} \qquad \text{in } Q, \tag{4.8}$$

$$\nabla \cdot \underline{\underline{\sigma}} = \mathbf{0} \qquad \text{in } Q, \tag{4.9}$$

$$\mathbf{v} = -\kappa(n) \nabla p \qquad \text{in } Q, \tag{4.10}$$

$$(\nabla \cdot \mathbf{u})' + \nabla \cdot \mathbf{v} = 0 \qquad \text{in } Q, \tag{4.11}$$

$$\kappa(n) = \frac{\beta}{8\mu_b} n^2 \qquad \text{in } Q, \tag{4.12}$$

$$n = \nabla \cdot \mathbf{u} + n^0 \qquad \text{in } Q. \tag{4.13}$$

The above system is obtained from (3.44)–(3.52) by assuming that there are no volumetric source terms either in the balance of linear momentum or in the balance of mass, i.e. $\mathbf{F} = \mathbf{0}$ in (3.45) and $S = 0$ in (3.47), respectively. Due to the differences between classical continuum mechanics and porous media theory briefly addressed

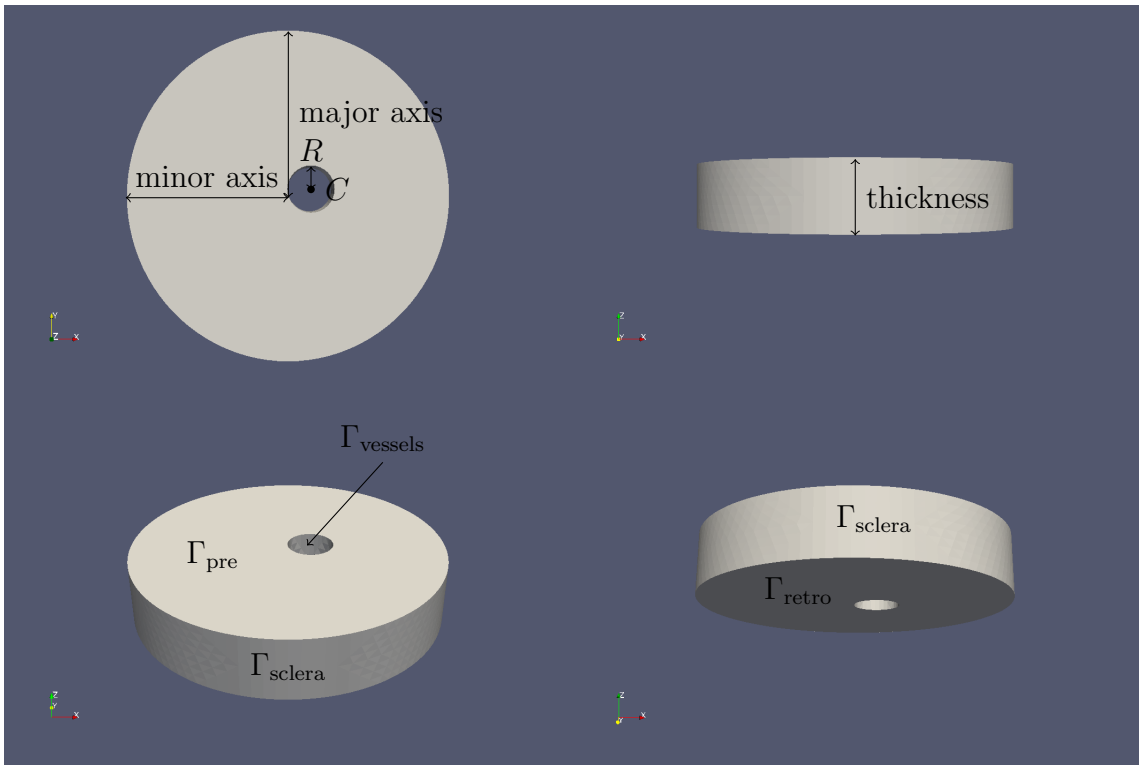

Figure 4.7. Schematic representation of the geometry of the lamina cribrosa used in the numerical experiments: (top left and top right) geometrical parameters; (bottom left and bottom right) boundary surfaces: Γ_{pre}, prelaminar surface; Γ_{retro}, retrolaminar surface; Γ_{sclera}, interface with the sclera; Γ_{vessels}, interface with the central retinal vessels. See Table 4.2 for parameter values.

Table 4.2
Model geometrical and physical parameters. See Figure 4.7 for parameter definition.

Parameter	Value	Reference
Laminar major axis	$0.079\,\mathrm{cm}$	[168]
Laminar minor axis	$0.077\,\mathrm{cm}$	[168]
Center of the central retinal vessels passage, $C(x_C, y_C)$	$(0.011\,\mathrm{cm}, 0.0033\,\mathrm{cm})$	[168]
Radius of central retinal vessels passage, R	$\approx 0.0113\,\mathrm{cm}$	[168]
Laminar thickness	$0.03\,\mathrm{cm}$	[169]
Laminar first elastic parameter, μ^e	$1.2 \times 10^6\,\mathrm{dyn\,cm^{-2}}$	[84]
Laminar second elastic parameter, λ^e	$\approx 7.8 \times 10^6\,\mathrm{dyn\,cm^{-2}}$	-
Laminar first viscous parameter, μ^v	$\approx 2.8 \times 10^4\,\mathrm{dyn\,s\,cm^{-2}}$	-
Laminar second viscous parameter, λ^v	$\approx 1.8 \times 10^5\,\mathrm{dyn\,s\,cm^{-2}}$	-
Reference laminar capillary radius, R_c	$3 \times 10^{-4}\,\mathrm{cm}$	[170]
Blood dynamic viscosity in capillaries, μ_b	$0.1001\,\mathrm{g\,cm^{-1}\,s^{-1}}$	[170]
Vascular porosity in the reference configuration, n^0	0.1567	[171]
Scleral radius, R_{sc}	$1.2\,\mathrm{cm}$	[83, 169]
Scleral thickness, h_{sc}	$0.078\,\mathrm{cm}$	[169]

in Chapter 2, care is needed when estimating the partial elastic (μ^e, λ^e) and viscous (μ^v, λ^v) parameters for porous materials, like the lamina cribrosa. These parameters appear to be *drained* properties, i.e. properties that can be measured in tests where the fluid pressure is held constant [20,42]. Since these parameters transfer the microscopic behavior of the real solid phase to the macroscale, they should be expressed in terms of quantities characterizing the real solid material and the empty porous solid, as discussed in Chapter 2. Moreover, to our knowledge, there are only few studies addressing the viscoelastic material properties of the ONH [166, 167] and further research is needed to characterized them. Thus, we estimated these parameters as follows:

- *Laminar first elastic parameter*, $\mu^e = 1.2 \times 10^6\,\mathrm{dyn\,cm^{-2}}$: this parameter is taken from the work of Woo et al. [84]. They characterized the material properties of human cornea and sclera by doing tests on enucleated human eyes, 1–3 days post mortem. Due to the loss of pressure caused by histology preparation [1], we assume that the experiments of Woo et al. have been performed in a drained environment.

- *Laminar second elastic parameter*, $\lambda^e = 7.8 \times 10^6\,\mathrm{dyn\,cm^{-2}}$: as pointed out at the end of Section 2.4.4, unlike classical linear elasticity, the hypothesis of solid incompressibility does not cause the partial compression modulus K^e, and thus λ^e, to blow up. Hence, rather than estimating λ^e from μ^e by taking a Poisson's ratio very close to 0.5, we first estimate K^e with the upper bound introduced by Coussy [20]
$$K^e = (1 - n^0) K^e_{SR} \frac{4\mu^e}{4\mu^e + 3n^0 K^e_{SR}}, \tag{4.14}$$
where K^e_{SR} is the bulk modulus of the real macroscopic material. Then, we take the limit of (4.14) for $K^e_{SR} \to \infty$ in order to simulate solid incompressibility, thereby obtaining
$$K^e = \frac{4(1 - n^0)}{3n^0} \mu^e,$$

from which λ^e can be computed as follows

$$\lambda^e = K^e - \frac{2}{3}\mu^e.$$

- *Laminar first and second viscous parameters*, μ^v and λ^v: as discussed in Chapter 2, the Voigt model does not exhibit stress relaxation. Thus, its material parameters can be characterized using either creep tests or its response to a harmonic input. When subject to a harmonic input of frequency ω, the loss angle γ of the Voigt model satisfies

$$\tan\gamma(\omega) = \frac{\eta}{E}, \tag{4.15}$$

where η and E are the dashpot and spring coefficients, respectively [36]. Identifying E with the partial Young's modulus E^e and using standard linear elasticity, we get

$$E = E^e = \frac{9K^e\mu^e}{3K^e + \mu^e}.$$

Equation (4.15) is then used to find η by fitting data from Palko et al. [167], as shown in Figure 4.8. Despite the poor fit shown in Figure 4.8, considering the theoretical analysis discussed in Chapter 3, the Voigt model is a necessary preliminary step towards the use of more realistic viscoelastic models. After finding η and identifying it as the *viscous Young's modulus* E^v, we estimate μ^v and λ^v by assuming

$$\frac{\mu^v}{\mu^e} = \frac{\lambda^v}{\lambda^e} = \frac{E^v}{E^e}.$$

Finally, the constant β appearing in (4.7) is estimated as follows

$$\beta = \frac{R_c^2}{n^0},$$

where R_c and n^0 are the reference laminar capillary radius and the vascular porosity in the reference configuration listed in Table 4.2, respectively.

The system (4.8)–(4.13) has to be equipped with initial and boundary conditions. In the viscoelastic case ($\delta > 0$), we impose

$$\mathbf{u} = \mathbf{u}^0 \quad \text{in } \Omega \quad \text{at } t = t_{\text{start}},$$

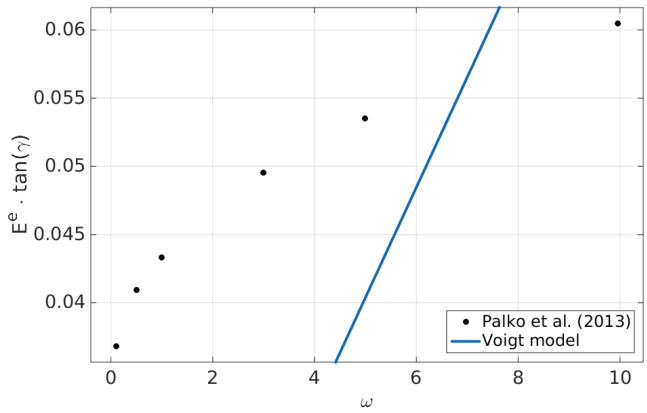

Figure 4.8. Data from Palko et al. [167] fitted using the Voigt model described in Chapter 2. The poor fit denotes that a more appropriate viscoelastic model is needed for the lamina cribrosa.

whereas, in the elastic case ($\delta = 0$), we impose

$$\nabla \cdot \mathbf{u} = d_0 \quad \text{in } \Omega \quad \text{at } t = t_{\text{start}}.$$

Regarding the boundary conditions, blood flow is driven by the difference between the arterial pressure in the short PCAs and the venous pressure in the CRV (see Figure 4.4). Thus, using the notation introduced in Figure 4.7 for the boundary surfaces of the computational domain, we consider the following boundary conditions for the balance of mass (4.12):

- Since laminar capillaries are embedded into the laminar beams (see Figure 4.4) and their blood flow does not contribute to the perfusion of either the prelaminar or the retrolaminar region, as discussed in Section 4.1.2, we impose no-flux conditions on $\Gamma_{\text{pre}} \cup \Gamma_{\text{retro}}$:

$$\mathbf{v} \cdot \mathbf{n} = 0 \qquad \text{on } \Gamma_{\text{pre}} \cup \Gamma_{\text{retro}}. \tag{4.16}$$

- Since blood drainage in the lamina occurs through the CRV (see Section 4.1.2), we impose

$$p = P_v \qquad \text{on } \Gamma_{\text{vessels}}, \tag{4.17}$$

  where $P_v = 20\,\text{mmHg}$ is the blood pressure in the CRV [172].

- As described in Section 4.1.2, the vasculature supplying the lamina cribrosa region arise directly from the short PCAs or from the circle of Zinn-Haller, which, if present, is a complete or incomplete ring of vessels within the perineural sclera formed by the confluence of branches of the short PCAs. In the following sections, we are going to assume that the circle of Zinn-Haller is a complete ring, so that the lamina is nourished by vessels arising from the whole interface with the sclera, Γ_{sclera}. Under this assumption, we impose a Dirichlet boundary condition on Γ_{sclera}

$$p = P_a \qquad \text{on } \Gamma_{\text{sclera}}, \tag{4.18}$$

where P_a is the blood pressure in the circle oh Zinn-Haller and the short PCAs feeding the lamina. Measuring this pressure is challenging with current methodologies. At present, CDI can be used to measure velocity profiles in short PCAs. However, this is particularly difficult due to the fact that PCAs are close to the size limit that can be studied. Using velocity profiles, time profiles for P_a can be determined by solving inverse problems as described by Guidoboni et al. [172]. In this work we are going to use a much simpler approach: since both the short PCAs and the vessels forming the circle of Zinn-Haller are arterioles, from an anatomical perspective, P_a is estimated by starting from the pressure $P_v = 20\,\text{mmHg}$ in the CRV [172], and then adding the pressure drops across large venules, small venules and capillaries used by Arciero et al. [170] for the retinal vasculature

$$\begin{aligned} p = P_a &= 20 + 1.41 + 2.30 + 5.04 \\ &= 28.75\,\text{mmHg} \approx 30\,\text{mmHg} \qquad \text{on } \Gamma_{\text{sclera}}. \end{aligned} \tag{4.19}$$

The value $P_a = 30\,\text{mmHg}$ is also reasonable when compared to the pressure at the end of arterioles used by Guidoboni et al. [172].

Boundary conditions are also needed for the balance of linear momentum (4.9). From equations (3.10)–(3.17), we could impose either Dirichlet boundary conditions on any of the components of the solid displacement $\mathbf{u}$ or Neumann boundary conditions on any of the components of the *total* stress tensor $\underline{\underline{\sigma}}$. In order to correctly impose Neumann boundary conditions on $\underline{\underline{\sigma}}$, it is important to distinguish between boundary surfaces where matrix pores are *sealed* and boundary surfaces where pores are *exposed* [68]. On the sealed portion of the boundary, the hydraulic pressure contributes to the total stress $\underline{\underline{\sigma}}$ within the matrix. On the exposed portion of the boundary, only the *effective* or viscoelastic component of the stress $\underline{\underline{\sigma}}_e + \delta\underline{\underline{\sigma}}_v$ is specified, since there the fluid pressure does not contribute to the support of the matrix. By taking these observations into account and assuming that the lamina cribrosa deforms under the combined action of IOP, RLTp and scleral tension (see Figure 4.6), we consider the following boundary conditions for the balance of linear momentum:

- The prelaminar Γ_{pre} and retrolaminar Γ_{retro} surfaces are subject to the IOP and the RLTp, respectively. As discussed before about the Neumann boundary condition (4.16), matrix pores, i.e. blood vessels, on Γ_{pre} and Γ_{retro} are assumed to be sealed, and, thus, the fluid pressure contributes to the total stress $\underline{\underline{\sigma}}$. Therefore, we set:

$$\underline{\underline{\sigma}}\mathbf{n} = -\text{IOP}\,\mathbf{n} \qquad \text{on } \Gamma_{\text{pre}}, \tag{4.20}$$

$$\underline{\underline{\sigma}}\mathbf{n} = -\text{RLTp}\,\mathbf{n} \qquad \text{on } \Gamma_{\text{retro}}. \tag{4.21}$$

- At the interface Γ_{vessels} between the lamina cribrosa and the central retinal vessels, laminar blood vessels are exposed and drain into the CRV. Thus, the mechanical stress P_{CRA} exerted by the CRA onto Γ_{vessels} is carried only by the effective component $\underline{\underline{\sigma}}_e + \delta\underline{\underline{\sigma}}_v$ of the stress tensor. Thus, we set

$$(\underline{\underline{\sigma}}_e + \delta\underline{\underline{\sigma}}_v)\mathbf{n} = -P_{\text{CRA}}\,\mathbf{n} \qquad \text{on } \Gamma_{\text{vessels}},$$

which, thanks to (4.17), can be rewritten in terms of the total stress tensor $\underline{\underline{\sigma}}$

$$\underline{\underline{\sigma}}\mathbf{n} = (\underline{\underline{\sigma}}_e + \delta\underline{\underline{\sigma}}_v - p\underline{\underline{I}})\mathbf{n} = -(P_{\text{CRA}} + P_v)\mathbf{n} \qquad \text{on } \Gamma_{\text{vessels}}. \tag{4.22}$$

Here, we take $P_{\text{CRA}} = 40\,\text{mmHg}$ [172].

- At the interface Γ_{sclera} between the lamina cribrosa and the sclera, we set

$$\mathbf{e}_3 \cdot \mathbf{u} = 0 \qquad \text{on } \Gamma_{\text{sclera}}, \tag{4.23}$$

to prevent displacement of the lamina in the z direction, i.e. in the sagittal direction. Moreover, the lamina is subject to the scleral tension T_{sc}, which can be estimated using Laplace's law

$$T_{\text{sc}} = \frac{\text{IOP}\,R_{\text{sc}}}{2h_{\text{sc}}}, \tag{4.24}$$

where R_{sc} and h_{sc} are the scleral radius and thickness, whose values are specified in Table 4.2. Equation (4.24) is valid under the assumption that the sclera can

be modeled as a perfect sphere. Since blood vessels are exposed also on Γ_{sclera}, T_{sc} is carried only by the solid matrix and thus

$$\mathbf{e}_1 \cdot (\underline{\underline{\sigma}}_e + \delta\underline{\underline{\sigma}}_v)\mathbf{n} = \mathbf{e}_1 \cdot T_{\text{sc}}\mathbf{n}, \quad \mathbf{e}_2 \cdot (\underline{\underline{\sigma}}_e + \delta\underline{\underline{\sigma}}_v)\mathbf{n} = \mathbf{e}_2 \cdot T_{\text{sc}}\mathbf{n} \qquad \text{on } \Gamma_{\text{sclera}},$$

where T_{sc} is taken with a positive sign because the lamina is pulled by the sclera. From (4.19), the last equation can be rewritten in terms of the total stress $\underline{\underline{\sigma}}$

$$\mathbf{e}_1 \cdot \underline{\underline{\sigma}}\mathbf{n} = \mathbf{e}_1 \cdot (T_{\text{sc}} - P_a)\mathbf{n}, \quad \mathbf{e}_2 \cdot \underline{\underline{\sigma}}\mathbf{n} = \mathbf{e}_2 \cdot (T_{\text{sc}} - P_a)\mathbf{n} \qquad \text{on } \Gamma_{\text{sclera}}. \quad (4.25)$$

4.4.2 Results

The predictions of the mathematical model for the lamina cribrosa displacement are validated using two different experimental studies. These two validation test cases are performed on a mesh with 41292 tetrahedra and 86698 triangular faces. The work by Yang et al. [173] reports histomorphometric data for the IOP-induced displacement of the anterior laminar surface of monkeys. After setting IOP to 10 mmHg, the ONH and peripapillary sclera from both eyes of three glaucoma monkey models (one eye normal, one eye given laser-induced glaucoma) were trephinated and serial-sectioned. The embedded tissue block face was stained and imaged after each cut. Images were aligned and stacked to create 3D reconstructions. Regional laminar, scleral flange, and peripapillary scleral position and thickness were compared between the normal and glaucomatous eyes of each monkey and between treatment groups by analysis of variance.

Due to the loss of pressure caused by tissue preparation [1], we numerically reproduce the experimental setting of Yang et al. by solving a stationary version of system (4.8)–(4.13) with the following boundary conditions:

- For the balance of mass:

$$\begin{aligned} \mathbf{v} \cdot \mathbf{n} &= 0 && \text{on } \Gamma_{\text{pre}} \cup \Gamma_{\text{retro}}, \\ p &= 0 && \text{on } \Gamma_{\text{vessels}} \cup \Gamma_{\text{sclera}}. \end{aligned}$$

- For the balance of linear momentum:

$$\begin{aligned}
\underline{\underline{\sigma}}\mathbf{n} &= -\mathrm{IOP}\,\mathbf{n} && \text{on } \Gamma_{\mathrm{pre}},\\
\underline{\underline{\sigma}}\mathbf{n} &= \mathbf{0} && \text{on } \Gamma_{\mathrm{retro}} \cup \Gamma_{\mathrm{vessels}},\\
\mathbf{e}_1 \cdot \underline{\underline{\sigma}}\mathbf{n} = 0, \quad \mathbf{e}_2 \cdot \underline{\underline{\sigma}}\mathbf{n} &= 0 && \text{on } \Gamma_{\mathrm{sclera}},\\
\mathbf{e}_3 \cdot \mathbf{u} &= 0 && \text{on } \Gamma_{\mathrm{sclera}},
\end{aligned}$$

  with $\mathrm{IOP} = 10\,\mathrm{mmHg}$.

The poro-viscoelastic system (4.8)–(4.13) is also scaled using

$$\sigma_c = \mathrm{IOP},$$

and setting all the other characteristic parameters to 1.

As shown in Figure 4.9, the model predicts a maximum posterior laminar displacement of $\approx 4.226 \times 10^{-3}\,\mathrm{cm} = 42.26\,\mu\mathrm{m}$, which is approximately half the value reported by Yang et al. for the normal eyes of their three monkey models ($\approx 100\,\mu\mathrm{m}$). We believe our prediction is in very good agreement with these experimental data, given that:

- We put no effort in choosing geometrical and material parameters that would match the properties of the normal eyes of the monkey models.

- Our model estimates the anterior laminar displacement, which is the relative position with respect to the undeformed lamina configuration, i.e. for $\mathrm{IOP} = 0\,\mathrm{mmHg}$. On the other hand, Yang et al. measure the lamina cribrosa *position* relative to a reference plane at the level of the Bruch's membrane opening, called the BMO plane, as shown in Figure 2B in [173]. Such Figure suggests that the position of the BMO plane could be rather different from the anterior surface of the lamina cribrosa in the undeformed configuration, thereby explaining the discrepancy between the experimental data and our prediction.

We compared the displacements of the lamina cribrosa predicted by our mathematical model also with the experimental data obtained by Morgan et al. [174], for

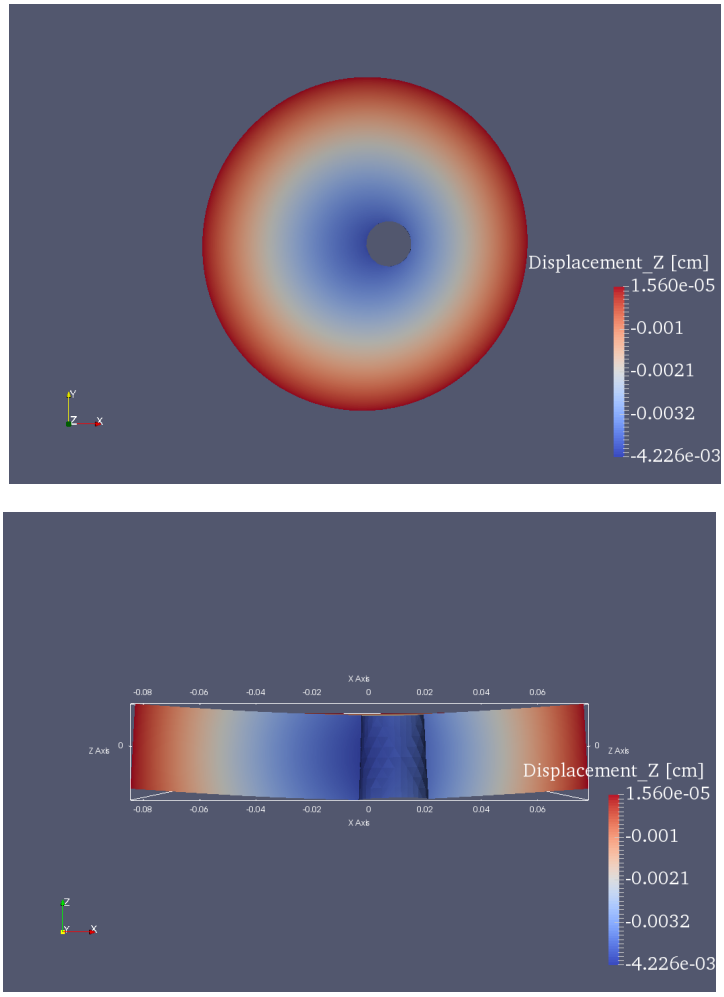

Figure 4.9. Model predictions for the continuous laminar displacement map in the sagittal direction for the experiment by Yang et al. [173]. Data are displayed on the deformed mesh.

different values of IOP and RLTp. In their study, the anterior chamber and lateral ventricles of eight dogs were cannulated to control IOP and cerebrospinal fluid pressure (CSFp), respectively. The depth of the optic disc surface, which reflects the underlying anterior laminar movement, was performed at each value of IOP and CSFp via confocal scanning laser tomography. Starting from baseline (corresponding to IOP = 15 mmHg and CSFp = 0 mmHg), IOP was elevated up to an average of 32 mmHg, via steps between 3 and 5 mmHg. In a second set of experiments, starting from baseline, CSFp was elevated up to an average of 12 mmHg, via steps between 2 and 4 mmHg. Morgan et al. report their results using the quantity ΔMaxD, which is the difference in the maximum disc depth with respect to baseline.

In order to reproduce the experimental setting of Morgan et al. numerically, we solve a stationary version of system (4.8)–(4.13) with the following boundary conditions:

- For the balance of mass:

$$\begin{aligned} \mathbf{v}\cdot\mathbf{n} &= 0 && \text{on } \Gamma_{\text{pre}}\cup\Gamma_{\text{retro}},\\ p &= P_v && \text{on } \Gamma_{\text{vessels}},\\ p &= P_a && \text{on } \Gamma_{\text{sclera}}. \end{aligned}$$

- For the balance of linear momentum:

$$\begin{aligned} \underline{\underline{\sigma}}\mathbf{n} &= -\text{IOP}\,\mathbf{n} && && \text{on } \Gamma_{\text{pre}},\\ \underline{\underline{\sigma}}\mathbf{n} &= -\text{RLTp}\,\mathbf{n} && && \text{on } \Gamma_{\text{retro}},\\ \underline{\underline{\sigma}}\mathbf{n} &= -(P_{\text{CRA}}+P_v)\mathbf{n} && && \text{on } \Gamma_{\text{vessels}},\\ \mathbf{e}_1\cdot\underline{\underline{\sigma}}\mathbf{n} &= \mathbf{e}_1\cdot(T_{\text{sc}}-P_a)\mathbf{n}, && \mathbf{e}_2\cdot\underline{\underline{\sigma}}\mathbf{n} = \mathbf{e}_1\cdot(T_{\text{sc}}-P_a)\mathbf{n} && \text{on } \Gamma_{\text{sclera}},\\ \mathbf{e}_3\cdot\mathbf{u} &= 0 && && \text{on } \Gamma_{\text{sclera}}. \end{aligned}$$

We also scale the poro-viscoelastic system (4.8)–(4.13) using

$$x_c = 1\,\text{cm}, \qquad t_c = 1\,\text{s}, \qquad u_c = 1\,\text{cm},$$

and

$$p_c = P_v, \qquad \sigma_c = \text{RLTp}, \qquad v_c = \frac{\beta}{8\mu_b}(n^0)^2 p_c/x_c.$$

In order to relate CSFp and RLTp, we use the following linear relation (in mmHg), derived by Morgan et al. in a previous work [113]:

$$\text{RLTp} = \begin{cases} 0.07\ \text{CSFp} + 2.9200 & \text{for CSFp} \leq 1.33, \\ 0.82\ \text{CSFp} + 1.9225 & \text{for CSFp} > 1.33. \end{cases} \tag{4.26}$$

Then, we solve the system with RLTp = 2.92 mmHg, which corresponds to CSFp = 0 mmHg according to (4.26), and with IOP varying between 15 mmHg and 33 mmHg. Next, we solve the system by fixing IOP = 15 mmHg, and varying RLTp in the range that corresponds to CSFp $\in$ [0 mmHg, 12 mmHg] via (4.26). Since Morgan et al. [174] do not provide geometric and elastic properties of the eyes they examined, we use the physiologically representative values listed in Table 4.2.

In Figure 4.10, we compare the maximum disc depth ΔMaxD measured by Morgan et al. [174] with the theoretical predictions obtained via our mathematical model. The agreement between model predictions and experimental data is very satisfactory. The high lamina cribrosa movements predicted by our model in the high range of translaminar pressure difference IOP$-$CSFp are due to our hypothesis of a mechanically homogeneous, linear, and isotropic laminar tissue. Evidence suggests that these are only approximations and that the tissues are inhomogeneous [115], nonlinear [75, 84, 114, 162–164], and anisotropic [75, 114, 162–164].

Finally, we theoretically investigate the influence of viscoelasticity on the perfusion of the lamina cribrosa. Utilizing our mathematical model, we simulate and compare the behavior of the integrated rate of change of blood kinetic energy W

$$W = (\kappa(n)\nabla p, \nabla p),$$

which has been introduced in equation (3.30), treating the lamina as an elastic or a viscoelastic medium when sudden external forces are applied.

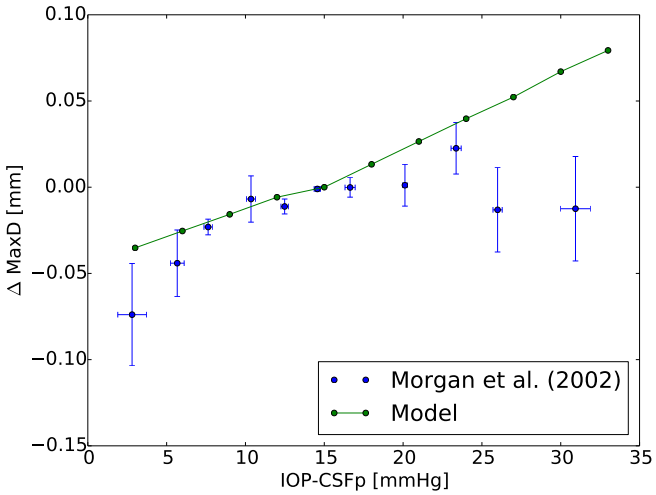

Figure 4.10. Comparison between model predictions and experimental measurements of the anterior lamina displacements. Changes of maximum optic disc depth ΔMaxD with respect to the baseline at IOP$-$CSFp$=$ 15 mmHg are reported as a function of the IOP$-$CSFp difference. The predictions of the mathematical model (green line) are compared with experimental data by Morgan et al. [174].

We solve system (4.8)–(4.13) in the space-time domain $Q = \Omega \times (0, T), T = 2\,\mathrm{s}$, with the following boundary conditions:

- For the balance of mass:

$$\begin{aligned} \mathbf{v} \cdot \mathbf{n} &= 0 && \text{on } \Gamma_{\text{pre}} \cup \Gamma_{\text{retro}}, \\ p &= P_v && \text{on } \Gamma_{\text{vessels}}, \\ p &= P_a && \text{on } \Gamma_{\text{sclera}}. \end{aligned}$$

- For the balance of linear momentum:

$$\begin{aligned} \underline{\underline{\sigma}}\mathbf{n} &= -\mathrm{IOP}\,\mathbf{n} && \text{on } \Gamma_{\text{pre}}, \\ \underline{\underline{\sigma}}\mathbf{n} &= -\mathrm{RLTp}\,\mathbf{n} && \text{on } \Gamma_{\text{retro}}, \\ \underline{\underline{\sigma}}\mathbf{n} &= -(P_{\text{CRA}} + P_v)\mathbf{n} && \text{on } \Gamma_{\text{vessels}}, \\ \mathbf{e}_1 \cdot \underline{\underline{\sigma}}\mathbf{n} = \mathbf{e}_1 \cdot (T_{\text{sc}} - P_a)\mathbf{n}, \quad \mathbf{e}_2 \cdot \underline{\underline{\sigma}}\mathbf{n} &= \mathbf{e}_1 \cdot (T_{\text{sc}} - P_a)\mathbf{n} && \text{on } \Gamma_{\text{sclera}}, \\ \mathbf{e}_3 \cdot \mathbf{u} &= 0 && \text{on } \Gamma_{\text{sclera}}, \end{aligned}$$

with

$$\mathrm{IOP} = \begin{cases} 15\,\mathrm{mmHg} & \text{if } t \leq 0.75\,\mathrm{s} \cup t > 1.25\,\mathrm{s}, \\ 17\,\mathrm{mmHg} & \text{if } 0.75\,\mathrm{s} < t \leq 1.25\,\mathrm{s}. \end{cases}$$

We also scale the poro-viscoelastic system (4.8)–(4.13) using

$$x_c = 1\,\mathrm{cm}, \qquad t_c = 1\,\mathrm{s}, \qquad u_c = 0.004\,\mathrm{cm},$$

and

$$p_c = P_v, \qquad \sigma_c = \mathrm{RLTp}, \qquad v_c = \frac{\beta}{8\mu_b}(n^0)^2 p_c / x_c.$$

When subject to a sudden force, such as, for example, an increase in IOP due to rubbing of the eye, the lamina undergoes a sudden deformation in the elastic model, i.e. it behaves like a linear spring (see Section 2.4.4). However, using the Voigt model to describe the viscoelastic behavior of the lamina, the deformation will be

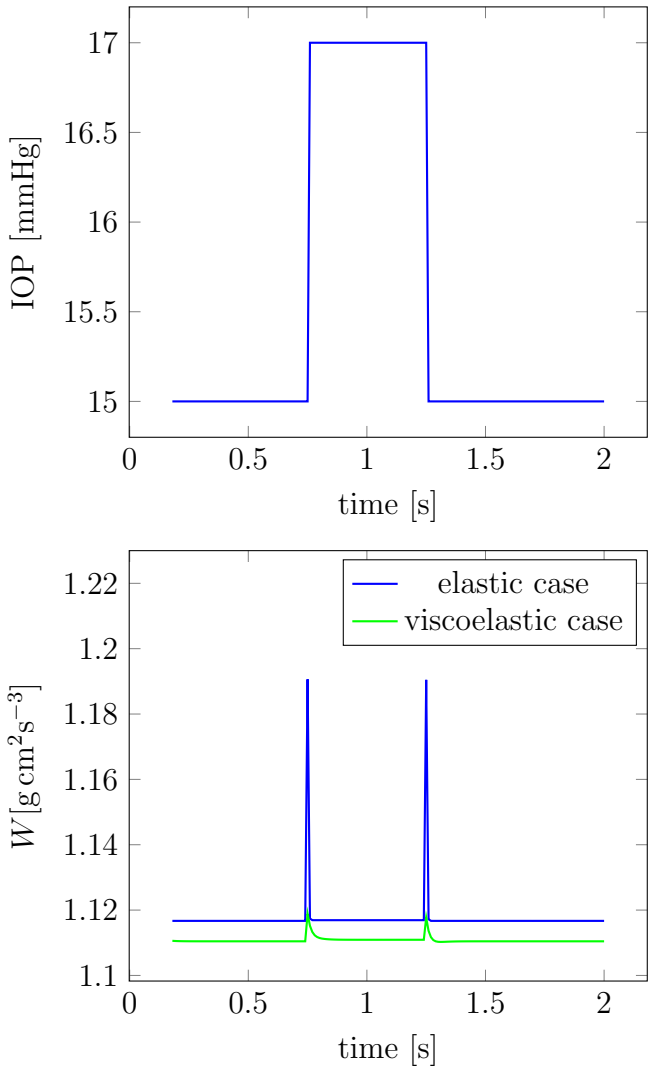

Figure 4.11. (top) IOP fluctuation pattern tested in the model; (bottom) integrated time rate of change of blood kinetic energy W in response to IOP variations treating the lamina cribrosa as an elastic (blue curve) or a viscoelastic (green curve) medium.

gradually built up, thereby reducing tissue susceptibility to damage. In other words, the viscoelastic biomechanical properties of an intact and healthy lamina cribrosa enable it to absorb sudden changes in force and transfer it slowly to the surrounding structures, including blood vessels and capillaries, thereby lowering the susceptibility to vessel hemorrhage and rupture.

Figure 4.11 shows that the absence or presence of structural viscoelasticity influence noticeably W as the lamina experiences sudden changes in IOP. More precisely, without viscoelasticity (Figure 4.11(bottom), blue curve), W exhibits sharp peaks at the IOP switch-on and switch-off times, suggesting perfusion instability. Conversely, in the presence of viscoelasticity (Figure 4.11(bottom), green curve) W remains bounded at lower levels.

4.4.3 Discussion

This thesis introduces a mathematical model that can serve as a virtual laboratory to theoretically investigate lamina cribrosa perfusion. To our knowledge, this is the first model combining mechanics and hemodynamics of the lamina cribrosa into a single framework. In this thesis, we use it to study the influence of tissue viscoelasticity on the perfusion of the lamina cribrosa.

In order to validate the model, we compare its predictions with data from independent experimental studies. Figures 4.9 and 4.10 show that the model-predicted values of laminar displacements are consistent with clinical measurements [173, 174]. Most of the geometrical and physiological parameters of the model were directly available from published literature, as shown in Table 4.2, whereas some had to be estimated, for example the viscous parameters μ^v and λ^v. These parameters vary among individuals. In particular, they could vary with age [110], ethnicity [175], disease [75, 164], thereby affecting the mechanical and hemodynamical response of the laminar tissue to external forces, such as IOP and RLTp. Patient-specific geometric and physiological properties would improve model predictions.

Influences of tissue viscoelasticity on lamina perfusion are investigated by computing the integrated rate of change of blood kinetic energy W treating the lamina as an elastic or a viscoelastic medium in response to sudden temporal IOP variations (see Figure 4.11). Our findings suggest that the lack of viscoelasticity may increase the lamina susceptibility to localized damage due to peaks in W as IOP experiences

sudden changes in time, as they normally occur during the day. In other words, if the lamina viscoelasticity is not intact, sudden IOP changes will be translated to lamina hemodynamics, possibly leading to perfusion instabilities. On the other hand, if the lamina viscoelasticity is intact, sudden changes will be absorbed by the tissue and we will not see perfusion instabilities. The importance of viscoelasticity in the tissue has been evidenced also in other studies [166, 167]. The clinical implications of lamina perfusion deficits during IOP variation should be further investigated to elucidate their impact on glaucoma pathophysiology. Next steps of our work will be devoted to investigating the existence of possible correlations between the magnitude of the peaks in W and IOP or OPP fluctuations in glaucoma and other ocular pathologies.

Our model for the lamina cribrosa has some limitations. Here we summarize those that are more relevant to our discussion. The constitutive model for the laminar tissue is homogeneous, linear and isotropic. Evidence suggests that these are only approximations and that the tissues are non homogeneous [115], nonlinear [75,84,114,162–164], and anisotropic [75,114,162–164]. An extension of the model to more realistic constitutive equations for the laminar tissue [164] would help, for example, to improve model predictions for the laminar displacement, stress and strain distributions in response to external loads. It would also help to better characterize vascular permeability.

Blood is the only fluid phase of our poro-viscoelastic model and its flow is only driven by the pressure gradient in the capillaries. Vascular autoregulation and neurovascular coupling are not taken into account. Expanding the model to incorporate a mechanistic autoregulation description, similar to the one developed by Arciero et al. [170], could help to investigate the hemodynamic consequences of IOP alterations in subjects who suffer from metabolic or endothelial dysfunctions [1]. In order to do this, multiphasic models (e.g. a viscoelastic solid filled with viscous fluid containing nutrients) based on porous media theory can be developed. The same strategy can also be used to investigate the effects of nutrients availability on the non-uniform growth and remodeling of the collagen within the lamina [75].

5. CONCLUSIONS AND FUTURE DIRECTIONS

The mathematical modeling of the interplay between biomechanics and perfusion in the ONH is still at its early stages, but is quickly attracting attention. Elucidating the complex interactions of ONH perfusion and tissue structure in health and disease using current imaging methodologies is difficult, and mathematical modeling provides an approach to solving these limitations. One of the main difficulties lies in the fact that the biophysical phenomena governing the ONH physiology occur at different scales in time and space. In order to address and theoretically investigate these multiscale problems, we used a modeling approach based on the theory of porous media. We devoted particular attention to the description of a viscous fluid streaming through a viscoelastic solid skeleton, a situation that is often encountered in many areas of biomechanics. The resulting system of balance equations is solved via a numerical method based on a novel hybridizable discontinuous Galerkin finite element discretization. This method is obtained by carefully blending the approaches by Cockburn et al. [19] and Qiu et al. [55, 57] for the diffusion equation and linear elasticity with a fixed-point map for the nonlinear dependence of the permeability on the volumetric solid strain.

In the case of stationary problems, our HDG method computes both primal (solid displacement and fluid pressure) and dual (total stresses and discharge velocities) variables simultaneously with optimal order of accuracy. Dual variables often represent quantities of primary interest in engineering. For example, stresses drive the non-uniform growth and remodeling of the collagen within the lamina cribrosa [75], whereas discharge velocities are related to the blood perfusion of the laminar tissue. Unless dual variables are computed directly, they require the evaluation of gradients of primal variables. However, numerical differentiation is a particularly delicate pro-

cedure that usually suffers from a loss in approximation accuracy [47]. The HDG method proposed here does not suffer from this loss of accuracy because all the variables are approximated directly.

Similarly to other HDG methods devised for other applications, our approach inherits some extremely interesting features of DG schemes: it can handle all sorts of complicated meshes and discontinuous data, provide high-order accurate solutions, can be used to perform h/p adaptivity, and retains very good scalability properties. Moreover, thanks to hybridization, our method becomes computationally competitive with traditional continuous Galerkin approaches [52]. However, hybridization is not just an implementation trick. Rather, it endows HDG methods with some attractive convergence properties that allow to enhance the accuracy of the approximate solution by local postprocessing. Also, Phillips and Wheeler [18] provided evidence that numerical methods for poroelasticity based on continuous Galerkin approaches may suffer from locking, or nonphysical pressure oscillations. Model simulations shown in Section 3.3.3 suggest that our HDG method suppresses locking to a very good degree.

Similarly to other multiphysics problem, the poro-viscoelastic system (3.44)–(3.54) can be ill-conditioned. In other words, the quality of the numerical solutions and the convergence of the fixed point map proposed here are affected by the values of the model parameters (like permeability and viscoelastic parameters) and the different scaling of the variables. Convergence properties of the HDG method can be restored by scaling the poro-viscoelastic system and reformulating it in terms of new dimensionless variables. This technique is equivalent to precondition the poro-viscoelastic system. However, care is needed when using this approach, since several characteristic scales may be involved in the problem at hand and, thus, the choice of characteristic scales may be a non trivial issue. Moreover, as reported in Section 3.3.2, there might be situations where scaling does not improve the convergence of the fixed point algorithm. These results suggest that, depending on the regime of motion, it might be necessary to use a different preconditioning strategy or a different iterative method

than the fixed point approach used here. We are currently exploring iterative methods based on operator-splitting and augmented Lagrangian strategies [30].

In Chapter 4, the poro-viscoelastic model is used to theoretically investigate the influence of tissue viscoelasticity on the perfusion of the lamina cribrosa in the ONH. Our theoretical results suggest that even physiological changes in IOP may induce pathological changes in lamina perfusion if the lamina viscoelasticity provided by the collagen fibers is not intact (due, e.g., to aging or disease). The clinical implications of lamina perfusion deficits during IOP variation should be further investigated to elucidate their impact on glaucoma pathophysiology.

We are currently working on extending our model to account for:

- more realistic nonlinear constitutive equations for the laminar tissue;
- effects of nutrients availability on the non-uniform growth and remodeling of collagen within the lamina;
- blood flow autoregulation in the laminar vasculature.

The accurate modeling and simulation of multiscale and multiphysics problems is still an open area of research, and therefore the modeling of the ONH offers stimulating opportunities for groundbreaking activities from both the clinical and theoretical viewpoints. The application of advanced modeling to reveal the mechanistic interplay of previously unseen physiologic relationships holds the potential to advance medical care in ophthalmic disease and provide patients and clinicians new hope for future diagnosis and therapy.

LIST OF REFERENCES

LIST OF REFERENCES

[1] D. Prada, A. Harris, G. Guidoboni, B. Siesky, A. M. Huang, and J. Arciero. Autoregulation and neurovascular coupling in the optic nerve head. *Survey of Ophthalmology*, 61(2):164–186, 2016.

[2] H. A. Quigley and A. T. Broman. The number of people with glaucoma worldwide in 2010 and 2020. *British Journal of Ophthalmology*, 90(3):262–267, 2006.

[3] The AGIS Investigators. The advanced glaucoma intervention study (agis): 7. the relationship between control of intraocular pressure and visual field deterioration. *American Journal of Ophthalmology*, 130(4):429–40, 2000.

[4] A. L. Coleman and J. Caprioli. The logic behind target intraocular pressure. *American Journal of Ophthalmology*, 147(3):379–380, 2009.

[5] M. A. Kass, D. K. Heuer, E. J. Higginbotham EJ, C. A. Johnson, J. L. Keltner, J. P. Miller, R. K. Parrish 2nd, M. R. Wilson, and M. O. Gordon. The ocular hypertension treatment study: A randomized trial determines that topical ocular hypotensive medication delays or prevents the onset of primary open-angle glaucoma. *Archives of Ophthalmology*, 120(6):701–713, 2002.

[6] M. Leske, A. Heijl, M. Hussein, B. Bengtsson, L. Hyman, E. Komaroff, and Early Manifest Glaucoma Trial Group. Factors for glaucoma progression and the effect of treatment: The early manifest glaucoma trial. *Archives of Ophthalmology*, 121(1):48–56, 2003.

[7] P. R. Lichter, D. C. Musch, B. W. Gillespie, K. E. Guire, N. K. Janz, P. A. Wren, R. P. Mills, and CIGTS Study Group. Interim clinical outcomes in the collaborative initial glaucoma treatment study comparing initial treatment randomized to medications or surgery. *Ophthalmology*, 108(11):1943–1953, 2001.

[8] F. C. Hollows and P. A. Graham. Intra-ocular pressure, glaucoma, and glaucoma suspects in a defined population. *British Journal of Ophthalmology*, 50(10):570–586, 1966.

[9] R. Shah and R. P. Wormald. Glaucoma. *BMJ Clinical Evidence*, 2011.

[10] J. Caprioli and A. L. Coleman. Blood pressure, perfusion pressure, and glaucoma. *American Journal of Ophthalmology*, 149(5):704–712, 2010.

[11] H. A. Quigley. *Pathophysiology of the Optic Nerve Head in Glaucoma*. Butterworths, London, Boston, 1986.

[12] V. P. Costa, A. Harris, D. Anderson, R. Stodtmeister, F. Cremasco, H. Kergoat, J. Lovasik, I. Stalmans, O. Zeitz, I. Lanzl, K. Gugleta, and L. Schmetterer. Ocular perfusion pressure in glaucoma. *Acta Ophthalmologica*, 92(4):e252–e266, 2014.

[13] R. de Boer. *Theory of Porous Media: Highlights in the Historical Development and Current State*. Springer Berlin Heidelberg, 2000.

[14] F. J. Gaspar, F. J. Lisbona, and P. N. Vabishchevich. A finite difference analysis of biot's consolidation model. *Applied Numerical Mathematics*, 44(4):487–506, 2003.

[15] R. W. Lewis and B. A. Schrefler. *The Finite Element Method in the Static and Dynamic Deformation and Consolidation of Porous Media*. Wiley, New York, 1999.

[16] D. Boffi, F. Brezzi, and M. Fortin. *Mixed Finite Element Methods and Applications*. Springer Series in Computational Mechanics. Springer Berlin Heidelberg, Berlin, 2013.

[17] P. J. Phillips. *Finite Element Methods in Linear Poroelasticity: Theoretical and Computational Results*. PhD thesis, The University of Texas at Austin, 2005.

[18] P. J. Phillips and M. F. Wheeler. A coupling of mixed and discontinuous galerkin finite-element methods for poroelasticity. *Computational Geosciences*, 12(4):417–435, 2008.

[19] B. Cockburn, J. Gopalakrishnan, and R. Lazarov. Unified hybridization of discontinuous galerkin, mixed, and continuous galerkin methods for second order elliptic problems. *SIAM Journal on Numerical Analysis*, 47(2):1319–1365, 2009.

[20] O. Coussy. *Poromechanics*. John Wiley & Sons, 2004.

[21] S. Whitaker. *The Method of Volume Averaging*. Springer Netherlands, 1999.

[22] B. Markert. *Porous Media Viscoelasticity with Application to Polymeric Foams*. PhD thesis, Institut für Mechanik der Universität Stuttgart, 2005.

[23] M. H. Friedman. *Principles and Models of Biological Transport*. Springer-Verlag New York, 2008.

[24] A. Hazel. Lecture notes for math 45061: Continuum mechanics.

[25] C. Truesdell. *Thermodynamics of Diffusion*, pages 219–236. Springer New York, New York, NY, 1984.

[26] R. De Boer and W. Ehlers. On the problem of fluid- and gas-filled elasto-plastic solids. *International Journal of Solids and Structures*, 22(11):1231–1242, 1986.

[27] C. A. Eringen. *Theory of Micropolar Elasticity*, pages 101–248. Springer New York, New York, NY, 1999.

[28] W. Ehlers. *Foundations of Multiphasic and Porous Materials*, pages 3–86. Springer Berlin Heidelberg, Berlin, Heidelberg, 2002.

[29] J. Nocedal and S. J. Wright. *Numerical Optimization*. Springer, New York, 2nd edition, 2006.

[30] R. Glowinski. *Variational Methods for the Numerical Solution of Nonlinear Elliptic Problems*. Society for Industrial and Applied Mathematics, Philadelphia, PA, USA, 2015.

[31] V. I. Osipov. *Physicochemical Theory of Effective Stress in Soils*. Springer International Publishing, 2015.

[32] R. M. Bowen. Incompressible porous media models by use of the theory of mixtures. *International Journal of Engineering Science*, 18(9):1129–1148, 1980.

[33] B. D. Coleman and M. E. Gurtin. Thermodynamics with internal state variables. *The Journal of Chemical Physics*, 47(2):597–613, 1967.

[34] K. C. Valanis. *Irreversible Thermodynamics of Continuous Media: Internal Variable Theory*, volume 77 of *CISM International Centre for Mechanical Sciences*. Springer-Verlag Wien, 1971.

[35] Y. C. Fung. *Biomechanics: Mechanical Properties of Living Tissues*. Springer-Verlag, New York, 1981.

[36] W. N. Findley, J. S. Y. Lai, and K. Onaran. *Creep and Relaxation of Nonlinear Viscoelastic Materials: With an Introduction to Linear Viscoelasticity*. North-Holland, Amsterdam, New York, Oxford, 1976.

[37] W. Ehlers. On thermodynamics of elasto-plastic porous media. *Archives of Mechanics*, 41:73–93, 1989.

[38] S. Salsa. *Partial Differential Equations in Action: from Modelling to Theory*. Universitext. Springer, Milano, 2009.

[39] L. Bociu, G. Guidoboni, R. Sacco, and J. T. Webster. Analysis of nonlinear poro-elastic and poro-visco-elastic models. *Archive for Rational Mechanics and Analysis*, pages 1–75, 2016.

[40] D. Picard and M. Fafard. *Three Dimensional Constitutive Viscoelastic Model for Isotropic Materials*, chapter 12. InTech, Rijeka, Croatia, 2011.

[41] N. Huber and C. Tsakmakis. Finite deformation viscoelasticity laws. *Mechanics of Materials*, 32(1):1–18, 2000.

[42] S. Terragni. Poroelastic computational modeling of biological tissues: Application to the mechanics of the eye. Master's thesis, Politecnico di Milano, Milano, Italy, 2013.

[43] E. Detournay and A. H. D. Cheng. *Fundamentals of Poroelasticity*, pages 113–171. Pergamon Press, 1993.

[44] R. de Boer. *Trends in Continuum Mechanics of Porous Media*. Springer Netherlands, 2005.

[45] P. K. Kundu, I. M. Cohen, and D. R. Dowling. *Fluid mechanics*. Academic Press, Amsterdam, Boston, Heidelberg, 6th edition, 2015.

[46] T. Ricken and J. Bluhm. Remodeling and growth of living tissue: A multiphase theory. *Archive of Applied Mechanics*, 80(5):453–465, 2010.

[47] A. Quarteroni, R. Sacco, and F. Saleri. *Numerical Mathematics*. Texts in applied mathematics. Springer, Berlin, 2007.

[48] D. N. Arnold, F. Brezzi, B. Cockburn, and L. D. Marini. Unified analysis of discontinuous galerkin methods for elliptic problems. *SIAM Journal on Numerical Analysis*, 39(5):1749–1779, 2001.

[49] B. Cockburn. *Static Condensation, Hybridization, and the Devising of the HDG Methods*, pages 129–177. Springer International Publishing, 2016.

[50] D. N. Arnold and F. Brezzi. Mixed and nonconforming finite element methods : Implementation, postprocessing and error estimates. *ESAIM: Mathematical Modelling and Numerical Analysis - Modlisation Mathmatique et Analyse Numrique*, 19(1):7–32, 1985.

[51] F. J. Sayas. From raviart-thomas to hdg, 2013.

[52] R. M. Kirby, S. J. Sherwin, and B. Cockburn. To cg or to hdg: A comparative study. *Journal of Scientific Computing*, 51(1):183–212, 2012.

[53] B. Cockburn, J. Gopalakrishnan, and F. J. Sayas. A projection-based error analysis of hdg methods. *Mathematics of Computation*, 79(271):1351–1367, 7 2010.

[54] B. Cockburn, B. Dong, J. Guzmán, M. Restelli, and R. Sacco. A hybridizable discontinuous galerkin method for steady-state convection-diffusion-reaction problems. *SIAM Journal of Scientific Computing*, 31(5):3827–3846, 2009.

[55] W. Qiu and K. Shi. An hdg method for convection diffusion equation. *Journal of Scientific Computing*, 66(1):346–357, 2016.

[56] N. C. Nguyen, J. Peraire, and B. Cockburn. An implicit high-order hybridizable discontinuous galerkin method for nonlinear convectiondiffusion equations. *Journal of Computational Physics*, 228(23):8841–8855, 2009.

[57] W. Qiu, J. Shen, and K. Shi. An hdg method for linear elasticity with strong symmetric stresses, 2013.

[58] H. Kabaria, A. J. Lew, and B. Cockburn. A hybridizable discontinuous galerkin formulation for non-linear elasticity. *Computer Methods in Applied Mechanics and Engineering*, 283:303–329, 2015.

[59] B. Cockburn and F. Sayas. Divergence-conforming hdg methods for stokes flows. *Mathematics of Computation*, 83(288):1571–1598, 2014.

[60] J. Peraire, N. C. Nguyen, and B. Cockburn. *A Hybridizable Discontinuous Galerkin Method for the Compressible Euler and Navier-Stokes Equations*. 2010.

[61] W. Qiu and K. Shi. A superconvergent hdg method for the incompressible navierstokes equations on general polyhedral meshes. *IMA Journal of Numerical Analysis*, 36(4):1943–1967, 2016.

[62] N. C. Nguyen, J. Peraire, and B. Cockburn. High-order implicit hybridizable discontinuous galerkin methods for acoustics and elastodynamics. *Journal of Computational Physics*, 230(10):3695–3718, 2011.

[63] N. C. Nguyen, J. Peraire, and B. Cockburn. Hybridizable discontinuous galerkin methods for the time-harmonic maxwell's equations. *Journal of Computational Physics*, 230(19):7151–7175, 2011.

[64] H. Chen, W. Qiu, and K. Shi. A superconvergent hdg method for the maxwell equations, 2016.

[65] J. P. Sheldon, S. T. Miller, and J. S. Pitt. A hybridizable discontinuous galerkin method for modeling fluidstructure interaction. *Journal of Computational Physics*, 326:91–114, 2016.

[66] A. Zenisek. The existence and uniqueness theorem in biot's consolidation theory. *Applications of Mathematics*, 29(3):194–211, 1984.

[67] S. Owczarek. A galerkin method for biot consolidation model. *Mathematics and Mechanics of Solids*, 15(1):42–56, 2010.

[68] R. E. Showalter. Diffusion in poro-elastic media. *Journal of Mathematical Analysis and Applications*, 251(1):310–340, 2000.

[69] R. E. Showalter and N. Su. Partially saturated flow in a poroelastic medium. *Discrete and Continuous Dynamical Systems - Series B*, 1(4):403–420, 2001.

[70] R. E. Showalter and U. Stefanelli. Diffusion in poro-plastic media. *Mathematical Methods in the Applied Sciences*, 27:2131–2151, 2004.

[71] Y. Cao, S. Chen, and A. J. Meir. Analysis and numerical approximations of equations of nonlinear poroelasticity. *Discrete and Continuous Dynamical Systems - Series B*, 18(5):1253–1273, 2013.

[72] Y. Cao, S. Chen, and A. J. Meir. Steady flow in a deformable porous medium. *Mathematical Methods in the Applied Sciences*, 37(7):1029–1041, 2014.

[73] Y. Cao, S. Chen, and A. J. Meir. Quasilinear poroelasticity: Analysis and hybrid finite element approximation. *Numerical Methods for Partial Differential Equations*, 31(4):1174–1189, 2015.

[74] P. Causin, G. Guidoboni, A. Harris, D. Prada, R. Sacco, and S. Terragni. A poroelastic model for the perfusion of the lamina cribrosa in the optic nerve head. *Mathematical Biosciences*, 257:33–41, 2014.

[75] R. Grytz, I. A. Sigal, J. W. Ruberti, G. Meschke, and J. C. Downs. Lamina cribrosa thickening in early glaucoma predicted by a microstructure motivated growth and remodeling approach. *Mechanics of Materials*, 44:99–109, 2012.

[76] R. Stenberg. A family of mixed finite elements for the elasticity problem. *Numerische Mathematik*, 53(5):513–538, 1988.

[77] M. Farhloul and M. Fortin. Dual hybrid methods for the elasticity and the stokes problems: A unified approach. *Numerische Mathematik*, 76(4):419–440, 1997.

[78] B. Cockburn and K. Shi. Superconvergent hdg methods for linear elasticity with weakly symmetric stresses. *IMA Journal of Numerical Analysis*, 33(3):747–770, 2013.

[79] C. Lehrenfeld. *Hybrid Discontinuous Galerkin Methods for Solving Incompressible Flow Problems*. PhD thesis, RWTH Aachen University, 2010.

[80] X. S. Li, J. W. Demmel, J. R. Gilbert, L. Grigori, M. Shao, and I. Yamazaki. SuperLU Users' Guide. Technical Report LBNL-44289, Lawrence Berkeley National Laboratory, September 1999. `http://crd.lbl.gov/~xiaoye/SuperLU/`. Last update: March 2016.

[81] X. S. Li and J. W. Demmel. SuperLU DIST: A scalable distributed-memory sparse direct solver for unsymmetric linear systems. *ACM Trans. Mathematical Software*, 29(2):110–140, June 2003.

[82] J. D. Logan. *Applied Mathematics*. John Wiley & Sons, Hoboken, New Jersey, 4th edition, 2013.

[83] G. Guidoboni, A. Harris, L. Carichino, Y. Arieli, and B. A. Siesky. Effect of intraocular pressure on the hemodynamics of the central retinal artery: a mathematical model. *Mathematical Biosciences and Engineering*, pages 523–546, 2014.

[84] S. L-Y Woo, A. S. Kobayashi, W. A. Schlegel, and C. Lawrence. Nonlinear material properties of intact cornea and sclera. *Experimental Eye Research*, 14(1):29–39, 1972.

[85] P. J. Phillips and M. F. Wheeler. A coupling of mixed and continuous galerkin finite element methods for poroelasticity i: the continuous in time case. *Computational Geosciences*, 11(2):131–144, 2007.

[86] S. I. Barry and G. N. Mercer. Exact Solutions for Two-Dimensional Time-Dependent Flow and Deformation Within a Poroelastic Medium. *Journal of Applied Mechanics*, 66:536–540, 1999.

[87] Y. Saad and M. H. Schultz. Gmres: A generalized minimal residual algorithm for solving nonsymmetric linear systems. *SIAM J. Sci. Stat. Comput.*, 7(3):856–869, July 1986.

[88] R. Barrett, M. Berry, T. Chan, J. Demmel, J. Donato, J. Dongarra, V. Eijkhout, R. Pozo, C. Romine, and H. van der Vorst. *Templates for the Solution of Linear Systems: Building Blocks for Iterative Methods*. Society for Industrial and Applied Mathematics, 1994.

[89] E. F. Kaasschieter and A. J. H. Frijns. Squeezing a sponge: A three dimensional solution in poroelasticity. *Computational Geosciences*, 7:49–59, 2003.

[90] S. M. Drance, G. R. Douglas, K. Wijsman, M. Schulzer, and R. J. Britton. Response of blood flow to warm and cold in normal and low-tension glaucoma patients. *American Journal of Ophthalmology*, 105(1):35–39, 1988.

[91] J. Flammer, S. Orgül, V. P. Costa, N. Orzalesi, G. K. Krieglstein, L. M. Serra, J. P. Renard, and E. Stefánsson. The impact of ocular blood flow in glaucoma. *Progress in Retinal and Eye Research*, 21(4):359–393, 2002.

[92] F. Galassi, B. Giambene, and R. Varriale. Systemic vascular dysregulation and retrobulbar hemodynamics in normal-tension glaucoma. *Investigative Ophthalmology & Visual Science*, 52(7):4467–4471, 2011.

[93] P. Hamard, H. Hamard, and J. Dufaux. Blood flow rate in the microvasculature of the optic nerve head in primary open angle alaucoma. a new approach. *Survey of Ophthalmology*, 38:S87–S94, 1994.

[94] P. Hamard, H. Hamard, J. Dufaux, and S. Quesnot. Optic nerve head blood flow using a laser doppler velocimeter and haemorheology in primary open angle glaucoma and normal pressure glaucoma. *British Journal of Ophthalmology*, 78(6):449–453, 1994.

[95] A. Harris, E. Rechtman, B. Siesky, C. Jonescu-Cuypers, L. McCranor, and H. J. Garzozi. The role of optic nerve blood flow in the pathogenesis of glaucoma. *Ophthalmology Clinics of North America*, 18(3):345–353, 2005.

[96] T. Wong and P. Mitchell. The eye in hypertension. *The Lancet*, 369(9559):425–435, 2007.

[97] A. Alm and A. Bill. Ocular and optic nerve blood flow at normal and increased intraocular pressures in monkeys (macaca irus): A study with radioactively labelled microspheres including flow determinations in brain and some other tissues. *Experimental Eye Research*, 15(1):15–29, 1973.

[98] K. R. Porsaa. Experimental studies on the vasomotor innervation of the retinal arteries (tr. by r. fraser). *Archives of Internal Medicine*, 78(3), 1946.

[99] O. B. Paulson, S. Strandgaard, and L. Edvinsson. Cerebral autoregulation. *Cerebrovascular and Brain Metabolism Reviews*, 2(2):161–192, 1990.

[100] R. M. Berne, R. M. Knabb, S. W. Ely, and R. Rubio. Adenosine in the local regulation of blood flow: A brief overview. *Federation Proceedings*, 42(15):3136–3142, 1983.

[101] H. Rein. Vasomotorische regulationen. *Ergebnisse der Physiologie*, 32(1):28–72, 1931.

[102] B. Folkow, R. R. Sonnenschein, and D. L. Wright. Loci of neurogenic and metabolic effects on precapillary vessels of skeletal muscle. *Acta Physiologica Scandinavica*, 81(4):459–471, 1971.

[103] O. Lundgren. Autoregulation of intestinal blood flow: Physiology and pathophysiology. *Journal of Hypertension*, 7(4):S79–S84, 1989.

[104] M. Carlström, C. S. Wilcox, and W. J. Arendshorst. Renal autoregulation in health and disease. *Physiological Reviews*, 95(2):405–511, 2015.

[105] G. Garhöfer, H. Resch, G. Weigert, S. Lung, C. Simader, and L. Schmetterer. Short-term increase of intraocular pressure does not alter the response of retinal and optic nerve head blood flow to flicker stimulation. *Investigative Ophthalmology & Visual Science*, 46(5):1721–1725, 2005.

[106] G. Garhöfer, C. Zawinka, K. H. Huemer, L. Schmetterer, and G. T. Dorner. Flicker lightinduced vasodilatation in the human retina: Effect of lactate and changes in mean arterial pressure. *Investigative Ophthalmology & Visual Science*, 44(12):5309–5314, 2003.

[107] C. E. Riva, J. E. Grunwald, and B. L. Petrig. Autoregulation of human retinal blood flow. an investigation with laser doppler velocimetry. *Investigative Ophthalmology & Visual Science*, 27(12):1706–1712, 1986.

[108] C. E. Riva, M. Hero, P. Titze, and B. Petrig. Autoregulation of human optic nerve head blood flow in response to acute changes in ocular perfusion pressure. *Graefe's Archive for Clinical and Experimental Ophthalmology*, 235(10):618–626, 1997.

[109] P. J. Mackenzie and G. A. Cioffi. Vascular anatomy of the optic nerve head. *Canadian Journal of Ophthalmology*, 43(3):308–312, 2008.

[110] C. F. Burgoyne. A biomechanical paradigm for axonal insult within the optic nerve head in aging and glaucoma. *Experimental Eye Research*, 93(2):120–132, 2011.

[111] F. C. Delori and K. P. Pflibsen. Spectral reflectance of the human ocular fundus. *Applied Optics*, 28(6):1061–1077, 1989.

[112] B. Marek, A. Harris, P. Kanakamedala, E. Lee, A. Amireskandari, L. Carichino, G. Guidoboni, L. A. Tobe, and B. Siesky. Cerebrospinal fluid pressure and glaucoma: Regulation of trans-lamina cribrosa pressure. *British Journal of Ophthalmology*, 98(6):721–725, 2014.

[113] W. H. Morgan, D. Y. Yu, V. A. Alder, S. J. Cringle, R. L. Cooper, P. H. House, and I. J. Constable. The correlation between cerebrospinal fluid pressure and retrolaminar tissue pressure. *Investigative Ophthalmology & Visual Science*, 39(8):1419–1428, 1998.

[114] R. Grytz, G. Meschke, and J. B. Jonas. The collagen fibril architecture in the lamina cribrosa and peripapillary sclera predicted by a computational remodeling approach. *Biomechanics and Modeling in Mechanobiology*, 10(3):371–382, 2011.

[115] M. D. Roberts, V. Grau, J. Grimm, J. Reynaud, A. J. Bellezza, C. F. Burgoyne, and J. C. Downs. Remodeling of the connective tissue microarchitecture of the lamina cribrosa in early experimental glaucoma. *Investigative Ophthalmology & Visual Science*, 50(2):681–690, 2009.

[116] M. Winkler, B. Jester, C. Nien-Shy, S. Massei, D. S. Minckler, J. V. Jester, and D. J. Brown. High resolution three-dimensional reconstruction of the collagenous matrix of the human optic nerve head. *Brain Research Bulletin*, 81(2–3):339–348, 2010.

[117] M. R. Hernandez, H. Miao, and T. Lukas. Astrocytes in glaucomatous optic neuropathy. In C. Nucci, L. Cerulli, N. N. Osborne, and G. Bagetta, editors, *Glaucoma: An Open Window to Neurodegeneration and Neuroprotection*, volume 173 of *Progress in Brain Research*, pages 353–373. Elsevier, 2008.

[118] A. Harris, C. J. Cuypers, and L. Kagemann. *Atlas of Ocular Blood Flow: Vascular Anatomy, Pathophysiology and Metabolism*. Butterworth-Heinemann, Philadelphia, 2nd edition, 2010.

[119] S. S. Hayreh. The blood supply of the optic nerve head and the evaluation of it - myth and reality. *Progress in Retinal and Eye Research*, 20(5):563–593, 2001.

[120] S. S. Hayreh. The 1994 Von Sallman lecture the optic nerve head circulation in health and disease. *Experimental Eye Research*, 61(3):259–272, 1995.

[121] S. S. Hayreh. Inter-individual variation in blood supply of the optic nerve head. *Documenta Ophthalmologica*, 59(3):217–246, 1985.

[122] S. Singh. The central artery of the retina ii. a study of its distribution and anastomoses. *British Journal of Ophthalmology*, 44(5):280–299, 1960.

[123] E. Onda, G. A. Cioffi, D. R. Bacon, and E. M. Van Buskirk. Microvasculature of the human optic nerve. *American Journal of Ophthalmology*, 120(1):92–102, 1995.

[124] L. Pasquale, J. B. Jonas, and D. R. Anderson. *Anatomy and Physiology*, pages 3–13. Kugler Publications, Amsterdam, 2009.

[125] K. Ohno-Matsui, S. Futagami, S. Yamashita, and T. Tokoro. Zinnhaller arterial ring observed by icg angiography in high myopia. *British Journal of Ophthalmology*, 82(12):1357–1362, 1998.

[126] T. Awai. Angioarchitecture of intraorbital part of human optic nerve. *Japanese Journal of Ophthalmology*, 29(1):79–98, 1985.

[127] R. Inoue, M. Hangai, Y. Kotera, H. Nakanishi, S. Mori, S. Morishita, and N. Yoshimura. Three-dimensional high-speed optical coherence tomography imaging of lamina cribrosa in glaucoma. *Ophthalmology*, 116(2):214–222, 2009.

[128] Z. Nadler, B. Wang, G. Wollstein, J. E. Nevins, H. Ishikawa, R. Bilonick, L. Kagemann, I. A. Sigal, R. D. Ferguson, A. Patel, D. X. Hammer, and J. S. Schuman. Repeatability of in vivo 3d lamina cribrosa microarchitecture using adaptive optics spectral domain optical coherence tomography. *Biomedical Optics Express*, 5(4):1114–1123, 2014.

[129] V. J. Srinivasan, D. C. Adler, Y. Chen, I. Gorczynska, R. Huber, J. S. Duker, J. S. Schuman, and J. G. Fujimoto. Ultrahigh-speed optical coherence tomography for three-dimensional and en face imaging of the retina and optic nerve head. *Investigative Ophthalmology & Visual Science*, 49(11):5103–5110, 2008.

[130] B. Wang, J. E. Nevins, Z. Nadler, G. Wollstein, H. Ishikawa, R. A. Bilonick, L. Kagemann, I. A. Sigal, I. Grulkowski, J. J. Liu, M. Kraus, C. D. Lu, J. Hornegger, J. G. Fujimoto, and J. S. Schuman. Reproducibility of in-vivo oct measured three-dimensional human lamina cribrosa microarchitecture. *PLoS One*, 9(4):e95526, 2014.

[131] C. F. Burgoyne, J. C. Downs, A. J. Bellezza, J. K. F. Suh, and R. T. Hart. The optic nerve head as a biomechanical structure: A new paradigm for understanding the role of iop-related stress and strain in the pathophysiology of glaucomatous optic nerve head damage. *Progress in Retinal and Eye Research*, 24(1):39–73, 2005.

[132] J. C. Downs, M. D. Roberts, C. F. Burgoyne, and R. T. Hart. Multiscale finite element modeling of the lamina cribrosa microarchitecture in the eye. In *2009 Annual International Conference of the IEEE Engineering in Medicine and Biology Society*, pages 4277–4280, 2009.

[133] D. R. Anderson. Vascular supply to the optic nerve of primates. *American Journal of Ophthalmology*, 70(3):341–351, 1970.

[134] D. R. Anderson. Ultrastructure of human and monkey lamina cribrosa and optic nerve head. *Archives of Ophthalmology*, 82(6):800–814, 1969.

[135] I. A. Sigal, B. Wang, N. G. Strouthidis, T. Akagi, and M. J. A. Girard. Recent advances in oct imaging of the lamina cribrosa. *British Journal of Ophthalmology*, 98(Suppl 2):ii34–ii39, 2014.

[136] M. F. Lieberman, A. E. Maumenee, and W. R. Green. Histologic studies of the vasculature of the anterior optic nerve. *American Journal of Ophthalmology*, 82(3):405–423, 1976.

[137] X. D. Ye, A. M. Laties, and R. A. Stone. Peptidergic innervation of the retinal vasculature and optic nerve head. *Investigative Ophthalmology & Visual Science*, 31(9):1731–1737, 1990.

[138] G. Ferrari-Dileo. Beta 1 and beta 2 adrenergic binding sites in bovine retina and retinal blood vessels. *Investigative Ophthalmology & Visual Science*, 29(5):695–699, 1988.

[139] A. M. Hoste, P. J. Boels, D. L. Brutsaert, and J. J. De Laey. Effect of alpha-1 and beta agonists on contraction of bovine retinal resistance arteries in vitro. *Investigative Ophthalmology & Visual Science*, 30(1):44–50, 1989.

[140] C: E. Riva, M. Geiser, B. L. Petrig, and the Ocular Blood Flow Research Association. Ocular blood flow assessment using continuous laser doppler flowmetry. *Acta Ophthalmologica*, 88(6):622–629, 2010.

[141] C. E. Riva, E. Logean, and B. Falsini. Visually evoked hemodynamical response and assessment of neurovascular coupling in the optic nerve and retina. *Progress in Retinal and Eye Research*, 24(2):183–215, 2005.

[142] Y. Jia, J. C. Morrison, J. Tokayer, O. Tan, L. Lombardi, B. Baumann, C. D. Lu, W. Choi, J. G. Fujimoto, and D. Huang. Quantitative oct angiography of optic nerve head blood flow. *Biomedical Optics Express*, 3(12):3127–3137, 2012.

[143] D. Huang, E. A. Swanson, C. P. Lin, J. S. Schuman, W. G. Stinson, W. Chang, M. R. Hee, T. Flotte, K. Gregory, C. A. Puliafito, and et al. Optical coherence tomography. *Science*, 254(5035):1178–1181, 1991.

[144] Y. Jia, O. Tan, J. Tokayer, B. Potsaid, Y. Wang, J. J. Liu, M. F. Kraus, H. Subhash, J. G. Fujimoto, J. Hornegger, and D. Huang. Split-spectrum amplitude-decorrelation angiography with optical coherence tomography. *Optics Express*, 20(4):4710–4725, 2012.

[145] T. H. Williamson and A. Harris. Color doppler ultrasound imaging of the eye and orbit. *Survey of Ophthalmology*, 40(4):255–267, 1996.

[146] K. Srikanth, M. A. Kumar, S. Selvasundari, and M. L. Prakash. Colour doppler imaging of ophthalmic artery and central retinal artery in glaucoma patients with and without diabetes mellitus. *Journal of Clinical & Diagnostic Research*, 8(4):VC01–VC02, 2014.

[147] A. Harris, I. Januleviciene, and B. Siesky. *Clinical Measurements of Ocular Blood Flow*, pages 19–56. Kugler Publications, Amsterdam, 2009.

[148] T. Sugiyama, T. Utsumi, I. Azuma, and H. Fujii. Measurement of optic nerve head circulation: Comparison of laser speckle and hydrogen clearance methods. *Japanese Journal of Ophthalmology*, 40(3):339–343, 1996.

[149] J. Takayama, A. Tomidokoro, K. Ishii, Y. Tamaki, Y. Fukaya, T. Hosokawa, and M. Araie. Time course of the change in optic nerve head circulation after an acute increase in intraocular pressure. *Investigative Ophthalmology & Visual Science*, 44(9):3977–3985, 2003.

[150] Y. Tamaki, M. Araie, Y. Fukaya, M. Nagahara, A. Imamura, M. Honda, R. Obata, and K. Tomita. Effects of lomerizine, a calcium channel antagonist, on retinal and optic nerve head circulation in rabbits and humans. *Investigative Ophthalmology & Visual Science*, 44(11):4864–4871, 2003.

[151] Y. Tamaki, M. Araie, E. Kawamoto, S. Eguchi, and H. Fujii. Non-contact, two-dimensional measurement of tissue circulation in choroid and optic nerve head using laser speckle phenomenon. *Experimental Eye Research*, 60(4):373–383, 1995.

[152] K. Tomita, M. Araie, Y. Tamaki, M. Nagahara, and T. Sugiyama. Effects of nilvadipine, a calcium antagonist, on rabbit ocular circulation and optic nerve head circulation in ntg subjects. *Investigative Ophthalmology & Visual Science*, 40(6):1144–1151, 1999.

[153] Y. Tamaki, M. Araie, K. Tomita, and A. Tomidokoro. Time-course of changes in nicardipine effects on microcirculation in retina and optic nerve head in living rabbit eyes. *Japanese journal of ophthalmology*, 40(2):202–211, 1996.

[154] Y. Tamaki, M. Araie, K. Tomita, and H. Urashima. Effects of pranidipine, a new calcium antagonist, on circulation in the choroid, retina and optic nerve head. *Current Eye Research*, 19(3):241–247, 1999.

[155] K. Tomita, A. Tomidokoro, Y. Tamaki, M. Araie, M. Matsubara, and Y. Fukaya. Effects of semotiadil, a novel calcium antagonist, on the retina and optic nerve head circulation. *Journal of Ocular Pharmacology and Therapeutics*, 16(3):231–239, 2009.

[156] T. Sugiyama, M. Araie, C. E. Riva, L. Schmetterer, and S. Orgul. Use of laser speckle flowgraphy in ocular blood flow research. *Acta Ophthalmologica*, 88(7):723–729, 2010.

[157] H. A. Quigley. Glaucoma. *The Lancet*, 377(9774):1367–1377, 2011.

[158] H. Dongqi and R. Zenqin. A biomathematical model for pressure-dependent lamina cribrosa behavior. *Journal of Biomechanics*, 32(6):579–584, 1999.

[159] E. A. Sander, J. C. Downs, R. T. Hart, C. F. Burgoyne, and E. A. Nauman. A cellular solid model of the lamina cribrosa: Mechanical dependence on morphology. *Journal of Biomechanical Engineering*, 128(6):879–889, 2006.

[160] I. A. Sigal, J. G. Flanagan, I. Tertinegg, and C. R. Ethier. Modeling individual-specific human optic nerve head biomechanics. part i: Iop-induced deformations and influence of geometry. *Biomechanics and Modeling in Mechanobiology*, 8(2):85–98, 2009.

[161] I. A. Sigal, J. G. Flanagan, I. Tertinegg, and C. R. Ethier. Modeling individual-specific human optic nerve head biomechanics. part ii: Influence of material properties. *Biomechanics and Modeling in Mechanobiology*, 8(2):99–109, 2009.

[162] R. Grytz and G. Meschke. Constitutive modeling of crimped collagen fibrils in soft tissues. *Journal of the Mechanical Behavior of Biomedical Materials*, 2(5):522–533, 2009.

[163] R. Grytz and G. Meschke. A computational remodeling approach to predict the physiological architecture of the collagen fibril network in corneo-scleral shells. *Biomechanics and Modeling in Mechanobiology*, 9(2):225–235, 2010.

[164] R. Grytz, C. A. Girkin, V. Libertiaux, and J. C. Downs. Perspectives on biomechanical growth and remodeling mechanisms in glaucoma. *Mechanics Research Communications*, 42:92–106, 2012.

[165] M. J. Girard, E. Birgersson, H. L. Leo, A. Thiery, and T. Chuangsuwanich. Factors influencing lamina cribrosa microcapillary hemodynamics and oxygen concentrations. In *ARVO 2016 Annual Meeting Abstracts: 426, Glaucoma Biomechanics*, 2016.

[166] J. C. Downs, J. K. F. Suh, K. A. Thomas, A. J. Bellezza, R. T. Hart, and C. F. Burgoyne. Viscoelastic material properties of the peripapillary sclera in normal and early-glaucoma monkey eyes. *Investigative Ophthalmology & Visual Science*, 46(2):540–546, 2005.

[167] J. R. Palko, S. Iwabe, X. Pan, G. Agarwal, A. M. Komáromy, and J. Liu. Biomechanical properties and correlation with collagen solubility profile in the posterior sclera of canine eyes with an adamts10 mutationscleral biomechanics and collagen solubility. *Investigative Ophthalmology & Visual Science*, 54(4):2685–2695, 2013.

[168] J. B. Jonas, C. Y. Mardin, U. S. Schrehardt, and G. O. Naumann. Morphometry of the human lamina cribrosa surface. *Investigative Ophthalmology & Visual Science*, 32(2):401–405, 1991.

[169] I. A. Sigal, J. G. Flanagan, I. Tertinegg, and C. R. Ethier. Finite element modeling of optic nerve head biomechanics. *Investigative Ophthalmology & Visual Science*, 45(12):4378–4387, 2004.

[170] J. Arciero, A. Harris, B. Siesky, A. Amireskandari, V. Gershuny, A. Pickrell, and G. Guidoboni. Theoretical analysis of vascular regulatory mechanisms contributing to retinal blood flow autoregulation. *Investigative Ophthalmology & Visual Science*, 54(8):5584–5593, 2013.

[171] C. Balaratnasingam, M. H. Kang, P. Yu, G. Chan, W. H. Morgan, S. J. Cringle, and D. Y. Yu. Comparative quantitative study of astrocytes and capillary distribution in optic nerve laminar regions. *Experimental Eye Research*, 121:11–22, 2014.

[172] G. Guidoboni, A. Harris, S. Cassani, J. Arciero, B. Siesky, A. Amireskandari, L. Tobe, P. Egan, I. Januleviciene, and J. Park. Intraocular pressure, blood pressure, and retinal blood flow autoregulation: A mathematical model to clarify their relationship and clinical relevance. *Investigative Ophthalmology & Visual Science*, 55(7):4105–4118, 2014.

[173] H. Yang, J. C. Downs, C. Girkin, L. Sakata, A. Bellezza, H. Thompson, and C. F. Burgoyne. 3-d histomorphometry of the normal and early glaucomatous monkey optic nerve head: Lamina cribrosa and peripapillary scleral position and thickness. *Investigative Ophthalmology & Visual Science*, 48(10):4597–607, 2007.

[174] W. H. Morgan, B. C. Chauhan, D. Y. Yu, S. J. Cringle, V. A. Alder, and P. H. House. Optic disc movement with variations in intraocular and cerebrospinal fluid pressure. *Investigative Ophthalmology & Visual Science*, 43(10):3236–3242, 2002.

[175] Y. Dongmei, S. McPheeters, G. Johnson, U. Utzinger, and J. P. Vande Geest. Microstructural differences in the human posterior sclera as a function of age and race. *Investigative Ophthalmology & Visual Science*, 52(2):821–829, 2011.

APPENDICES

Appendix A. Constitutive equations in mixed form

Constitutive Equation of the Total Stress Tensor in Mixed Form

Proposition A.0.1 *The constitutive equation* (3.67) *for the total stress tensor* $\underline{\underline{\sigma}}^{(j+1)}$

$$\begin{aligned}\underline{\underline{\sigma}}^{(j+1)} &= 2\mu^{ve}\underline{\underline{\varepsilon}}(\mathbf{u}^{(j+1)}) + \lambda^{ve}(\nabla\cdot\mathbf{u}^{(j+1)})\underline{\underline{I}} \\ &\quad - \frac{\delta}{\Delta t}(2\mu^{v}\underline{\underline{\varepsilon}}(\mathbf{u}^{i}) + \lambda^{v}(\nabla\cdot\mathbf{u}^{i})\underline{\underline{I}}) - p^{(j+1)}\underline{\underline{I}},\end{aligned} \tag{A.1}$$

can be rewritten in mixed form as

$$c_1\underline{\underline{\sigma}}^{(j+1)} + c_2(\operatorname{tr}\underline{\underline{\sigma}}^{(j+1)})\underline{\underline{I}} - \underline{\underline{\varepsilon}}(\mathbf{u}^{(j+1)}) + P_T p^{(j+1)}\underline{\underline{I}} = -c_3\underline{\underline{\varepsilon}}(\mathbf{u}^{(j)}) - c_4(\nabla\cdot\mathbf{u}^{i})\underline{\underline{I}}, \tag{A.2}$$

with

$$c_1 = \frac{1}{2\mu^{ve}}, \qquad c_2 = -\frac{\lambda^{ve}}{2\mu^{ve}(2\mu^{ve}+3\lambda^{ve})} = -\frac{1}{2\mu^{ve}\left(\dfrac{2\mu^{ve}}{\lambda^{ve}}+3\right)}, \tag{A.3}$$

$$c_3 = \frac{\delta}{\Delta t}(2\mu^{v}c_1), \qquad c_4 = \frac{\delta}{\Delta t}(2\mu^{v}c_2 + \lambda^{v}P_T), \tag{A.4}$$

$$P_T = c_1 + 3c_2. \tag{A.5}$$

Proof Let us introduce a fourth order tensor $\overset{4}{C}$ acting on a second order tensor $\underline{\underline{T}}$ as follows

$$\overset{4}{C}\,\underline{\underline{T}} = 2\mu^{ve}\underline{\underline{T}} + \lambda^{ve}(\operatorname{tr}\underline{\underline{T}})\underline{\underline{I}}. \tag{A.6}$$

Using (A.6), we can rewrite (A.1) as

$$\underline{\underline{\sigma}}^{(j+1)} = \overset{4}{C}\,\underline{\underline{\varepsilon}}(\mathbf{u}^{(j+1)}) - \frac{\delta}{\Delta t}(2\mu^{v}\underline{\underline{\varepsilon}}(\mathbf{u}^{i}) + \lambda^{v}(\nabla\cdot\mathbf{u}^{i})\underline{\underline{I}}) - p^{(j+1)}\underline{\underline{I}}.$$

Multiplying the last equation by $\overset{4}{\mathcal{A}} = \left(\overset{4}{C}\right)^{-1}$ and rearranging terms, we obtain

$$\overset{4}{\mathcal{A}}\,\underline{\underline{\sigma}}^{(j+1)} - \underline{\underline{\varepsilon}}(\mathbf{u}^{(j+1)}) + p^{(j+1)}\overset{4}{\mathcal{A}}\,\underline{\underline{I}} = -\frac{\delta}{\Delta t}(2\mu^{v}\overset{4}{\mathcal{A}}\,\underline{\underline{\varepsilon}}(\mathbf{u}^{i}) + \lambda^{v}(\nabla\cdot\mathbf{u}^{i})\overset{4}{\mathcal{A}}\,\underline{\underline{I}}). \tag{A.7}$$

The fourth order tensor $\overset{4}{\mathcal{A}}$ is formally equivalent to the compliance tensor $\overset{4}{\mathcal{B}}$ in Hooke-type elasticity laws $\overset{4}{\mathcal{B}}\underline{\underline{\sigma}} = \underline{\underline{\varepsilon}}(\mathbf{u})$, which means that $\overset{4}{\mathcal{A}}$ acts on a second order tensor $\underline{\underline{T}}$ as follows

$$\overset{4}{\mathcal{A}}\underline{\underline{T}} = \frac{1}{2\mu^{ve}}\underline{\underline{T}} - \frac{\lambda^{ve}}{2\mu^{ve}(2\mu^{ve}+3\lambda^{ve})}(\operatorname{tr}\underline{\underline{T}})\underline{\underline{I}}. \tag{A.8}$$

Using $\underline{\underline{T}} = \underline{\underline{\sigma}}$ in (A.8) and comparing the result with (A.2), (A.7), we immediately get (A.3). Using $\underline{\underline{T}} = \underline{\underline{I}}$ in (A.8) and the definition of c_1, c_2, we have

$$\overset{4}{\mathcal{A}}\underline{\underline{I}} = c_1\underline{\underline{I}} + c_2(\operatorname{tr}\underline{\underline{I}})\underline{\underline{I}} = (c_1+3c_2)\underline{\underline{I}},$$

which, compared with (A.2) and (A.7), implies (A.5). Plugging $\underline{\underline{T}} = \underline{\underline{\varepsilon}}(\mathbf{u}^i)$ in (A.8), we get

$$\overset{4}{\mathcal{A}}\underline{\underline{\varepsilon}}(\mathbf{u}^i) = c_1\underline{\underline{\varepsilon}}(\mathbf{u}^i) + c_2(\operatorname{tr}\underline{\underline{\varepsilon}}(\mathbf{u}^i))\underline{\underline{I}} = c_1\underline{\underline{\varepsilon}}(\mathbf{u}^i) + c_2(\nabla\cdot\mathbf{u}^i)\underline{\underline{I}},$$

by definition of $\underline{\underline{\varepsilon}}(\mathbf{u}^i)$. Using the last equation and the definition of P_T, the right hand side of (A.7) reads

$$\begin{aligned}
&-\frac{\delta}{\Delta t}(2\mu^v\overset{4}{\mathcal{A}}\underline{\underline{\varepsilon}}(\mathbf{u}^i) + \lambda^v(\nabla\cdot\mathbf{u}^i)\overset{4}{\mathcal{A}}\underline{\underline{I}}) \\
&\qquad = -\frac{\delta}{\Delta t}(2\mu^v(c_1\underline{\underline{\varepsilon}}(\mathbf{u}^i) + c_2(\nabla\cdot\mathbf{u}^i)\underline{\underline{I}}) + \lambda^v(\nabla\cdot\mathbf{u}^i)P_T\underline{\underline{I}}) \\
&\qquad = -\frac{\delta}{\Delta t}2\mu^v c_1\underline{\underline{\varepsilon}}(\mathbf{u}^i) - \frac{\delta}{\Delta t}(2\mu^v c_2 + \lambda^v P_T)(\nabla\cdot\mathbf{u}^i)\underline{\underline{I}},
\end{aligned}$$

which proves (A.4). □

Appendix B. Scaling

In this appendix, we will show how problem (3.44)–(3.54) can be scaled and reformulated in terms of dimensionless variables.

Scaling is a technique used to rewrite a problem in terms of new dimensionless variables. This procedure is useful, or even necessary in some situations, especially when comparing the magnitude of various terms in an equation and understanding whether some of them can be neglected [82]. Another application is provided in Section 3.3.2, where scaling is used to precondition system (3.44)–(3.54) and restore the accuracy of the HDG method.

For example, significant changes in OPP occur within one cardiac cycle ($\approx 1\,\mathrm{s}$), implying that this problem has a *characteristic time scale* $t_c = 1\,\mathrm{s}$. In some cases, there are multiple time scales. For example, OPP itself has also been shown to follow a pattern of circadian variations ($24\,\mathrm{h}$) [12]. Problems can also be characterized by different space scales:

- Perfusion of the lamina cribrosa in the ONH involves at least 3 orders of magnitude as we progress from the capillaries running within the laminar beams ($\approx 1 \times 10^{-6}\,\mathrm{m}$) to the dimensions of the optic nerve canal ($\approx 1 \times 10^{-3}\,\mathrm{m}$) [1].
- There is evidence that IOP elevation causes the lamina to remodel into a thicker more posterior structure by incorporating more connective tissue [75]. This remodeling process involves both macroscopic effect, such as IOP ($\approx 1 \times 10^{-3}\,\mathrm{m}$), and mechanisms occurring at the level of the collagen fibers forming the connective tissue of the lamina cribrosa ($\approx 1 \times 10^{-8}\,\mathrm{m}$).

Thus, for some problems, choosing appropriate characteristic time and spatial scales could be quite a delicate task and must be carried out with care. Once a characteristic

scale x_c has been identified for a variable, say x, a new dimensionless variable $\bar{x}$ can be introduced by

$$\bar{x} = \frac{x}{x_c}.$$

Ideally, x_c has to be chosen so that it represents the order of magnitude or approximate size of x. In this case, the dimensionless variable $\bar{x}$ will be of order unity. After characteristic scales are chosen for the independent and dependent variables, the problem can be reformulated in terms of the new dimensionless variables. The result will be a problem in dimensionless form, where all the variables and parameters are dimensionless.

Let us introduce the following dimensionless variables

$$\mathbf{x}^* = \frac{\mathbf{x}}{x_c}, \qquad t^* = \frac{t}{t_c}, \qquad \mathbf{u}^* = \frac{\mathbf{u}}{u_c},$$
$$p^* = \frac{p}{p_c}, \qquad \underline{\underline{\sigma}}^* = \frac{\underline{\underline{\sigma}}}{\sigma_c}, \qquad \mathbf{v}^* = \frac{\mathbf{v}}{v_c},$$

where $x_c, t_c, u_c, p_c, \sigma_c$, and v_c represent characteristic scales for the position vector $\mathbf{x}$, time t, the solid displacement $\mathbf{u}$, the fluid pressure p, the total stress $\underline{\underline{\sigma}}$, and the discharge velocity $\mathbf{v}$, respectively. Denoting by $\nabla^*(\cdot)$ and $(\cdot)_{t^*}$ the partial derivatives

with respect to $\mathbf{x}^*$ and t^*, respectively, the dimensionless form of system (3.44)–(3.54) to be solved in the scaled domain $Q^* = \Omega^* \times \left(\frac{t_{\text{start}}}{t_c}, \frac{t_{\text{end}}}{t_c} \right)$ reads:

$$\underline{\underline{\sigma}}^* = 2\frac{\mu^e u_c}{x_c \sigma_c} \underline{\underline{\varepsilon}}^*(\mathbf{u}^*) + \frac{\lambda^e u_c}{x_c} (\nabla^* \cdot \mathbf{u}^*) \underline{\underline{I}} + \delta \left(2\frac{\mu^v u_c}{x_c t_c \sigma_c} \underline{\underline{\varepsilon}}^*(\mathbf{u}^*_{t^*}) + \frac{\lambda^v u_c}{x_c t_c \sigma_c} (\nabla^* \cdot \mathbf{u}^*_{t^*}) \underline{\underline{I}} \right) - \frac{p_c}{\sigma_c} p^* \underline{\underline{I}} \qquad \text{in } Q^*, \tag{B.1}$$

$$\nabla^* \cdot \underline{\underline{\sigma}}^* = \frac{x_c}{\sigma_c} \mathbf{F} \qquad \text{in } Q^*, \tag{B.2}$$

$$\frac{x_c v_c}{\kappa p_c} \mathbf{v}^* + \nabla^* p^* = \mathbf{0} \qquad \text{in } Q^*, \tag{B.3}$$

$$\frac{u_c}{t_c v_c} (\nabla^* \cdot \mathbf{u}^*)_{t^*} + \nabla^* \cdot \mathbf{v}^* = \frac{x_c}{v_c} S \qquad \text{in } Q^*, \tag{B.4}$$

$$n^* = \frac{u_c}{x_c} \nabla^* \cdot \mathbf{u}^* + n^0 \qquad \text{in } Q^*, \tag{B.5}$$

$$\mathbf{u}^* = \frac{\mathbf{g}_S^D}{u_c} \qquad \text{on } \Gamma_S^{D,*}, \tag{B.6}$$

$$\underline{\underline{\sigma}}^* \mathbf{n} = \frac{\mathbf{g}_S^N}{\sigma_c} \qquad \text{on } \Gamma_S^{N,*}, \tag{B.7}$$

$$p^* = \frac{g_F^D}{p_c} \qquad \text{on } \Gamma_F^{D,*}, \tag{B.8}$$

$$\mathbf{v}^* \cdot \mathbf{n} = \frac{g_F^N}{v_c} \qquad \text{on } \Gamma_F^{N,*}, \tag{B.9}$$

subject to the following initial conditions:

$$\mathbf{u}^* = \frac{\mathbf{u}^0}{u_c} \quad \text{in } \Omega \quad \text{at } t^* = \frac{t_{\text{start}}}{t_c} \qquad (\text{case } \delta > 0), \tag{B.10}$$

$$\nabla^* \cdot \mathbf{u}^* = \frac{d_0 x_c}{u_c} \quad \text{in } \Omega \quad \text{at } t^* = \frac{t_{\text{start}}}{t_c} \qquad (\text{case } \delta = 0). \tag{B.11}$$

Appendix C. Error tables

Table C.1
Linear stationary validation test in 2D. Relative errors for different triangulations with the lowest order method $k = 1$.

$e^{\sigma}_{h,\mathrm{rel}}$	e.c.r.	$e^{u}_{h,\mathrm{rel}}$	e.c.r.	$e^{v}_{h,\mathrm{rel}}$	e.c.r.	$e^{p}_{h,\mathrm{rel}}$	e.c.r.
$9.0633e-02$	-	$5.9250e-01$	-	$2.0335e-01$	-	$3.1450e-01$	-
$4.4912e-02$	1.01	$1.1336e-01$	2.39	$4.1566e-02$	2.29	$3.3734e-02$	3.22
$1.1526e-02$	1.96	$1.4270e-02$	2.99	$1.0566e-02$	1.98	$4.2664e-03$	2.98
$2.9031e-03$	1.99	$1.7848e-03$	3.00	$2.6522e-03$	1.99	$5.3503e-04$	3.00
$7.2722e-04$	2.00	$2.2302e-04$	3.00	$6.6367e-04$	2.00	$6.6944e-05$	3.00
$1.8190e-04$	2.00	$2.7869e-05$	3.00	$1.6595e-04$	2.00	$8.3708e-06$	3.00
$4.5484e-05$	2.00	$3.4829e-06$	3.00	$4.1488e-05$	2.00	$1.0465e-06$	3.00
$1.1372e-05$	2.00	$4.3532e-07$	3.00	$1.0372e-05$	2.00	$1.3082e-07$	3.00
$e^{\overline{u}}_{h,\mathrm{rel}}$	e.c.r.	$e^{\overline{p}}_{h,\mathrm{rel}}$	e.c.r.	$e^{\hat{u}}_{h,\mathrm{rel}}$	e.c.r.	$e^{\hat{p}}_{h,\mathrm{rel}}$	e.c.r.
$3.6850e-02$	-	$1.3478e-02$	-	$2.6333e-01$	-	$8.0934e-02$	-
$9.6455e-03$	1.93	$1.6196e-03$	3.06	$4.8075e-02$	2.45	$4.7290e-02$	0.78
$1.1220e-03$	3.10	$2.1420e-04$	2.92	$1.1971e-02$	2.01	$1.2098e-02$	1.97
$1.2608e-04$	3.15	$2.7550e-05$	2.96	$3.0137e-03$	1.99	$3.0421e-03$	1.99
$1.4332e-05$	3.14	$3.4890e-06$	2.98	$7.5743e-04$	1.99	$7.6161e-04$	2.00
$1.6805e-06$	3.09	$4.3880e-07$	2.99	$1.8992e-04$	2.00	$1.9047e-04$	2.00
$2.0240e-07$	3.05	$5.5011e-08$	3.00	$4.7551e-05$	2.00	$4.7622e-05$	2.00
$2.4799e-08$	3.03	$6.8862e-09$	3.00	$1.1897e-05$	2.00	$1.1906e-05$	2.00

Table C.2
Linear stationary validation test in 2D. Relative errors for different triangulations for $k = 2$.

$e^{\sigma}_{h,\text{rel}}$	e.c.r.	$e^{u}_{h,\text{rel}}$	e.c.r.	$e^{v}_{h,\text{rel}}$	e.c.r.	$e^{p}_{h,\text{rel}}$	e.c.r.
$4.9426e-02$	-	$2.4498e-01$	-	$1.3022e-02$	-	$2.6498e-02$	-
$4.8793e-03$	3.34	$1.2156e-02$	4.33	$4.6465e-03$	1.49	$3.6580e-03$	2.86
$6.2053e-04$	2.98	$7.7057e-04$	3.98	$5.9004e-04$	2.98	$2.3198e-04$	3.98
$7.7892e-05$	2.99	$4.8328e-05$	3.99	$7.4025e-05$	2.99	$1.4551e-05$	3.99
$9.7465e-06$	3.00	$3.0231e-06$	4.00	$9.2600e-06$	3.00	$9.1031e-07$	4.00
$1.2186e-06$	3.00	$1.8898e-07$	4.00	$1.1576e-06$	3.00	$5.6908e-08$	4.00
$1.5233e-07$	3.00	$1.1811e-08$	4.00	$1.4470e-07$	3.00	$3.5570e-09$	4.00
$1.9042e-08$	3.00	$7.3825e-10$	4.00	$1.8087e-08$	3.00	$2.2239e-10$	4.00
$e^{\overline{u}}_{h,\text{rel}}$	e.c.r.	$e^{\overline{p}}_{h,\text{rel}}$	e.c.r.	$e^{\hat{u}}_{h,\text{rel}}$	e.c.r.	$e^{\hat{p}}_{h,\text{rel}}$	e.c.r.
$2.0531e-03$	-	$5.4584e-05$	-	$2.2518e-02$	-	$5.4311e-02$	-
$8.8000e-05$	4.54	$3.8506e-05$	0.50	$5.7572e-03$	1.97	$6.0290e-03$	3.17
$4.5545e-06$	4.27	$3.2559e-06$	3.56	$7.4917e-04$	2.94	$7.6945e-04$	2.97
$2.6069e-07$	4.13	$2.2809e-07$	3.84	$9.5330e-05$	2.97	$9.6683e-05$	2.99
$1.5534e-08$	4.07	$1.4949e-08$	3.93	$1.2014e-05$	2.99	$1.2101e-05$	3.00
$9.4586e-10$	4.04	$9.5434e-10$	3.97	$1.5076e-06$	2.99	$1.5131e-06$	3.00
$5.8328e-11$	4.02	$6.0265e-11$	3.99	$1.8881e-07$	3.00	$1.8916e-07$	3.00
$7.5128e-12$	2.96	$6.6232e-12$	3.19	$2.3623e-08$	3.00	$2.3645e-08$	3.00

Table C.3
Linear stationary validation test in 2D. Relative errors for different triangulations for $k = 3$.

$e^{\sigma}_{h,\text{rel}}$	e.c.r.	$e^{u}_{h,\text{rel}}$	e.c.r.	$e^{v}_{h,\text{rel}}$	e.c.r.	$e^{p}_{h,\text{rel}}$	e.c.r.
$1.8681e-03$	-	$1.1066e-02$	-	$8.5125e-03$	-	$1.3113e-02$	-
$4.2643e-04$	2.13	$1.0420e-03$	3.41	$4.0723e-04$	4.39	$3.1720e-04$	5.37
$2.7132e-05$	3.97	$3.3012e-05$	4.98	$2.5805e-05$	3.98	$1.0060e-05$	4.98
$1.7044e-06$	3.99	$1.0350e-06$	5.00	$1.6178e-06$	4.00	$3.1558e-07$	4.99
$1.0669e-07$	4.00	$3.2369e-08$	5.00	$1.0118e-07$	4.00	$9.8718e-09$	5.00
$6.6717e-09$	4.00	$1.0117e-09$	5.00	$6.3239e-09$	4.00	$3.0859e-10$	5.00
$4.1706e-10$	4.00	$3.1671e-11$	5.00	$3.9525e-10$	4.00	$1.1281e-11$	4.77
$2.6432e-11$	3.98	$7.0336e-12$	2.17	$2.7008e-11$	3.87	$2.0587e-11$	-0.87
$e^{\overline{u}}_{h,\text{rel}}$	e.c.r.	$e^{\overline{p}}_{h,\text{rel}}$	e.c.r.	$e^{\hat{u}}_{h,\text{rel}}$	e.c.r.	$e^{\hat{p}}_{h,\text{rel}}$	e.c.r.
$1.1941e-04$	-	$1.6376e-05$	-	$1.2331e-02$	-	$2.0455e-03$	-
$5.0594e-06$	4.56	$3.8697e-07$	5.40	$5.6086e-04$	4.46	$5.9180e-04$	1.79
$1.1125e-07$	5.51	$8.6639e-09$	5.48	$3.6593e-05$	3.94	$3.7667e-05$	3.97
$2.2435e-09$	5.63	$1.5808e-10$	5.78	$2.3298e-06$	3.97	$2.3649e-06$	3.99
$4.5075e-11$	5.64	$2.6590e-12$	5.89	$1.4686e-07$	3.99	$1.4797e-07$	4.00
$1.1122e-12$	5.34	$1.8195e-12$	0.55	$9.2157e-09$	3.99	$9.2510e-09$	4.00
$1.8489e-12$	-0.73	$5.8533e-12$	-1.69	$5.7712e-10$	4.00	$5.7826e-10$	4.00
$6.9632e-12$	-1.91	$2.0586e-11$	-1.81	$3.6771e-11$	3.97	$4.1599e-11$	3.80

Table C.4
Nonlinear stationary validation test in 2D. Relative errors for different triangulations for $k = 1$.

$e^{\sigma}_{h,\mathrm{rel}}$	e.c.r.	$e^{u}_{h,\mathrm{rel}}$	e.c.r.	$e^{v}_{h,\mathrm{rel}}$	e.c.r.	$e^{p}_{h,\mathrm{rel}}$	e.c.r.
$9.0904e-02$	-	$6.6505e-01$	-	$2.6774e-01$	-	$2.0332e-01$	-
$4.5911e-02$	0.99	$1.2678e-01$	2.39	$1.1259e-01$	1.25	$2.8830e-02$	2.82
$1.1777e-02$	1.96	$1.5914e-02$	2.99	$2.5847e-02$	2.12	$3.2432e-03$	3.15
$2.9636e-03$	1.99	$1.9875e-03$	3.00	$6.6182e-03$	1.97	$4.0696e-04$	2.99
$7.4186e-04$	2.00	$2.4816e-04$	3.00	$1.6646e-03$	1.99	$5.0880e-05$	3.00
$1.8549e-04$	2.00	$3.0999e-05$	3.00	$4.1710e-04$	2.00	$6.3612e-06$	3.00
$4.6368e-05$	2.00	$3.8734e-06$	3.00	$1.0438e-04$	2.00	$7.9527e-07$	3.00
$1.1591e-05$	2.00	$4.8408e-07$	3.00	$2.6106e-05$	2.00	$9.9418e-08$	3.00
$e^{\overline{u}}_{h,\mathrm{rel}}$	e.c.r.	$e^{\overline{p}}_{h,\mathrm{rel}}$	e.c.r.	$e^{\hat{u}}_{h,\mathrm{rel}}$	e.c.r.	$e^{\hat{p}}_{h,\mathrm{rel}}$	e.c.r.
$2.8865e-02$	-	$4.3253e-02$	-	$2.4288e-01$	-	$1.7209e-01$	-
$1.2914e-02$	1.16	$1.0236e-02$	2.08	$5.0078e-02$	2.28	$4.9856e-02$	1.79
$1.5472e-03$	3.06	$1.0575e-03$	3.28	$1.2120e-02$	2.05	$1.2185e-02$	2.03
$1.7175e-04$	3.17	$1.2685e-04$	3.06	$3.0212e-03$	2.00	$3.0466e-03$	2.00
$1.9113e-05$	3.17	$1.5633e-05$	3.02	$7.5780e-04$	2.00	$7.6187e-04$	2.00
$2.2016e-06$	3.12	$1.9478e-06$	3.00	$1.8994e-04$	2.00	$1.9049e-04$	2.00
$2.6204e-07$	3.07	$2.4340e-07$	3.00	$4.7552e-05$	2.00	$4.7623e-05$	2.00
$3.1886e-08$	3.04	$3.0433e-08$	3.00	$1.1897e-05$	2.00	$1.1906e-05$	2.00

Table C.5
Nonlinear stationary validation test in 2D. Relative errors for different triangulations for $k = 2$.

$e^{\sigma}_{h,\mathrm{rel}}$	e.c.r.	$e^{u}_{h,\mathrm{rel}}$	e.c.r.	$e^{v}_{h,\mathrm{rel}}$	e.c.r.	$e^{p}_{h,\mathrm{rel}}$	e.c.r.
$5.0150e-02$	-	$2.7276e-01$	-	$1.2042e-01$	-	$5.2908e-02$	-
$4.9322e-03$	3.35	$1.3512e-02$	4.34	$1.1774e-02$	3.35	$2.9652e-03$	4.16
$6.2465e-04$	2.98	$8.5589e-04$	3.98	$2.3493e-03$	2.33	$2.4258e-04$	3.61
$7.8263e-05$	3.00	$5.3671e-05$	4.00	$2.9133e-04$	3.01	$1.4995e-05$	4.02
$9.7853e-06$	3.00	$3.3571e-06$	4.00	$3.6600e-05$	2.99	$9.3986e-07$	4.00
$1.2230e-06$	3.00	$2.0985e-07$	4.00	$4.5829e-06$	3.00	$5.8773e-08$	4.00
$1.5286e-07$	3.00	$1.3116e-08$	4.00	$5.7320e-07$	3.00	$3.6732e-09$	4.00
$1.9107e-08$	3.00	$8.1978e-10$	4.00	$7.1666e-08$	3.00	$2.2957e-10$	4.00
$e^{\overline{u}}_{h,\mathrm{rel}}$	e.c.r.	$e^{\overline{p}}_{h,\mathrm{rel}}$	e.c.r.	$e^{\hat{u}}_{h,\mathrm{rel}}$	e.c.r.	$e^{\hat{p}}_{h,\mathrm{rel}}$	e.c.r.
$3.4712e-03$	-	$7.4377e-03$	-	$3.0831e-02$	-	$6.4819e-02$	-
$1.2849e-04$	4.76	$1.8566e-04$	5.32	$5.7943e-03$	2.41	$6.0674e-03$	3.42
$6.4304e-06$	4.32	$1.3579e-05$	3.77	$7.4990e-04$	2.95	$7.7308e-04$	2.97
$3.6237e-07$	4.15	$8.3896e-07$	4.02	$9.5341e-05$	2.98	$9.6790e-05$	3.00
$2.1439e-08$	4.08	$5.3069e-08$	3.98	$1.2014e-05$	2.99	$1.2104e-05$	3.00
$1.3010e-09$	4.04	$3.3344e-09$	3.99	$1.5076e-06$	2.99	$1.5132e-06$	3.00
$8.0093e-11$	4.02	$2.0883e-10$	4.00	$1.8881e-07$	3.00	$1.8916e-07$	3.00
$8.1647e-12$	3.29	$1.3397e-11$	3.96	$2.3623e-08$	3.00	$2.3645e-08$	3.00

Table C.6
Nonlinear stationary validation test in 2D. Relative errors for different triangulations for $k = 3$.

$e^{\sigma}_{h,\mathrm{rel}}$	e.c.r.	$e^{u}_{h,\mathrm{rel}}$	e.c.r.	$e^{v}_{h,\mathrm{rel}}$	e.c.r.	$e^{p}_{h,\mathrm{rel}}$	e.c.r.
$2.0480e-03$	-	$1.2568e-02$	-	$2.8157e-02$	-	$1.5601e-02$	-
$4.3131e-04$	2.25	$1.1567e-03$	3.44	$3.4496e-03$	3.03	$6.2526e-04$	4.64
$2.7415e-05$	3.98	$3.6626e-05$	4.98	$2.0943e-04$	4.04	$2.1723e-05$	4.85
$1.7209e-06$	3.99	$1.1481e-06$	5.00	$1.4155e-05$	3.89	$7.3305e-07$	4.89
$1.0769e-07$	4.00	$3.5902e-08$	5.00	$8.9467e-07$	3.98	$2.3199e-08$	4.98
$6.7336e-09$	4.00	$1.1221e-09$	5.00	$5.6055e-08$	4.00	$7.2715e-10$	5.00
$4.2091e-10$	4.00	$3.5137e-11$	5.00	$3.5056e-09$	4.00	$2.3231e-11$	4.97
$2.6624e-11$	3.98	$8.8950e-12$	1.98	$2.1940e-10$	4.00	$2.0009e-11$	0.22
$e^{\overline{u}}_{h,\mathrm{rel}}$	e.c.r.	$e^{\overline{p}}_{h,\mathrm{rel}}$	e.c.r.	$e^{\hat{u}}_{h,\mathrm{rel}}$	e.c.r.	$e^{\hat{p}}_{h,\mathrm{rel}}$	e.c.r.
$3.1938e-04$	-	$1.2335e-03$	-	$1.2275e-02$	-	$4.2138e-03$	-
$1.1144e-05$	4.84	$7.1919e-06$	7.42	$5.6474e-04$	4.44	$6.2487e-04$	2.75
$2.2300e-07$	5.64	$1.5269e-07$	5.56	$3.6623e-05$	3.95	$3.8056e-05$	4.04
$4.0676e-09$	5.78	$3.2263e-09$	5.56	$2.3301e-06$	3.97	$2.3716e-06$	4.00
$7.9753e-11$	5.67	$6.4740e-11$	5.64	$1.4686e-07$	3.99	$1.4808e-07$	4.00
$1.7883e-12$	5.48	$1.6288e-12$	5.31	$9.2158e-09$	3.99	$9.2526e-09$	4.00
$2.2274e-12$	-0.32	$4.7409e-12$	-1.54	$5.7713e-10$	4.00	$5.7827e-10$	4.00
$8.8267e-12$	-1.99	$1.9997e-11$	-2.08	$3.7169e-11$	3.96	$4.1314e-11$	3.81

Table C.7
Linear time dependent validation test in 2D. Absolute errors for different triangulations for $k = 1$.

e_h^σ	e.c.r.	e_h^u	e.c.r.	e_h^v	e.c.r.	e_h^p	e.c.r.
$1.6810e+02$	-	$6.6763e+00$	-	$5.7616e+01$	-	$2.5082e+01$	-
$1.0749e+02$	0.65	$3.5199e+00$	0.92	$2.8608e+01$	1.01	$1.2043e+01$	1.06
$5.4428e+01$	0.98	$1.6706e+00$	1.08	$1.5683e+01$	0.87	$6.6078e+00$	0.87
$2.7749e+01$	0.97	$8.2154e-01$	1.02	$7.8989e+00$	0.99	$3.3290e+00$	0.99
$1.3990e+01$	0.99	$4.0717e-01$	1.01	$3.9279e+00$	1.01	$1.6555e+00$	1.01
$7.0580e+00$	0.99	$2.0280e-01$	1.01	$1.9541e+00$	1.01	$8.2357e-01$	1.01
$3.5722e+00$	0.98	$1.0120e-01$	1.00	$9.7406e-01$	1.00	$4.1051e-01$	1.00
$1.8180e+00$	0.97	$5.0553e-02$	1.00	$4.8621e-01$	1.00	$2.0491e-01$	1.00
$e_h^{\overline{u}}$	e.c.r.	$e_h^{\overline{p}}$	e.c.r.	$e_h^{\hat{u}}$	e.c.r.	$e_h^{\hat{p}}$	e.c.r.
$6.3145e+00$	-	$2.3331e+01$	-	$1.3455e+01$	-	$5.3718e+01$	-
$3.4211e+00$	0.88	$1.1914e+01$	0.97	$7.4138e+00$	0.86	$2.5080e+01$	1.10
$1.6560e+00$	1.05	$6.5913e+00$	0.85	$3.4296e+00$	1.11	$1.3503e+01$	0.89
$8.1981e-01$	1.01	$3.3269e+00$	0.99	$1.6668e+00$	1.04	$6.7316e+00$	1.00
$4.0696e-01$	1.01	$1.6552e+00$	1.01	$8.2046e-01$	1.02	$3.3293e+00$	1.02
$2.0278e-01$	1.00	$8.2354e-01$	1.01	$4.0715e-01$	1.01	$1.6517e+00$	1.01
$1.0120e-01$	1.00	$4.1050e-01$	1.00	$2.0279e-01$	1.01	$8.2217e-01$	1.01
$5.0553e-02$	1.00	$2.0491e-01$	1.00	$1.0120e-01$	1.00	$4.1010e-01$	1.00

Table C.8
Linear time dependent validation test in 2D. Absolute errors for different triangulations for $k = 2$.

e_h^σ	e.c.r.	e_h^u	e.c.r.	e_h^v	e.c.r.	e_h^p	e.c.r.
$3.7538e+01$	-	$2.1811e+00$	-	$1.2534e+01$	-	$2.9845e+00$	-
$1.0482e+01$	1.84	$3.2138e-01$	2.76	$1.1225e+00$	3.48	$3.6194e-01$	3.04
$3.9796e+00$	1.40	$1.6972e-01$	0.92	$4.0671e-01$	1.46	$1.7634e-01$	1.04
$1.9473e+00$	1.03	$8.7328e-02$	0.96	$2.0625e-01$	0.98	$8.8877e-02$	0.99
$9.7212e-01$	1.00	$4.4104e-02$	0.99	$1.0330e-01$	1.00	$4.4424e-02$	1.00
$4.8603e-01$	1.00	$2.2126e-02$	1.00	$5.1597e-02$	1.00	$2.2175e-02$	1.00
$2.4303e-01$	1.00	$1.1080e-02$	1.00	$2.5772e-02$	1.00	$1.1074e-02$	1.00
$1.2152e-01$	1.00	$5.5438e-03$	1.00	$1.2877e-02$	1.00	$5.5330e-03$	1.00
$e_h^{\overline{u}}$	e.c.r.	$e_h^{\overline{p}}$	e.c.r.	$e_h^{\hat{u}}$	e.c.r.	$e_h^{\hat{p}}$	e.c.r.
$1.9888e+00$	-	$2.2334e+00$	-	$3.3878e+00$	-	$6.6705e+00$	-
$3.0516e-01$	2.70	$3.5694e-01$	2.65	$6.8980e-01$	2.30	$7.5245e-01$	3.15
$1.6810e-01$	0.86	$1.7595e-01$	1.02	$3.5618e-01$	0.95	$3.6174e-01$	1.06
$8.7126e-02$	0.95	$8.8826e-02$	0.99	$1.7809e-01$	1.00	$1.7995e-01$	1.01
$4.4079e-02$	0.98	$4.4417e-02$	1.00	$8.8960e-02$	1.00	$8.9392e-02$	1.01
$2.2123e-02$	0.99	$2.2174e-02$	1.00	$4.4433e-02$	1.00	$4.4486e-02$	1.01
$1.1080e-02$	1.00	$1.1074e-02$	1.00	$2.2205e-02$	1.00	$2.2182e-02$	1.00
$5.5437e-03$	1.00	$5.5330e-03$	1.00	$1.1098e-02$	1.00	$1.1074e-02$	1.00

Table C.9
Linear time dependent validation test in 2D. Absolute errors for different triangulations for $k = 3$.

e_h^σ	e.c.r.	e_h^u	e.c.r.	e_h^v	e.c.r.	e_h^p	e.c.r.
$1.8783e+01$	-	$7.0904e-01$	-	$2.4144e+00$	-	$1.0198e+00$	-
$8.1848e+00$	1.20	$3.5044e-01$	1.02	$9.6746e-01$	1.32	$4.1244e-01$	1.31
$3.9161e+00$	1.06	$1.7557e-01$	1.00	$4.2975e-01$	1.17	$1.8464e-01$	1.16
$1.9453e+00$	1.01	$8.8033e-02$	1.00	$2.0934e-01$	1.04	$8.9955e-02$	1.04
$9.7210e-01$	1.00	$4.4172e-02$	0.99	$1.0369e-01$	1.01	$4.4559e-02$	1.01
$4.8604e-01$	1.00	$2.2135e-02$	1.00	$5.1652e-02$	1.01	$2.2192e-02$	1.01
$2.4303e-01$	1.00	$1.1081e-02$	1.00	$2.5778e-02$	1.00	$1.1076e-02$	1.00
$1.2152e-01$	1.00	$5.5439e-03$	1.00	$1.2878e-02$	1.00	$5.5333e-03$	1.00
$e_h^{\overline{u}}$	e.c.r.	$e_h^{\overline{p}}$	e.c.r.	$e_h^{\hat{u}}$	e.c.r.	$e_h^{\hat{p}}$	e.c.r.
$6.6789e-01$	-	$9.7606e-01$	-	$1.4408e+00$	-	$2.2705e+00$	-
$3.3917e-01$	0.98	$4.0853e-01$	1.26	$7.4552e-01$	0.95	$8.6498e-01$	1.39
$1.7399e-01$	0.96	$1.8421e-01$	1.15	$3.6198e-01$	1.04	$3.7822e-01$	1.19
$8.7832e-02$	0.99	$8.9903e-02$	1.03	$1.7879e-01$	1.02	$1.8210e-01$	1.05
$4.4146e-02$	0.99	$4.4553e-02$	1.01	$8.9027e-02$	1.01	$8.9662e-02$	1.02
$2.2132e-02$	1.00	$2.2191e-02$	1.01	$4.4442e-02$	1.00	$4.4519e-02$	1.01
$1.1081e-02$	1.00	$1.1076e-02$	1.00	$2.2206e-02$	1.00	$2.2186e-02$	1.00
$5.5439e-03$	1.00	$5.5333e-03$	1.00	$1.1099e-02$	1.00	$1.1075e-02$	1.00

Table C.10
Nonlinear time dependent validation test in 2D. Absolute errors for different triangulations for $k = 1$.

e_h^σ	e.c.r.	e_h^u	e.c.r.	e_h^v	e.c.r.	e_h^p	e.c.r.
$7.1164e+00$	-	$2.3799e-01$	-	$2.2314e+00$	-	$5.5134e+00$	-
$3.2846e+00$	1.12	$1.1138e-01$	1.10	$8.7231e-01$	1.36	$1.0455e+00$	2.40
$1.6829e+00$	0.96	$5.1288e-02$	1.12	$4.7392e-01$	0.88	$4.7845e-01$	1.13
$8.6110e-01$	0.97	$2.5185e-02$	1.03	$2.3901e-01$	0.99	$2.2263e-01$	1.10
$4.3387e-01$	0.99	$1.2492e-02$	1.01	$1.1911e-01$	1.00	$1.0551e-01$	1.08
$2.1905e-01$	0.99	$6.2239e-03$	1.01	$5.9339e-02$	1.01	$5.1158e-02$	1.04
$1.1100e-01$	0.98	$3.1075e-03$	1.00	$2.9600e-02$	1.00	$2.5166e-02$	1.02
$5.6625e-02$	0.97	$1.5526e-03$	1.00	$1.4781e-02$	1.00	$1.2478e-02$	1.01
$e_h^{\overline{u}}$	e.c.r.	$e_h^{\overline{p}}$	e.c.r.	$e_h^{\hat{u}}$	e.c.r.	$e_h^{\hat{p}}$	e.c.r.
$2.2844e-01$	-	$5.2255e+00$	-	$4.9096e-01$	-	$1.0613e+01$	-
$1.0822e-01$	1.08	$1.0346e+00$	2.34	$2.3464e-01$	1.07	$2.1675e+00$	2.29
$5.0833e-02$	1.09	$4.7724e-01$	1.12	$1.0527e-01$	1.16	$9.7705e-01$	1.15
$2.5131e-02$	1.02	$2.2249e-01$	1.10	$5.1094e-02$	1.04	$4.5007e-01$	1.12
$1.2486e-02$	1.01	$1.0549e-01$	1.08	$2.5171e-02$	1.02	$2.1217e-01$	1.08
$6.2231e-03$	1.00	$5.1156e-02$	1.04	$1.2495e-02$	1.01	$1.0260e-01$	1.05
$3.1074e-03$	1.00	$2.5166e-02$	1.02	$6.2268e-03$	1.00	$5.0401e-02$	1.03
$1.5526e-03$	1.00	$1.2478e-02$	1.01	$3.1082e-03$	1.00	$2.4973e-02$	1.01

Table C.11
Nonlinear time dependent validation test in 2D. Absolute errors for different triangulations for $k = 2$.

e_h^σ	e.c.r.	e_h^u	e.c.r.	e_h^v	e.c.r.	e_h^p	e.c.r.
$1.2041e+00$	-	$6.9380e-02$	-	$3.9853e-01$	-	$2.0488e-01$	-
$3.4587e-01$	1.80	$1.0414e-02$	2.74	$3.5279e-02$	3.50	$3.5545e-02$	2.53
$1.3324e-01$	1.38	$5.5433e-03$	0.91	$1.2548e-02$	1.49	$1.7058e-02$	1.06
$6.5255e-02$	1.03	$2.8579e-03$	0.96	$6.3525e-03$	0.98	$8.7613e-03$	0.96
$3.2597e-02$	1.00	$1.4448e-03$	0.98	$3.1841e-03$	1.00	$4.4439e-03$	0.98
$1.6308e-02$	1.00	$7.2513e-04$	0.99	$1.5914e-03$	1.00	$2.2372e-03$	0.99
$8.1558e-03$	1.00	$3.6318e-04$	1.00	$7.9502e-04$	1.00	$1.1223e-03$	1.00
$4.0782e-03$	1.00	$1.8173e-04$	1.00	$3.9729e-04$	1.00	$5.6203e-04$	1.00
$e_h^{\overline{u}}$	e.c.r.	$e_h^{\overline{p}}$	e.c.r.	$e_h^{\hat{u}}$	e.c.r.	$e_h^{\hat{p}}$	e.c.r.
$6.3126e-02$	-	$1.4665e-01$	-	$1.0750e-01$	-	$5.0188e-01$	-
$9.9015e-03$	2.67	$3.5027e-02$	2.07	$2.2517e-02$	2.26	$7.3916e-02$	2.76
$5.4906e-03$	0.85	$1.7019e-02$	1.04	$1.1648e-02$	0.95	$3.5019e-02$	1.08
$2.8513e-03$	0.95	$8.7563e-03$	0.96	$5.8307e-03$	1.00	$1.7775e-02$	0.98
$1.4439e-03$	0.98	$4.4433e-03$	0.98	$2.9147e-03$	1.00	$8.9532e-03$	0.99
$7.2502e-04$	0.99	$2.2371e-03$	0.99	$1.4562e-03$	1.00	$4.4910e-03$	1.00
$3.6317e-04$	1.00	$1.1223e-03$	1.00	$7.2783e-04$	1.00	$2.2487e-03$	1.00
$1.8173e-04$	1.00	$5.6203e-04$	1.00	$3.6382e-04$	1.00	$1.1251e-03$	1.00

Table C.12
Nonlinear time dependent validation test in 2D. Absolute errors for different triangulations for $k = 3$.

e_h^σ	e.c.r.	e_h^u	e.c.r.	e_h^v	e.c.r.	e_h^p	e.c.r.
$6.0037e-01$	-	$2.2958e-02$	-	$7.6159e-02$	-	$5.5499e-02$	-
$2.7308e-01$	1.14	$1.1430e-02$	1.01	$2.9935e-02$	1.35	$3.4718e-02$	0.68
$1.3091e-01$	1.06	$5.7407e-03$	0.99	$1.3218e-02$	1.18	$1.7158e-02$	1.02
$6.5161e-02$	1.01	$2.8819e-03$	0.99	$6.4440e-03$	1.04	$8.7962e-03$	0.96
$3.2593e-02$	1.00	$1.4471e-03$	0.99	$3.1970e-03$	1.01	$4.4488e-03$	0.98
$1.6308e-02$	1.00	$7.2542e-04$	1.00	$1.5928e-03$	1.01	$2.2378e-03$	0.99
$8.1558e-03$	1.00	$3.6322e-04$	1.00	$7.9520e-04$	1.00	$1.1223e-03$	1.00
$4.0782e-03$	1.00	$1.8173e-04$	1.00	$3.9732e-04$	1.00	$5.6204e-04$	1.00
$e_h^{\overline{u}}$	e.c.r.	$e_h^{\overline{p}}$	e.c.r.	$e_h^{\hat{u}}$	e.c.r.	$e_h^{\hat{p}}$	e.c.r.
$2.1633e-02$	-	$5.3733e-02$	-	$4.6765e-02$	-	$1.2012e-01$	-
$1.1065e-02$	0.97	$3.4411e-02$	0.64	$2.4337e-02$	0.94	$7.3441e-02$	0.71
$5.6896e-03$	0.96	$1.7118e-02$	1.01	$1.1841e-02$	1.04	$3.5346e-02$	1.06
$2.8753e-03$	0.98	$8.7911e-03$	0.96	$5.8541e-03$	1.02	$1.7855e-02$	0.99
$1.4463e-03$	0.99	$4.4481e-03$	0.98	$2.9170e-03$	1.00	$8.9642e-03$	0.99
$7.2531e-04$	1.00	$2.2378e-03$	0.99	$1.4565e-03$	1.00	$4.4925e-03$	1.00
$3.6321e-04$	1.00	$1.1223e-03$	1.00	$7.2787e-04$	1.00	$2.2489e-03$	1.00
$1.8173e-04$	1.00	$5.6204e-04$	1.00	$3.6383e-04$	1.00	$1.1251e-03$	1.00

Table C.13
Effect of varying the elastic Lamé parameters in the validation test case 1 in 2D. Local bases of degree $k = 1$ have been used. The fluid pressure $p_h|_K$ was taken in $P^{k+1}(K)$.

$e^{\sigma}_{h,\mathrm{rel}}$	e.c.r.	$e^{u}_{h,\mathrm{rel}}$	e.c.r.	$e^{v}_{h,\mathrm{rel}}$	e.c.r.	$e^{p}_{h,\mathrm{rel}}$	e.c.r.
$9.1918e-02$	-	$2.2084e+07$	-	$2.0335e-01$	-	$3.1450e-01$	-
$6.9495e-02$	0.40	$4.1434e+06$	2.41	$5.3348e-02$	1.93	$4.0850e-02$	2.94
$1.5486e-02$	2.17	$5.2383e+05$	2.98	$1.0566e-02$	2.34	$4.2656e-03$	3.26
$3.7966e-03$	2.03	$6.5671e+04$	3.00	$2.6522e-03$	1.99	$5.3497e-04$	3.00
$9.3380e-04$	2.02	$8.2150e+03$	3.00	$6.6367e-04$	2.00	$6.6937e-05$	3.00
$2.3116e-04$	2.01	$1.0271e+03$	3.00	$1.6595e-04$	2.00	$8.3702e-06$	3.00
$5.7483e-05$	2.01	$1.2839e+02$	3.00	$4.1488e-05$	2.00	$1.0465e-06$	3.00
$e^{\overline{u}}_{h,\mathrm{rel}}$	e.c.r.	$e^{\overline{p}}_{h,\mathrm{rel}}$	e.c.r.	$e^{\hat{u}}_{h,\mathrm{rel}}$	e.c.r.	$e^{\hat{p}}_{h,\mathrm{rel}}$	e.c.r.
$1.4347e-01$	-	$1.3478e-02$	-	$9.1063e+06$	-	$8.0934e-02$	-
$1.7157e-01$	-0.26	$3.2924e-02$	-1.29	$2.8498e+05$	5.00	$5.8218e-02$	0.48
$2.0016e-02$	3.10	$2.1344e-04$	7.27	$1.3156e+04$	4.44	$1.2098e-02$	2.27
$2.1347e-03$	3.23	$2.7508e-05$	2.96	$5.9237e+02$	4.47	$3.0421e-03$	1.99
$2.2934e-04$	3.22	$3.4904e-06$	2.98	$2.6405e+01$	4.49	$7.6161e-04$	2.00
$2.5626e-05$	3.16	$4.4081e-07$	2.99	$1.1717e+00$	4.49	$1.9047e-04$	2.00
$2.9834e-06$	3.10	$5.5287e-08$	3.00	$5.1887e-02$	4.50	$4.7622e-05$	2.00

Table C.14
Accuracy of $\mathbf{u}_h$ and $\hat{\mathbf{u}}_h$ is restored in test case 1 in 2D by taking the characteristic total stress $\sigma_c = 2\mu_e = 1.2 \times 10^7$ Pa, and all the other characteristic parameters equal to 1.

e_h^σ	e.c.r.	e_h^u	e.c.r.	e_h^v	e.c.r.	e_h^p	e.c.r.
$9.1231e-02$	-	$1.8760e+00$	-	$2.0335e-01$	-	$3.1450e-01$	-
$5.7464e-02$	0.67	$4.0787e-01$	2.20	$4.1566e-02$	2.29	$3.3734e-02$	3.22
$1.4718e-02$	1.97	$5.0453e-02$	3.02	$1.0566e-02$	1.98	$4.2664e-03$	2.98
$3.6795e-03$	2.00	$6.1684e-03$	3.03	$2.6522e-03$	1.99	$5.3503e-04$	3.00
$9.1625e-04$	2.01	$7.5771e-04$	3.03	$6.6367e-04$	2.00	$6.6944e-05$	3.00
$2.2838e-04$	2.00	$9.3737e-05$	3.01	$1.6595e-04$	2.00	$8.3708e-06$	3.00
$5.6994e-05$	2.00	$1.1652e-05$	3.01	$4.1488e-05$	2.00	$1.0465e-06$	3.00
$e_h^{\overline{u}}$	e.c.r.	$e_h^{\overline{p}}$	e.c.r.	$e_h^{\hat{u}}$	e.c.r.	$e_h^{\hat{p}}$	e.c.r.
$1.4947e-01$	-	$1.3478e-02$	-	$7.2379e-01$	-	$8.0934e-02$	-
$1.4276e-01$	0.07	$1.6196e-03$	3.06	$2.4489e-01$	1.56	$4.7290e-02$	0.78
$1.6596e-02$	3.10	$2.1420e-04$	2.92	$3.0738e-02$	2.99	$1.2098e-02$	1.97
$1.8477e-03$	3.17	$2.7550e-05$	2.96	$4.3311e-03$	2.83	$3.0421e-03$	1.99
$2.0754e-04$	3.15	$3.4890e-06$	2.98	$8.3123e-04$	2.38	$7.6161e-04$	2.00
$2.4087e-05$	3.11	$4.3880e-07$	2.99	$1.9388e-04$	2.10	$1.9047e-04$	2.00
$2.8801e-06$	3.06	$5.5011e-08$	3.00	$4.7774e-05$	2.02	$4.7622e-05$	2.00

Table C.15
Accuracy of $\mathbf{u}_h$ and $\hat{\mathbf{u}}_h$ is restored in test case 2 in 2D by taking the characteristic total stress $\sigma_c = 2\mu_e = 1.2 \times 10^7$ Pa, and all the other characteristic parameters equal to 1.

e_h^σ	e.c.r.	e_h^u	e.c.r.	e_h^v	e.c.r.	e_h^p	e.c.r.
$9.1231e-02$	-	$1.8760e+00$	-	$2.6764e-01$	-	$1.9098e-01$	-
$5.7464e-02$	0.67	$4.0787e-01$	2.20	$1.1337e-01$	1.24	$2.9488e-02$	2.70
$1.4718e-02$	1.97	$5.0453e-02$	3.02	$2.6078e-02$	2.12	$3.2740e-03$	3.17
$3.6795e-03$	2.00	$6.1684e-03$	3.03	$6.6773e-03$	1.97	$4.0928e-04$	3.00
$9.1625e-04$	2.01	$7.5771e-04$	3.03	$1.6790e-03$	1.99	$5.1099e-05$	3.00
$2.2838e-04$	2.00	$9.3737e-05$	3.01	$4.2057e-04$	2.00	$6.3883e-06$	3.00
$5.6994e-05$	2.00	$1.1652e-05$	3.01	$1.0522e-04$	2.00	$8.0286e-07$	2.99
$e_h^{\overline{u}}$	e.c.r.	$e_h^{\overline{p}}$	e.c.r.	$e_h^{\hat{u}}$	e.c.r.	$e_h^{\hat{p}}$	e.c.r.
$1.4947e-01$	-	$4.3902e-02$	-	$7.2379e-01$	-	$1.4888e-01$	-
$1.4276e-01$	0.07	$1.0768e-02$	2.03	$2.4489e-01$	1.56	$5.0258e-02$	1.57
$1.6596e-02$	3.10	$1.0588e-03$	3.35	$3.0738e-02$	2.99	$1.2198e-02$	2.04
$1.8477e-03$	3.17	$1.2313e-04$	3.10	$4.3311e-03$	2.83	$3.0471e-03$	2.00
$2.0754e-04$	3.15	$1.4941e-05$	3.04	$8.3123e-04$	2.38	$7.6190e-04$	2.00
$2.4087e-05$	3.11	$1.8571e-06$	3.01	$1.9388e-04$	2.10	$1.9049e-04$	2.00
$2.8802e-06$	3.06	$2.4551e-07$	2.92	$4.7774e-05$	2.02	$4.7623e-05$	2.00

Table C.16
Approximation errors for $P_{\text{ref}}/U_{\text{ref}} = 1 \times 10^4\,\text{Pa}\,\text{m}^{-1}$ in the validation test case 1 in 2D. Local bases of degree $k = 1$ have been used. The fluid pressure $p_h|_K$ was taken in $P^{k+1}(K)$.

$e^{\sigma}_{h,\text{rel}}$	e.c.r.	$e^{u}_{h,\text{rel}}$	e.c.r.	$e^{v}_{h,\text{rel}}$	e.c.r.	$e^{p}_{h,\text{rel}}$	e.c.r.
$1.2972e-01$	-	$3.1964e+02$	-	$2.0335e-01$	-	$3.1450e-01$	-
$6.1348e-02$	1.08	$6.6987e+01$	2.25	$4.1566e-02$	2.29	$3.3734e-02$	3.22
$1.5570e-02$	1.98	$8.0962e+00$	3.05	$1.0566e-02$	1.98	$4.2664e-03$	2.98
$3.8633e-03$	2.01	$9.8720e-01$	3.04	$2.6522e-03$	1.99	$5.3503e-04$	3.00
$9.5814e-04$	2.01	$1.2147e-01$	3.02	$6.6367e-04$	2.00	$6.6944e-05$	3.00
$2.3835e-04$	2.01	$1.5050e-02$	3.01	$1.6595e-04$	2.00	$8.3708e-06$	3.00
$5.9426e-05$	2.00	$1.8725e-03$	3.01	$4.1488e-05$	2.00	$1.0465e-06$	3.00
$e^{\overline{u}}_{h,\text{rel}}$	e.c.r.	$e^{\overline{p}}_{h,\text{rel}}$	e.c.r.	$e^{\hat{u}}_{h,\text{rel}}$	e.c.r.	$e^{\hat{p}}_{h,\text{rel}}$	e.c.r.
$1.3026e+02$	-	$1.3478e-02$	-	$2.0620e+02$	-	$8.0934e-02$	-
$2.3392e+01$	2.48	$1.6196e-03$	3.06	$4.1327e+01$	2.32	$4.7290e-02$	0.78
$2.2898e+00$	3.35	$2.1420e-04$	2.92	$4.3523e+00$	3.25	$1.2098e-02$	1.97
$2.2989e-01$	3.32	$2.7550e-05$	2.96	$4.5898e-01$	3.25	$3.0421e-03$	1.99
$2.3830e-02$	3.27	$3.4890e-06$	2.98	$4.9658e-02$	3.21	$7.6161e-04$	2.00
$2.5963e-03$	3.20	$4.3880e-07$	2.99	$5.6080e-03$	3.15	$1.9047e-04$	2.00
$2.9717e-04$	3.13	$5.5011e-08$	3.00	$6.5967e-04$	3.09	$4.7622e-05$	2.00

Table C.17
Approximation errors for $P_{\text{ref}} = 1 \times 10^4\,\text{Pa}, U_{\text{ref}} = 1\,\text{m}$ in the validation test case 2 in 2D. Local bases of degree $k = 1$ have been used. The fluid pressure $p_h|_K$ was taken in $P^{k+1}(K)$.

$e^{\sigma}_{h,\text{rel}}$	e.c.r.	$e^{u}_{h,\text{rel}}$	e.c.r.	$e^{v}_{h,\text{rel}}$	e.c.r.	$e^{p}_{h,\text{rel}}$	e.c.r.
$1.2974e+01$	-	$6.8121e+04$	-	$8.2089e-01$	-	$3.9167e+01$	-
$2.6880e+01$	-1.05	$7.7707e+04$	-0.19	$1.3521e+00$	-0.72	$6.0584e+01$	-0.63
$1.9811e+01$	0.44	$5.4491e+04$	0.51	$7.6147e-01$	0.83	$4.2564e+01$	0.51
$1.1597e+01$	0.77	$2.6187e+04$	1.06	$3.9461e-01$	0.95	$2.3866e+01$	0.83
$7.7878e+00$	0.57	$1.5571e+04$	0.75	$5.4963e-01$	-0.48	$1.6046e+01$	0.57
$6.2401e+00$	0.32	$1.1648e+04$	0.42	$2.7818e-01$	0.98	$1.2725e+01$	0.33
$e^{\overline{u}}_{h,\text{rel}}$	e.c.r.	$e^{\overline{p}}_{h,\text{rel}}$	e.c.r.	$e^{\hat{u}}_{h,\text{rel}}$	e.c.r.	$e^{\hat{p}}_{h,\text{rel}}$	e.c.r.
$6.2200e+04$	-	$3.0496e+01$	-	$7.4287e+04$	-	$4.1732e+01$	-
$7.6857e+04$	-0.31	$5.4891e+01$	-0.85	$8.0277e+04$	-0.11	$8.3134e+01$	-0.99
$5.4154e+04$	0.51	$4.0415e+01$	0.44	$5.4638e+04$	0.56	$5.1960e+01$	0.68
$2.6110e+04$	1.05	$2.3106e+01$	0.81	$2.6088e+04$	1.07	$2.7533e+01$	0.92
$1.5553e+04$	0.75	$1.5798e+01$	0.55	$1.5541e+04$	0.75	$1.7577e+01$	0.65
$1.1644e+04$	0.42	$1.2656e+01$	0.32	$1.1636e+04$	0.42	$1.3405e+01$	0.39

Table C.18
Effect of reducing the temporal step size Δt in the linear time dependent test case 3 in 2D. The mesh was fixed and Δt was taken as $\Delta t = T/r$ with $r = [20, 40, 80, 160, 320, 640, 1280, 2560]$. We used the formulation with $p_h|_K \in P^{k+1}(K), k = 1$. Absolute errors increase as Δt decreases.

e_h^σ	e.c.r.	e_h^u	e.c.r.	e_h^v	e.c.r.	e_h^p	e.c.r.
$1.2999e+01$	-	$4.4127e-01$	-	$3.9682e+00$	-	$1.6738e+00$	-
$2.7748e+01$	-1.09	$8.2154e-01$	-0.90	$7.8989e+00$	-0.99	$3.3292e+00$	-0.99
$5.7654e+01$	-1.06	$1.5988e+00$	-0.96	$1.5702e+01$	-0.99	$6.6171e+00$	-0.99
$1.2184e+02$	-1.08	$3.1623e+00$	-0.98	$3.1256e+01$	-0.99	$1.3171e+01$	-0.99
$2.6150e+02$	-1.10	$6.3069e+00$	-1.00	$6.2333e+01$	-1.00	$2.6267e+01$	-1.00
$5.5674e+02$	-1.09	$1.2666e+01$	-1.01	$1.2447e+02$	-1.00	$5.2450e+01$	-1.00
$1.1529e+03$	-1.05	$2.5373e+01$	-1.00	$2.4874e+02$	-1.00	$1.0481e+02$	-1.00
$2.3389e+03$	-1.02	$5.0785e+01$	-1.00	$4.9726e+02$	-1.00	$2.0954e+02$	-1.00
$e_h^{\overline{u}}$	e.c.r.	$e_h^{\overline{p}}$	e.c.r.	$e_h^{\hat{u}}$	e.c.r.	$e_h^{\hat{p}}$	e.c.r.
$4.4031e-01$	-	$1.6726e+00$	-	$8.9520e-01$	-	$3.3843e+00$	-
$8.1980e-01$	-0.90	$3.3269e+00$	-0.99	$1.6668e+00$	-0.90	$6.7315e+00$	-0.99
$1.5954e+00$	-0.96	$6.6125e+00$	-0.99	$3.2440e+00$	-0.96	$1.3379e+01$	-0.99
$3.1556e+00$	-0.98	$1.3162e+01$	-0.99	$6.4141e+00$	-0.98	$2.6632e+01$	-0.99
$6.2934e+00$	-1.00	$2.6248e+01$	-1.00	$1.2777e+01$	-0.99	$5.3109e+01$	-1.00
$1.2638e+01$	-1.01	$5.2414e+01$	-1.00	$2.5639e+01$	-1.00	$1.0605e+02$	-1.00
$2.5317e+01$	-1.00	$1.0474e+02$	-1.00	$5.1336e+01$	-1.00	$2.1193e+02$	-1.00
$5.0674e+01$	-1.00	$2.0939e+02$	-1.00	$1.0273e+02$	-1.00	$4.2367e+02$	-1.00

Table C.19
Effect of reducing the temporal step size Δt in the linear time dependent test case 3 in 2D. The mesh was fixed and Δt was taken as $\Delta t = T/r$ with $r = [20, 40, 80, 160, 320, 640, 1280, 2560]$. We used the formulation with $p_h|_K \in P^{k+1}(K), k = 4$. Absolute errors decrease linearly with Δt as expected.

e_h^σ	e.c.r.	e_h^u	e.c.r.	e_h^v	e.c.r.	e_h^p	e.c.r.
$3.8573e+00$	-	$1.7429e-01$	-	$4.2036e-01$	-	$1.8066e-01$	-
$1.9404e+00$	0.99	$8.7882e-02$	0.99	$2.0830e-01$	1.01	$8.9518e-02$	1.01
$9.7162e-01$	1.00	$4.4158e-02$	0.99	$1.0357e-01$	1.01	$4.4509e-02$	1.01
$4.8599e-01$	1.00	$2.2134e-02$	1.00	$5.1640e-02$	1.00	$2.2187e-02$	1.00
$2.4303e-01$	1.00	$1.1083e-02$	1.00	$2.5786e-02$	1.00	$1.1078e-02$	1.00
$1.2152e-01$	1.00	$5.5472e-03$	1.00	$1.2896e-02$	1.00	$5.5394e-03$	1.00
$6.0792e-02$	1.00	$2.7794e-03$	1.00	$6.4757e-03$	0.99	$2.7784e-03$	1.00
$3.0694e-02$	0.99	$1.4009e-03$	0.99	$3.3082e-03$	0.97	$1.4108e-03$	0.98
$e_h^{\overline{u}}$	e.c.r.	$e_h^{\overline{p}}$	e.c.r.	$e_h^{\hat{u}}$	e.c.r.	$e_h^{\hat{p}}$	e.c.r.
$1.7389e-01$	-	$1.8055e-01$	-	$3.5396e-01$	-	$3.6571e-01$	-
$8.7680e-02$	0.99	$8.9465e-02$	1.01	$1.7848e-01$	0.99	$1.8121e-01$	1.01
$4.4056e-02$	0.99	$4.4483e-02$	1.01	$8.9679e-02$	0.99	$9.0100e-02$	1.01
$2.2084e-02$	1.00	$2.2174e-02$	1.00	$4.4952e-02$	1.00	$4.4913e-02$	1.00
$1.1057e-02$	1.00	$1.1072e-02$	1.00	$2.2506e-02$	1.00	$2.2426e-02$	1.00
$5.5345e-03$	1.00	$5.5361e-03$	1.00	$1.1262e-02$	1.00	$1.1213e-02$	1.00
$2.7731e-03$	1.00	$2.7768e-03$	1.00	$5.6380e-03$	1.00	$5.6239e-03$	1.00
$1.3977e-03$	0.99	$1.4099e-03$	0.98	$2.8301e-03$	0.99	$2.8547e-03$	0.98

Table C.20
Linear stationary validation test in 3D. Relative errors for different triangulations with the lowest order method $k = 1$.

$e^{\sigma}_{h,\text{rel}}$	e.c.r.	$e^{u}_{h,\text{rel}}$	e.c.r.	$e^{v}_{h,\text{rel}}$	e.c.r.	$e^{p}_{h,\text{rel}}$	e.c.r.
$5.8651e-01$	-	$3.7733e+00$	-	$5.8901e-01$	-	$2.7938e+00$	-
$1.9029e-01$	1.62	$5.2659e-01$	2.84	$1.9146e-01$	1.62	$3.2981e-01$	3.08
$5.4064e-02$	1.82	$6.6167e-02$	2.99	$5.2890e-02$	1.86	$4.0593e-02$	3.02
$1.4252e-02$	1.92	$8.6656e-03$	2.93	$1.3590e-02$	1.96	$5.0043e-03$	3.02
$3.5835e-03$	1.99	$1.1659e-03$	2.89	$3.4223e-03$	1.99	$6.2271e-04$	3.01
$8.8788e-04$	2.01	$1.5304e-04$	2.93	$8.5727e-04$	2.00	$7.7741e-05$	3.00
$2.2053e-04$	2.01	$1.9587e-05$	2.97	$2.1444e-04$	2.00	$9.8088e-06$	2.99
$e^{\overline{u}}_{h,\text{rel}}$	e.c.r.	$e^{\overline{p}}_{h,\text{rel}}$	e.c.r.	$e^{\hat{u}}_{h,\text{rel}}$	e.c.r.	$e^{\hat{p}}_{h,\text{rel}}$	e.c.r.
$2.2057e-01$	-	$2.1711e-01$	-	$1.6371e+00$	-	$6.4946e-01$	-
$3.6397e-02$	2.60	$1.9903e-02$	3.45	$2.2443e-01$	2.87	$2.0757e-01$	1.65
$9.3696e-03$	1.96	$1.8717e-03$	3.41	$5.1621e-02$	2.12	$5.8367e-02$	1.83
$2.1757e-03$	2.11	$1.4869e-04$	3.65	$1.2873e-02$	2.00	$1.5047e-02$	1.96
$3.8523e-04$	2.50	$1.2718e-05$	3.55	$3.1699e-03$	2.02	$3.7914e-03$	1.99
$5.6174e-05$	2.78	$1.2987e-06$	3.29	$7.8409e-04$	2.02	$9.4972e-04$	2.00
$7.4849e-06$	2.91	$1.3766e-06$	-0.08	$1.9539e-04$	2.00	$2.3755e-04$	2.00

Table C.21
Linear stationary validation test in 3D. Relative errors for different triangulations and polynomial degree $k = 2$.

$e^{\sigma}_{h,\text{rel}}$	e.c.r.	$e^{u}_{h,\text{rel}}$	e.c.r.	$e^{v}_{h,\text{rel}}$	e.c.r.	$e^{p}_{h,\text{rel}}$	e.c.r.
$2.7380e-01$	-	$1.5294e+00$	-	$3.0596e-01$	-	$1.0503e+00$	-
$5.2196e-02$	2.39	$1.3228e-01$	3.53	$5.3969e-02$	2.50	$8.4262e-02$	3.64
$7.4312e-03$	2.81	$8.7767e-03$	3.91	$7.5438e-03$	2.84	$5.5677e-03$	3.92
$9.6430e-04$	2.95	$5.6320e-04$	3.96	$9.7195e-04$	2.96	$3.5212e-04$	3.98
$1.2110e-04$	2.99	$3.5896e-05$	3.97	$1.2248e-04$	2.99	$2.2067e-05$	4.00
$1.5112e-05$	3.00	$2.2678e-06$	3.98	$1.5345e-05$	3.00	$1.3804e-06$	4.00
$4.3342e-06$	1.80	$2.0254e-06$	0.16	$2.1608e-05$	-0.49	$5.2700e-05$	-5.25
$e^{\overline{u}}_{h,\text{rel}}$	e.c.r.	$e^{\overline{p}}_{h,\text{rel}}$	e.c.r.	$e^{\hat{u}}_{h,\text{rel}}$	e.c.r.	$e^{\hat{p}}_{h,\text{rel}}$	e.c.r.
$3.6265e-02$	-	$6.1856e-03$	-	$5.2212e-01$	-	$2.3047e-01$	-
$2.4286e-03$	3.90	$1.3067e-03$	2.24	$5.5574e-02$	3.23	$6.4748e-02$	1.83
$1.6708e-04$	3.86	$4.0284e-05$	5.02	$7.0207e-03$	2.98	$9.1884e-03$	2.82
$1.1195e-05$	3.90	$1.1525e-06$	5.13	$8.9948e-04$	2.96	$1.1859e-03$	2.95
$7.1904e-07$	3.96	$4.9457e-08$	4.54	$1.1337e-04$	2.99	$1.4943e-04$	2.99
$4.5498e-08$	3.98	$3.0374e-08$	0.70	$1.4220e-05$	3.00	$1.8717e-05$	3.00
$2.0206e-06$	-5.47	$5.2706e-05$	-10.76	$2.6904e-06$	2.40	$5.2888e-05$	-1.50

Table C.22
Linear stationary validation test in 3D. Relative errors for different triangulations and polynomial degree $k = 3$.

$e^{\sigma}_{h,\mathrm{rel}}$	e.c.r.	$e^{u}_{h,\mathrm{rel}}$	e.c.r.	$e^{v}_{h,\mathrm{rel}}$	e.c.r.	$e^{p}_{h,\mathrm{rel}}$	e.c.r.
$1.3595e-01$	-	$7.1002e-01$	-	$1.1059e-01$	-	$3.3265e-01$	-
$1.2275e-02$	3.47	$2.9841e-02$	4.57	$1.2670e-02$	3.13	$1.9008e-02$	4.13
$8.6573e-04$	3.83	$1.0069e-03$	4.89	$8.8195e-04$	3.84	$6.4094e-04$	4.89
$5.6073e-05$	3.95	$3.2042e-05$	4.97	$5.6660e-05$	3.96	$2.0413e-05$	4.97
$3.5428e-06$	3.98	$1.0055e-06$	4.99	$3.5663e-06$	3.99	$6.4120e-07$	4.99
$2.2223e-07$	3.99	$3.1484e-08$	5.00	$2.2382e-07$	3.99	$4.2202e-08$	3.93
$e^{\overline{u}}_{h,\mathrm{rel}}$	e.c.r.	$e^{\overline{p}}_{h,\mathrm{rel}}$	e.c.r.	$e^{\hat{u}}_{h,\mathrm{rel}}$	e.c.r.	$e^{\hat{p}}_{h,\mathrm{rel}}$	e.c.r.
$3.4352e-03$	-	$3.9899e-04$	-	$1.8337e-01$	-	$1.9518e-01$	-
$1.4701e-04$	4.55	$3.9320e-05$	3.34	$1.3031e-02$	3.81	$1.6669e-02$	3.55
$4.0412e-06$	5.19	$9.0138e-07$	5.45	$8.7319e-04$	3.90	$1.1762e-03$	3.82
$8.9659e-08$	5.49	$2.0902e-08$	5.43	$5.6107e-05$	3.96	$7.5774e-05$	3.96
$1.9885e-09$	5.49	$1.5048e-08$	0.47	$3.5539e-06$	3.98	$4.7719e-06$	3.99
$1.4265e-09$	0.48	$3.7148e-08$	-1.30	$2.2361e-07$	3.99	$3.0113e-07$	3.99

Table C.23
Nonlinear stationary validation test in 3D. Relative errors for different triangulations for $k = 1$.

$e^{\sigma}_{h,\mathrm{rel}}$	e.c.r.	$e^{u}_{h,\mathrm{rel}}$	e.c.r.	$e^{v}_{h,\mathrm{rel}}$	e.c.r.	$e^{p}_{h,\mathrm{rel}}$	e.c.r.
$5.8560e-01$	-	$3.7739e+00$	-	$5.7216e-01$	-	$1.5595e+00$	-
$1.9016e-01$	1.62	$5.2699e-01$	2.84	$1.9608e-01$	1.54	$1.7695e-01$	3.14
$5.4090e-02$	1.81	$6.6165e-02$	2.99	$5.4205e-02$	1.85	$2.1287e-02$	3.06
$1.4261e-02$	1.92	$8.6607e-03$	2.93	$1.3923e-02$	1.96	$2.6112e-03$	3.03
$3.5848e-03$	1.99	$1.1655e-03$	2.89	$3.5050e-03$	1.99	$3.2412e-04$	3.01
$8.8800e-04$	2.01	$1.5302e-04$	2.93	$8.7760e-04$	2.00	$4.0420e-05$	3.00
$e^{\overline{u}}_{h,\mathrm{rel}}$	e.c.r.	$e^{\overline{p}}_{h,\mathrm{rel}}$	e.c.r.	$e^{\hat{u}}_{h,\mathrm{rel}}$	e.c.r.	$e^{\hat{p}}_{h,\mathrm{rel}}$	e.c.r.
$2.1789e-01$	-	$2.8152e-01$	-	$1.6398e+00$	-	$6.5767e-01$	-
$3.6065e-02$	2.59	$2.0765e-02$	3.76	$2.2451e-01$	2.87	$2.0758e-01$	1.66
$9.2859e-03$	1.96	$1.9281e-03$	3.43	$5.1582e-02$	2.12	$5.8357e-02$	1.83
$2.1676e-03$	2.10	$1.9609e-04$	3.30	$1.2869e-02$	2.00	$1.5047e-02$	1.96
$3.8480e-04$	2.49	$2.1915e-05$	3.16	$3.1697e-03$	2.02	$3.7914e-03$	1.99
$5.6157e-05$	2.78	$2.5769e-06$	3.09	$7.8409e-04$	2.02	$9.4972e-04$	2.00

Table C.24
Nonlinear stationary validation test in 3D. Relative errors for different triangulations for $k = 2$.

$e^{\sigma}_{h,\mathrm{rel}}$	e.c.r.	$e^{u}_{h,\mathrm{rel}}$	e.c.r.	$e^{v}_{h,\mathrm{rel}}$	e.c.r.	$e^{p}_{h,\mathrm{rel}}$	e.c.r.
$2.7103e-01$	-	$1.5306e+00$	-	$3.1379e-01$	-	$5.0867e-01$	-
$5.2179e-02$	2.38	$1.3235e-01$	3.53	$5.7713e-02$	2.44	$4.3798e-02$	3.54
$7.4349e-03$	2.81	$8.7764e-03$	3.91	$7.9869e-03$	2.85	$2.9665e-03$	3.88
$9.6473e-04$	2.95	$5.6310e-04$	3.96	$1.0395e-03$	2.94	$1.8966e-04$	3.97
$1.2112e-04$	2.99	$3.5893e-05$	3.97	$1.3135e-04$	2.98	$1.1911e-05$	3.99
$1.5113e-05$	3.00	$2.2677e-06$	3.98	$1.6465e-05$	3.00	$7.4617e-07$	4.00
$e^{\overline{u}}_{h,\mathrm{rel}}$	e.c.r.	$e^{\overline{p}}_{h,\mathrm{rel}}$	e.c.r.	$e^{\hat{u}}_{h,\mathrm{rel}}$	e.c.r.	$e^{\hat{p}}_{h,\mathrm{rel}}$	e.c.r.
$3.6417e-02$	-	$9.0363e-03$	-	$5.2096e-01$	-	$2.3427e-01$	-
$2.4610e-03$	3.89	$1.0237e-03$	3.14	$5.5530e-02$	3.23	$6.4804e-02$	1.85
$1.6938e-04$	3.86	$4.9414e-05$	4.37	$7.0177e-03$	2.98	$9.1887e-03$	2.82
$1.1265e-05$	3.91	$2.0191e-06$	4.61	$8.9938e-04$	2.96	$1.1859e-03$	2.95
$7.2048e-07$	3.97	$8.9102e-08$	4.50	$1.1337e-04$	2.99	$1.4943e-04$	2.99
$4.5527e-08$	3.98	$3.7285e-08$	1.26	$1.4220e-05$	3.00	$1.8717e-05$	3.00

Table C.25
Nonlinear stationary validation test in 3D. Relative errors for different triangulations for $k = 3$.

$e^{\sigma}_{h,\mathrm{rel}}$	e.c.r.	$e^{u}_{h,\mathrm{rel}}$	e.c.r.	$e^{v}_{h,\mathrm{rel}}$	e.c.r.	$e^{p}_{h,\mathrm{rel}}$	e.c.r.
$1.3585e-01$	-	$7.1027e-01$	-	$1.0280e-01$	-	$1.5989e-01$	-
$1.2273e-02$	3.47	$2.9852e-02$	4.57	$1.2878e-02$	3.00	$1.0129e-02$	3.98
$8.6592e-04$	3.83	$1.0070e-03$	4.89	$1.1027e-03$	3.55	$4.1431e-04$	4.61
$5.6077e-05$	3.95	$3.2042e-05$	4.97	$7.3590e-05$	3.91	$1.3648e-05$	4.92
$3.5429e-06$	3.98	$1.0055e-06$	4.99	$4.6780e-06$	3.98	$4.3294e-07$	4.98
$2.2224e-07$	3.99	$3.1492e-08$	5.00	$2.9413e-07$	3.99	$4.6424e-08$	3.22
$e^{\overline{u}}_{h,\mathrm{rel}}$	e.c.r.	$e^{\overline{p}}_{h,\mathrm{rel}}$	e.c.r.	$e^{\hat{u}}_{h,\mathrm{rel}}$	e.c.r.	$e^{\hat{p}}_{h,\mathrm{rel}}$	e.c.r.
$3.5841e-03$	-	$1.9569e-03$	-	$1.8335e-01$	-	$1.9563e-01$	-
$1.4595e-04$	4.62	$6.0481e-05$	5.02	$1.3018e-02$	3.82	$1.6664e-02$	3.55
$4.0175e-06$	5.18	$1.6777e-06$	5.17	$8.7305e-04$	3.90	$1.1766e-03$	3.82
$8.9508e-08$	5.49	$4.0178e-08$	5.38	$5.6106e-05$	3.96	$7.5781e-05$	3.96
$2.0140e-09$	5.47	$1.8273e-08$	1.14	$3.5539e-06$	3.98	$4.7721e-06$	3.99
$1.6045e-09$	0.33	$4.4418e-08$	-1.28	$2.2361e-07$	3.99	$3.0213e-07$	3.98

Table C.26
Linear time dependent validation test in 3D. Absolute errors for different triangulations for $k = 1$.

e_h^{σ}	e.c.r.	e_h^{u}	e.c.r.	e_h^{v}	e.c.r.	e_h^{p}	e.c.r.
$1.5427e+03$	-	$1.3390e+01$	-	$2.4186e+02$	-	$1.0673e+02$	-
$7.9359e+02$	0.96	$3.1514e+00$	2.09	$9.8780e+01$	1.29	$4.2899e+01$	1.32
$3.9514e+02$	1.01	$1.0838e+00$	1.54	$5.3687e+01$	0.88	$2.3340e+01$	0.88
$1.9970e+02$	0.98	$4.9133e-01$	1.14	$2.6979e+01$	0.99	$1.1736e+01$	0.99
$1.3484e+13$	-35.97	$1.8634e+10$	-35.14	$7.9870e+11$	-34.79	$7.9007e+10$	-32.65
$e_h^{\overline{u}}$	e.c.r.	$e_h^{\overline{p}}$	e.c.r.	$e_h^{\hat{u}}$	e.c.r.	$e_h^{\hat{p}}$	e.c.r.
$1.0356e+00$	-	$9.5653e+01$	-	$1.2499e+01$	-	$2.6304e+02$	-
$2.6855e+00$	-1.37	$4.1535e+01$	1.20	$4.2620e+00$	1.55	$6.8960e+01$	1.93
$1.0017e+00$	1.42	$2.3159e+01$	0.84	$1.1409e+00$	1.90	$2.5666e+01$	1.43
$4.7885e-01$	1.06	$1.1713e+01$	0.98	$3.7164e-01$	1.62	$8.9629e+00$	1.52
$1.0285e+10$	-34.32	$7.1964e+10$	-32.52	$1.0255e+10$	-34.68	$3.9138e+10$	-32.02

Table C.27
Linear time dependent validation test in 3D. Absolute errors for different triangulations for $k = 2$.

e_h^{σ}	e.c.r.	e_h^{u}	e.c.r.	e_h^{v}	e.c.r.	e_h^{p}	e.c.r.
$4.2423e+02$	-	$4.5936e+00$	-	$5.5461e+01$	-	$2.5077e+01$	-
$7.5376e+01$	2.49	$1.0569e+00$	2.12	$6.6159e+00$	3.07	$2.8754e+00$	3.12
$2.1277e+01$	1.82	$1.3458e-01$	2.97	$2.3205e+00$	1.51	$1.0155e+00$	1.50
$9.5236e+00$	1.16	$3.6604e-02$	1.88	$1.0983e+00$	1.08	$4.8038e-01$	1.08
$4.6957e+00$	1.02	$1.8551e-02$	0.98	$5.4570e-01$	1.01	$2.3864e-01$	1.01
$e_h^{\overline{u}}$	e.c.r.	$e_h^{\overline{p}}$	e.c.r.	$e_h^{\hat{u}}$	e.c.r.	$e_h^{\hat{p}}$	e.c.r.
$2.6065e+00$	-	$2.1087e+01$	-	$9.4588e+00$	-	$6.1608e+01$	-
$9.5821e-01$	1.44	$2.7791e+00$	2.92	$1.3696e+00$	2.79	$4.7213e+00$	3.71
$1.2344e-01$	2.96	$1.0078e+00$	1.46	$1.1987e-01$	3.51	$1.1187e+00$	2.08
$3.6036e-02$	1.78	$4.7946e-01$	1.07	$2.8057e-02$	2.10	$3.6716e-01$	1.61
$1.8480e-02$	0.96	$2.3853e-01$	1.01	$9.9850e-03$	1.49	$1.2776e-01$	1.52

Table C.28
Linear time dependent validation test in 3D. Absolute errors for different triangulations for $k = 3$.

e_h^{σ}	e.c.r.	e_h^{u}	e.c.r.	e_h^{v}	e.c.r.	e_h^{p}	e.c.r.
$1.9470e+02$	-	$1.6007e+00$	-	$2.5045e+01$	-	$1.1036e+01$	-
$4.4014e+01$	2.15	$1.5927e-01$	3.33	$5.3221e+00$	2.23	$2.3295e+00$	2.24
$1.9236e+01$	1.19	$7.5442e-02$	1.08	$2.2241e+00$	1.26	$9.7234e-01$	1.26
$9.3870e+00$	1.04	$3.7522e-02$	1.01	$1.0925e+00$	1.03	$4.7767e-01$	1.03
$1.2018e+02$	-3.68	$9.9671e-02$	-1.41	$5.4540e-01$	1.00	$2.3848e-01$	1.00
$e_h^{\overline{u}}$	e.c.r.	$e_h^{\overline{p}}$	e.c.r.	$e_h^{\hat{u}}$	e.c.r.	$e_h^{\hat{p}}$	e.c.r.
$6.5877e-01$	-	$9.6628e+00$	-	$2.9660e+00$	-	$2.8412e+01$	-
$1.3836e-01$	2.25	$2.2606e+00$	2.10	$2.6385e-01$	3.49	$3.7734e+00$	2.91
$7.1678e-02$	0.95	$9.6498e-01$	1.23	$8.4774e-02$	1.64	$1.0709e+00$	1.82
$3.6989e-02$	0.95	$4.7676e-01$	1.02	$2.8898e-02$	1.55	$3.6507e-01$	1.55
$2.6116e-02$	0.50	$2.3837e-01$	1.00	$5.2602e-02$	-0.86	$1.2767e-01$	1.52

Table C.29
Nonlinear time dependent validation test in 3D. Absolute errors for different triangulations for $k = 1$.

e_h^σ	e.c.r.	e_h^u	e.c.r.	e_h^v	e.c.r.	e_h^p	e.c.r.
$3.0986e+02$	-	$5.7947e-01$	-	$1.8003e+00$	-	$1.8635e+02$	-
$6.4209e+01$	2.27	$1.3817e-01$	2.07	$9.7686e-01$	0.88	$3.6275e+01$	2.36
$3.9916e+00$	4.01	$1.1459e-02$	3.59	$5.2948e-01$	0.88	$7.6172e-01$	5.57
$1.9946e+00$	1.00	$4.7935e-03$	1.26	$2.6595e-01$	0.99	$2.5376e-01$	1.59
$6.7731e+11$	-38.30	$9.0106e+08$	-37.45	$4.9870e+10$	-37.45	$2.5109e+11$	-39.85
$e_h^{\overline{u}}$	e.c.r.	$e_h^{\overline{p}}$	e.c.r.	$e_h^{\hat{u}}$	e.c.r.	$e_h^{\hat{p}}$	e.c.r.
$4.3122e-01$	-	$1.7049e+02$	-	$1.1298e+00$	-	$3.4916e+02$	-
$1.2870e-01$	1.74	$3.5200e+01$	2.28	$2.0035e-01$	2.50	$5.4613e+01$	2.68
$1.0657e-02$	3.59	$7.5520e-01$	5.54	$1.2154e-02$	4.04	$8.3691e-01$	6.03
$4.6687e-03$	1.19	$2.5327e-01$	1.58	$3.6313e-03$	1.74	$1.9377e-01$	2.11
$5.0632e+08$	-36.66	$2.2525e+11$	-39.69	$4.9473e+08$	-36.99	$1.4392e+11$	-39.43

VITA

VITA

Education :

- 2013–2016: Ph.D. in Applied Mathematics, Indiana University-Purdue University Indianapolis (IUPUI), Indianapolis, IN, USA.
- 2007–2012: M.Sc. in Mathematical Engineering, Politecnico di Milano, Milano, Italy. US equivalence: Master of Science in Applied Mathematics.
- B2003–2007: B.Sc. in Aerospace Engineering, Politecnico di Milano, Milano, Italy.

Work experience :

- 2013–2016: Graduate Teaching Assistant, IUPUI, Indianapolis, IN, USA.
  - MATH 16500: Analytic Geometry and Calculus I.
  - MATH 16600: Analytic Geometry and Calculus II.
  - MATH 26100: Multivariate Calculus.
- 2015, 2016: visiting student at the Institut de Recherche en Mathématiques, Interactions et Applications (LabEx IRMIA), Université de Strasbourg, Strasbourg, France.
- Fall 2015: Instructor, IUPUI, Indianapolis, IN, USA. MATH 22100: Calculus for Technology I.
- February 2011–October 2011: Trainee, ABB Switzerland Ltd, Corporate Research, Dättwil.

Selected publications :

- P. Causin, G. Guidoboni, A. Harris, D. Prada, R. Sacco, and S. Terragni. A poroelastic model for the perfusion of the lamina cribrosa in the optic nerve head. Mathematical Biosciences, 257(0):33 41, 2014.

- D. Prada, M. Bellini, I. Stevanovic, L. Lemaitre, J. Victory, J. Vobecky, R. Sacco, and P. Lauritzen. On the performance of multiobjective evolutionary algorithms in automatic parameter extraction of power diodes. Power Electronics, IEEE Transactions on, 30(9):49864997, September 2015.
- D. Prada, A. Harris, G. Guidoboni, B. Siesky, A. M. Huang, and J. Arciero. Autoregulation and neurovascular coupling in the optic nerve head. Survey of Ophthalmology, 61(2):164186, 2016.
- A. Hungria, D. Prada and F. J. Sayas, HDG methods for elastodynamics, 2016, arXiv:1611.05824.